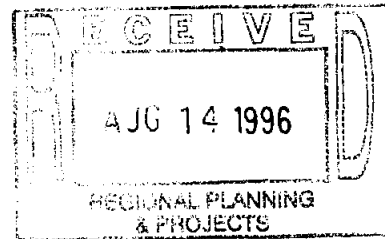# NUMERICAL STUDY OF THIN-FILM

FLOWS AND OPEN-CHANNEL FLOWS

Srinivas Chippada

Rice University
Department of Mechanical Engineering and Materials Science

February 1996

Acknowledgments

NUMERICAL STUDY OF THIN-FILM FLOWS AND OPEN-CHANNEL FLOWS

Srinivas Chippada

Abstract

A numerical procedure is developed capable of simulating gravity-driven film flows in two-dimensions. The moving boundary problem is handled through the ALE formulation. In the case of turbulent fluid flows, the two-equations $k - \epsilon$ closure model is used to model the turbulence. A Chorin-type projection scheme is utilized to decouple the velocity and pressure fields, and the spatial discretization is done using the Finite Element Method.

Thin liquid films draining down vertical or inclined planes are susceptible to long wavelength disturbances. An extensive numerical study of the surface wave instability in isothermal thin film flows is done by solving the full-scale nonlinear system. Temporal stability analysis of a spatially periodic disturbance reveals interesting wave dynamics. The transition from nearly sinusoidal supercritical waves to broad-banded solitary waves is found to go through a quasi-periodic regime. In this quasi-periodic state, the fundamental mode and several of its harmonics are in an oscillatory state, with continuous exchange of energy. An extensive parametric search has been done to obtain the phase boundary delineating the quasi-periodic regime. Complex wave interactions such as wave-splitting and wave-merging are discussed. Spatial stability analysis akin to the usual experimental studies is done and comparisons are made with the experiments.

For the development of successful theories capable of predicting the formation of bedforms, it is essential to understand the turbulent fluid flow on top of the bed. To this end, mean flow and turbulence characteristics for flow over artificial stream-wise periodic bedforms are obtained. Due to the local accelerations associated with stream-line bending, very large velocities and stresses are found to exist at the tip of the dune. The separation wake turbulence is found to completely dominate the wall-generated turbulence, and the maximum turbulence intensity levels occur at a distance, approximately equal to the dune height, away from the bed. The accuracy of the rigid-lid approximation is determined by computing the flow field with and without the rigid-lid approximation. The rigid-lid approximation is found to over-predict the shear at the dune crest.

Lastly, the mean flow and turbulence characteristics in hydraulic jump are obtained. In the case of flow with inlet supercritical Froude number 2.0, a small recirculation zone is found to exist at the foot of the jump. The mixing layer turbulence associated with the surface roller and the recirculation zone are found to dominate the wall-generated turbulence.

R	radius of curvature
s	specific density of sediment
S_b	total bed load transport across a cross-section
S_s	total suspended load transport across a cross-section
t	time
T	non-dimensional transport parameter
Δt	time increment
u	velocity component in the x-direction
u_*	shear velocity at the bed
$u_{*,cr}$	critical shear velocity for threshold motion
U	mean velocity in the x-direction
v	velocity component in the y-direction
w^x	mesh particle velocity in the x direction
w^y	mesh particle velocity in the y direction
w_s	suspended sediment particle fall velocity
(x,y,z)	Cartesian coordinates
$\mathbf{X}$	Material coordinates
$\mathbf{x}$	spatial coordinates
$\hat{\mathbf{x}}$	referential coordinates
Z	non-dimensional suspension parameter
x_i	Cartesian coordinate in i-th direction
$\Delta x, \Delta y$	spatial increment in x and y directions

Greek Letters

| ϵ | turbulent dissipation rate |

κ	von Karman const.
μ	coefficient of viscosity
∇	$\left(\frac{\partial}{\partial x}, \frac{\partial}{\partial y}\right)$, gradient operator
ν	laminar kinematic viscosity
ν_T	turbulent kinematic viscosity
Φ_α	shape function
ρ	fluid density
σ	surface tension
σ_{ij}	stress tensor
τ	tangential direction
τ_c	critical shear stress for threshold motion given by Shields
τ_w	shear stress at the wall
θ	angle of inclination of the bed with the horizontal; also, referred to as energy slope

Subscripts

i, j, k	directions of Cartesian coordinate
t	derivative with time
x	derivative w. r. t. x
α, β, γ	nodal number
$, i$	partial derivative w. r. t. x_i

Superscripts

n	n-th time steps
$*$	refers to dimensional value
$\prime$	fluctuating quantity

Nondimensional Numbers

Fr Froude number. $Fr = \frac{U}{\sqrt{gH}}$

G Thickness parameter. $G = \frac{gh_0^3}{\nu^2}$

Re Reynolds number. $Re = \frac{UH}{\nu}$

S Surface tension parameter. $S = \frac{\sigma h_0}{3\rho\nu^2}$

T $\sigma / \left(3\rho\nu^{4/3} g^{1/3} \right)$

We Weber number. $We = \frac{U}{\sqrt{\frac{\sigma}{\rho H}}}$

Note: Only the most important symbols are listed above. The symbols are defined the first time they are used. Symbols are also subject to alteration on occasion.

Table of Contents

List of Figures

List Of Tables

Chapter 1

Introduction

1.1 Motivation

In recent years, due to the tremendous progress achieved in computer architecture and computational algorithms, numerical modeling is being increasingly used in the study of many scientific and engineering problems. Computational Fluid Dynamics (CFD) has evolved into a powerful tool and is used not only in simulating industrial and naturally occurring fluid flows, but also in the deeper understanding of the subject of Fluid Mechanics itself. For example, CFD models based on the Direct Numerical Simulation (DNS) are being used in understanding the very difficult problem of *turbulence*. In this dissertation, a numerical model is developed capable of simulating a variety of gravity-driven free surface flows.

The fluid flow problems numerically simulated are the *thin-film* flows and *open-channel* flows. Both, *thin-film* flows and *open-channel* flows are geometrically similar and belong to the same class of gravity-driven flows, shown in Fig.1.1. Gravity is the driving force and drag at the solid wall due to fluid viscosity is the opposing force. The difference between the two flows, is mainly due to the vastly different length scales. In *thin-film* flows, the film thickness is very small and is in the order of millimeters. Consequently, surface tension is very important and generates surface waves of the gravity-capillary type on the gas-liquid interface. The fluid flow, however, is laminar in nature. In *open-channel* flows, the film is very thick, usually in the order of meters, and the fluid flow is almost always turbulent in

nature. Surface tension is not significant in these scales, and the interfacial waves are primarily of the gravity-type.

The motivation for studying thin-film flows arise from their film cooling and film coating applications. The interfacial waves on the gas-liquid interface are known to increase heat and mass transfer in both the liquid and gaseous phases. Open-channel flows have applications in several areas of hydraulics, geology and sedimentology. In the vast field of open-channel flow hydraulics itself, we study in detail two fluid flow phenomena. First is the study of turbulent fluid flow over artificial bedforms. A detailed mean flow and turbulence field is essential for understanding the formation of bedform features such as ripples, dunes and anti-dunes. The second problem studied is the hydraulic jump, which is known to occur in supercritical open-channel flows. The free surface rises abruptly and intense turbulent mixing takes place in the jump region. Due to their energy dissipating capability, the hydraulic jumps are widely used in dams, spillways and other outlet works.

1.2　Course of the study

The fluid flow is governed by the continuum conservation of mass and conservation of momentum equations, and these are described in chapter 2. Also stated are the important non-dimensional numbers arising in the gravity-driven fluid flows. The various flow regimes pertaining to the simple flow over an inclined plane are also discussed.

The biggest challenge in simulating these gravity-driven flows comes from the presence of a free boundary, which in our case is the air-liquid interface. Its location is usually not known *a priori*, and needs to be determined as part of the solution. A mixed Eulerian- Lagrangian procedure called the Arbitrary Lagrangian- Eulerian
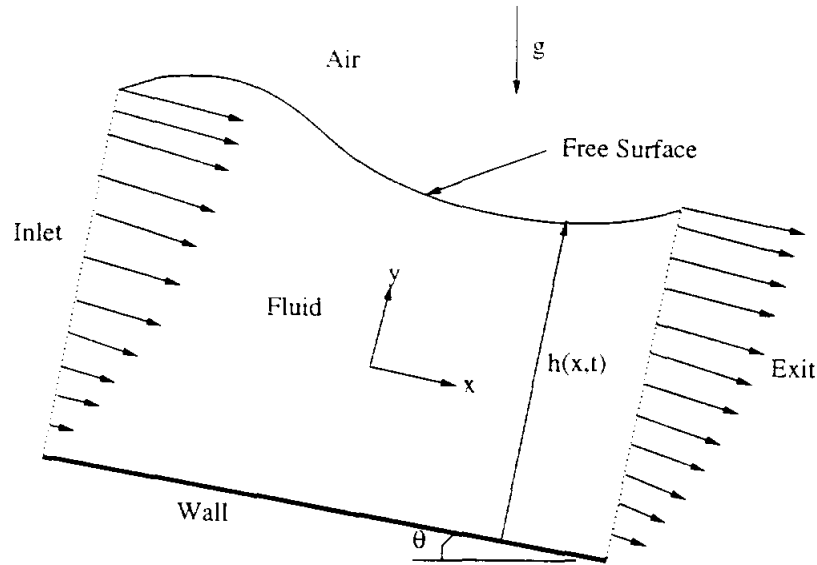
Figure 1.1: Gravity-driven flow over an inclined plane

(ALE) formulation is employed to handle the moving boundary, and the essential aspects of this procedure are described in chapter 3.

In open-channel flows, the fluid flow is almost always turbulent in nature. Even though it is believed by many, that an accurate and direct solution of the Navier–Stokes equations can simulate turbulence, the present computational resources prohibit such an effort for realistic fluid-flow problems. At the moment, there is no recourse except to solve the Reynolds Averaged Navier–Stokes (RANS) equations, and this is what is done in this work. In addition, a two-equation $k - \epsilon$ model along with Boussinesq Eddy Viscosity hypothesis is used, and the essential features of this turbulence modeling are described briefly in chapter 4.

The spatial and temporal discretization aspects of the Navier–Stokes equations are briefly outlined in chapter 5. The presence of the boundary conditions in terms of pressure, makes the primitive variable $(u - v - p)$ formulation, the popular method of choice in the numerical simulation of these moving boundary problems. A Chorin-

type splitting scheme is used to decouple the pressure from the velocities, thus permitting us to solve for u, v and p in a sequential manner. The Galerkin Finite Element method with three-node triangular elements are employed in the spatial discretization.

Chapters 2-5 explain the mathematical and numerical aspects of our model. The next three chapters deal with specific applications.

Thin-film flows are of crucial importance in many heat transfer equipment and coating applications. A variety of fascinating interfacial dynamics occur in these flows and these are studied in detail in chapter 6. The approach used is similar to classical hydrodynamic stability analysis. Disturbances of different wavelengths and frequencies are imposed on the basic solution, and the interfacial stability is characterized based on the response of the system to these disturbances.

In open-channel flows themselves, we simulate two very important and difficult problems. First, is the turbulent fluid flow over artificial streamwise periodic bed-forms (chapter 7). The formation of ripples, dunes and anti-dunes on the river bed is due to a complex interplay between the turbulent fluid flow, sediment transport and bed dynamics. Thus, an understanding of the turbulent fluid flow over the artificial bedforms is an important step in the understanding of the formation of bedforms. The second problem simulated is the celebrated *hydraulic jump*. The formation of hydraulic jump in open-channel flows, is marked with the presence of high gradient regions which are very hard to simulate. The hydraulic jump is analogous to the shock formation in compressible flows and is studied in chapter 8.

Finally, some general conclusions and future research directions are discussed in chapter 9.

Chapter 2

Flow Over An Inclined Plane

2.1 Introduction

Though, the fluid flow problems considered in this work have application in widely different areas of engineering, the underlying physics is the same and can be modeled as viscous fluid flowing down an inclined plane under the action of gravity (Fig.1.1). The fluid domain is bounded below by an impermeable and rigid wall and above by a gas-liquid interface, which is free to deform. The planar wall is inclined at an angle θ with the horizontal. x-axis is aligned in the streamwise direction and the and y-axis is perpendicular to it. The gas-liquid interface is represented as height $h(x,t)$ from the x-axis. Gravity is the driving force and the drag at the solid-liquid interface is the opposing force. However, these two primary forces are not always in balance, thus, giving rise to additional forces such as inertial forces, pressure forces and capillary forces. All of these forces play an important role in determining the internal and external dynamics of the fluid flow.

2.2 Governing Equations

In nature, the fluid flow problems are always three-dimensional. However, we restrict ourselves to only two-dimensional flows. Thus, the spanwise (z) direction length scale is assumed to be infinitely large and the fluid velocities and gradients in the z direction are neglected. We further, confine ourselves to incompressible,

Newtonian and isothermal flows only. The governing equations are the conservation of momentum as given by the Navier–Stokes equations and the conservation of mass.

$$\frac{\partial u}{\partial t} + u\frac{\partial u}{\partial x} + v\frac{\partial u}{\partial y} = -\frac{1}{\rho}\frac{\partial p}{\partial x} + g\sin\theta + \nu\nabla^2 u \tag{2.1}$$

$$\frac{\partial v}{\partial t} + u\frac{\partial v}{\partial x} + v\frac{\partial v}{\partial y} = -\frac{1}{\rho}\frac{\partial p}{\partial y} - g\cos\theta + \nu\nabla^2 v \tag{2.2}$$

$$\frac{\partial u}{\partial x} + \frac{\partial v}{\partial y} = 0 \tag{2.3}$$

$u = u(x, y, t)$ and $v = v(x, y, t)$ are the instantaneous fluid velocities in x and y directions respectively, and $p = p(x, y, t)$ is the instantaneous pressure. $\nabla^2 = \left(\frac{\partial^2}{\partial x^2} + \frac{\partial^2}{\partial y^2}\right)$ is the Laplacian operator and $\nabla = \left(\frac{\partial}{\partial x}, \frac{\partial}{\partial y}\right)$ is the gradient operator. ρ and ν are the liquid density and kinematic viscosity, respectively. The Eqs.2.1-2.3 are for the liquid phase. A similar set of equations are also required for the gaseous phase. However, in the applications considered in this work, the density of gaseous phase (usually air) is in general much smaller than the density of the liquid phase (usually water). The gaseous phase can then be assumed to be passive and the fluid motions in that phase can be neglected, and no equations need to be solved in the gaseous phase. The position of the gas-liquid interface is completely determined by the fluid dynamics in the liquid phase alone, and in such situations, the gas-liquid interface is also referred to as a *free surface*. Eqs.2.1-2.3 represent a set of three coupled partial differential equations to be solved for the three unknowns u, v and p. However, the equations do not form a closed set since the fluid domain or the free surface height $h(x, t)$ is not known *a priori* and needs to be determined also.

2.3 Boundary Conditions

To solve the system of Eqs.2.1-2.3, boundary conditions are required. On the wall boundary, the familiar no-slip and impermeability conditions are imposed as follows:

$$\left.\begin{array}{rcl} u & = & 0 \\ \\ v & = & 0 \end{array}\right\} \text{ at } y = 0. \tag{2.4}$$

The boundary conditions at the free surface $y = h(x,t)$, are more complicated and involve the fluid stresses. The stresses in the liquid and gaseous phase are related through the interfacial tension as follows:

$$\left.\begin{array}{rcl} \left(-p + 2\mu\dfrac{\partial u_n}{\partial n}\right)_l & = & \left(-p + 2\mu\dfrac{\partial u}{\partial n}\right)_g + \dfrac{\sigma}{R} \\ \\ \mu_l\left(\dfrac{\partial u_n}{\partial \tau} + \dfrac{\partial u_\tau}{\partial n}\right)_l & = & \mu_g\left(\dfrac{\partial u_n}{\partial \tau} + \dfrac{\partial u_\tau}{\partial n}\right)_g \end{array}\right\} \text{ at } y = h(x,t). \tag{2.5}$$

The subscripts l and g refer to the liquid and gaseous phases. σ is the surface tension, and n and τ are the unit normal and tangential directions on the free surface $y = h(x,t)$. μ is the dynamic viscosity. R is the radius of curvature at the free surface and is calculated as follows:

$$\frac{1}{R} = \frac{\frac{\partial^2 h}{\partial x^2}}{\left[1 + \left(\frac{\partial h}{\partial x}\right)^2\right]^{3/2}} \tag{2.6}$$

Since, the gaseous phase is assumed to be passive, the dynamic normal and tangential stresses in the gaseous phase are neglected and the stress boundary conditions at the interface simplify to:

$$\left.\begin{array}{rcl} -p + 2\mu\dfrac{\partial u_n}{\partial n} & = & -p_g + \dfrac{\sigma}{R} \\ \\ \dfrac{\partial u_n}{\partial \tau} + \dfrac{\partial u_\tau}{\partial n} & = & 0 \end{array}\right\} \text{ at } y = h(x,t). \tag{2.7}$$

p_g is the pressure in the gaseous phase and it is assumed to be spatially nonvarying and set to a datum pressure of zero. Additional simplifications can be made depending on the practical application being modeled. In the case of open channel flows the film depth is quite large and the gravitational and inertial forces dominate the capillary forces and the surface tension term in the free surface boundary condition can be neglected. However, in thin film flows this is not the case and surface tension cannot be neglected. In fact it is the interfacial tension which is responsible for the onset of wave motion in the case of thin film flows.

The above described boundary conditions at the free surface are only the dynamic boundary conditions. In addition to those dynamic stress boundary conditions we also need to satisfy the kinematic condition as follows:

$$(u_n)_l = (u_n)_i = (u_n)_g \quad \text{at} \quad y = h(x,t). \tag{2.8}$$

The subscript i refers to the interface. The above condition can be reformulated to represent the gas-liquid as a material interface resulting in the following boundary condition at the interface:

$$\frac{\partial h}{\partial t} + u\frac{\partial h}{\partial x} = v \quad \text{at} \quad y = h(x,t). \tag{2.9}$$

The above kinematic condition is the usually imposed boundary condition at the interface along with the stress conditions given by Eq.2.7.

A variety of boundary conditions at the the inlet and exit boundaries have been used, and they are stated in the later chapters dealing with applications.

2.4 Nondimensionalization

Considerable insight can be gained into the physics of the fluid flow through nondimensionalization. Let H be the characteristic length and U the characteristic velocity. Typically, H can be taken to be the mean film thickness and U the average velocity. The nondimensional parameters are denoted with a superscript $*$. The nondimensional independent variables are defined as:

$$x^* = x/H \quad ; \quad y^* = y/H \quad ; \quad t^* = tU/H. \tag{2.10}$$

The nondimensional dependent variables are defined as:

$$u^* = u/U \quad ; \quad v^* = v/U \quad ; \quad p^* = p/(\rho U^2) \quad ; \quad h^* = h/H. \tag{2.11}$$

Based on the above defined scaling, the nondimensional governing equations are given by:

$$\frac{\partial u^*}{\partial t^*} + u^* \frac{\partial u^*}{\partial x^*} + v^* \frac{\partial u^*}{\partial y^*} = -\frac{\partial p^*}{\partial x^*} + \frac{1}{Fr^2} \sin\theta + \frac{1}{Re} \left(\frac{\partial^2 u^*}{\partial x^{*2}} + \frac{\partial^2 u^*}{\partial y^{*2}} \right) \tag{2.12}$$

$$\frac{\partial v^*}{\partial t^*} + u^* \frac{\partial v^*}{\partial x^*} + v^* \frac{\partial v^*}{\partial y^*} = -\frac{\partial p^*}{\partial y^*} - \frac{1}{Fr^2} \cos\theta + \frac{1}{Re} \left(\frac{\partial^2 v^*}{\partial x^{*2}} + \frac{\partial^2 v^*}{\partial y^{*2}} \right) \tag{2.13}$$

$$\frac{\partial u^*}{\partial x^*} + \frac{\partial v^*}{\partial y^*} = 0 \tag{2.14}$$

The boundary conditions also need to be nondimensionalized, and they are written as:

$$u^* = v^* = 0 \quad \text{at} \quad y = 0; \tag{2.15}$$

$$
\left.
\begin{aligned}
\frac{1}{Re}\left(\frac{\partial u_\tau^*}{\partial n} + \frac{\partial u_n^*}{\partial \tau}\right) &= 0 \\
-p^* + \frac{2}{Re}\frac{\partial u_n^*}{\partial n} &= -p_g^* + \frac{1}{We^2 R^*} \\
\frac{\partial h^*}{\partial t^*} + u^*\frac{\partial h^*}{\partial x^*} &= v^*
\end{aligned}
\right\} \quad \text{at } y^* = h^*(x^*, t^*). \tag{2.16}
$$

The nondimensional numbers that fall out from the above nondimensionalization procedure are:

- $Re = (\rho U H)/\mu$, the Reynolds number[1].

- $Fr = U/\sqrt{gH}$, the Froude number[2].

- $We = U/\sqrt{\sigma/(\rho H)}$, the Weber number[3].

The nature of the film flow is largely determined by the Reynolds number, the Weber number, and the Froude number. Similar to the flow through pipes, the Reynolds number determines the transition form laminar to turbulent flow. The critical Reynolds. for transition to turbulence in the case of gravity-driven flows over inclined planes has been found to $Re_{crit} = 250 - 500$ (Fulford 1964). The Froude number is the ratio of fluid velocity to the celerity of the gravity wave, and determines the onset of gravity waves in water films. For Froude numbers in the range $Fr = 1 - 2$, gravity waves appear on the free surface (Fulford 1964). Weber number is the ratio of fluid velocity to the celerity of the capillary wave, and determines the onset of capillary waves in water films. The capillary waves appear on the water surface in the range of $We = 1$ (Fulford 1964).

---

[1] Alternate definition of Reynolds number based on the hydraulic radius have been used by some researchers.

[2] Some researchers define the Froude number as $Fr = U^2/(gH)$.

[3] Many alternate definitions of the Weber number exist, such as, $We = \sigma/(\rho U^2 H)$, and $We = \sigma/(\rho g H^2)$.

Chapter 3

Numerical Modeling of the Free Boundary Problem

3.1 Introduction

Boundary/Initial value problems in which the fluid domain has an unknown physical boundary and which needs to be determined as part of the solution procedure are called moving boundary problems or free boundary problems (Floryan & Rasmussen 1989). Problems of this nature are of interest in open channel flows, phase change problems, jets, flame propagation, groundwater seepage, metal forming processes, draining film flows, and various other fields of engineering and science. The unknown boundary is usually an interface between liquid and gas or two immiscible liquids or fluid and solid. Moving boundary problems are highly nonlinear and analytical solutions are extremely difficult to obtain. Hence, numerical methods are widely used in the modeling of free boundary problems.

All numerical methods developed to handle moving boundaries can be divided into the following two categories: interface capturing and interface tracking (Floryan & Rasmussen 1989). In the interface capturing methods, the physical details of the interface are resolved. No special attention need be paid to the interface with the possible exception of use of fine mesh in the vicinity of the interface. The nonlinearity in this case is material in nature with sharply changing fluid properties across the interface. In the interface tracking procedures, the physical details of the interface are not resolved and the interface is modeled as a discontinuity and explicitly

tracked. The nonlinearity in this case is a geometrical one, with an unknown fluid domain. The fluid domains of interest to us are bounded below by a solid wall and above a moving gas-liquid interface (Fig.1.1). The interface between the liquid and gas has a finite thickness spanning a few molecular diameters. It is extremely difficult to resolve this thin layer, and hence, the interface is often modeled as a surface with zero thickness (discontinuity). This gives rise to an excess surface energy, which is nothing but the interfacial tension or the surface tension. The numerical procedure developed and used in this work is an interface tracking algorithm.

The interface tracking algorithms can further be classified as: (i) Eulerian; (ii) Lagrangian; and (iii) mixed Eulerian-Lagrangian methods. In the Eulerian description of flow, the grid points are stationary in the laboratory frame of reference and the fluid moves in and out of the computational cells. The Marker and Cell (MAC) method (Harlow & Welch 1966) and the volume of Fluid (VOF) method (Hirt & Nichols 1981) are some of the popular and successful Eulerian methods developed to handle moving boundary problems. The Eulerian methods can handle arbitrarily large free surface deformations without significant loss of accuracy. The main disadvantage of these methods is that the interface is not sharply defined and it is difficult to impose boundary conditions at the interface. In the Lagrangian methods, the grid points move with the local fluid velocity, and the fluid within a computational cell remains within that cell at all times. The main advantages are that the interface is sharply defined and the boundary conditions at the interface are easier to impose. The main disadvantage is mesh tangling and the loss of accuracy due to severe mesh distortion. Hirt, Cook & Butler (1970) developed a pure Lagrangian procedure to handle incompressible fluid flows with free boundaries. Various mixed Eulerian-Lagrangian methods have been developed to combine the

advantages of pure Lagrangian and pure Eulerian methods without their disadvantages. The method used in this work to handle moving boundaries belongs to the mixed Eulerian-Lagrangian family and is called the Arbitrary Lagrangian-Eulerian (ALE) method.

An universal method capable of handling all types of free boundary problems is not yet available. The numerical method that is to be chosen is strongly dependent on the physical problem that is to be modeled. Our primary interest is the study of liquid flow down inclined planes with a physical geometry that is usually of the form shown in Fig.1.1. The important features of this geometry are: (i) logically rectangular geometry; (ii) existence of a strong mean flow; (iii) free surface deformation normal to the mean flow; and (iv) the representation of the air-liquid interface as a single-valued function of the stream-wise co-ordinate x. For this type of problem it is advantageous to let the grid points move only in the y-direction without moving them in the x-direction. This is what is done in our ALE formulation.

3.2   ALE formulation

The ALE description of the fluid flow is also called the referential kinematic description of flow, since the governing equations are written in a frame of reference that is moving independently of the fluid motion. The ALE method is usually attributed to Amsden & Hirt (1973). A number of extensions of this work have been proposed since then, and has been widely used in the modeling of several fluid flow problems (e.g. Hirt, Amsden & Cook 1974; Chan 1975; Pracht 1975; Hughes, Liu & Zimmerman 1981; Ramaswamy & Kawahara 1987a; Huerta & Liu 1988; Soulaimani, Fortin, Dhatt & Ouellet 1991) and fluid-structure interaction problems (e.g. Donea, Giuliani & Halleaux 1982; Donea 1983; Belytschko & Flanagan 1982; Liu, Chang,

Chen & Belytschko 1988). The ALE formulation has been derived by Donea etal (1982), Ramaswamy & Kawahara (1987a), Soulaimani etal (1991), Lacroix & Garon (1992), among many others, and is briefly described next.

Let B_0 be the open region occupied by the fluid at time $t = 0$ (Fig.3.1). The position vector of point P in the material domain is denoted by $\mathbf{X} = (\mathbf{X_1}, \mathbf{X_2})$; and $\mathbf{X}$ are called the material coordinates. Note that, a two-dimensional space is being assumed, and the extension to three-dimensions is straight forward. B_t is the open region occupied by the fluid body B_0 at some later time $t > 0$. The position vector of the point p in the spatial domain B_t is denoted by $\mathbf{x} = (\mathbf{x_1}, \mathbf{x_2})$; and $\mathbf{x}$ are called the spatial coordinates. The mapping from the material domain to the spatial domain is written as:

$$\mathbf{x} = \phi(\mathbf{X}, \mathbf{t}) \tag{3.1}$$

It is assumed that the above mapping is continuous, single-valued and possesses a unique inverse Eulerian description of the form:

$$\mathbf{X} = \phi^{-1}(\mathbf{x}, \mathbf{t}) \tag{3.2}$$

In the Lagrangian formulation, the fluid motion is described in terms of the material coordinates $\mathbf{X}$, and the frame of reference translates along with the material point $\mathbf{X}$. The material or Lagrangian velocity is defined as:

$$\dot{\phi}(\mathbf{X}, \mathbf{t}) = \frac{\partial}{\partial t}\phi(\mathbf{X}, \mathbf{t}), \tag{3.3}$$

and the material acceleration is defined as:

$$\ddot{\phi}(\mathbf{X}, \mathbf{t}) = \frac{\partial^2}{\partial t^2}\phi(\mathbf{X}, \mathbf{t}) \tag{3.4}$$
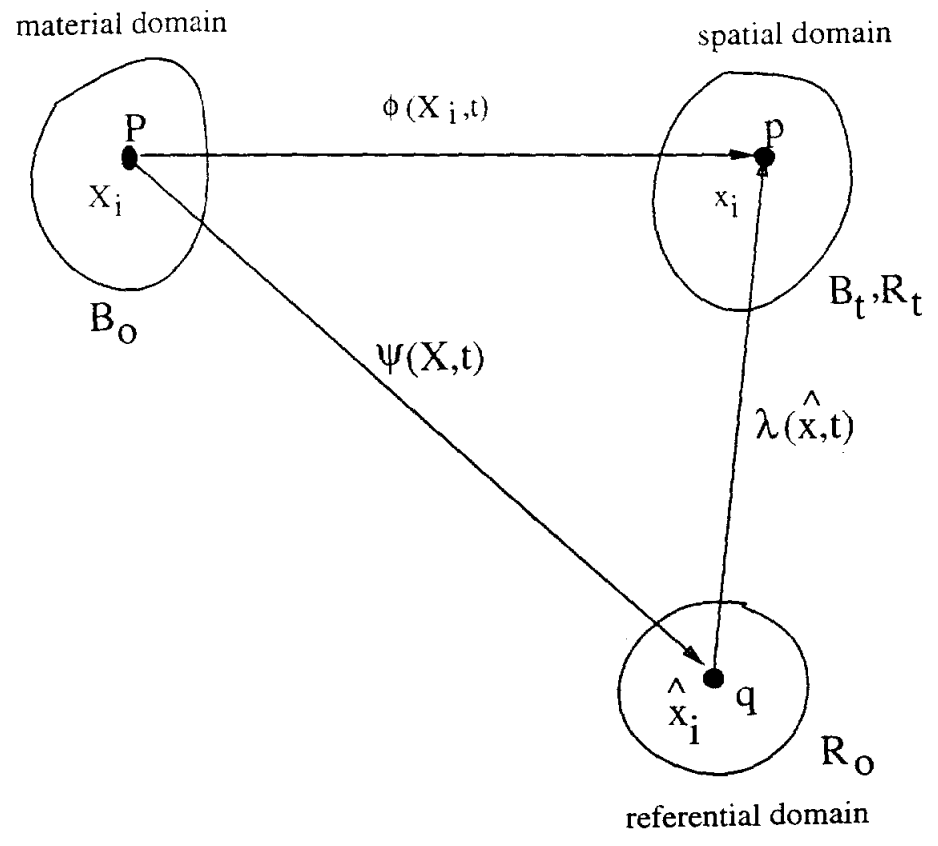
Figure 3.1: Referential kinematic description

The Lagrangian description of motion is widely used in the Solid Mechanics studies. Note that, no nonlinear convective terms arise in this formulation. A pure Lagrangian formulation in Fluid Mechanics is seldom used, since the trajectories of the fluid particles are very complex and the numerical meshes can get very distorted and entangled.

In the spatial or Eulerian formulation, the motion is followed in terms of the spatial coordinates $\mathbf{x}$. This amounts to a frame of reference that is fixed or moving with a predefined velocity. The spatial or Eulerian velocity is defined as:

$$\mathbf{u}(\mathbf{x}, t) = \frac{\partial}{\partial t}\phi(\mathbf{X}, t)|_{\mathbf{X}=\phi^{-1}(\mathbf{x},t)} = \frac{\partial}{\partial t}\phi(\mathbf{x}, t) \tag{3.5}$$

The Eulerian acceleration can be shown to be of the following form:

$$\mathbf{a}(\mathbf{x}, t) = \frac{\partial}{\partial t}\mathbf{u}(\phi(\mathbf{X}, t), t)|_{\mathbf{X}=\phi^{-1}(\mathbf{x},t)} = \frac{\partial \mathbf{u}}{\partial t}(\mathbf{x}, t) + \mathbf{u}(\mathbf{x}, t) \cdot \nabla \mathbf{u}(\mathbf{x}, t) \tag{3.6}$$

Note that in the Eulerian description of flow, nonlinear advection terms appear. The Eulerian description of flow is widely used in the Fluid Mechanics studies. The nonlinear advective terms $\mathbf{u}(\mathbf{x}, t) \cdot \nabla \mathbf{u}(\mathbf{x}, t)$ are the main cause for most of the difficulties in the Fluid Mechanics studies.

In the ALE formulation, a third domain called the referential domain R is defined as shown in Fig.3.1. At time $t = 0$, it occupies an open region R_0. The referential body has its own independent motion and coincides with the material body B_t at some later time $t > 0$, i.e. $R_t \equiv B_t$. The referential coordinates are written as $\hat{\mathbf{x}} = (\hat{\mathbf{x}}_1, \hat{\mathbf{x}}_2)$. The referential point q arrives at the spatial point p at time t through the referential motion λ defined as:

$$\mathbf{x} = \lambda(\hat{\mathbf{x}}, t). \tag{3.7}$$

The velocity of the referential motion $w(x,t)$ is given by:

$$w(x,t) = \frac{\partial}{\partial t}\lambda(\hat{x},t)\,|_{\hat{x}=\lambda^{-1}(x,t)}. \tag{3.8}$$

All the quantities defined on the referential domain are denoted with a superscript hat. For example,

$$w(x,t) = w(\lambda(\hat{x},t),t) = \hat{w}(\hat{x},t). \tag{3.9}$$

The relative motion of the fluid body with respect to the referential motion can be expressed as:

$$\hat{x} = \lambda^{-1}(x,t) = \lambda^{-1}(\phi(X,t),t) = \psi(X,t). \tag{3.10}$$

The relative velocity of the fluid motion with respect to the referential motion can be written as:

$$\hat{V}^{\psi}(\hat{x},t) = \frac{\partial}{\partial t}\psi(X,t)|_{X=\psi^{-1}(\hat{x},t)} \tag{3.11}$$

The material point P and referential point q arrive at the spatial point p through independent motions, which are related as follows:

$$x = \lambda(\hat{x},t) = \lambda(\psi(X,t),t) = \phi(X,t). \tag{3.12}$$

From the above relation, we can derive the following:

$$\begin{aligned}
u(x,t) = \hat{u}(\hat{x},t) &= \frac{\partial}{\partial t}\lambda(\psi(X,t),t)\,|_{X=\psi^{-1}(\hat{x},t)} \\
&= \frac{\partial\lambda}{\partial t}(\hat{x},t) + \hat{F}(\hat{x},t)\,\hat{V}^{\psi}(\hat{x},t) \\
&= \hat{w}(\hat{x},t) + \hat{F}(\hat{x},t)\,\hat{V}^{\psi}(\hat{x},t)
\end{aligned} \tag{3.13}$$

The deformation gradient $\hat{F}(\hat{x},t)$ is defined as:

$$\hat{F}_{ij}(\hat{\mathbf{x}}, \mathbf{t}) = \frac{\partial \mathbf{x_i}}{\partial \hat{\mathbf{x}_j}} \tag{3.14}$$

The spatial acceleration in the referential coordinates can be shown to be:

$$
\begin{aligned}
a(\mathbf{x}, \mathbf{t}) &= \hat{a}(\hat{\mathbf{x}}, \mathbf{t}) = \frac{\partial}{\partial t}\hat{\mathbf{u}}(\hat{\mathbf{x}}, \mathbf{t})|_{\mathbf{X}=\psi^{-1}(\hat{\mathbf{x}}, \mathbf{t})} \\
&= \frac{\partial}{\partial t}\hat{\mathbf{u}}(\hat{\mathbf{x}}, \mathbf{t}) + \left(\hat{\mathbf{V}}^{\psi}(\hat{\mathbf{x}}, \mathbf{t}) \cdot \hat{\nabla}\right)\hat{\mathbf{u}}(\hat{\mathbf{x}}, \mathbf{t})
\end{aligned} \tag{3.15}
$$

From Eq.3.13, $\hat{V}^{\psi}$ is replaced in the above equation resulting in:

$$\hat{\mathbf{a}}(\hat{\mathbf{x}}, \mathbf{t}) = \frac{\partial \mathbf{u}}{\partial \mathbf{t}}(\hat{\mathbf{x}}, \mathbf{t}) + \left[\left(\hat{\mathbf{F}}^{-1}\left(\hat{\mathbf{u}} - \hat{\mathbf{w}}\right)\right) \cdot \hat{\nabla}\right]\hat{\mathbf{u}}(\hat{\mathbf{x}}, \mathbf{t}) \tag{3.16}$$

The above expression, represents the fluid acceleration in the referential kinematic description. Comparing the spatial acceleration (Eq.3.6) with the referential acceleration (Eq.3.16), the difference is that gradients are with respect to the referential coordinates and the spatial velocity $\mathbf{u}(\mathbf{x}, \mathbf{t})$ is replaced with the relative velocity $\hat{V}^{\psi}$.

The conservation of momentum equation in the spatial description is given by:

$$\rho(\mathbf{x}, \mathbf{t})(\frac{\partial \mathbf{u}}{\partial \mathbf{t}}(\mathbf{x}, \mathbf{t}) + \mathbf{u}(\mathbf{x}, \mathbf{t}) \cdot \nabla \mathbf{u}(\mathbf{x}, \mathbf{t})) = \rho(\mathbf{x}, \mathbf{t})\mathbf{f}(\mathbf{x}, \mathbf{t}) + \nabla \cdot \sigma(\mathbf{x}, \mathbf{t}), \tag{3.17}$$

where $\rho(\mathbf{x}, \mathbf{t})$ is the local fluid density, $\mathbf{f}(\mathbf{x}, \mathbf{t})$ is the body force, $\sigma(\mathbf{x}, \mathbf{t})$ is the Cauchy stress tensor, and $\nabla(\mathbf{x}, \mathbf{t})$ is the divergence operator. In the referential kinematic description, the above momentum conservation equation becomes:

$$
\begin{aligned}
\hat{\rho}(\mathbf{x}, \mathbf{t})\hat{\mathbf{J}}\left[\frac{\partial \hat{\mathbf{u}}}{\partial \mathbf{t}}(\hat{\mathbf{x}}, \mathbf{t}) + \left(\left(\hat{\mathbf{F}}^{-1}\left(\hat{\mathbf{u}} - \hat{\mathbf{w}}\right)\right) \cdot \hat{\nabla}\right)\hat{\mathbf{u}}(\hat{\mathbf{x}}, \mathbf{t})\right] &= \hat{\rho}(\hat{\mathbf{x}}, \mathbf{t})\hat{\mathbf{J}}\hat{\mathbf{f}}(\hat{\mathbf{x}}, \mathbf{t}) \\
&\quad + \hat{\nabla} \cdot \hat{\mathbf{P}}(\hat{\mathbf{x}}, \mathbf{t}),
\end{aligned} \tag{3.18}
$$

where $\hat{J} = det\,\hat{\mathbf{F}}$, and $\hat{\mathbf{P}} = \hat{J}\sigma\hat{\mathbf{F}}^{-1}$ is the Piola-Kirchoff tensor of the first kind. Similarly, the conservation of mass equation in referential description is given by:

$$\frac{\partial \hat{\rho}}{\partial t}(\hat{x}.t) + \left[\left(\hat{F}^{-1}(u - w) \right) \cdot \hat{\nabla} \right] \hat{\rho}(\hat{x}.t) + \hat{\rho}(\hat{x}.t) \left[\left(\hat{F}^{-1}\hat{\nabla} \right) \cdot \hat{u}(\hat{x},t) \right] = 0. \quad (3.19)$$

In the case of incompressible this reduces to:

$$\left(\hat{F}^{-1}\hat{\nabla} \right) \cdot \hat{u}(\hat{x},t) = 0 \quad (3.20)$$

In the case of free boundary problems, the referential motion is related to the fluid motion. For example, at the free boundary, the mesh points are moved normal to the free boundary with the fluid velocity, to prevent loss or gain of fluid material. If a discrete time-stepping procedure is used to solve the momentum and mass conservation equations, the previous time step fluid particle velocities can be used to approximate the referential motion. In that case, the time-stepping procedure is only of first order accuracy in time and the governing equations in the ALE formulation can be written as:

$$\frac{\partial u}{\partial t} + (u - w^x)\frac{\partial u}{\partial x} + (v - w^y)\frac{\partial u}{\partial y} = gsin\theta - \frac{1}{\rho}\frac{\partial p}{\partial x} + \nu\nabla^2 u \quad (3.21)$$

$$\frac{\partial v}{\partial t} + (u - w^x)\frac{\partial v}{\partial x} + (v - w^y)\frac{\partial v}{\partial y} = -gcos\theta - \frac{1}{\rho}\frac{\partial p}{\partial y} + \nabla^2 v \quad (3.22)$$

$$\frac{\partial u}{\partial x} + \frac{\partial v}{\partial y} = 0 \quad (3.23)$$

Note that if there is no referential motion, the mesh velocities $w^x = 0$ and $w^y = 0$, and the ALE formulation reduces to the Eulerian or spatial formulation. If the referential motion coincides with the fluid motion, then $w^x = u$, $w^y = v$, and the ALE formulation reduces to the Lagrangian or material formulation. The relation between the above described three formulations can be expressed as:

$$\underbrace{\frac{D}{Dt}}_{Lagrangian} \equiv \underbrace{\frac{\partial}{\partial t} + u \cdot \nabla}_{Eulerian} \equiv \underbrace{\frac{\partial}{\partial t} + (u - w) \cdot \nabla}_{ALE}. \quad (3.24)$$

3.3   The concept of vertical spines

The most important thing in the ALE approach is the choice of the referential motion. The aim is to chose a referential motion, so that the free boundary is followed accurately without severe mesh distortion. The type of problems we are interested in, provide us with a simple referential motion, that is very easy to implement. Physical domain generally consists of an inlet or upstream end where the flow enters, an exit or downstream end through which the fluid leaves, a solid-liquid interface at the bottom and a liquid-gas interface at the top (Fig.1.1). For these type of problems it is advantageous to let the grid points move in the vertical direction only, but restrict their motion in the horizontal direction. For this purpose, the free surface is parameterized using vertical spines as shown in Fig.3.2. The free surface, and consequently the numerical mesh points, slide up and down along the vertical spines. The numerical grid points are however, fixed in the horizontal direction ($w^x = 0$). This type of a referential motion, lets us follow the free surface movement accurately, without significant mesh distortion.
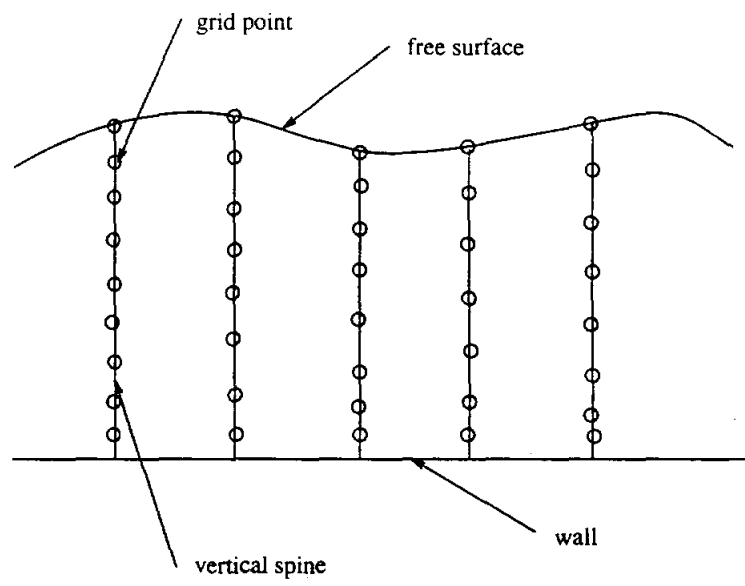
Figure 3.2: Free surface resting on vertical spines

Chapter 4

Numerical Modeling of Turbulence

4.1 Introduction

When the nondimensional Reynolds number Re, which represents the ratio of inertial forces to the viscous forces, is over a certain cut-off value Re_c, the nature of the fluid flow undergoes a drastic change, going from a well defined simple laminar flow to a highly complex irregular and random turbulent flow. Hinze(1975) defines turbulence as

> Turbulent fluid motion is an irregular condition of flow in which the various quantities show a random variation with time and space coordinates, so that statistically distinct average values can be discerned.

The most important thing to note is that even though the fluid flow may appear to be irregular and random, the statistical quantities such as mean and variance retain physical relevance. Among the applications considered in this dissertation, the open channel flows, which refers to gravity-driven flows occurring in nature such as rivers, streams, channels etc., are usually turbulent in nature. On the other hand, thin-film flows, which refer to very thin liquid films draining down vertical or inclined walls, are mostly laminar in nature.

It is believed that the 3-D Navier–Stokes equations can be used to simulate the turbulent fluid flows. The biggest challenge to numerical modeling of turbulent fluid flows comes from the existence of widely varying length scales requiring a very fine mesh to resolve all the scales of motion. A turbulent fluid flow requires Re^2 mesh

points in 2-D and $Re^{9/4}$ mesh points in 3-D, where Re is the Reynolds number. Even for a fluid flow with Reynolds number 10^4, we will need 10^8 mesh points in 2-D itself and this is far beyond the capacity of the present day computers. This leaves us with no other recourse but to model the turbulence through some approximate models. The most common approach is the Reynolds Averaging, which is described briefly in the next section.

4.2 Reynolds Averaged Equations

The Reynolds averaging procedure filters out the turbulent fluctuations from the mean flow and the resulting equations are called the Reynolds Averaged Navier–Stokes equations (RANS). The fluid velocities and pressure are expressed as the sum of the mean (in an appropriate sense) and a turbulent fluctuation as follows:

$$
\begin{aligned}
u_i &= \bar{u}_i + u_i' \\
p &= \bar{p} + p'
\end{aligned}
\tag{4.1}
$$

The mean quantities are denoted by an over bar and the fluctuating components are denoted by the superscript "'". The averaging employed could be either time averaging, or space averaging or ensemble averaging. All the averaging are identical if the ergodicity hypothesis is assumed. The Reynolds averaged continuity and momentum equations are:

$$
\frac{\partial \bar{u}_j}{\partial x_j} = 0
\tag{4.2}
$$

$$
\rho \left(\frac{\partial \bar{u}_i}{\partial t} + \frac{\partial}{\partial x_j} (\bar{u}_i \bar{u}_j) \right) = f_i + \frac{\partial}{\partial x_j} \sigma_{ij}.
\tag{4.3}
$$

σ_{ij} is the stress tensor given by:

$$\sigma_{ij} = -\bar{p}\delta_{ij} + \mu \left(\bar{u}_{i,j} + \bar{u}_{j,i} \right) - \rho \overline{u_i' u_j'}. \tag{4.4}$$

μ is the dynamic viscosity of the fluid, $u_{i,j}$ is the velocity gradient of the fluid flow, and δ_{ij} is the Kronecker delta. Due to the nonlinear advection terms the fluctuating components do not disappear with Reynolds averaging but reappear as $\overline{u_i' u_j'}$ which are called the apparent stresses or Reynolds stresses. These new quantities (six of them) are to be determined from the mean flow field and presents us with the classic closure problem. These terms are modeled using physical and dimensional arguments and the unknown coefficients are tuned using experimental data.

4.3 Eddy viscosity hypothesis

As long as the continuum assumption is not validated, the Navier–Stokes equations can be assumed to model the physics of the fluid flow accurately. Due to the Reynolds averaging, however, information is lost irretrievably. Through closure models we try to put at least part of the information back into the mathematical model. No amount of complex and accurate modeling, however, can make the RANS equations as accurate as the original Navier–Stokes equations. This is the penalty we pay for resorting to averaging.

Turbulence models can be broadly classified into Boussinesq models, and non-Boussinesq models. In the Boussinesq models, the Boussinesq Eddy Viscosity hypothesis is invoked and the Reynolds stresses are written as:

$$-\rho \overline{u_i' u_j'} = \mu_T \left(\bar{u}_{i,j} + \bar{u}_{j,i} \right) - \frac{2k}{3}\delta_{ij}, \tag{4.5}$$

where,

$$k = \frac{1}{2}\overline{u_i' u_i'}, \tag{4.6}$$

is the turbulence kinetic energy. Note that, the expression for the Reynolds stresses is analogous to the original stress tensor proposed by Stokes. The term $2k/3$ is added to the Eq.4.5 to make it valid if a contraction is applied. The term $2k/3$ can be considered as turbulent pressure. As opposed to the laminar viscosity (μ), the turbulent eddy viscosity (μ_T) is a property of the flow, and not a property of the fluid substance. Originally, Boussinesq assumed the eddy viscosity to be a constant scalar (Hinze 1975, pp.23). However, a constant scalar turbulent viscosity is not true for most realistic fluid flows. The turbulent eddy viscosity varies with space and time and is a function of the fluid flow field. It is known that, turbulence leads to intense mixing with the attendant increase in momentum diffusion. The Boussinesq Eddy Viscosity hypothesis, thus tries to model the turbulence as an increase in the effective fluid viscosity or mixing coefficient. With the Boussinesq eddy viscosity hypothesis, the stress tensor σ_{ij} is of the form:

$$\sigma_{ij} = - \left(\bar{p} + \frac{2k}{3} \right) \delta_{ij} + (\mu + \mu_T) [\bar{u}_{i,j} + \bar{u}_{j,i}] \tag{4.7}$$

Hinze (1975) has a discussion about the various admissible forms for the Reynolds stress $-\rho \overline{u_i' u_j'}$. In the above equation a scalar eddy viscosity is assumed. However, we could assume second-order eddy viscosity of the form:

$$-\rho \overline{u_i' u_j'} = (\mu_T)_{ik} [\bar{u}_{j,k} + \bar{u}_{k,j}] \tag{4.8}$$

Or else, we could also assume a fourth-order eddy viscosity of the form:

$$-\rho \overline{u_i' u_j'} = (\mu_T)_{ijkl} [\bar{u}_{k,l} + \bar{u}_{l,k}] \tag{4.9}$$

However, the above given second-order and fourth order eddy viscosity forms do not give us a stress tensor that is invariant under all rigid body motions.

An eddy viscosity hypothesis does not give us a turbulence model complete in all respects. The other alternative is to solve for the Reynolds stress $-\rho\overline{u_i' u_j'}$ directly. This usually means, we need to solve six additional partial differential equations for the six independent Reynolds stress components. However, even these models are not completely rigorous, as an effort to derive equations for the second order Reynolds stress terms results in third-order correlations of the $\overline{u_i' u_j' u_k'}$, which need to be modeled. This is the classical closure problem in turbulence, with the net result that we have more equations than unknowns. In spite of their drawbacks, the eddy viscosity models are the most commonly used turbulence models. The turbulence model used by us also makes the eddy viscosity hypothesis. Thus, we model turbulence by solving the RANS along with the Boussinesq eddy viscosity hypothesis.

4.4 Eddy viscosity models

Once we invoke the Boussinesq eddy viscosity hypothesis, the whole turbulence modeling reduces to finding the eddy viscosity (μ_T). The turbulence closure models which solve the RANS along with the Boussinesq eddy hypothesis can further be classified into:

1. Zero-equation models

2. One-equation models

3. Two-equation models

The above classification is based on the number of additional transport equations that are to be solved in addition to the RANS to compute the eddy viscosity μ_T.

The most popular of the zero-equation models is the Prandtl's mixing length hypothesis and relates the eddy viscosity to the mean velocity gradient as follows:

$$\nu_T = C_\mu l_m^2 \mid \frac{\partial \bar{u}}{\partial y} \mid .$$

(4.10)

The above relation involves a single unknown parameter, namely, the mixing length l_m, which is specified empirically. For example, in the case of boundary layer flows, the mixing length is assumed to vary linearly with the distance from the wall. In the above equation, $\nu_T = \mu_T/\rho$ is the kinematic eddy viscosity. The mixing length models are very easy to incorporate and do not increase the computational time excessively, as no additional equations need to be solved. However, they are employed in very simple shear and boundary layer flows, where it is easy to specify the mixing length. For complex flows such as separating boundary layer flows, the specification of the length scale is not straightforward and the mixing length models are rarely used in such complex flows. The turbulent fluid flows to be simulated in this dissertation are complex, involving boundary layer separations and both the wall generated turbulence mechanisms and the mixing layer turbulence mechanisms are present simultaneously. Thus, the mixing length models will be expected to perform poorly in this instances and are not considered.

A simple dimensional arguments, will show us that the eddy viscosity is influenced by a turbulent length scale and a turbulent time scale. Thus a means of evaluating these two turbulence scales are required. The one equation models attempt to compute the velocity scale through a advection-diffusion type transport equation and specify the length scale empirically. However, since the length scale is specified empirically, these models in general do not perform much better than the mixing length models. The most general turbulence model requires the solution

of two partial differential equations, to determine both the time and length scales accurately, without having to specify any of them empirically.

There are several two-equation models that have been proposed to model turbulence. Some of them are $k - kl$, $k - \omega$ and $k - \epsilon$ models. They differ from each other in the parameters that are solved for directly. The $k - l$ model solves for the turbulence kinetic energy k and the turbulence length scale l. In $k - \omega$ model, the turbulent vorticity scale is obtained in addition to the k. Whereas, in the $k - \epsilon$ model, the dissipation rate of the turbulence kinetic energy rate is computed in addition to k. No matter what we solve for, the idea is to put them together through dimensional arguments to compute the eddy viscosity. In the context of hydrodynamic flows, the two-equation $k - \epsilon$ model has been shown to give reasonably good results. According to the ASCE Task Committee (1988) appointed to look into the use of turbulence models for simulation of hydraulic flows, $k - \epsilon$ model is the one being most widely used. In this dissertation, the two-equation $k - \epsilon$ model is used which is described briefly in the next section.

4.5 $k - \epsilon$ turbulence model

k denotes the turbulence kinetic energy k and ϵ is rate of dissipation of the turbulence kinetic energy. These two variable are defined in terms of the fluctuating components as follows:

$$k = \frac{1}{2}\overline{u_i'^2}, \tag{4.11}$$

$$\epsilon = \nu \overline{\frac{\partial u_i'}{\partial x_k} \frac{\partial u_i'}{\partial x_k}} \tag{4.12}$$

The $k - \epsilon$ used by us is the one originally proposed by Launder & Spalding (1974). The turbulence quantities k and ϵ are determined through the solution of advection-diffusion type transport equations given by:

$$\frac{Dk}{Dt} = \frac{\partial}{\partial x_k}\left[\frac{\nu_T}{\sigma_k}\frac{\partial k}{\partial x_k}\right] + \nu_T\left(\frac{\partial \bar{u}_i}{\partial x_k} + \frac{\partial \bar{u}_k}{\partial x_i}\right)\frac{\partial \bar{u}_i}{\partial x_k} - \epsilon \tag{4.13}$$

$$\frac{D\epsilon}{Dt} = \frac{\partial}{\partial x_k}\left[\frac{\nu_T}{\sigma_\epsilon}\frac{\partial \epsilon}{\partial x_k}\right] + C_1\nu_T\frac{\epsilon}{k}\left(\frac{\partial \bar{u}_i}{\partial x_k} + \frac{\partial \bar{u}_k}{\partial x_i}\right)\frac{\partial \bar{u}_i}{\partial x_k} - C_2\frac{\epsilon^2}{k} \tag{4.14}$$

After finding k and ϵ, the eddy viscosity ν_T is computed from the following relation:

$$\nu_T = C_\mu k^2/\epsilon \tag{4.15}$$

The constants in these equations are (Launder & Spalding 1974):

$$C_\mu = 0.09, \quad C_1 = 1.44, \quad C_2 = 1.92, \quad \sigma_k = 1.0, \quad \sigma_\epsilon = 1.3$$

Note that, $G = \nu_T\left(\bar{u}_{i,k} + \bar{u}_{k,i}\right)\bar{u}_{i,k}$ in the above equations represent the generation of turbulence kinetic energy. The turbulence field derives its energy from the mean flow which is then cascaded into the smallest eddies where it is dissipated into heat through viscous dissipation. The ϵ terms represents this dissipation of the turbulence kinetic energy. It should be noted that, the $k - \epsilon$ model presented in this section has been originally derived for pipe flows. The open channel flows, are in some respects similar to the pipe flows. They are bounded below by a rigid wall and above by a free surface, which is in many respects similar to the centerline axis of symmetry in pipe flows. However, it has been speculated for some years that the presence of the free surface dampens the turbulence since the free surface also acts like a wall, albeit friction-less. However, no satisfactory and well-accepted turbulence models

exist for open-channel flows even though Celik (1980), among many others tried to modify the $k - \epsilon$ model to be suitable for open-channel flows.

4.6 Boundary Conditions for $k - \epsilon$ Model

The turbulence model as presented above is a high Reynolds number model and is valid only in the fully turbulent regime. However, close to the wall there exists a small layer where the viscous effects dominate over the turbulence effects (viscous sublayer). The $k - \epsilon$ turbulence model presented previously is not valid in this region. Modifications have been proposed to the original $k - \epsilon$ turbulence, so that they remain valid for low Reynolds number regions also (Launder & Spalding 1974). However, the more popular approach has been to use the original $k - \epsilon$ model itself, and specify the boundary conditions at the wall using the wall function approach. In this method, the first computational point is not placed right on the wall, but is kept at a small distance away from the wall so that it lies in the fully turbulent log layer as shown in Fig.4.1.

In the small layer close to the wall, the turbulence mechanism is assumed to be in equilibrium. That is, the generation of turbulence kinetic energy is equal to the dissipation of the turbulence kinetic energy, $G = \epsilon$, and there is no advection or diffusion of the turbulence kinetic energy. In this limit, the $k - \epsilon$ model reduces to the mixing length hypothesis, and the universal log-law is assumed to be valid close to the wall. The boundary conditions for k and ϵ are imposed as follows:

$$k_P = \frac{u_*^2}{\sqrt{C_\mu}} \tag{4.16}$$

$$\epsilon_P = \frac{u_*^3}{\kappa y_P \left(1 - e^{-y_P^+/26}\right)} \tag{4.17}$$
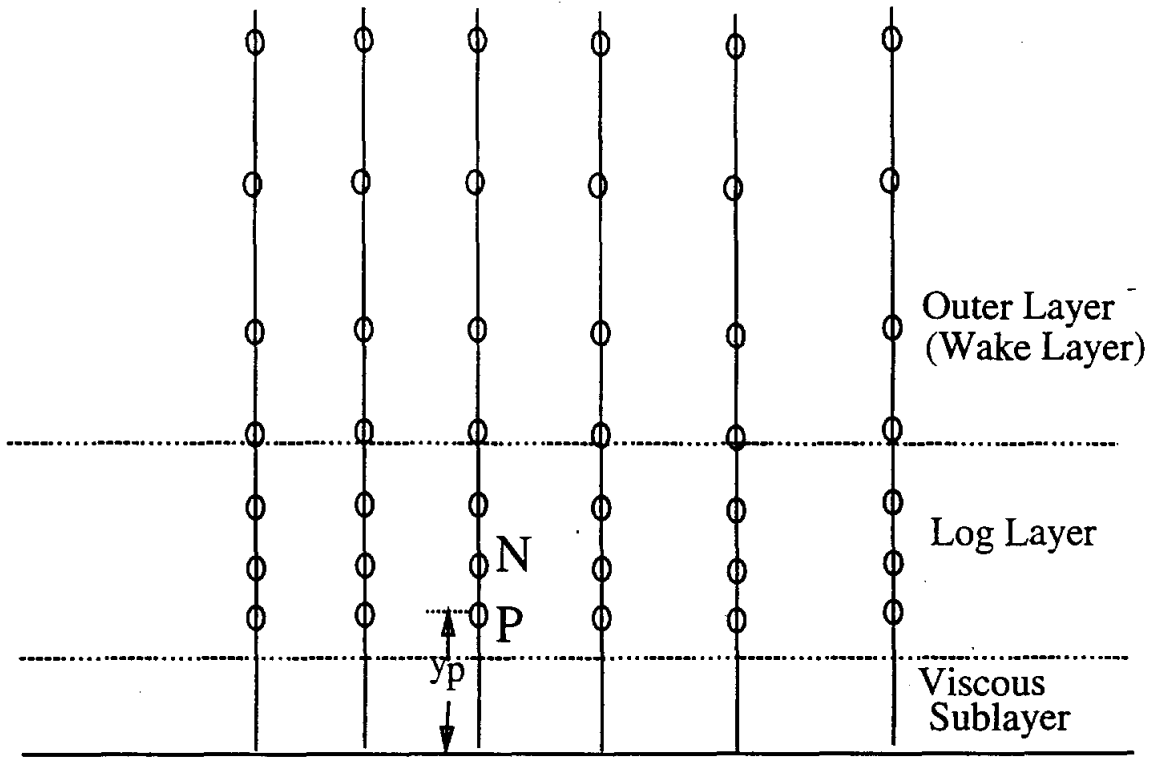
Figure 4.1: The near-wall node placement.

where, $y_P^+ = y_P u_* / \nu$, and y_P is the normal distance from the wall. The boundary conditions for u and v at the wall are imposed as:

$$u_P = \begin{cases} u_* y_P^+ & \text{if } y_P^+ < 11.6 \\ \dfrac{u_*}{\kappa} \ln \left(E y_P^+ \right) & \text{if } y_P^+ \geq 11.6 \end{cases}$$

(4.18)

$$v_P = 0$$

(4.19)

Specifying the normal velocity to be zero violates the continuity requirement, but since the wall layer is very thin, the error should be negligible. E is a function of wall roughness and is equal to 9.0 for smooth walls. Apart from convenience, the wall function approach is very advantageous computationally, since it bypasses the high gradient region close to the wall. Moreover, information pertaining to factors such as wall roughness, pressure gradient, curvature etc. can be introduced through these wall functions. To determine the friction velocity $u_* = \sqrt{\tau_w / \rho}$, the approach proposed by Benim & Zinser (1985). It is assumed that u_N lies on the same logarithmic curve as u_P, and the friction velocity is computed as (see Fig.4.1):

$$u_* = \begin{cases} u_N / y_N^+ & \text{if } y_N^+ < 11.6 \\ \kappa u_N / \ln \left(E y_N^+ \right) & \text{if } y_N^+ \geq 11.6 \end{cases}$$

(4.20)

At the free surface the normal gradients of k and ϵ are taken to be zero (plane of symmetry).

$$\left. \begin{array}{l} \dfrac{\partial k}{\partial n} = 0 \\[2mm] \dfrac{\partial \epsilon}{\partial n} = 0 \end{array} \right\} \quad \text{at} \quad y = h(x, t)$$

(4.21)

Boundary conditions at the inlet and exit are problem specific. In this dissertation we use periodic conditions in our modeling of the turbulent fluid flow over

artificial bedforms (chapter 7). In the hydraulic jump simulation (chapter 8), the following boundary conditions k and ϵ are imposed at the inlet:

$$k(0,y,t) = \begin{cases} 0 & \text{if undeveloped inlet flow} \\ \left(1 - \dfrac{y}{y_1}\right) \dfrac{u_*^2}{\sqrt{C_\mu}} & \text{if fully developed inlet flow} \end{cases} \qquad (4.22)$$

$$\epsilon(0,y,t) = \begin{cases} 0 & \text{if undeveloped inlet flow} \\ \left(1 - \dfrac{y}{y_1}\right) \left[\dfrac{u_*^3}{\kappa y \left(1 - e^{-y^+/26}\right)}\right] & \text{if fully developed inlet flow} \end{cases} \qquad (4.23)$$

The boundary conditions at the inlet imposed in the case of fully developed flow are similar to that proposed by Alfrink & van Rijn (1983). In the above equations, y_1 stands for the height of the free surface at the inlet. In the hydraulic jump simulation, fully developed conditions are imposed at the exit as follows:

$$\frac{\partial k}{\partial x}(x = L, y, t) = 0 \qquad (4.24)$$

$$\frac{\partial \epsilon}{\partial x}(x = L, y, t) = 0 \qquad (4.25)$$

4.7 Surface Roughness

The surface of the bottom wall is usually very irregular and rough. In turbulent flows it is common to represent the roughness of the bed in terms of the equivalent sand roughness height k_s. The influence of the wall roughness on laminar flows is minimal. However, in turbulent flows, they can influence the fluid flow considerably, by breaking up the laminar sublayer (White 1991). The relative roughness of the wall can be expressed in terms of the parameter:

$$k_s^+ = \frac{k_s u_*}{\nu}, \qquad (4.26)$$

where, ν is the laminar viscosity and u_* is the friction velocity. White (1991) defines the following three roughness regimes:

1. hydraulically smooth wall: $k_s^+ < 4$

2. transitional-roughness regime: $4 < k_s^+ < 60$

3. fully rough flow: $k_s^+ > 60$.

If the roughness elements are very small and are submerged within the laminar sublayer, then the flow is considered to be hydraulically smooth and roughness has no effect on the velocity profile. The nature of the flow is mostly influenced by the fluid viscosity in the hydraulically smooth wall regime. In the fully rough flow regime, the laminar sublayer in broken by the roughness elements, and the fluid flow at the wall is determined by the roughness elements and the viscous effects are negligible in comparison. For the intermediate transitional regime, both viscosity and roughness effects influence the fluid flow.

In the numerical model we incorporate the influence of the wall roughness using the expressions provided by Rosten & Worrell (1988). In this model the functional dependence of E on the wall roughness is given by:

$$E = \begin{cases} E_m & \text{if } k_s^+ < 3.7 \\[2mm] \dfrac{1}{\left[a\,(k_s^+/b)^2 + (1-a)/E_m^2\right]^{1/2}} & \text{if } 3.7 < k_s^+ < 100 \\[2mm] b/k_s^+ & \text{if } k_s^+ > 100 \end{cases} \qquad (4.27)$$

In the above expression, $E_m = 9$, $b = 29.7$, $a = (1 + 2X^3 - 3X^2)$, and $X = 0.02248\,(100 - k_s^+)\,/(k_s^+)^{0.564}$.

4.8 Note on the RANS equations

For the sake of completeness, we list below the RANS equations used by us:

$$\frac{\partial u}{\partial t} + u\frac{\partial u}{\partial x} + v\frac{\partial u}{\partial y} = -\frac{1}{\rho}\frac{\partial p}{\partial x} - g\sin\theta + (\nu + \nu_T)\nabla^2 u \tag{4.28}$$

$$\frac{\partial v}{\partial t} + u\frac{\partial v}{\partial x} + v\frac{\partial v}{\partial y} = -\frac{1}{\rho}\frac{\partial p}{\partial y} + g\cos\theta + (\nu + \nu_T)\nabla^2 v \tag{4.29}$$

$$\frac{\partial u}{\partial x} + \frac{\partial v}{\partial y} = 0 \tag{4.30}$$

In the above equations, u and v are the mean fluid flow velocities. $p = \bar{p} + 2k/3$ is the pressure, and the turbulent pressure is absorbed into the original mean pressure. Note that, the RANS as stated above simplify the original stress tensor given in Eq.4.7. The eddy viscosity is a spatially varying quantity, and the divergence of the stress tensor is strictly not equal to Laplacian of the velocity. However, to retain the full stress tensor would necessitate the solution of the x-momentum and y-momentum equations in a coupled fashion. Moreover, Lemos (1992b) found numerical oscillations when he tried to retain the full stress tensor form in free surface problems.

Chapter 5

Numerical Procedure

5.1 Introduction

In the previous two chapters, the two most important elements of the numerical procedure, namely, the ALE formulation and the $k - \epsilon$ turbulence model, have been described. The rest of the numerical details are briefly illustrated in this chapter.

When trying to solve the Navier–Stokes equations, one is faced with the question of which primary variables to chose. The mathematical system (Eqs.2.1-2.3) as presented in chapter 2 has $u - v - p$ as the primary variables. There exist alternate formulations, which employ stream function - vorticity ($\psi - \omega$), or velocity - vorticity as the primary variables. The biggest problem with solving the incompressible Navier–Stokes equations comes from the pressure. Since, no time derivative for pressure appears in the formulation, time-stepping for pressure is not straightforward, as it is for velocities. The vorticity formulation, eliminates pressure by taking curl of the momentum equations. However, in free surface problems it is advantageous to have $u - v - p$ (also called primitive variables) as the primary variables. This is because, at the free surface we have a boundary condition in terms of pressure, namely, the normal stress condition (Eq.2.7). In recent years the $u - v - p$ method is also gaining popularity, due to decoupling introduced by the projection schemes. In these projection schemes, the velocity components and pressure are decoupled from each other and can be solved in a sequential manner, thus providing significant savings in computational time and memory. In this dissertation, we use the primitive

variables $(u - v - p)$ as the primary variables and solve them using the Chorin-type projection scheme which is described briefly in the next section.

5.2 Time stepping procedure

Knowing the previous time step velocities u^n, v^n, the next time-level velocities u^{n+1}, v^{n+1} are obtained as follows:

Step1 The intermediate velocities $\tilde{u}^{n+1}$, $\tilde{v}^{n+1}$ are obtained by solving the momentum equations dropping the pressure gradient terms.

$$\frac{\tilde{u}^{n+1} - u^n}{\Delta t} - \nu \nabla^2 \tilde{u}^{n+1} = f_x^n - (u^n - w^x) \frac{\partial u^n}{\partial x} - (v^n - w^y) \frac{\partial u^n}{\partial y} \quad (5.1)$$

$$\frac{\tilde{v}^{n+1} - v^n}{\Delta t} - \nu \nabla^2 \tilde{v}^{n+1} = f_y^n - (u^n - w^x) \frac{\partial v^n}{\partial x} - (v^n - w^y) \frac{\partial v^n}{\partial y} \quad (5.2)$$

f_x^n and f_y^n are the body forces in the x and y directions respectively. w^x, w^y are the mesh velocities or the referential velocities which come from the ALE formulation described in chapter 3. The appropriate Dirichlet and Neumann boundary conditions are imposed in this step. Note that the diffusions terms are treated implicitly, whereas the nonlinear advection terms are computed explicitly, making our numerical procedure semi-implicit in time.

Step 2 The pressure is determined from the Poisson equation which is obtained by projecting the intermediate velocities onto the divergence free spaces. The boundary conditions for pressure are the homogeneous Neumann condition $p_{,n} = 0$ on all boundaries except the free surface where a Dirichlet boundary condition determined from the normal stress continuity is imposed. If

the domain is periodic in the streamwise direction, then periodic boundary conditions are imposed for pressure.

$$\frac{1}{\rho} \nabla^2 p = \frac{1}{\Delta t} \left(\frac{\partial \tilde{u}^{n+1}}{\partial x} + \frac{\partial \tilde{v}^{n+1}}{\partial y} \right) \tag{5.3}$$

Step 3 The final velocities u^{n+1}, v^{n+1} are calculated from:

$$\frac{u^{n+1} - \tilde{u}^{n+1}}{\Delta t} = -\frac{1}{\rho} \frac{\partial p}{\partial x} \tag{5.4}$$

$$\frac{v^{n+1} - \tilde{v}^{n+1}}{\Delta t} = -\frac{1}{\rho} \frac{\partial p}{\partial y} \tag{5.5}$$

The philosophy of the Fractional Step Method is to first determine the approximate velocities $\tilde{u}^{n+1}, \tilde{v}^{n+1}$ satisfying the boundary conditions but which are not necessarily divergence-free. Theses approximate velocities are then projected onto divergence free spaces resulting in final divergence free velocities u^{n+1}, v^{n+1}. This method of discretizing Navier-Stokes equations in time is widely used (e.g., Chorin 1967; Temam 1971; Patankar 1980; Pironneau 1982; Donea, Giuliani & Laval 1982; Mizukami & Tsuchiya 1984; Kim & Moin 1985; Ramaswamy & Kawahara 1987b; Van Kan 1986; Glowinski 1986; Bell, Colella & Glaz 1989; Gresho 1990; Gresho & Chan 1990; Le & Moin 1991; Oden 1992; Finlayson 1992; Ramaswamy, Jue & Akin 1992).

5.3   Spatial discretization

The spatial discretization of the fluid domain is done using three-node triangular elements. In two-dimensions, the simplest element we could have are the triangular

elements, hence they are also called as simplex elements. The interpolation functions are linear in these elements, and the variables are taken to be residing at the vertices of the element. Equal-order approximation, that is the same level of approximation, which in our case is linear approximation, is used for both velocities and pressure. The equal order approximation (also called non-staggered grids) for the velocity and pressure has been used by several researchers in the numerical solution of the Navier-Stokes equations (e.g. Schneider, Raithby & Yovanovich 1978; Rice & Schnipke 1986; Ramaswamy & Kawahara 1987c; Shaw 1991; Zienkiewicz & Wu 1991; Zienkiewicz & Wu 1992; Behr, Franca & Tezduyar 1992; Gresho, Chan, Christon & Hindmarsh 1994).

The velocities and pressure are approximated by the linear interpolation function Φ_α in each local triangular element as:

$$u_i = \Phi_\alpha u_{\alpha i} \tag{5.6}$$

$$p = \Phi_\alpha p_\alpha \tag{5.7}$$

In the conventional Galerkin-Bubnov finite element method, the weighting functions are same as the interpolating functions. In linear triangular elements, the spatial gradients are constant, and the three-node triangular elements are also called as Constant Strain Triangles in the Solid Mechanics literature.

Let us define the following matrices:

$$D_{\alpha\beta} = \nu \int_{\Omega_e^n} \Phi_{\alpha,i} \Phi_{\beta,i} \, d\Omega \tag{5.8}$$

$$A_{\alpha\beta\gamma j} = \int_{\Omega_e^n} \Phi_\alpha \Phi_{\beta,j} \Phi_\gamma \, d\Omega \tag{5.9}$$

$$L_{\alpha\beta} = \int_{\Omega_e^n} \Phi_{\alpha,i} \Phi_{\beta,i} \, d\Omega \tag{5.10}$$

$$M_{\alpha\beta} = \int_{\Omega_e^n} \Phi_\alpha \Phi_\beta \, d\Omega \tag{5.11}$$

$$C_{\alpha\beta i} = \int_{\Omega_e^n} \Phi_\alpha \Phi_{\beta,i} \, d\Omega \tag{5.12}$$

$$F_{\alpha i} = \int_{\Omega_e^n} \Phi_\alpha f_i \, d\Omega \tag{5.13}$$

$M_{\alpha\beta}$ is the mass matrix, $D_{\alpha\beta}$ is the diffusion matrix, $A_{\alpha\beta\gamma j}$ is the advection matrix, $L_{\alpha\beta}$ is the Laplacian matrix, $C_{\alpha\beta i}$ is the gradient matrix, and $F_{\alpha i}$ is the body force vector. Note that the transpose of the gradient matrix $C_{\alpha\beta i}^T$ is the divergence matrix. The subscripts α and β refer to the local node numbers, and take the values $1, 2, 3$, since we are using three-node triangular elements. Ω_e^n is the domain of the local triangular element, with the subscript e referring to the fact that it is an element level quantity, and the superscript n refers to the time level of the domain. In addition to the above matrices, we define a lumped mass matrix $M_{\alpha\beta}^L$ which is obtained by lumping the off-diagonal elements of the consistent mass matrix $M_{\alpha\beta}$ on to the diagonal.

The Fractional Step Method in the Finite Element formulation become:

Step 1

$$\left[\frac{1}{\Delta t} M_{\alpha\beta} + D_{\alpha\beta} \right] \tilde{u}_{\beta i}^{n+1} = \frac{1}{\Delta t} M_{\alpha\beta} u_{\beta i}^n - A_{\alpha\beta\gamma j} \left(u_{\beta j}^n - w_{\beta j}^n \right) u_{\gamma i}^n + F_{\alpha i} \tag{5.14}$$

Step 2

$$\frac{1}{\rho} L_{\alpha\beta} p_\beta^{n+1} = \frac{1}{\Delta t} C_{\alpha\beta i}^T \tilde{u}_{\beta i}^{n+1} \tag{5.15}$$

Step 3

$$\frac{1}{\Delta t} M_{\alpha\beta}^{L} u_{\beta i}^{n+1} = \frac{1}{\Delta t} M_{\alpha\beta}^{L} \tilde{u}_{\beta i}^{n} - \frac{1}{\rho} C_{\alpha\beta i} \tilde{p}_{\beta}^{n+1} \qquad (5.16)$$

Note that in this step, the lumped mass matrix is used.

The above element level equations are assembled onto a global matrix, and solved for the global velocity and pressure field.

5.4   Mesh generation

The first step in the mesh generation process is the placement of the vertical spines along the streamwise direction. The placement of the vertical spines is dictated by the physics of the fluid flow being investigated. Usually we require fine spacing for the vertical spines in high gradient regions. In the turbulent flow over artificial bedforms simulation, the vertical spines are close-packed near the peak of the dune, since very high gradients exist in this region and the boundary layer separates just downstream of the dune. In the simulation of hydraulic jump, we find that the free surface rises abruptly across the jump region. Hence large spatial gradients occur in the jump region, and fine spacing is required in the jump region. Unfortunately, we do not *a priori* know the location of the jump, and hence place the vertical spines in an equi-distant manner and try to capture the high gradient regions accurately by taking sufficiently large number of spines. In the case of thin film flows, a uniform distribution of vertical spines is sufficient and in a sense appropriate since the traveling wave phenomena is being investigated.

A general mapping strategy described by Anderson, Tannehill & Pletcher (1984) is used to achieve arbitrary spine placement.

$$\bar{x} = B + \frac{1}{\tau} sinh^{-1}\left[\left(\frac{x}{x_c} - 1\right) sinh\left(\tau B\right)\right], \quad 0 < \tau < \infty \qquad (5.17)$$

where

$$B = \frac{1}{2\tau} ln \left[\frac{1 + (e^{\tau} - 1)(x_c/L)}{1 + (e^{-\tau} - 1)(x_c/L)} \right].$$

Uniform spacing in the transformed space $\bar{x}$ produces unequal spacing in the x plane, depending on the values of x_c and τ. x_c corresponds to the point about which we desire fine mesh spacing. In the case of turbulent flow over dunes, x_c is chosen to be the dune crest. The fine spacing of the spines at the point x_c is controlled through the τ parameter. Large values of τ would give finer mesh spacing near the point x_c. In the turbulent flow simulations to be presented in chapter 7 $\tau = 5.0$ has been used.

After the placement of the vertical spines, it remains to assign nodes to each of the spines. Each of the spines are assigned a fixed number of nodes, and their placement along the spines is specified *a priori*. In the case of thin-film flows, the fluid flow is laminar, it suffices to place the nodes in an equi-distant manner along the vertical spines. However, in turbulent flow simulations, fine mesh spacing is desired near the wall to resolve the large gradients known to exist close to the wall. A logarithmic mapping is obtained using the mapping strategy proposed by Anderson, Tannehill & Pletcher (1984).

$$\bar{y} = 1 - \frac{ln \left\{ \left[\beta + 1 - \frac{y - b(x)}{h(x,t) - b(x)} \right] / \left[\beta - 1 + \frac{y - b(x)}{h(x,t) - b(x)} \right] \right\}}{ln \left[(\beta + 1)/(\beta - 1) \right]}, \quad 1 < \beta < \infty \quad (5.18)$$

An equal spacing in the $\bar{y}$ space results in fine mesh spacing near the bed $b(x)$ depending on the value of β. For large values of β we obtain uniform spacing, whereas for values of $\beta \to 1$, fine mesh spacing near the wall is obtained. In the turbulent flow simulation reported in this dissertation, the values of β are chosen in the range $1.001 - 1.01$.

To summarize, a uniform spacing in the transformed plane $(\bar{x}, \bar{y})$ results in nonuniform mesh spacing in the physical plane (x, y) depending on the values of x_c, β and τ.

5.5 Miscellaneous details

In the turbulent open-channel flow simulation, in addition to the RANS equations, advection-diffusion transport equations are to be solved for k and ϵ. These are very similar to the Eqs.5.1&5.2 which solve for the intermediate velocities $\tilde{u}^{n+1}, \tilde{v}^{n+1}$. The diffusion term is treated implicitly using the Euler Backward scheme and advection terms are treated explicitly using the Euler Forward scheme. The only difference is the presence of highly nonlinear forcing functions in the case of k and ϵ equations. A simple explicit treatment of these highly nonlinear terms was found to result in numerical oscillations. Therefore the following time discretization for the k and ϵ equations is used:

$$\frac{k^{n+1} - k^n}{\Delta t} - \nabla \left[\cdot \left(\nu + \frac{\nu_T}{\sigma_k} \right) \nabla k^{n+1} \right] + \left(\frac{\epsilon}{k} \right)^n k^{n+1} = G^n$$
$$- (u^n - w^x) \frac{\partial k^n}{\partial x} - (v^n - w^y) \frac{\partial k}{\partial y} \tag{5.19}$$

$$\frac{\epsilon^{n+1} - \epsilon^n}{\Delta t} - \nabla \left[\cdot \left(\nu + \frac{\nu_T}{\sigma_\epsilon} \right) \nabla \epsilon^{n+1} \right] + C_2 \left(\frac{\epsilon}{k} \right)^n \epsilon^{n+1} = C_1 \frac{\epsilon^n}{k^n} G^n$$
$$- (u^n - w^x) \frac{\partial \epsilon^n}{\partial x} - (v^n - w^y) \frac{\partial \epsilon}{\partial y} \tag{5.20}$$

The explicit first-order treatment of advection in Eqs.(5.1,5.2,5.19,5.20) results in negative diffusion being added to the system (Dukowicz & Ramshaw 1979). This is removed using the Balancing Tensor Diffusivity procedure. In this procedure the viscosity tensor is modified to be:

$$\nu_{\phi ij} = \nu_\phi \delta_{ij} + \frac{\Delta t}{2} (u_i - w_i)(u_j - w_j) \tag{5.21}$$

The variable ϕ represents $\tilde{u}$, $\tilde{v}$, k or ϵ, and ν_ϕ, the corresponding physical viscosity.

According to Rannacher (1992), the Chrorin's projection method introduces pressure stabilization in the numerical solution of the Navier–Stokes equations and is similar to the Petrov-Galerkin procedure of Hughes, Franca & Balestra (1986).

Unlike the solution of the Navier–Stokes equations, the k and ϵ equations have no implicit stabilization. A procedure called Selective Mass Lumping is used to introduce just enough numerical diffusion to stabilize the scheme. The idea is to do mass lumping to different extents on the left- and right- hand sides of the equations. The stabilization introduced by selective mass lumping is in some respect similar to the Lax-Friedrichs scheme in Finite Difference Method (Kawahara, Hirano & Tsubota 1982; Chippada, Ramaswamy & Wheeler 1994).

Shen (1992) has been able to show that $\tilde{u}^{n+1}$ and u^{n+1} are weakly first order approximations to $u(t_{n+1})$ and that p^{n+1} is weakly order $1/2$ approximation to $p(t_{n+1})$.

The free surface is updated through the solution of the kinematic free surface equation. An alternative formulation of the kinematic free surface equation can be derived:

$$\frac{\partial h}{\partial t} + \frac{\partial q}{\partial x} = 0 \tag{5.22}$$

where, $q(x,t) = \int_{b(x)}^{h(x,t)}$ is the flow rate. The above equation can be considered to be the conservative form of the original kinematic free surface equation. In the problems with periodic boundary conditions, the above equation is solved using the Fourier Spectral Method along with leap-frog time-stepping procedure. However, in the simulation of turbulent flow over artificial bedforms, even though we have periodic boundary conditions, we cannot use the Fourier Spectral Method since the mesh spacing is not uniform. Second-order Adams-Bashforth scheme is used in such

instances. Second-order Adams-Bashforth scheme is also used in the non-periodic domain simulations to be reported in the chapter on interfacial instabilities in thin-film flows (chapter 6). In the simulation of hydraulic jump, very large gradients exist in the jump region, since the free surface rises abruptly. Certain amount of numerical diffusion is needed to control the numerical oscillations, and this is done using the Selective Mass Lumping procedure (Chippada etal 1994).

Since, advection terms are treated implicitly, the numerical procedure is only conditionally stable and we need to satisfy the Courant-Friedrichs-Levy (CFL) condition. The time step is chosen automatically based on the stability condition in the following manner:

$$\Delta t = min \left[\frac{CFL}{\frac{|u|+\sqrt{gh\cos\theta}+\sqrt{\sigma/(\rho h)}}{\Delta x} + \frac{|v|}{\Delta y}} \right] \tag{5.23}$$

Thus, the time step is chosen such a way that the Courant number in each of the elements is less than one. Even though theoretically, we could take a Courant number of one and still have stability, this result is strictly valid only for linear problem only. The admissible Courant number is usually less than one for nonlinear problems, and the parameter CFL in the above equation lets us specify the Courant number. The CFL number has been specified in the range $0.05 - 0.40$, depending on the problem. Note that, in the above expression used to find the maximum admissible time step, $\sqrt{gh\cos\theta}$ is the celerity of a gravity wave and $\sqrt{\sigma/\rho h}$ is the celerity of a capillary wave.

The system of linear equations are solved using the Conjugate Gradient Method using the tridiagonal preconditioner.

Chapter 6

Interfacial Instabilities in Thin Film Flows

6.1 Introduction

Thin liquid films flowing down inclined walls, pipes and tubes occur widely in many engineering applications, e.g. film cooling, gas adsorption, condensers, evaporators, slot coating and dip painting. Thin film flows are unstable to long wavelength disturbances, and the gas-liquid interface tends to become corrugated, resulting in various surface wave motions. Traveling waves on the liquid-gas interface lead to increased heat and mass transfer both in the liquid and gaseous phases (Dukler 1972). In film coating applications, however, a constant thickness liquid film is desired. Thus, due to its obvious engineering importance, thin liquid film flows have been extensively studied since the seminal work of Kapitza & Kapitza (1949).

The thin film flow study can be classified into the following subgroups (Dukler 1972):

1. Study of the conditions under which waves exist. These studies try to explain *why* we observe waves on the interface, and if there is more than one type of wave, the ranges of parameters in which these different types of waves exist.

2. Study of the *quantitative* aspects of the surface waves, such as, the wave shape, the wave speed and other statistical features.

3. Study of the *influence* of these surface waves on the heat, mass and momentum transfer, both in the liquid and the gaseous phases.

The focus of our work is on the first two aspects, namely, the qualitative and quantitative study of the formation of surface waves on the gas-liquid interface.

The state of the art related to the thin film flow modeling has been reviewed recently by Chang (1994). He identifies four distinct wave regimes as shown in Fig.6.1:

Region I This is the wave inception region. Disturbances at the inlet are amplified downstream and form a monochromatic wave at the end of the region. If the flow entering is not artificially excited (natural noise) or if it is excited with a broad band noise, the disturbance is selectively amplified and at the end of inception region, monochromatic waves with frequency same as the maximum growth rate frequency predicted by the linear stability analysis are observed. However, if a single frequency forcing with small amplitude is applied to the incoming flow, then waves with the inlet frequency are amplified and at the end of region I monochromatic waves with frequency same as the inlet frequency are observed. The amplitude of the disturbance grows exponentially in this region. The waves are monochromatic (sinusoidal) and infinitesimal in amplitude and linear theories can be used to study this wave regime.

Region II In this region, however, the exponential growth rate is arrested due to nonlinear interactions and the amplitude of the wave saturates. Part of the energy of the fundamental mode gets channeled into its first harmonic due to the nonlinear interaction, and the wave shape is no longer sinusoidal.

Region III The primary surface wave instability exiting Region II travels for some distance downstream without visible change in wave shape, before succumbing to secondary side-band and subharmonic instabilities. Due to the subharmonic

instability, neighboring peaks coalesce, and due to the sideband instability longwave modulation of the wave amplitude takes place. These instabilities lead to very localized waveforms, namely, the tear drop humps. These tear drop humps are also referred to as solitary waves or solitary humps and have a very long gently trailing tail and a steep front preceded downstream by small capillary ripples. The Fourier content of this solitary wave is broad banded, with the fundamental and several of its harmonics possessing significant energy. The spacing between the humps is nonuniform and time varying even though the shape of the solitary wave itself may be nonvarying in time.

Region IV The solitary waves evolving from the region III finally succumb to transverse disturbances, and the subsequent waves are three-dimensional, irregular and random.

It should be pointed out, that the above described wave regions are only qualitative in nature, and based on observations. Not all of the aspects have been rigorously proved theoretically. Especially, the nonlinear wave regimes II, III & IV have so far been studied using simplified approximate nonlinear theories. The present study limits itself to nonlinear 2-D waves found to occur in regions II & III, and a full-scale nonlinear study based on the direct solution of the Navier–Stokes equations without any *a priori* approximations or simplifications is done. To date, only one other detailed direct numerical study of the thin film instability has been reported (Salamon, Armstrong & Brown 1994). Salamon etal (1994) assume a priori the existence of stationary waveforms and compute their shapes by solving the 2-D Navier–Stokes equations using FEM. The waveforms obtained in this manner are not always stable. Their relative stability can only be ascertained through the time integration of the initial value problem, and this is what is done in this study.
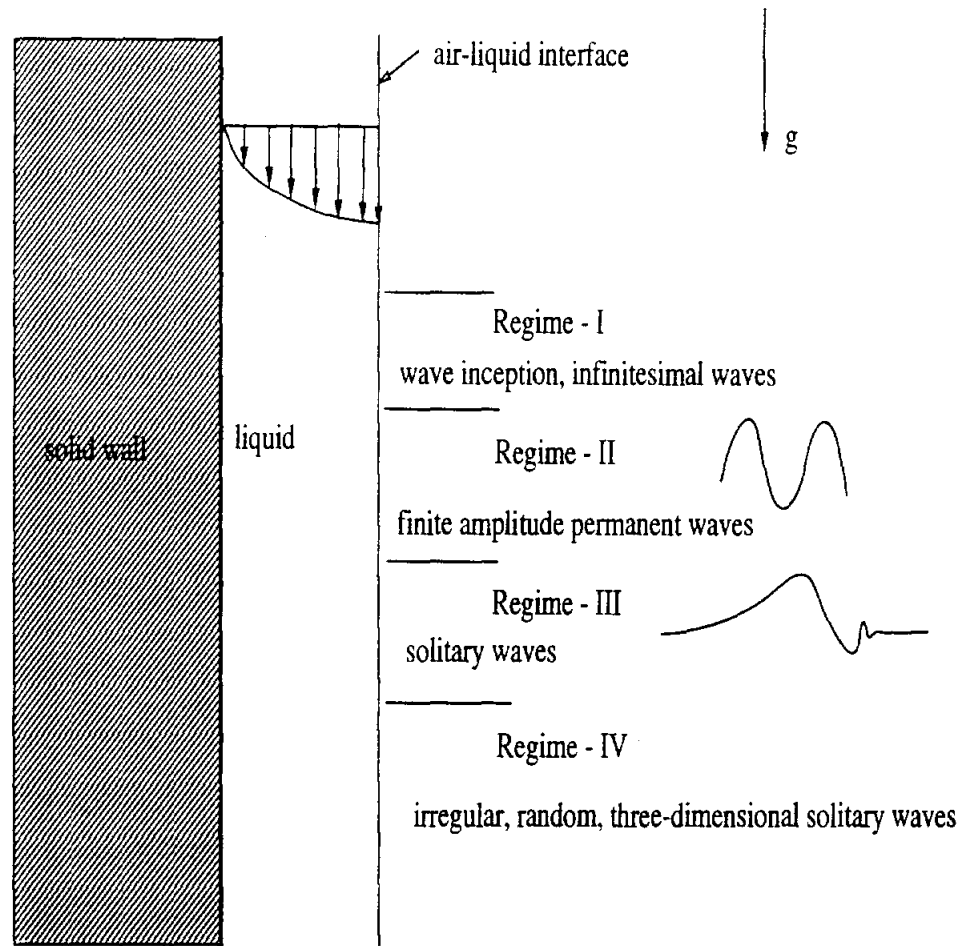
Figure 6.1: Surface wave regimes in thin liquid film draining down vertical wall. The figure is sketched based on the description given by Chang (1994).

6.2 Problem Definition and Non-dimensional Parameters

The model problem being considered is a thin liquid film draining down a straight wall inclined at an angle β to the horizontal as shown in Fig.6.2. x-axis is along the wall and is also referred to as the stream-wise direction. y-axis is perpendicular to the wall, positive upwards. $h(x, t)$ is the film thickness measured as the height of the gas-liquid interface from the wall. The fluid flow is assumed to be laminar, Newtonian, isothermal and incompressible. Further, it is assumed that the fluid flow is two-dimensional, i.e., no transverse or span-wise (z-direction) variations.

The dependent and independent variables can be non-dimensionalized in several ways and we chose to use the unperturbed film thickness h_0 as the characteristic length and ν/h_0 as the characteristic velocity, which is also called the viscous scaling. The non-dimensional governing equations are as follows:

$$\frac{\partial u}{\partial t} + u\frac{\partial u}{\partial x} + v\frac{\partial u}{\partial y} = -\frac{\partial p}{\partial x} + G\sin\beta + \frac{\partial^2 u}{\partial x^2} + \frac{\partial^2 u}{\partial y^2} \tag{6.1}$$

$$\frac{\partial v}{\partial t} + u\frac{\partial v}{\partial x} + v\frac{\partial v}{\partial y} = -\frac{\partial p}{\partial y} - G\cos\beta + \frac{\partial^2 v}{\partial x^2} + \frac{\partial^2 v}{\partial y^2} \tag{6.2}$$

$$\frac{\partial u}{\partial x} + \frac{\partial v}{\partial y} = 0 \tag{6.3}$$

The boundary conditions at the wall are the no-slip and impermeability conditions:

$$\left.\begin{array}{rcl} u &=& 0 \\ v &=& 0 \end{array}\right\} \quad \text{at} \quad y = 0. \tag{6.4}$$

Neglecting the motions in the gas phase, the boundary conditions at the free surface are as follows:
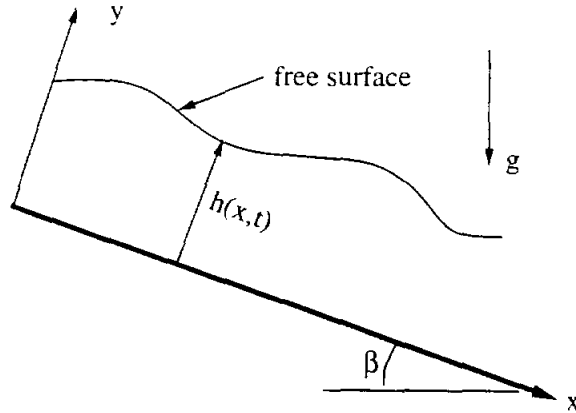
Figure 6.2: The physical configuration of a thin layer flowing down an inclined plane.

$$\left.\begin{array}{rcl} \left(\dfrac{\partial u_n}{\partial \tau} + \dfrac{\partial u_\tau}{\partial n}\right) & = & 0 \\[2ex] p - 2\left(\dfrac{\partial u_n}{\partial n}\right) & = & p_a - \dfrac{3S}{R} \\[2ex] \frac{\partial h}{\partial t} + u\frac{\partial h}{\partial x} & = & v \end{array}\right\} \quad \text{at} \quad y = h(x,t). \tag{6.5}$$

The first two conditions impose the continuity of the stress across the gas-liquid interface and the last condition represents the fact that the gas-liquid interface is a material surface and gets advected with the fluid particle velocity. As already explained in Chapters 2 & 5, only the two stress continuity conditions are imposed in the solution of the fluid flow given by Eq.(6.1-6.3) and the kinematic condition is used to update the free surface location every time step.

The non-dimensional numbers that appear due to our non-dimensionalization are:

- $G = gh_0^3/\nu^2$, measure of film thickness[1].

---

[1] Non-dimensional number G is referred to as Galileo number by some authors

- $S = \sigma h_0/(3\rho\nu^2)$, measure of surface tension.

The non-dimensional parameter S is not completely independent of G, since it is dependent on unperturbed film thickness h_0. We rewrite S as follows: $S = TG^{1/3}$, where $T = \sigma/(3\rho\nu^{4/3}g^{1/3})$. The non-dimensional parameter T^2 is a function of the fluid properties alone and fixing T in effect fixes the fluid and the film thickness is controlled by varying G. T for pure water at 15^0C is approximately 950 (Chang 1994).

Some authors use the horizontal velocity at the interface U_0 as the reference velocity resulting in the following non-dimensional parameters:

- $Re = U_0 h_0/\nu$, Reynolds number

- $We = \sigma/(\rho g h_0^2 \sin\beta)$, Weber number

The Reynolds number and the Weber number are related to the non-dimensional parameters G and S as follows:

$$Re = \frac{G\sin\beta}{2} \quad ; \quad We = \frac{3S}{G\sin\beta}$$

6.3 Literature Review

6.3.1 Nusselt Film Flow

If the flow is assumed to be laminar, smooth, two-dimensional and fully developed, the mathematical system given by Eqs.(6.1-6.3), reduce to the following simplified system (in dimensional co-ordinates):

$$\frac{d^2u}{dy^2} + \frac{g\sin\beta}{\nu} = 0 \tag{6.6}$$

---

[2]$\gamma = 3T = \sigma/(\rho\nu^{4/3}g^{1/3})$ is called the Kapitza number by some researchers.

$$\frac{dp}{dy} = -\rho g \cos \beta \tag{6.7}$$

The boundary conditions given by Eqs.(6.4,6.5) also simplify to:

$$u = 0 \quad \text{at} \quad y = 0 \tag{6.8}$$

$$\left.\begin{array}{rcl} \dfrac{du}{dy} &=& 0 \\[2mm] p &=& 0 \end{array}\right\} \quad \text{at} \quad y = h_0 \tag{6.9}$$

Eqs.(6.6,6.7) can be solved subject to the boundary conditions given by Eqs.(6.8,6.9), resulting in:

$$\begin{array}{rcl} U(y) &=& \dfrac{g \sin \beta}{\nu} \left(h_0 y - \dfrac{y^2}{2} \right) \\[3mm] V &=& 0 \\[3mm] P(y) &=& \rho g \cos \beta \, (h_0 - y) \end{array} \tag{6.10}$$

The above solution is usually attributed to Nusselt (1916) even though it is a special case of the series solution obtained by Hopf (1910) for flow over open, inclined, two-dimensional rectangular channels (Churchill 1988; Fulford 1964). The velocity at the interface U_0 is given by:

$$U_0 = \frac{g h_0^2}{2\nu} \sin \beta \tag{6.11}$$

and is 1.5 times the mean velocity given by:

$$U_{av} = \frac{g h_0^2}{3\nu} \sin \beta \tag{6.12}$$

The simple Nusselt flow given by Eq.(6.10) is a solution to the 2-D Navier–Stokes equations (Eqs.6.1-6.3) and satisfies the boundary conditions (Eqs.6.4,6.5). However, this basic flat-film solution is not observed in nature, since it is an unstable

solution for most ranges of parameters of interest. Hence, much of the theoretical interest has been to study the stability of the Nusselt flat film flow and to find the range of parameters for which this basic solution is unstable.

6.3.2 Linear stability

The classical hydrodynamic stability analysis involves imposing an infinitesimally small perturbation on the basic flow which in this case is the Nusselt film flow given by Eq.(6.10), and study its growth in either time or space, as the case may be. An infinitesimally small perturbation on the flat film is imposed as follows:

$$h(x,t) = 1 + h'(x,t), \quad h' \ll 1 \tag{6.13}$$

This perturbation of the interface results in small deviations of the velocity and pressure field from the base flow:

$$
\begin{aligned}
u(x,y,t) &= U(y) + u'(x,y,t) \\
v(x,y,t) &= v'(x,y,t) \\
p(x,y,t) &= P(y) + p'(x,y,t)
\end{aligned}
\tag{6.14}
$$

The deviations u',v' and p' are infinitesimally small, i.e., $u' \ll 1$, $v' \ll 1$ and $p' \ll 1$. The above perturbed flow field is substituted into the two-dimensional[3] Navier-stokes equations and linearized in u',v' and p' resulting in:

$$\frac{\partial u'}{\partial t} + U(y)\frac{\partial u'}{\partial x} + v'\frac{dU}{dy} = -\frac{\partial p'}{\partial x} + \nabla^2 u' \tag{6.15}$$

$$\frac{\partial v'}{\partial t} + U(y)\frac{\partial v'}{\partial x} = -\frac{\partial p'}{\partial y} + \nabla^2 v' \tag{6.16}$$

---

[3]As per the Squire's theorem (White 1991) it is enough to study the stability of parallel flow $U(y)$ for a two-dimensional disturbance.

$$\frac{\partial u'}{\partial x} + \frac{\partial v'}{\partial y} = 0 \tag{6.17}$$

Pressure is eliminated from Eqs.(6.15,6.16) by cross-differentiating and subtracting one from the other. The continuity equation is automatically satisfied by introducing a stream function ψ' of the form:

$$u' = \frac{\partial \psi'}{\partial y} \quad ; \quad v' = -\frac{\partial \psi'}{\partial x} \tag{6.18}$$

The above analysis results in a fourth-order partial differential equation for ψ' of the form:

$$\frac{\partial}{\partial t}\left(\nabla^2 \psi'\right) + U(y)\frac{\partial}{\partial x}\left(\nabla^2 \psi'\right) - \frac{d^2 U}{dy^2}\frac{\partial \psi'}{\partial x} = \nabla^2\left(\nabla^2 \psi'\right) \tag{6.19}$$

The initial disturbance is usually assumed to be exponential as follows:

$$\begin{aligned} h'(x,t) &= \delta exp\left[i\left(kx - \omega t\right)\right] \\ &= \delta exp\left[ik\left(x - ct\right)\right] \end{aligned} \quad , \quad \delta \ll 1 \tag{6.20}$$

One of the physical motivations behind using the exponential form for the disturbance is that, any function can expressed as a Fourier sum. Thus, knowing the response of the system to each of the harmonic disturbances, the response of the system for any general disturbance can be constructed through linear superposition. If the film flow is stable for all spatial wave numbers k or all frequencies ω, then, the base flow given by $U(y)$ can be said to be a stable solution. Even if there exists a single unstable k or ω, then the base solution is said to be unstable. In the harmonic disturbance given by Eq.(6.20), $k = 2\pi h_0/\lambda$ is the non-dimensional wave number, ω is the non-dimensional angular frequency and $c = \omega/k$ is the non-dimensional phase speed. λ is the wave length of the disturbance and δ is the amplitude of the disturbance. If k is fixed to be strictly real, and ω is allowed to be complex, the analysis

is termed temporal stability analysis. The disturbance in this case is periodic in the stream-wise direction and either decaying or growing in time depending on the sign of imaginary part of ω. The analysis is called spatial stability analysis, if ω is fixed to be strictly real and k is allowed to take complex values. The disturbance in this case is periodic in time and either growing or decaying in the stream-wise direction depending on the sign of the imaginary part of k. Both the analyses give the same critical conditions. Spatial stability and temporal stability results can be converted into one another through the Gaster transformation.

The stream function can be written as:

$$\psi' = \delta\phi(y)exp\left[ik(x - ct)\right],$$
(6.21)

and is substituted into Eq.(6.19), resulting in the well known Orr-Sommerfeld equation.

$$ik\left[(U(y) - c)(\phi'' - k^2\phi) - kU''\right] = \phi'''' - 2k^2\phi'' + k^4\phi$$
(6.22)

The superscript "′" denotes differentiation with respect to y. The four boundary conditions needed to solve the above fourth order linear differential equation are provided by the no-slip conditions at the wall and stress continuity equations at the interface.

$$\left.\begin{array}{rcl} \phi &=& 0 \\ \phi' &=& 0 \end{array}\right\} \text{ at } y = 0$$
(6.23)

$$\left.\begin{array}{rcl} \left[ik\left(U_0 - c\right) + 3k^2\right]\phi' &=& \phi''' + i3k^3S \\ \phi'' + k^2\phi &=& 0 \end{array}\right\} \text{ at } y = 1$$
(6.24)

At the interface, the boundary conditions are imposed at $y = 1$ instead of $y = 1 + h'$, since δ is infinitesimally small and the error introduced is $O(\delta^2)$. The kinematic condition at the interface provides another relation:

$$c - U_0 = \phi \quad \text{at} \quad y = 1 \tag{6.25}$$

The temporal stability is investigated by solving the Orr–Sommerfeld equation (Eq. 6.22) subject to the four boundary conditions given by Eqs.(6.23,6.24). Knowing $\phi(y)$, the complex wave speed is calculated from the kinematic condition (Eq.6.25). Let $c = c_r + ic_i$. c_r is the wave speed and kc_i determines the growth rate of the disturbance. A positive value of c_i implies there is exponential growth of the initial disturbance amplitude and the system is unstable, and vice versa if c_i is negative. $c_i = 0$ gives us the critical conditions, for which the disturbance neither grows nor decays.

Yih(1955) and Benjamin(1957) first formulated the interfacial instability in thin film flows in terms of the Orr-Sommerfeld equation. The Orr-Sommerfeld equation cannot be solved in a closed form manner. However, for very long wavelength disturbances ($k \ll 1$) and small Reynolds numbers ($Re \sim 1$), approximate analytical solutions for the Orr-Sommerfeld equation have been obtained by Benjamin(1957) and Yih(1963) using perturbation analysis. With certain simplifying assumptions, Anshus & Goren (1964) and Krantz & Goren (1971) obtained linear stability results not restricted to small Reynolds numbers. A complete solution of the Orr-Sommerfeld equation valid for all Reynolds numbers and all wave numbers requires numerical methods and this was done by Whitaker (1964), Pierson & Whitaker (1977) and Chin, Abernathy & Bertschy (1986) among many others.

The important conclusions that fall out of the linear stability analysis can be shown in the form of a phase diagram (Fig.6.3). The linear stability analysis predicts a cut-off Reynolds number for the onset of instability as follows:

$$G_c \sin \beta = \frac{5}{2} \cot \beta \tag{6.26}$$

The experimental confirmation of the above linear stability result for G_c was provided by Liu, Paul & Gollub (1993). In the case of vertically draining thin film, $G_c = 0$, implying that a vertically draining thin film is unstable for all Reynolds numbers. Linear stability analysis provides two neutral curves, $k_c = 0$ and $k_c = k_c(G, S, \beta)$ and for $G > G_c$ the region of instability is $0 < k < k_c(G, S, \beta)$. Short wavelength disturbances are damped by the capillarity action. For infinitesimal wavenumbers ($k \to 0$) linear stability predicts the phase speed to be $c = G$. If a non-dimensionalization based on the velocity at the interface (U_0) is used, then wave speed for $k \to 0$ is $c = 2U_0$. Another quantity of interest which comes out of the linear stability analysis is the wavenumber for which the disturbance grows the fastest, denoted by k_M. If no artificial excitations are imposed, then the waves that are most likely to be detected would be of the maximum growth rate wavenumber k_M. This was experimentally confirmed by Alekseenko, Nakoryakov & Pokusaev (1985).

6.3.3 Nonlinear Stability Analysis Based On Lubrication Approximation

The linear stability analysis described in the previous subsection is expected to be valid only in the wave inception region. Beyond wave inception, the wave amplitude grows exponentially and the nonlinearities can no longer be neglected. In the case of very thin layers ($G \sim O(1)$), the cut-off wavenumber k_c is small, so
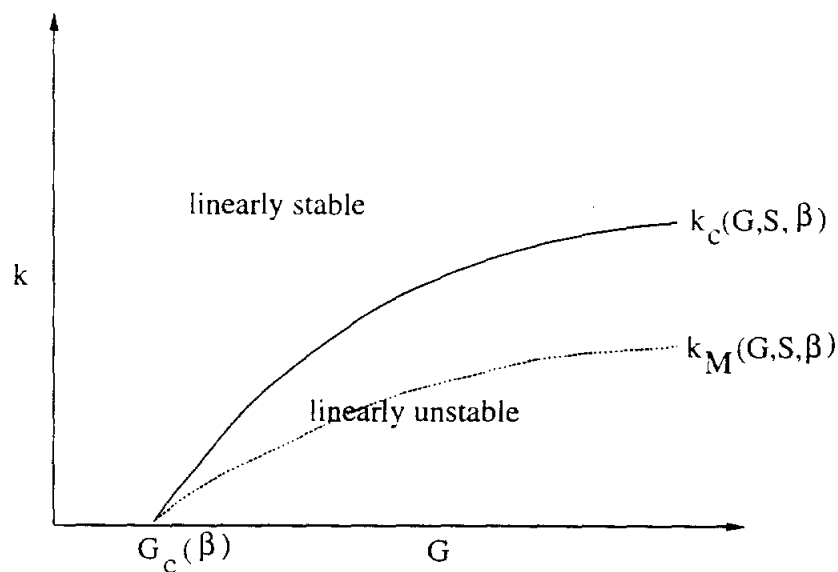
Figure 6.3: Stability diagram based on linear stability analysis

that the nonlinear extension of the stability analysis can be accommodated by the small-wavenumber approximation and the lubrication theory. The aim has been to replace the two-dimensional Navier-Stokes equations with a single nonlinear partial differential equation for the film thickness $h(x,t)$, and examine the stability of the thin film in terms of this nonlinear evolution equation. Benney (1966) first derived the nonlinear evolution equation for the two-dimensional flows, which was extended to three dimensions by Roskes (1970). There have been a number of extensions of this as discussed by Atherton & Homsy (1976) and Lin & Wang (1985). The methodology used for deriving the nonlinear evolution equation is briefly described next.

Let l_c be the characteristic length in the x-direction and is typically proportional to the wavelength of the disturbance. For very thin layers the disturbances are of

very long wavelength, i.e. $l_c \gg h_0$. Define a perturbation expansion parameter $\epsilon = h_0/l_c$, $\epsilon \ll 1$. The original system is rescaled as follows:

$$\xi = \epsilon x \quad ; \quad \eta = y \quad ; \quad \tau = \epsilon t \tag{6.27}$$

The following scaling for the non-dimensional parameters is assumed:

$$G \sim O(1) \quad ; \quad S = \overline{S}\epsilon^{-2} \quad ; \quad \overline{S} \sim O(1) \tag{6.28}$$

Surface tension is a stabilizing term in thin film instability as it weakens the initial exponential growth resulting in finite amplitude permanent waves. $S \sim O(\epsilon^{-2})$ is easily satisfied by most liquids. Only highly viscous oils may have a relatively smaller S. The dependent variables u, v and p are expressed as a power series in ϵ as follows:

$$u = u_0 + \epsilon u_1 + \epsilon^2 u_2 + \cdots \tag{6.29}$$

$$v = \epsilon \left(v_0 + \epsilon v_1 + \epsilon^2 v_2 + \cdots \right) \tag{6.30}$$

$$p = p_0 + \epsilon p_1 + \epsilon^2 p_2 + \cdots \tag{6.31}$$

The above asymptotic expansions are substituted into the governing equations (Eqs. 6.1 - 6.3) and boundary conditions (Eqs.6.4,6.5) and solved by grouping together equal order terms in ϵ. Going through the algebra one can derive the following expressions:

$$u_0 = G \sin \beta \left(h\eta - \frac{1}{2}\eta^2 \right) \tag{6.32}$$

$$v_0 = -G \sin \beta h_\xi \frac{\eta^2}{2} \tag{6.33}$$

$$p_0 = G\cos\beta\,(h - \eta) - 3\overline{S}h_{\xi\xi} \tag{6.34}$$

$$
\begin{aligned}
u_1 &= \left(Gh_\xi\cos\beta - 3\overline{S}h_{\xi\xi\xi}\right)\left(\frac{1}{2}\eta^2 - h\eta\right) \\
&\quad + \frac{1}{2}G\sin\beta h_\tau\left(\frac{1}{3}\eta^3 - h^2\eta\right) + \frac{1}{6}G^2\sin^2\beta hh_\xi\left(\frac{1}{4}\eta^4 - h^3\eta\right)
\end{aligned}
\tag{6.35}
$$

$$
\begin{aligned}
v_1 &= -G\cos\beta\left(\frac{\eta^3}{6}h_{\xi\xi} - \frac{\eta^2}{2}hh_{\xi\xi} - \frac{\eta^2}{2}h_\xi^2\right) \\
&\quad + 3\overline{S}\left(\frac{\eta^3}{6}h_{\xi\xi\xi\xi} - \frac{\eta^2}{2}hh_{\xi\xi\xi\xi} - \frac{\eta^2}{2}h_\xi h_{\xi\xi\xi}\right) \\
&\quad - \frac{1}{2}G\sin\beta\left(\frac{\eta^4}{12}h_{\tau\xi} - \frac{\eta^2}{2}h^2 h_{\tau\xi} - \eta^2 hh_\xi h_\tau\right) \\
&\quad - \frac{1}{6}G^2\sin^2\beta\left(\frac{\eta^5}{20}h_\xi^2 - 2\eta^2 h^3 h_\xi^2 + \frac{\eta^5}{20}hh_{\xi\xi} - \frac{\eta^2}{2}h^4 h_{\xi\xi}\right)
\end{aligned}
\tag{6.36}
$$

The leading order terms u_0, v_0 and p_0 are the lubrication theory results. The evaluated velocity is substituted into the kinematic equation, and all terms of higher order than $O(\epsilon)$ are dropped, resulting in the following nonlinear evolution equation for the film thickness $h(x,t)$:

$$h_t + Gh^2 h_x\sin\beta + \left[\frac{2G^2}{15}h^6 h_x\sin^2\beta - \frac{1}{3}Gh^3 h_x\cos\beta + Sh^3 h_{xxx}\right]_x = 0 \tag{6.37}$$

In obtaining the above equation the system has been rescaled back to the original (x, y, t). The second term in the above equation describes the wave propagation and steepening. The third term is a destabilizing force and is due to the mean shear flow. The fourth and the fifth terms are stabilizing forces and are due to hydrostatic pressure and surface tension force, respectively. For two-dimensional films, Sivashinsky & Michelson (1980) showed that in the large surface tension limit ($S \to \infty$), the evolution equation can be further simplified to the Kuramoto-Sivashinsky equation:

$$\phi_t + a\phi\phi_x + b\phi_{xx} + c\phi_{xxxx} = 0, \tag{6.38}$$

where $\phi = h - 1$ is the wave amplitude and a, b, and c are appropriate constants and angle $\beta = \frac{\pi}{2}$.

Much of the nonlinear stability analysis of thin film flows has been done using the Kuramoto-Sivashinsky equation (Eq.6.38) and the longwave evolution equation of the Benney type (Eq.6.37) due to their relative simplicity. The longwave evolution equation is a fully nonlinear equation and cannot be solved analytically. However, a weakly nonlinear analysis can be performed by retaining only the fundamental mode and its first harmonic. The weakly nonlinear analysis of Lin (1969), Gjevik (1970) and Nakaya (1975), all predict supercritical finite amplitude waves for wavenumbers just below the linear cut-off wavenumber k_c. They also predict a new phase boundary $k_s(G, S, \beta)$, below which no permanent waves can be observed (Fig.6.4). Pumir, Manneville & Pomeau (1983) and Joo, Davis & Bankoff (1991b), solved the longwave evolution equation numerically. They confirm the existence of supercritical saturated permanent waves for wavenumbers slightly lower than k_c. For wavenumbers much below the linear cut-off wavenumber k_c, they observe very long waves of the 'solitary' type.

6.3.4 Nonlinear Stability Analysis based on Boundary Layer equations

The nonlinear stability analysis described in the previous subsection is valid only for very thin layers, i.e. $G \sim O(1)$. For relatively thick layers, the inertial terms can no longer be neglected and the lubrication theory breaks down. Another approximate nonlinear stability theory valid for relatively thicker layers, i.e. $G \sim O(100)$, has been developed based on the boundary layer equations. With only the assumption that the disturbance wavelength is much longer than the film thickness ($\lambda \gg h_0$),

k

linearly stable

$k_c(G,S,\beta)$

supercritical

$k_s(G,S,\beta)$

subcritical

$G_c(\beta)$ G
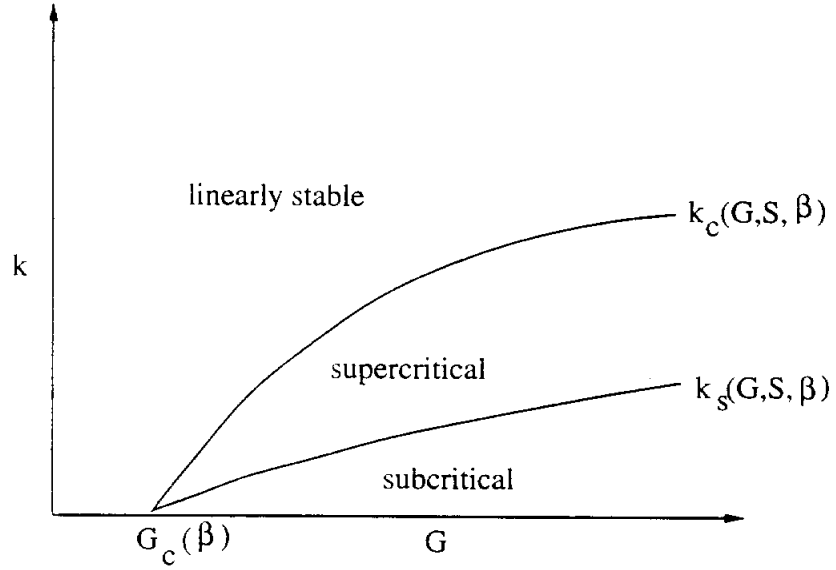
Figure 6.4: Stability diagram based on weakly nonlinear stability analysis

the original Navier-Stokes equations given by Eqs.(6.1-6.3) can be simplified to the following boundary layer equations:

$$\frac{\partial u}{\partial t} + u\frac{\partial u}{\partial x} + v\frac{\partial u}{\partial y} = G\sin\beta - G\cos\beta h_x + 3Sh_{xxx} + \frac{\partial^2 u}{\partial y^2} \tag{6.39}$$

$$\frac{\partial u}{\partial x} + \frac{\partial v}{\partial y} = 0 \tag{6.40}$$

The differences from the original Navier-Stokes equations is that pressure is taken to be the sum of hydrostatic and capillary pressures only, and the diffusion terms in the stream-wise direction are dropped. The boundary conditions also simplify to:

$$\left.\begin{array}{rcl} u &=& 0 \\ v &=& 0 \end{array}\right\} \quad \text{at} \quad y = 0 \tag{6.41}$$

$$\left. \begin{array}{rcl} \dfrac{\partial u}{\partial y} & = & 0 \\[2mm] \dfrac{\partial h}{\partial t} + u\dfrac{\partial h}{\partial x} & = & v \end{array} \right\} \quad \text{at} \quad y = h(x,t) \tag{6.42}$$

The above listed Boundary Layer system is much easier to solve than the original Navier-Stokes equations.

The boundary layer equations can further be simplified by assuming *a priori* the velocity profile and this approach is called the Integral Boundary Layer theory (Chang 1994) and is in the same spirit as the original Von Karman - Pohlhausen momentum integral approach. A number of different evolution equations have been derived, depending on the velocity profile imposed. A uniform velocity profile results in the shallow water theory of Dressler(1949). Alekseenko etal (1985) imposed a parabolic profile to derive a more appropriate evolution equation, which is further extended recently by Prokopiou, Cheng & Chang (1991) to higher-order accuracy. In the integral boundary layer theory, two evolution equations are obtained, one for the flow rate $q =. \int_0^h u\, dy$, and the other for the film thickness $h(x,t)$. A parabolic velocity profile results in the following evolution equations:

$$\frac{\partial q}{\partial t} + 1.2\frac{\partial}{\partial x}\left(\frac{q^2}{h}\right) = h\left(G\sin\beta - G\cos\beta\, h_x + 3S\left(\frac{1}{R}\right)_x\right) - 3\frac{q}{h^2} \tag{6.43}$$

$$\frac{\partial h}{\partial t} + \frac{\partial q}{\partial x} = 0 \tag{6.44}$$

With some additional approximations, the above two evolution equations can be combined into one second-order wave equation for the film thickness $h(x,t)$ (Alekseenko etal 1985). Lee & Mei (1995) derived an evolution equation, valid for large Reynolds numbers and moderate Weber numbers, based on the boundary layer approximation and *a priori* specification of a parabolic velocity profile. Chang, Demekhin

& Kopelevich (1993) solved the longwave boundary layer equations numerically, without *a priori* specification of the velocity profile.

In majority of the nonlinear studies based on the longwave boundary layer equations, finite amplitude permanent waves are assumed *a priori*, and the stationary equations are solved in a frame of reference translating with the wave speed c. Chang etal (1993) based on this type of analysis, predict slow-moving short nearly sinusoidal waves referred to as γ_1 family, and fast-moving long solitary waves with one or more primary humps referred to as the γ_2 family. Based on a detailed bifurcation analysis of the third-order dynamical system resulting from the assumption of stationary waves, Lee etal (1995) find a variety of bifurcation phenomena, such as limit cycles, heteroclininc orbits, chaotic attractors and homoclinic orbits.

6.3.5 Direct Numerical Studies

To study the complicated nonlinear flow developments without any *a priori* assumptions such as those made in the long-wave theory and the boundary layer theory, the complete Navier-Stokes equations need to be solved. Due to the irregular and time-varying flow domains involved, Finite Element Method (FEM) has been the popular method of choice (Bach & Villadsen 1984; Kheshgi & Scriven 1987; Malamataris & Papanastasiou 1991; Salamon, Armstrong & Brown 1994). Ho & Patera (1990) used Legendre Spectral Element Method, which is a higher order FEM. Bach & Villadsen(1984), Kheshgi & Scriven (1987) and Malamataris & Papanastasiou (1991) use a Lagrangian Finite Element Method to handle the moving boundary and control the mesh distortion through rezoning. Ho & Patera (1990) use a mixed Lagrangian- Eulerian approach and Salamon etal (1994) use the concept of vertical spines.

Kheshgi & Scriven(1987) and Ho & Patera(1990) make comparisons with the Orr-Sommerfeld linear stability predictions for the neutral wavenumbers. Ho & Patera (1990) compared the wave profile and wave speeds with the experimental measurements of Kapitza & Kapitza (1949). In finite length domains without periodic boundary conditions, Kheshgi & Scriven (1987) could not observe steady traveling waves. However, Malamataris & Papanastasiou (1991) using a modified free boundary condition show the existence of traveling waves in truncated domains.

Salamon etal (1994) did a comprehensive direct numerical study of traveling waves in vertical thin films and compared their results against the approximate long-wave and boundary layer theories. They assume a priori the existence of steady traveling waves and rewrite the governing equations in a frame of reference translating with the wave speed. They thus solve the steady state Navier-Stokes equations and compute the flow field, free surface profile and wave speed simultaneously for a given wavelength and Reynolds number. They found good agreement with the long-wave theory for small amplitude waves, but found their results to qualitatively diverge from the longwave results for large amplitude waves. The also studied the nonlinear interactions between the waves and the secondary subharmonic bifurcations to longer waves.

6.3.6 Experimental Studies

Experimental studies of falling films have been done by, among others, Kapitza & Kapitza (1949), Krantz & Goren (1971), Portalski & Clegg (1972), Alekseenko etal (1985), and Lacy, Sheintuck & Dukler (1991). As summarized by Alekseenko etal(1985), in most of the experiments performed, two-dimensional regular waves are observed only near the wave-inception line. The waves soon become three-

dimensional and irregular. In order to obtain two-dimensional wavetrains, the flow was disturbed at a fixed frequency by, for example, wire vibrations (Krantz & Goren 1971) and pulsations of flow rate (Kapitza & Kapitza 1949; Alekseenko etal 1985). Lacy etal. (1991) performed the experiments without artificial perturbations, and noticed that draining films exhibit deterministic chaos.

More recently, Liu, Paul and Gollub (1993) using sophisticated experimental techniques, measured the cut-off Reynolds number as a function of the angle of inclination of the plate. They found good agreement with the linear stability predictions for the cut-off Reynolds number, growth rates and wave velocities. They also demonstrated the primary instability to be convective in character and hence extremely sensitive to external noise at the source. Liu & Gollub (1993) found the primary surface wave instability to be susceptible to both side-band and subharmonic secondary instabilities but in different ranges of frequency. These secondary instabilities are also convective in nature and are one of the routes to spatio-temporal chaos. Liu & Gollub (1994) performed a systematic analysis of solitary wave dynamics in two dimensions and found the velocity of the solitary wave to be proportional to the wave height. Due to this amplitude dependence of the wave speed, the bigger amplitude waves travel faster and coalesce with smaller waves.

6.4   Course of the Study

From the review of the literature related to the thin film flow as outlined briefly in the previous section, we can infer the following:

1. The solution of the linear stability problem based on the Orr-Sommerfeld equation can be considered to be complete. The predictions of the linear stability theory have also been validated experimentally.

2. The thrust of the theoretical research in the past few years has been to derive model equations capable of studying the nonlinear evolution of the thin film flow. The longwave theories based on the lubrication approximation and the boundary layer approximation have been partially successful in explaining the nonlinear flow regimes. However, these nonlinear theories have only limited ranges of validity.

3. A complete nonlinear study of the thin film instability requires the solution of the Navier–Stokes equations. However, due to the presence of the free boundary, numerical solution of the Navier–Stokes equations is extremely difficult and computationally intensive. With the exception of Salamon etal (1994), all the other numerical studies are limited in scope and primarily aim to establish that their numerical procedure is capable of simulating the thin film flows.

The aim of this research is:

1. To develop an efficient and accurate numerical procedure capable of solving the free boundary Navier–Stokes equations arising in the thin film flows. In particular, the numerical method should be based on the solution of the initial value problem, so that the most stable waveform for the simulation parameters can be directly computed. The essentials of the numerical procedure are described in Chapters 3 & 5.

2. Utilize the numerical procedure to perform a detailed temporal stability analysis. In particular, we wish to study in detail the nonlinear flow regimes, namely the finite amplitude permanent wave regimes (Region II in Fig.6.1) and the solitary wave regimes (Region III in Fig.6.1). This is discussed in sections 6.5 & 6.6.

3. Study the wave interaction processes, such as, wave splitting and wave mergers, known to occur in thin film flow. This is discussed in section 6.7.1.

4. Lastly, we wish to establish our numerical procedure as a complement to laboratory experiments. What is studied in the laboratory, is the spatial stability analysis. A periodic disturbance is imposed at the inlet and its evolution in the streamwise direction is measured. To this end, we consider nonperiodic domains with absorbing boundary conditions at the exit and make comparisons with the experiments of Liu & Gollub (1994). This is discussed in section 6.7.3.

6.5 Comparison with experiments and previous numerical simulations

Kapitza & Kapitza (1949) obtained two-dimensional permanent waves on thin films draining down a vertical cylinder by artificially perturbing the flow rate at a fixed frequency and amplitude. Ho & Patera (1990) and Salamon etal (1994) compared their numerical results with the experimental findings of Kapitza & Kapitza (1949) for the two conditions listed in Table 6.1. These two experimental conditions are numerically simulated through our full-scale numerical procedure and compared with the experimental results of Kapitza & Kapitza (1949) and the numerical results of Ho & Patera (1990) and Salamon etal (1994).

fluid	$\frac{\sigma}{\rho}\left(\frac{cm^3}{s^2}\right)$	λ(cm)	$Q(\frac{cm^2}{s})$	G	S	k
alcohol at $16.8°C$	29	1.77	0.123	18.2	463.7	0.07
water at $19.6°C$	74	0.80	0.201	60.0	4410	0.14

Table 6.1: **Experimental conditions of Kapitza & Kapitza(1949) and the relevant non-dimensional parameters.**

What is investigated in experiments is the spatial stability, where a periodic disturbance is imposed at the inlet and its evolution in streamwise direction is determined. For periodic forcing at the inlet, sufficiently far downstream from the inlet, Kapitza & Kapitza (1949) observed saturation of the disturbance and the waves travel downstream with fixed wave speed and wavelength. Numerically, however, the equilibrium wave profile and wave speed are obtained through temporal stability analysis. A streamwise periodic disturbance with wavelength λ observed in the experiments is imposed as follows:

$$h(0, t) = 1 + \delta \cos(kx), \tag{6.45}$$

and its evolution in time is computed through the direct numerical solution of the full nonlinear system given by Eqs.6.1-6.3. $k = 2\pi h_o/\lambda$ is the nondimensional wavenumber, and the boundary conditions in the streamwise direction are:

$$\phi(x = 0) = \phi(x = \lambda), \tag{6.46}$$

where ϕ stands for h, u, v and p. Saturation of the disturbance in time implies steady traveling wave with fixed wave speed and wave profile. These numerically computed wave profile and wave speed are then compared with those obtained by Kapitza & Kapitza (1949).

The mean film thickness h_0 is needed for calculating the nondimensional parameters G, S and k. However, Kapitza & Kapitza (1949), do not provide the mean film thickness, and instead give the flow rate. Using the experimental flow rate q, the mean film thickness h_0 is computed as:

$$h_0 = \left(\frac{3\nu q}{g}\right)^{1/3}. \tag{6.47}$$

This mean film thickness is then used to compute the nondimensional parameters G, S and k. In the numerical formulation, the mean film thickness remains fixed in time, but the flow rate could vary with time. In fact, with the onset of wave motion, the flow rate increases, and the final steady flow rate in our numerical simulation would be greater than the experimental flow rate. The results of the nonlinear flow evolution are presented in terms of the film thickness $h(x, t)$ at various instants of time and the spatial spectral coefficients $c_n(t)$, defined as

$$h(x, t) = \sum_{n=-N}^{n=N} c_n(t) e^{inkx},$$

(6.48)

where $2N$ is the number of mesh divisions in the streamwise direction. The initial amplitude of the disturbance is set to $\delta = 0.05$.

The nonlinear flow evolution for the experimental condition $G = 18.2$, $S = 463.7$, $\beta = \pi/2$ and $k = 0.07$ is shown in Fig.6.5. The experimental wavenumber $k = 0.07$ is smaller than the linear cut-off wavenumber $k_c = 0.29$ (Whitaker 1964). Thus, in agreement with the linear theory, the amplitude of the disturbance grows exponentially initially (Fig.6.5a). Eventually, however, due to the stabilizing capillary force, the growth is arrested, resulting in steady traveling waves (Fig.6.5b). The dynamics of the the nonlinear processes can be better quantified through the spatial spectral coefficients $c_n(t)$ (Fig.6.5c). The fundamental mode and its harmonics grow exponentially initially. Eventually, due to the nonlinear stabilizing, they saturate in time, resulting in finite amplitude permanent waves traveling downstream at fixed wave speed c. The equilibrium wave profile obtained using the present method is compared with that reported by Kapitza & Kapitza (1949), Ho & Patera (1990) and Salamon etal (1994) in Fig.6.6. It is in excellent agreement with the experimental profile of Kapitza & Kapitza (1949) and the numerical profiles of Ho & Patera

(1990) and Salamon etal (1994). The dominant crest has a tear drop profile with a sharp downstream slope and a long gently sloping tail. The sharp hump is preceded immediately downstream by small capillary waves. The free surface profile is 'solitary wave' type and corresponds to the 'single wave' observed by Kapitza & Kapitza (1949) for wave numbers much smaller than the critical wave number k_c. The computed wave speed is $23.1cm/s$ which compares very well with the wave speed of $23.5cm/s$ reported by Salamon etal (1994) and $24.7cm/s$ reported by Ho & Patera (1990). The experimental wave speed reported by Kapitza & Kapitza (1949) is $19.5cm/s$ which is appreciably lesser than the numerically computed wave speeds. As pointed out by Ho & Patera (1990) and Salamon etal (1994), the experimental flow rate is imposed only as an initial condition in the numerical simulation, but due to the onset of wave motion, there is an increase in the flow rate. Salamon etal (1994) obtained better agreement with the experimental results when they adjusted their mean film thickness to take into account this aspect. Also shown in Fig.6.6 is the permanent wave profile obtained through the numerical solution of the integral boundary layer system based on the assumption of a parabolic velocity profile (Eqs.6.43,6.44). We find the wave profile obtained through the Integral Boundary Layer system to be in good agreement with that obtained experimentally and numerically through full-scale computations. The results shown in Figs.6.5 are obtained using a 65×11 mesh with time step control parameter $CFL = 0.1$. Doubling the number of nodes in x and y directions and reducing the time step size by half resulted in identical results as shown in Fig.6.7. The evolution of the harmonic modes is exactly the same for various mesh and time step parameters. Thus the solution computed by us is independent of the mesh size and the time step.

73
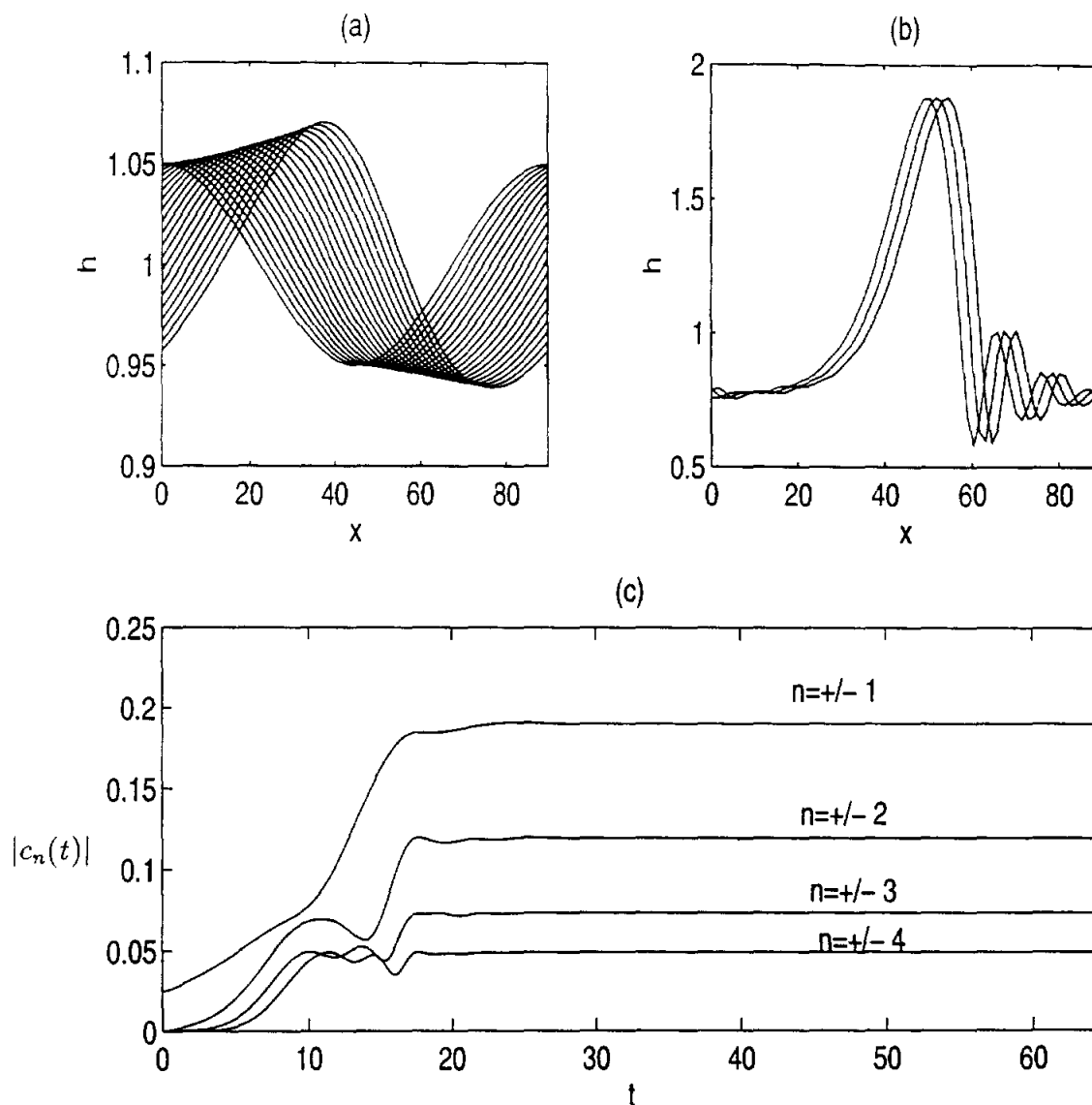
Figure 6.5: First experimental condition of Kapitza & Kapitza (1949), namely, G=18.2, S=463.7, k=0.07, $\beta = \frac{\pi}{2}$: (a) $h(x,t)$ for $t = 0.0$ to $t = 2.0$ in steps of 0.1; (b) $h(x,t)$ for $t = 64.6$ to $t = 64.8$ in steps of 0.1; (c) Evolution of spectral coefficients ($|c_n(t)|$ versus time).

(a)   (b)   (c)   (d)   (e)
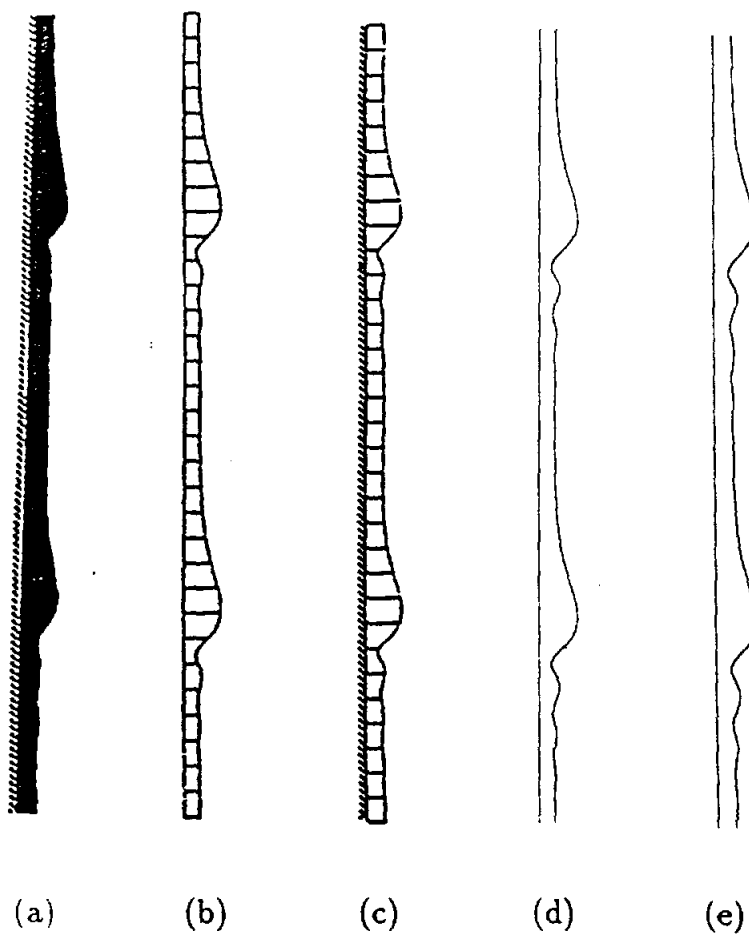
Figure 6.6: Wave shapes for $G = 18.2$, $S = 463.7$, $k = 0.07$, $\beta = \frac{\pi}{2}$, obtained by: (a) Kapitza & Kapitza (1949), (b) Salamon etal (1994), (c) Ho & Patera (1990), (d) Present numerical method, and (e) integral boundary layer theory.
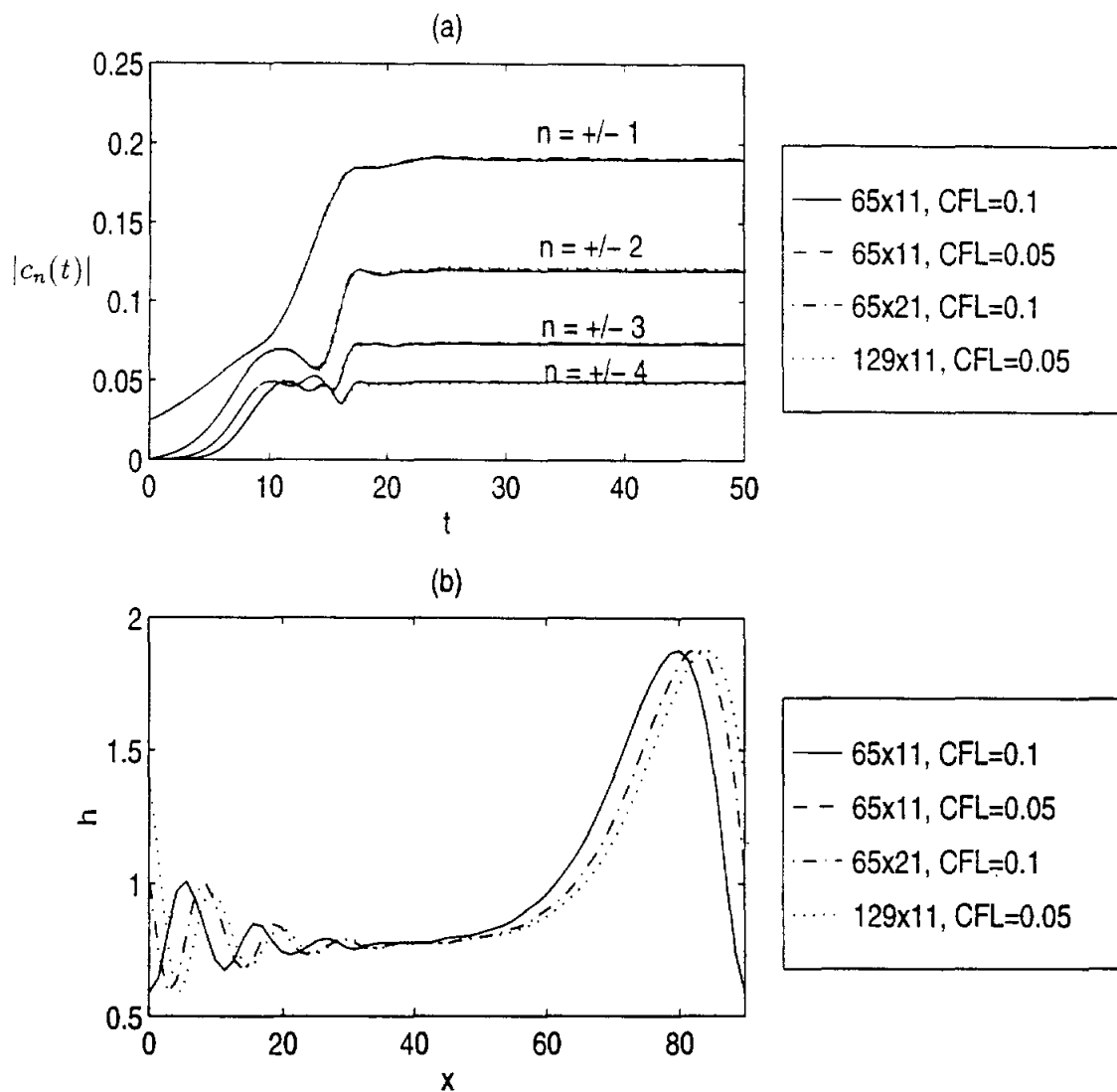
Figure 6.7: Mesh and time step independent study for $G = 18.2$, $S = 463.7$, $k = 0.07$ **and** $\beta = \frac{\pi}{2}$. **(a) Evolution of spatial spectral coefficients** ($|c_n(t)|$ **versus time); (b) Free surface profile** $h(x,t)$ **at** $t = 50$.

The evolution of the initially imposed sinusoidal perturbation with amplitude 0.05 for the case $G = 60.0$, $S = 4410.0$, $\beta = \pi/2$ and $k = 0.14$ is shown in Fig.6.8. The wavenumber $k = 0.14$ is smaller than the linear cut-off wavenumber $k_c \approx 0.30$. From the evolution of the spatial spectral coefficients shown in Fig.6.8(a), it is apparent that the amplitude of the wave grows exponentially initially. Unlike in the previous case however, the harmonic modes do not saturate in time. The spectral coefficients continuously oscillate in time, generating a quasi-periodic waveform. The fundamental mode and its harmonics are continuously exchanging energy , without settling to a stationary value. In fact, the total energy of the system defined as:

$$E(t) = \sum_{n=-N}^{n=N} |c_n(t)|^2, \tag{6.49}$$

was found to be continuously oscillating in time. The wave profiles at the two extremes, namely, when the fundamental mode has the minimum energy ($t = 77.75$) and when the fundamental mode has the maximum energy ($t = 78.90$) are shown in Fig.6.8(b). These two wave profiles along with the steady wave profiles obtained by other researchers are shown in Fig.6.9. The experimental wave profiles and the previously reported numerical wave profiles agree better with the wave profile at $t = 78.90$. A numerical solution of the Integral Boundary Layer system (Eqs.6.43,6.44) also revealed a similar quasi-periodic wave behaviour. The wave profiles obtained using the Integral Boundary Layer theory are also shown in Fig.6.9, and are found to be in close agreement with that obtained by us through the direct numerical solution of the Navier–Stokes equations. The results shown in Fig.6.8 has been obtained using a 65×11 mesh and time step control parameter $CFL = 0.1$. Numerical experimentation with various mesh sizes and time steps revealed identical behaviour. Starting with a different initial condition, namely an initial disturbance amplitude

of $\delta = 0.50$ instead of $\delta = 0.05$ also resulted in a similar behaviour (Fig.6.10). Thus, the behaviour exhibited by the system can be considered to be independent of numerical mesh and initial condition.

To summarize, for the first experimental condition (Fig.6.5), we obtain a steady travelling waveform with solitary hump shape, and both the wave profile and wave speed are in good agreement with that reported previously. For the second experimental condition (Fig.6.8), however, our full-scale computations predict a quasi-periodic waveform in contrast to the stationary waveforms reported previously. Recent experiments of Liu & Gollub (1994) indicates that this type of behaviour is also exhibited. In certain ranges of frequencies they could not observe saturated waves. This quasi-periodic behaviour is investigated in detail in the next section. Assuming for the moment, that our numerical results are correct, it remains to be explained why Kapitza & Kapitza (1949), Ho & Patera (1990) and Salamon etal (1994) did not observe this type of a behaviour. Since, the wave profiles are not necessarily sinusoidal, Kapitza & Kapitza (1949), defined the wave amplitude α as:

$$\alpha = \frac{h_{max} - h_{min}}{h_{max} + h_{min}}, \tag{6.50}$$

where h_{max} and h_{min}, are respectively, the maximum film thickness and the minimum film thickness. The wave amplitudes for different flow rates are given in Fig.13 of Kapitza & Kapitza (1949). The second experimental condition simulated by us corresponds to $Q = 0.201 cm^2/s$, and for this flow rate, they give two wave amplitudes, possibly because they did not observe well defined stationary travelling waves. The other possibility is that their test section is not long enough for them to be able to observe well defined quasi-periodic behaviour. From Fig.6.8(a), we find that the system needs about 40 nondimensional time units for the onset of
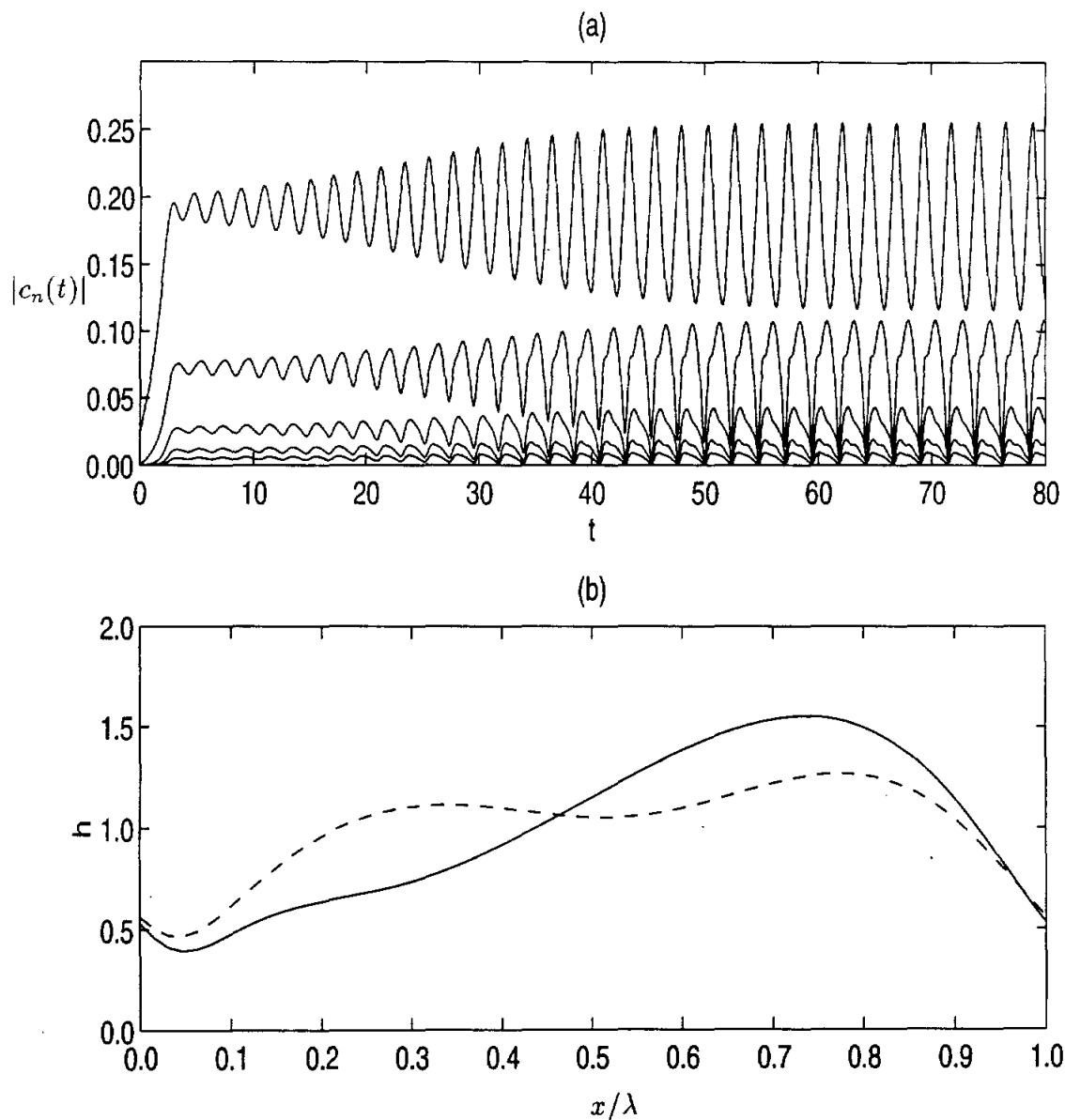
Figure 6.8: Nonlinear wave evolution for the second experimental condition of Kapitza & Kapitza (1949), namely, $G = 60.0$, $S = 4410.0$, $k = 0.14$ and $\beta = \pi/2$. (a) Evolution of the spatial spectral coefficients $|c_n(t)|$; and (b) film thickness at $t = 77.75$ (broken line) and $t = 78.90$ (continuous line).
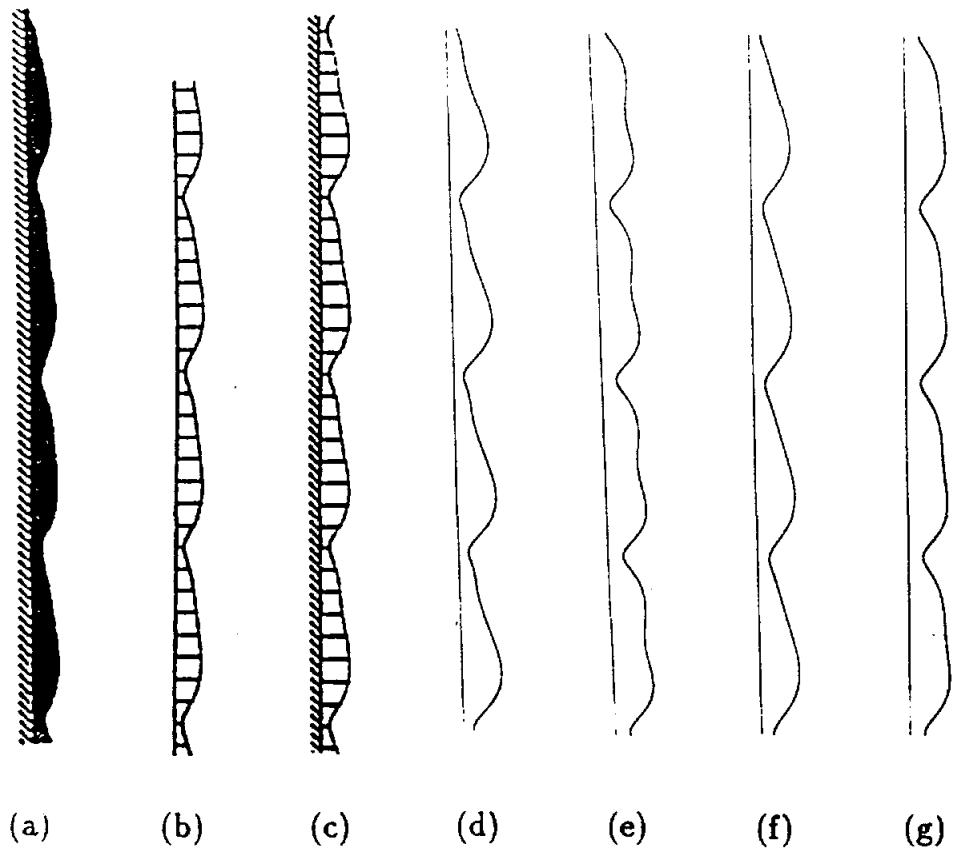
Figure 6.9: Wave shapes for $G = 60.0$, $S = 4410$, $k = 0.14$ and $\beta = \frac{\pi}{2}$, obtained by: (a) Kapitza & Kapitza (1949), (b) Salamon etal (1994), (c) Ho & Patera (1990), (d) Present numerical simulation at $t = 77.75$, (e) Present numerical simulation at $t = 78.90$, (f,g) integral boundary layer theory.
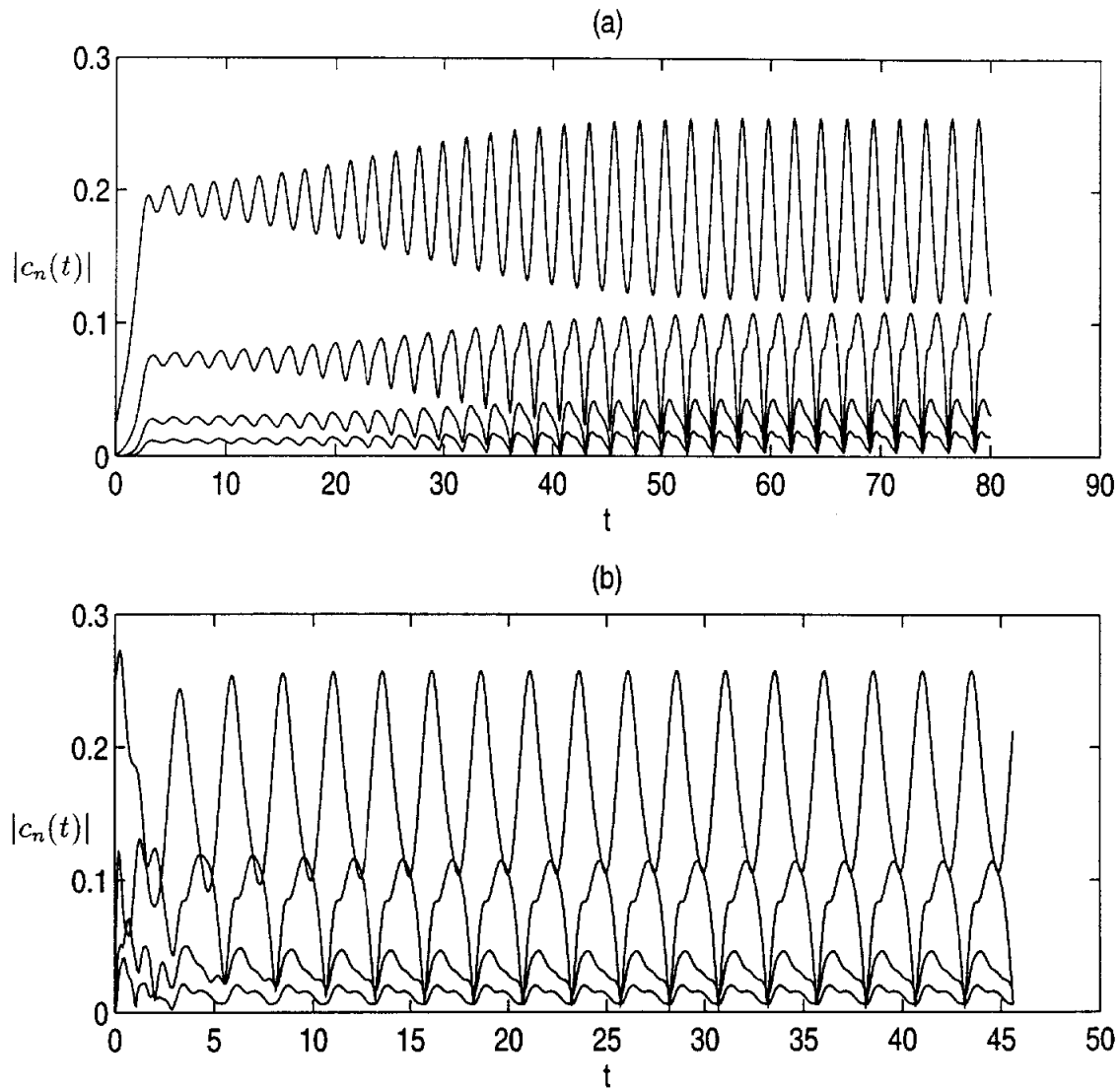
Figure 6.10: Nonlinear evolution of the spectral coefficients $|c_n(t)|$ with different initial conditions for $G = 60.0$, $S = 4410$, $k = 0.14$ and $\beta = \frac{\pi}{2}$. (a) Initial disturbance is a sinusoidal perturbation with amplitude $\delta = 0.05$; (b) initial disturbance is a sinusoidal perturbation with amplitude $\delta = 0.50$.

quasi-periodic behaviour. Based on our nondimensionalization this works out to be $t = 1.34s$, and at a wave speed of $19.7cm/s$, it would be approximately $26cm$, before well defined quasi-periodic behaviour can be observed. The length of the test section used by Kapitza & Kapitza (1949) is only $17cm$. Due to *a priori* assumption of steady traveling waveforms. Salamon etal (1994) could have missed this quasi-periodic behaviour.

6.6 Temporal Stability Analysis

From the previous section, it appears that for wavenumbers smaller than the linear cutoff wavenumber k_c, we do not always obtain steady travelling permanent waveforms. A similar result was shown experimentally by Liu & Gollub (1994). For excitation frequencies ω closer to linear cut-off frequency ω_c, they observed nearly sinusoidal saturated waves. As the frequency is reduced, however, in certain ranges of frequencies, they observed quasi-periodic evolution in the downstream direction. The film thickness is however, still periodic in time, but does not saturate in the streamwise direction. For much smaller wavenumbers, they observed steady travelling solitary waves. Thus, experimental evidence exists for quasi-periodic travelling waveforms. The experimentally investigated thin-film stability is a spatial one, where a periodic disturbances is imposed at the inlet and its evolution in the downstream direction is measured. Our full-scale computations, from the previous section, tell us that this type of quasi-periodic travelling waves are also observed in the temporal stability analysis. The quasi-periodic behaviour was also observed by Hooper & Grimshaw (1985) in their solutions of the Kuramoto–Sivashinsky (KS) equation and by Joo & Davis (1992) in their numerical solutions of the longwave evolution equation. Hooper & Grimshaw (1985) observed that for some wavenum-

bers the fundamental mode and its first harmonic are in a 'bouncy state', with continuous exchange of energy between them. Our own numerical solution of the integral boundary layer equations with the assumption of parabolic velocity profile also indicate that this type of quasi-periodic behaviour is exhibited. A detailed temporal stability analysis of the thin film flow is thus undertaken in this section, to obtain the phase boundaries for this quasi-periodic waveforms.

The long time behaviour of the system is uniquely determined by G, S, β and k. The nondimensional number S can be written as $S = TG^{1/3}$, where the new parameter $T = \sigma/(3\rho\nu^{4/3}g^{1/3})$ depends only on the fluid properties. We set $\beta = \pi/2$ and $T = 100$, and focus on vertical fluids with moderate surface tension. Temporal stability of the vertical thin film is investigated in the range $5 \leq G \leq 100$. For each G, initial disturbances of various wavenumbers k and amplitude δ are imposed and their nonlinear evolution is computed through the direct numerical solution of the full-scale system given by Eqs.6.1-6.3, subject to the boundary conditions given by Eqs.6.4,6.5. In addition, periodic boundary conditions are imposed in the streamwise direction and the initial flow field is imposed based on the lubrication approximation as follows:

$$u(x,y,0) = G\sin\beta \left[h(x,0)y - \frac{y^2}{2} \right] \tag{6.51}$$

$$v(x,y,0) = -G\sin\beta \left(\frac{\partial h}{\partial x} \Big|_{t=0} \right) \frac{y^2}{2}. \tag{6.52}$$

The initial amplitude of the disturbance δ is set to 0.05 for all the cases simulated in this section. First, results for $G = 5, 25 \& 100$ are presented. For each of these Reynolds number, three wavenumbers, namely, $k = k_M, k_M/2 \& k_M/4$ are simulated, and the results are shown next. Where required, the linear cutoff wavenumber k_c and

the maximum growth rate wavenumber k_M are taken to be that given by Whitaker (1964), who solved the linear stability Orr-Sommerfeld equation numerically.

Fig.6.11 shows the evolution of the spatial spectral coefficients $|c_n(t)|$ and the equilibrium wave form for $G = 5.0, \Gamma = 100.0$ and three different wave numbers, namely, $k = 0.10(\approx k_M)$, $k = 0.05(\approx k_M/2)$ and $k = 0.025(\approx k_M/4)$. The harmonic modes increase exponentially, in all the three cases. Due to the nonlinear interactions, there is transfer of energy from the fundamental mode to its harmonics. After some very complex interactions, the harmonics modes eventually saturate in all the three cases, implying steady travelling waveform. For $k = k_M$, the wave profile is not completely sinusoidal since the lower harmonics also possess non-zero energy (Fig.6.11b). As the wavenumber is further decreased, i.e. for $k = k_M/2$, several of the harmonics are excited, and the wave profile is 'solitary wave' like, with a tear drop hump preceded downstream by small capillary ripples (Fig.6.11d). Further reduction in the wavenumber results in a solitary wave type profile with two primary humps (Fig.6.11f). Also shown in Fig.6.11 are the final permanent waveforms predicted by the longwave evolution equation of the Benney type (Eq.6.37)[4]. We find excellent agreement between the full-scale computations and the longwave predictions. Thus, for small Reynolds number or alternatively for small thickness film flows, the longwave evolution equation gives us reasonably good predictions.

Many of the qualitative features observed in the simulations just discussed, support what is already known about the thin film dynamics. For wavenumbers lower than k_c, we find the flat Nusselt film flow to be unstable, and a small perturbation imposed on this solution grows exponentially as predicted by the linear stability

---

[4]The longwave predictions have been computed using the numerical code provided to us by Dr. S.W. Joo from Wayne State University. The details of this numerical scheme are discussed in Joo, Davis and Bankoff (1991b).
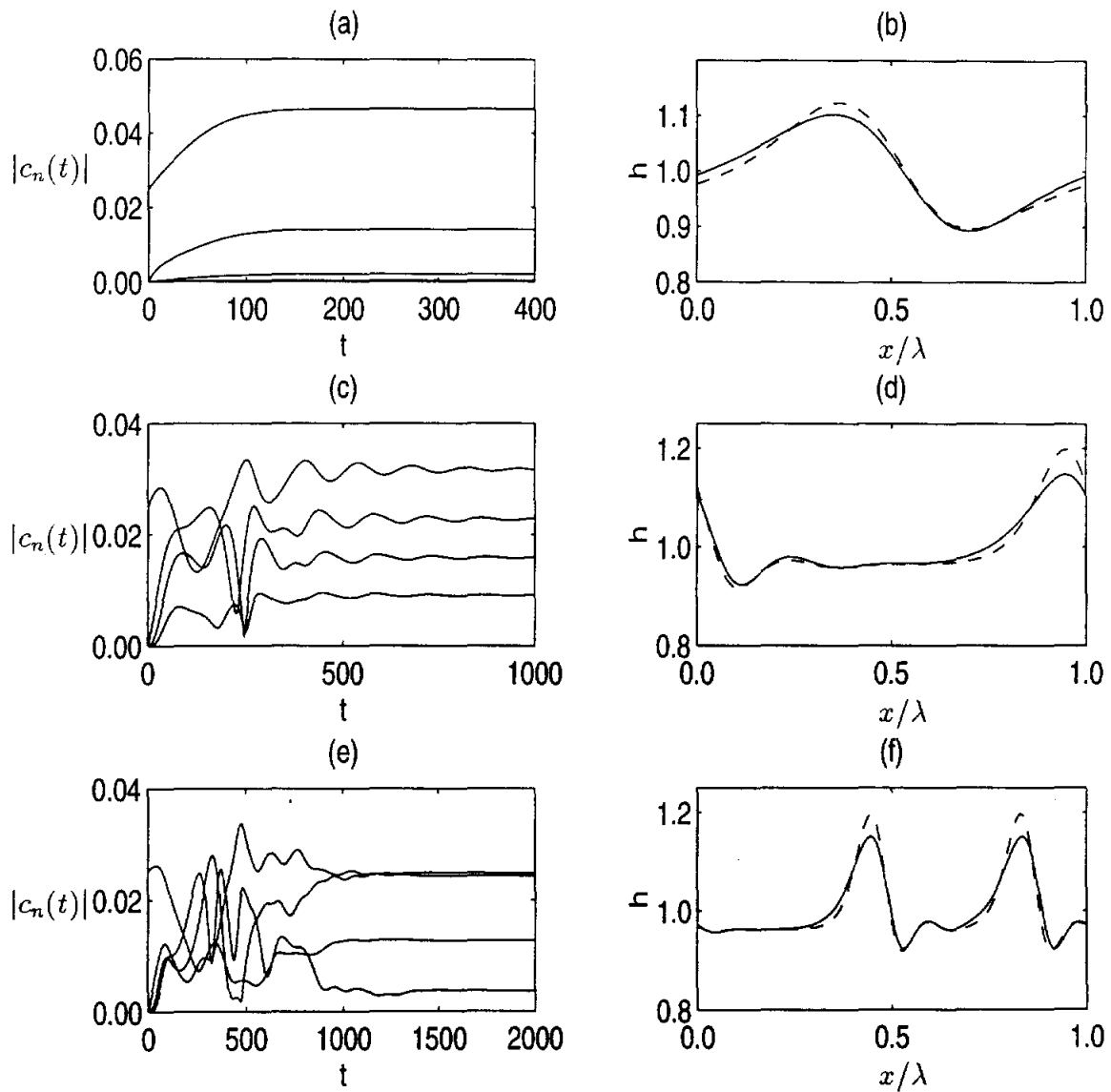
Figure 6.11: Evolution of the spectral coefficients $|c_n|(t)$ and the final waveform for $G = 5$, $T = 100$, $\beta = \pi/2$ and (a,b) $k = 0.10(\approx k_M)$; (c,d) $k = 0.05(\approx k_M/2)$; (e,f) $k = 0.025(\approx k_M/4)$. The waveform shown in broken line is obtained using the longwave evolution equation of the Benney type.

theory. However, as the wave amplitude grows, nonlinear interactions takeover, and the energy is channeled from the fundamental mode to its harmonics. In some way, this provided a stabilization and arrests the exponential growth. The nonlinearity by itself, however, is not capable of sustaining well defined permanent waveforms. The formation of well defined steady traveling waveforms on the gas-liquid interface is due to the presence of surface tension, which acts as a restoring force and cuts off the lower harmonics and limits the energy to only the first few modes. For wavenumbers close to k_c, these permanent waves are nearly sinusoidal in shape. But, for wavenumbers much smaller than k_c, these permanent waves are of the 'solitary wave' type.

The nonlinear evolution of the spatial harmonic coefficients $c_n(t)$ and the final permanent wave form for $G = 25$ and $k = 0.30 (\approx k_M)$, $k = 0.15 (\approx k_M/2)$ and $k = 0.075 (\approx k_M/4)$ are shown in Fig.6.12. The initial exponential growth is followed by equilibration of the modes for all the three wavenumbers resulting in finite amplitude permanent waveforms travelling downstream with fixed wave speed on the gas-liquid interface. The notable difference from the $G = 5$ case, is the substantially larger wave amplitude with the maximum wave height more than double the mean film thickness for the wave number $k = 0.075$ (Fig.6.12f). As the wavenumber is reduced the waveform changes from nearly sinusoidal waves to broad-banded solitary waves. Attempts to solve the longwave evolution equation of the Benney type (Eq.6.37) for $G = 25$ have resulted in numerical breakdown for all the three wavenumbers. This is to be expected since it is valid only for $G \sim O(1)$. The Integral Boundary Layer system given by Eqs.6.43,6.44 are numerically solved, and the resulting finite amplitude waveforms are also shown in Fig.6.12. The agreement between the full-scale computations and the boundary layer predictions is seen to be excellent.
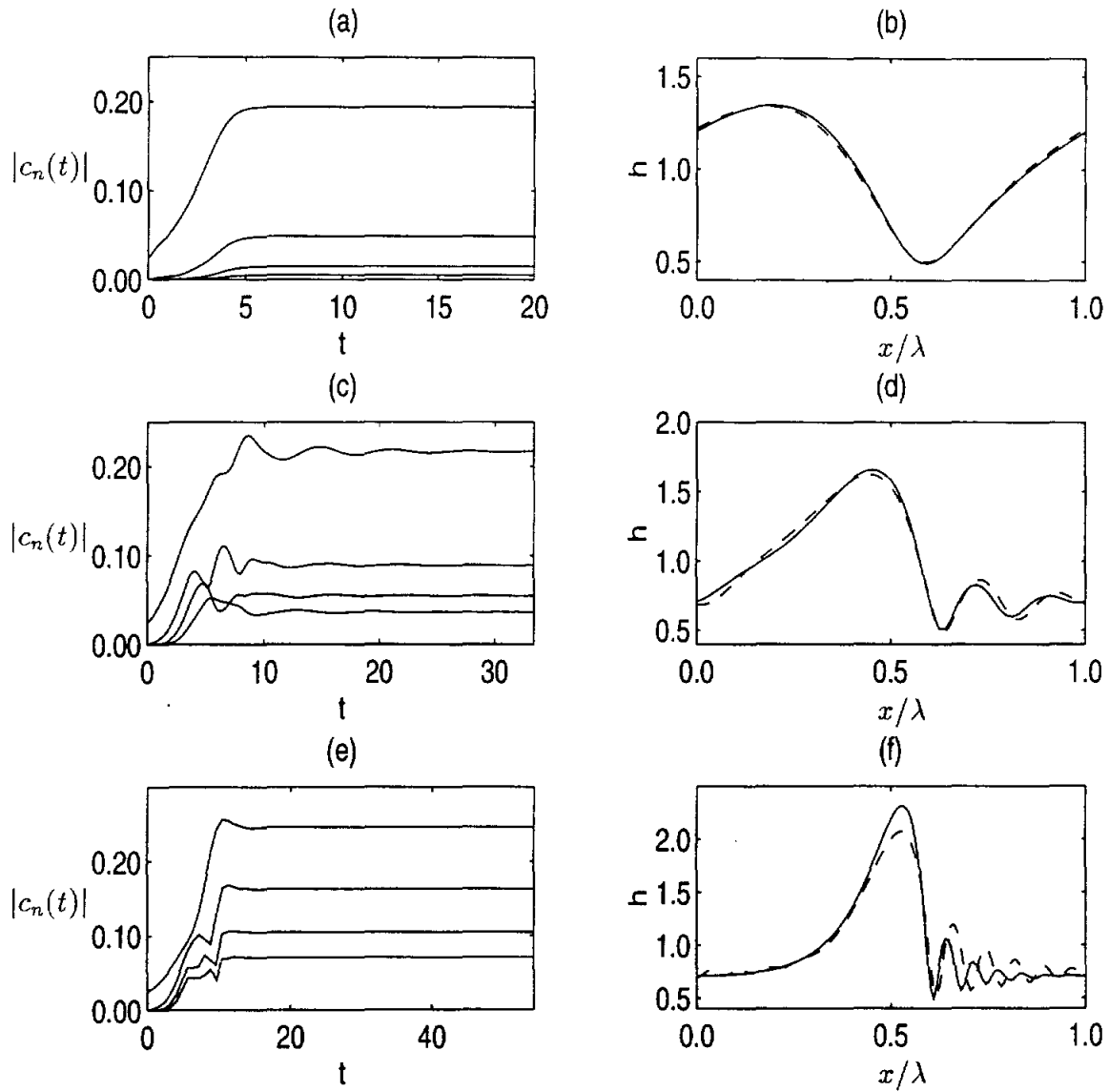
Figure 6.12: Evolution of the spectral coefficients $|c_n|(t)$ and the final waveform for $G = 25$, $T = 100$, $\beta = \pi/2$ and (a,b) $k = 0.30(\approx k_M)$; (c,d) $k = 0.15(\approx k_M/2)$; (e,f) $k = 0.075(\approx k_M/4)$. The waveform shown in broken line has been obtained using the integral boundary layer theory.

The nonlinear wave evolution for $G = 100$ and $k = 0.40(\approx k_M)$, $k = 0.20(\approx k_M/2)$ and $k = 0.10(\approx k_M/4)$, is shown in Fig.6.13. The harmonic modes evolution shown in Fig.6.13(a) is quite different from that seen previously for the low Reynolds numbers $G = 5$ and $G = 25$. The initial exponential growth is not followed by saturation of the modes but rather results in a fluctuating behavior. This corresponds to quasi-steady wave profiles and we do not observe steady permanent wave form as observed in the previous case $G = 5$ and $G = 25$. The wave form shown in Fig.6.13(b) is consequently not the permanent wave profile but is a wave profile as some given instant of time. A similar but more complex time behavior is observed in the $k = k_M/2$ case. This probably corresponds to a quasi-periodic wave profile with even more number of independent frequencies than the previous case $k = k_M$. Surprisingly for $k = k_M/4$ we obtain saturated solitary wave form with several small capillary waves in the front. A rigorous mesh and time step independent studies have been done to confirm this behavior.

To understand what is happening physically, during these quasi-periodic evolutions, free surface profiles at various instants of time are shown for $G = 100$ and $k = 0.20$ in Fig.6.14. For clarity the free surface profiles are shown over a three wavelength domain. To particularly note is the growth of the subsidiary peak just upstream of the primary wave and its coalescence with the primary wave. At the end of this coalescence there are only three subsidiary peaks between any two primary humps. Very soon a new subsidiary peak develops and starts growing and merges with the primary maxima and the process is repeated. It is this phenomenon which results in the fluctuations of the harmonic modes and a quasi-steady wave behavior. Recently, Liu and Gollub (1994) demonstrated a similar wave behavior experimentally. Thus, in the transition from nearly sinusoidal permanent waves to solitary
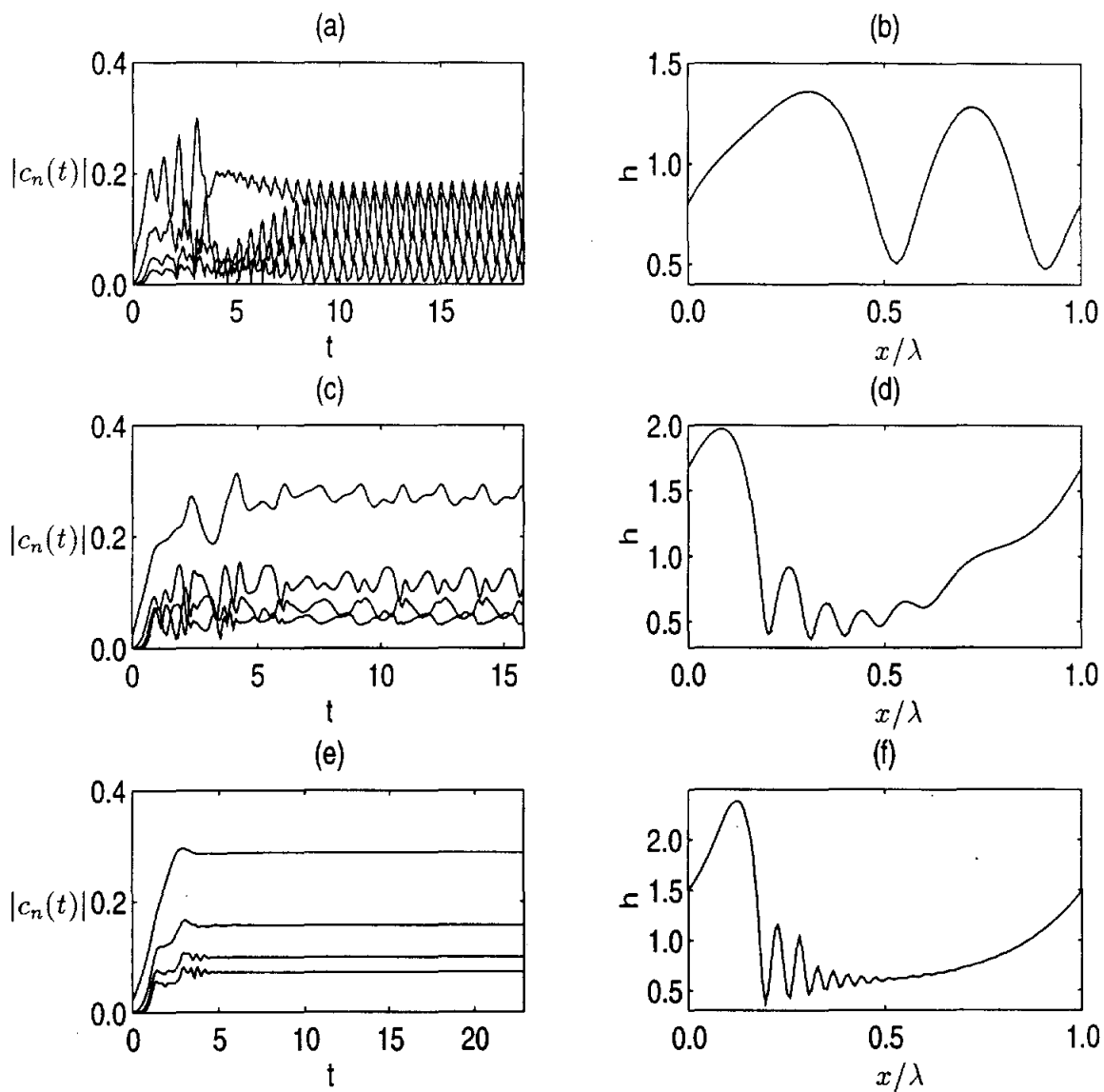
Figure 6.13: Evolution of the spectral coefficients $|c_n(t)|$ and the waveform for $G = 100$, $T = 100.0$, $\beta = \pi/2$ and (a,b) $k = 0.40(\approx k_M)$; (c,d) $k = 0.20(\approx k_M/2)$; (e,f) $k = 0.10(\approx k_M/4)$.

wave train there exists a band of wave numbers (frequencies) where the solitary humps are too closely packed resulting in very strong interaction between the primary hump and the subsidiary peaks, and no permanent wave form is observed in this case, but rather a quasi-steady behavior is observed.

To address the question of whether the quasi-periodic wave forms are likely even for smaller Reynolds numbers, we simulate the case $G = 25$, $T = 100$ and $\beta = \frac{\pi}{2}$ for wave numbers $k = 0.25, 0.23, 0.22$ and 0.20. The evolution of the harmonic modes for these cases is shown in Fig.6.15. Saturation of the harmonic modes is observed for all wave numbers except $k = 0.23$ in which case we observe fluctuations in the harmonic modes, most likely implying quasi-periodic wave forms. There is a remarkable change in the behavior of the modes even for a small change in the wave number as is evident from the cases $k = 0.23$ and $k = 0.22$. Thus, this apparent quasi-periodic wave evolution is not completely a high Reynolds number phenomena. Except, the band of wavenumbers for which this type of behavior is exhibited increases with increasing Reynolds numbers.

An extensive parametric search in the range $5 \leq G \leq 100$, has been performed to obtain the phase diagram shown in Fig.6.16. Starting from the linear cutoff wavenumber k_c, the nonlinear wave evolution has been obtained in steps of 0.01 up to $k = 0.10$, for the thickness parameters $G = 5, 25, 40, 60, 80 \& 100$. The prominent findings of this section including the phase diagram shown in Fig.6.16 can be summarized as follows:

1. The finite amplitude permanent waves are nearly sinusoidal for wavenumbers slightly smaller than k_c, and are broad-banded solitary humps for very small wavenumbers. This is in agreement with the predictions of the longwave theory based on the lubrication approximation, which is only valid for small Reynolds
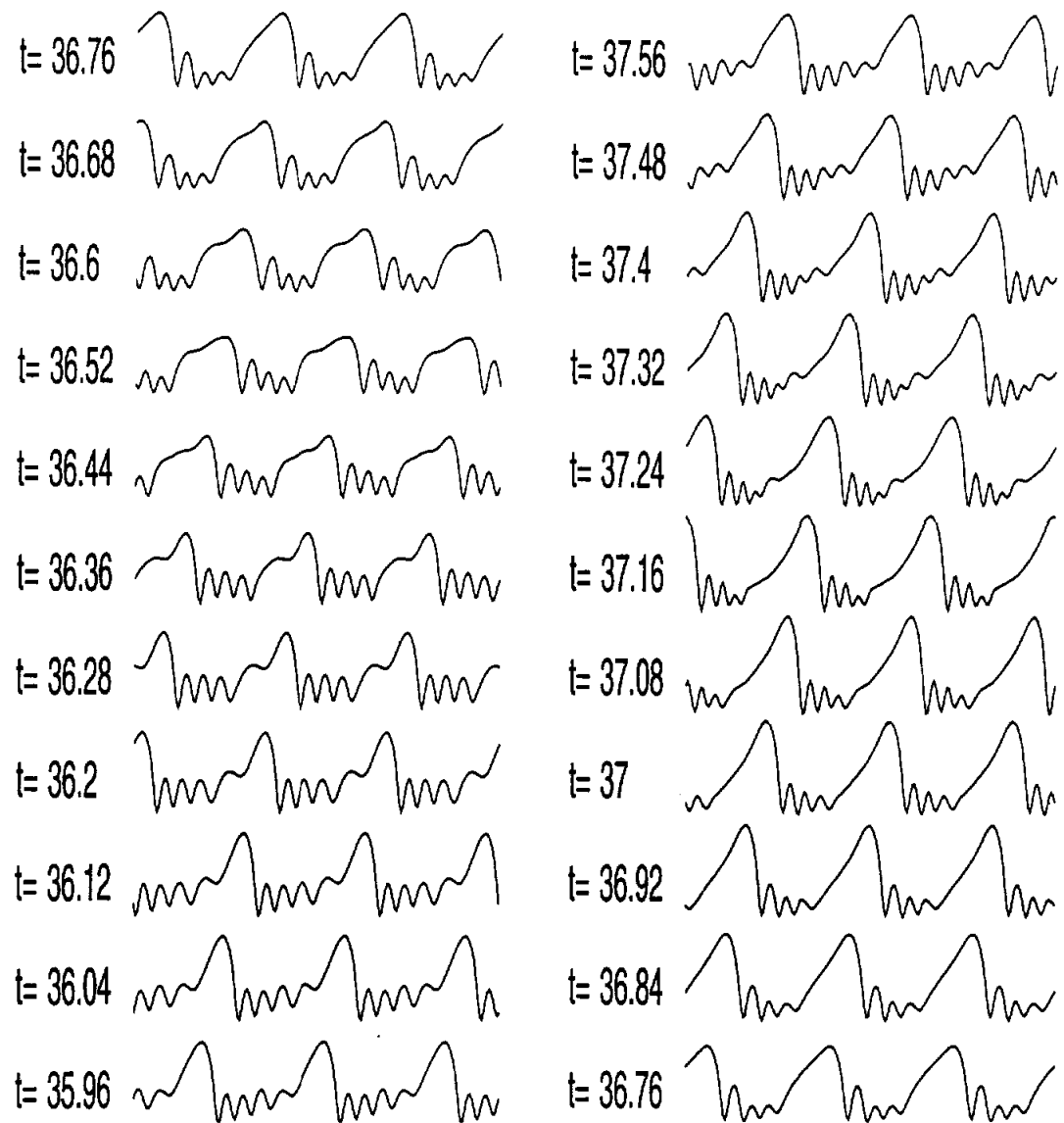
Figure 6.14: Free surface profiles at different instants of time shown in a three wavelength domain for $G = 100$, $T = 100$, $\beta = \pi/2$ and $k = 0.20$.
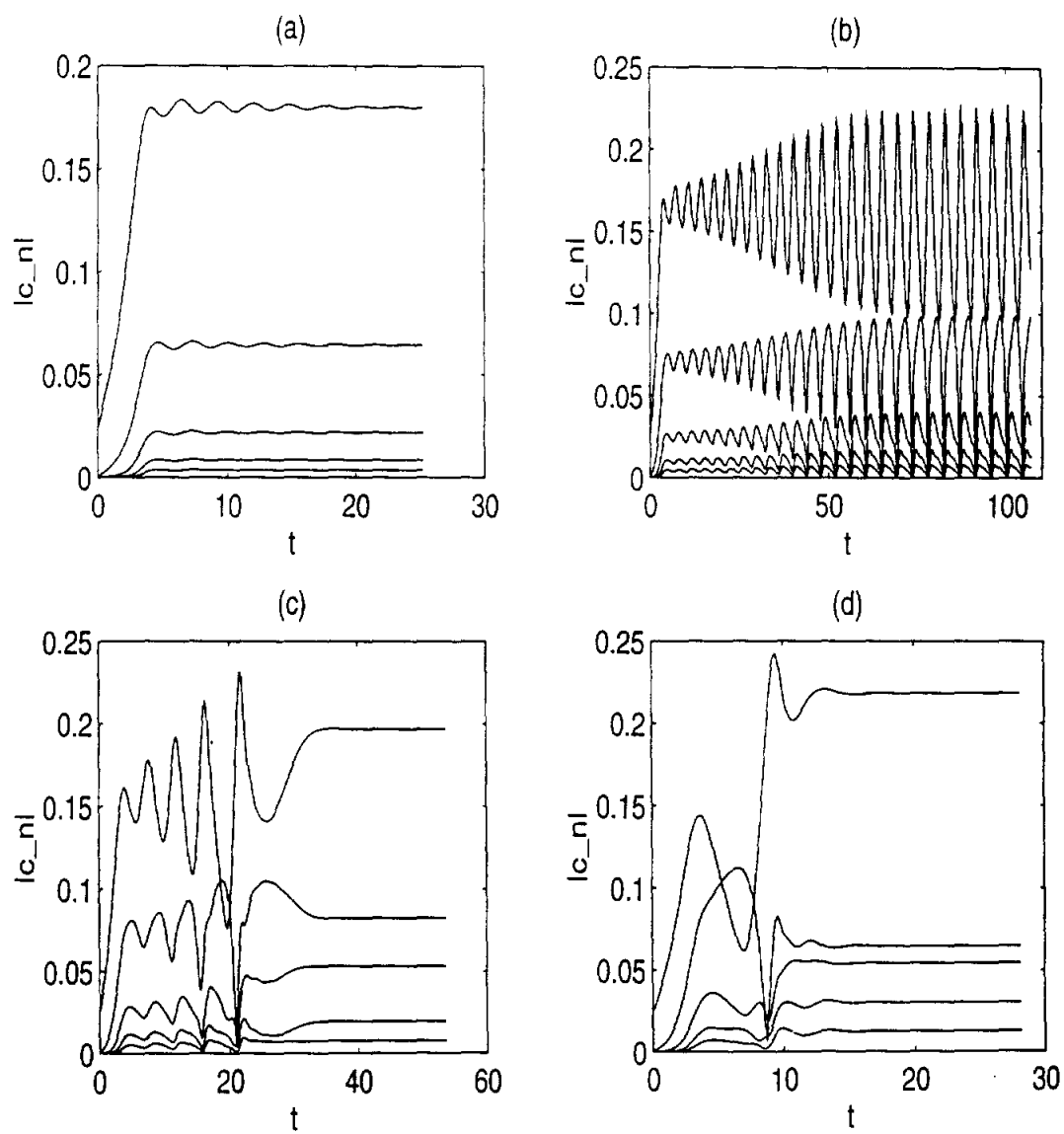
Figure 6.15: The evolution of the spectral coefficients $|c_n(t)|$ for $G = 25$, $T = 100$, $\beta = \pi/2$ and (a) $k = 0.25$; (b) $k = 0.23$; (c) $k = 022$; and (d) $k = 0.20$
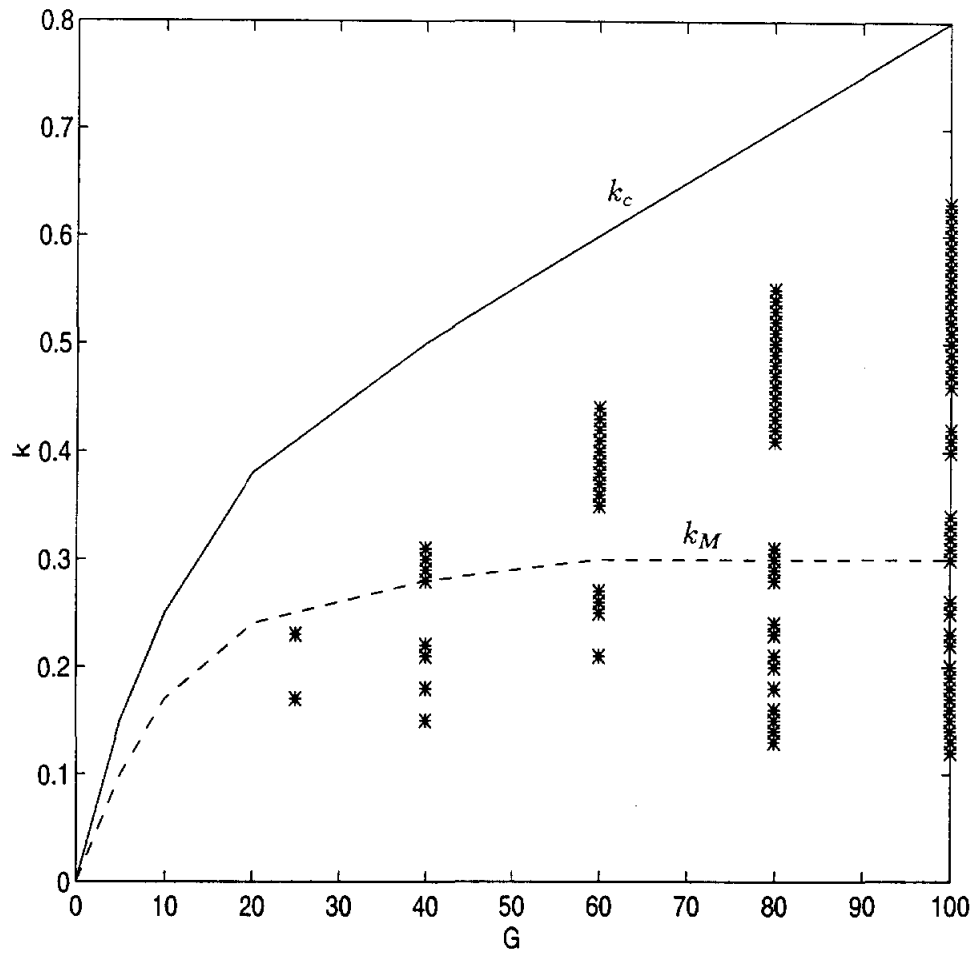
Figure 6.16: Phase diagram for thin film flow over a vertical plane obtained through full-scale computations. k_c and k_M are the cutoff and maximum growth rate wavenumbers predicted by the linear theory. The wavenumbers for which quasi-periodic evolution is observed are denoted by '*'.

numbers. The saturated nearly sinusoidal waves found close to the neutral curve correspond to the slow moving short wave γ_1 family of Chang etal (1993). The long solitary waves for very small wavenumbers correspond to the fast moving long wave γ_2 family of Chang etal (1993). Chang etal (1993) obtained these stationary wave families based on boundary layer approximations.

2. For intermediate range of numbers, no permanent waveforms were observed. Rather, a quasi-periodic wave evolution was observed. This type of wave evolution was observed experimentally by Liu & Gollub (1994), in their spatial evolution studies.

3. In the context of temporal stability, that is time evolution in spatial periodic domains, no previous systematic study of this quasi-periodic evolutions have been done, even though, they have been observed in the numerical simulations of the Kuramoto-Sivashinsky equation by Hooper & Grimshaw (1985), and in the numerical solution of the longwave evolution equation by Joo & Davis (1992). Our own numerical solutions indicate that this type of quasi-periodic behaviour is also exhibited by the integral boundary layer system.

4. In the context of time-periodic evolution is space (spatial stability), Cheng & Chang (1995) discuss the secondary instabilities in thin film flows. The formation of the permanent waveform is considered as the primary instability in thin film flow. This permanent wave travels downstream at a constant speed, but succumbs to the secondary instabilities, namely, the side-band and subharmonic instabilities. Due to these secondary instabilities, complicated coalescence occur between neighboring peaks and the evolution towards solitary waveform occurs. Ours is a space-periodic system evolving in time. Thus,

the quasi-periodic behavior is a manifestation of the side-band instability, albeit, a temporal one.

5. The quasi-periodic region is not contiguous, and for some intermediate wavenumbers permanent waveforms reappear. This is due to the secondary subharmonic instability.

6.7 Spatio-temporal evolution of the thin film instability

In the previous section, we studied the temporal evolution of the surface wave instability in a periodic domain. In reality, the fluid domains are not restricted by periodicity, and the surface wave evolves both spatially as well as temporally, allowing complex wave interactions such as wave-mergers and wave-splitting. Spatio-temporal evolution of the instability and the wave interaction processes are thus studied in this section.

6.7.1 Long domain with periodic boundary conditions

The parameters are chosen as $G = 5$, $T = 100$, $\beta = \pi/2$, and the length of the streamwise periodic domain is set to $20\lambda_M$, where λ_M is the maximum growth rate wavelength predicted by the linear theory. In the first 1/20th of the domain, i.e., $0 \leq x \leq \lambda_M$, the equilibrium wave profile (Fig.6.11b) computed previously is imposed as the initial condition and the rest of the domain is undisturbed. In the absence of external forcing, the natural waves that evolve downstream of the wave inception are of wavelength λ_M (Chang 1994). This type of an initial condition helps us understand how these natural waves evolve further downstream.

The dispersion of the initially imposed wave is shown in Fig.6.17(a). The primary surface wave instability being convective in nature, the initial wave is transported
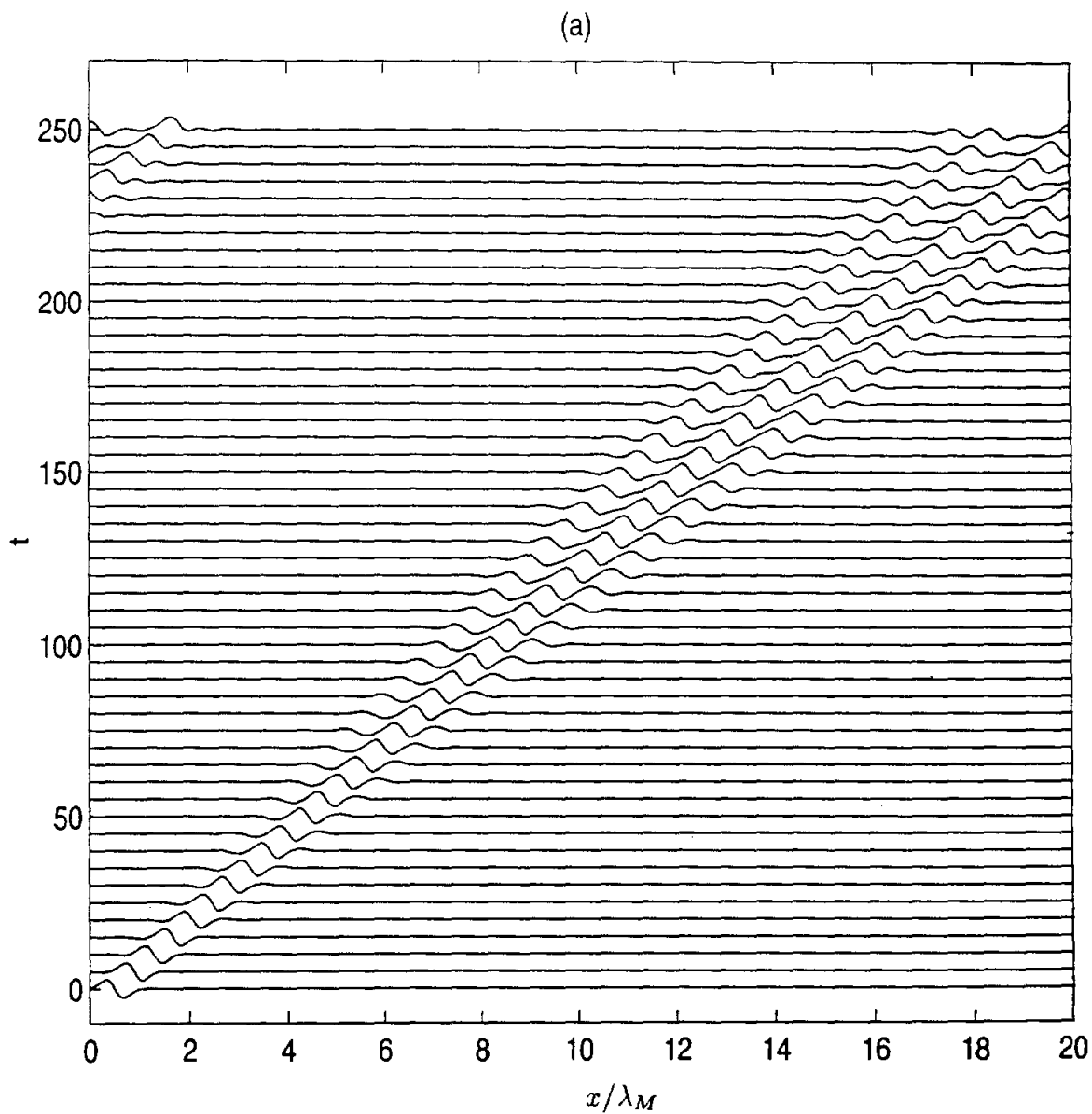
(a)

Figure 6.17: Spatio-temporal evolution in a long periodic domain for $G = 5.0$, $T = 100.0$ and $\beta = \pi/2$. The length of the domain $= 20\lambda_M$. The free surface profiles shown are in intervals of $\Delta t = 5$ from : (a) $t = 0$ to $t = 250$; (b) $t = 250$ to $t = 500$; (c) $t = 750$ to $t = 1000$; and (d) $t = 5240$ to $t = 5490$.

downstream. In the process, however, the initial wave disperses into several capillary waves. The front running wave quickly attains the shape of a solitary hump and travels downstream at a constant velocity and without further generation of waves. Each of the trailing waves as they travel downstream evolve into a solitary waves with sharp downstream slope and a gently sloping tail (Fig.6.17b). Thus, very far away from the source, the stable waveform is a solitary waveform. The domain being periodic, the wave leaving the domain at the right enters at the left. The speed of the wave is seen to be proportional to the wave amplitude. This fact was also observed experimentally by Liu & Gollub (1994). The larger amplitude solitary waves travel faster and run into small capillary waves (Fig.6.17c). There doesn't appear to be any repulsion between the two waves as they come close to each other. At the end of the wave coalescence, a still larger amplitude wave is formed, which travels downstream leaving behind a quiescent interface devoid of any small scale ripples. The coalescence between the large amplitude solitary wave and the relatively smaller amplitude capillary ripples is thus an inelastic one. This type of wave interactions go on for a long time, until the only type of waves seen on the interface are of the solitary-wave type (Fig.6.17d). The solitary pulses try to keep a certain distance from each other. If two solitary pulses get too close, then they start repelling each other, and this is the cause of the quasi-periodic behaviour observed previously in the temporal stability analysis (§6.6). At the same time, they cannot be too far apart, since small capillary ripples are bound to appear on the interface. These capillary ripples travel slower than the larger amplitude solitary pulse and eventually merge with the solitary pulse. Two solitary pulses of comparable amplitude, however, do not merge with each other. About $t = 2000$, a solitary wave train with 11 solitary pulses is formed in the domain. Even after integrating in time up to $t = 5490$, the

(b)

x/λ_M

(c)
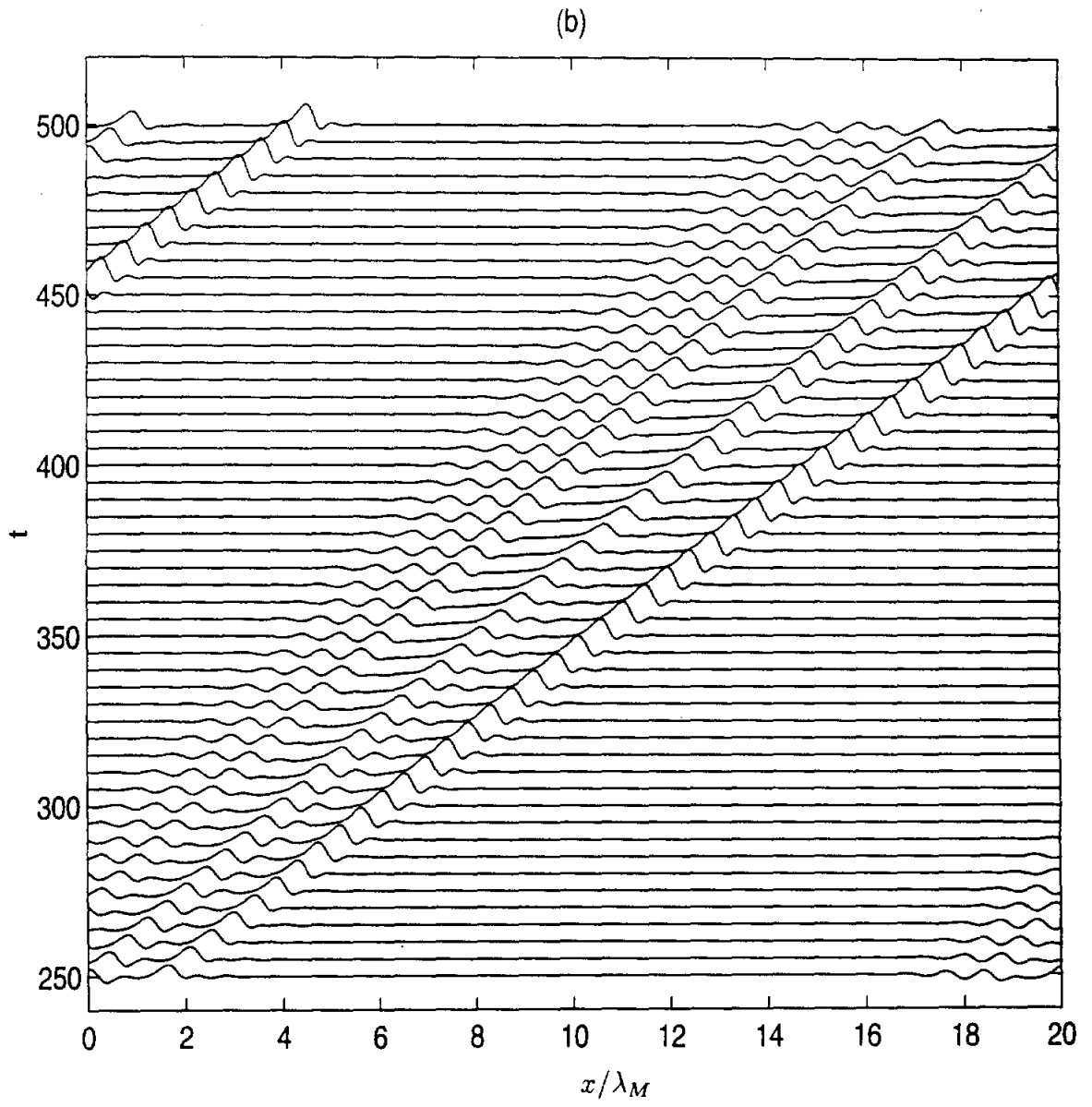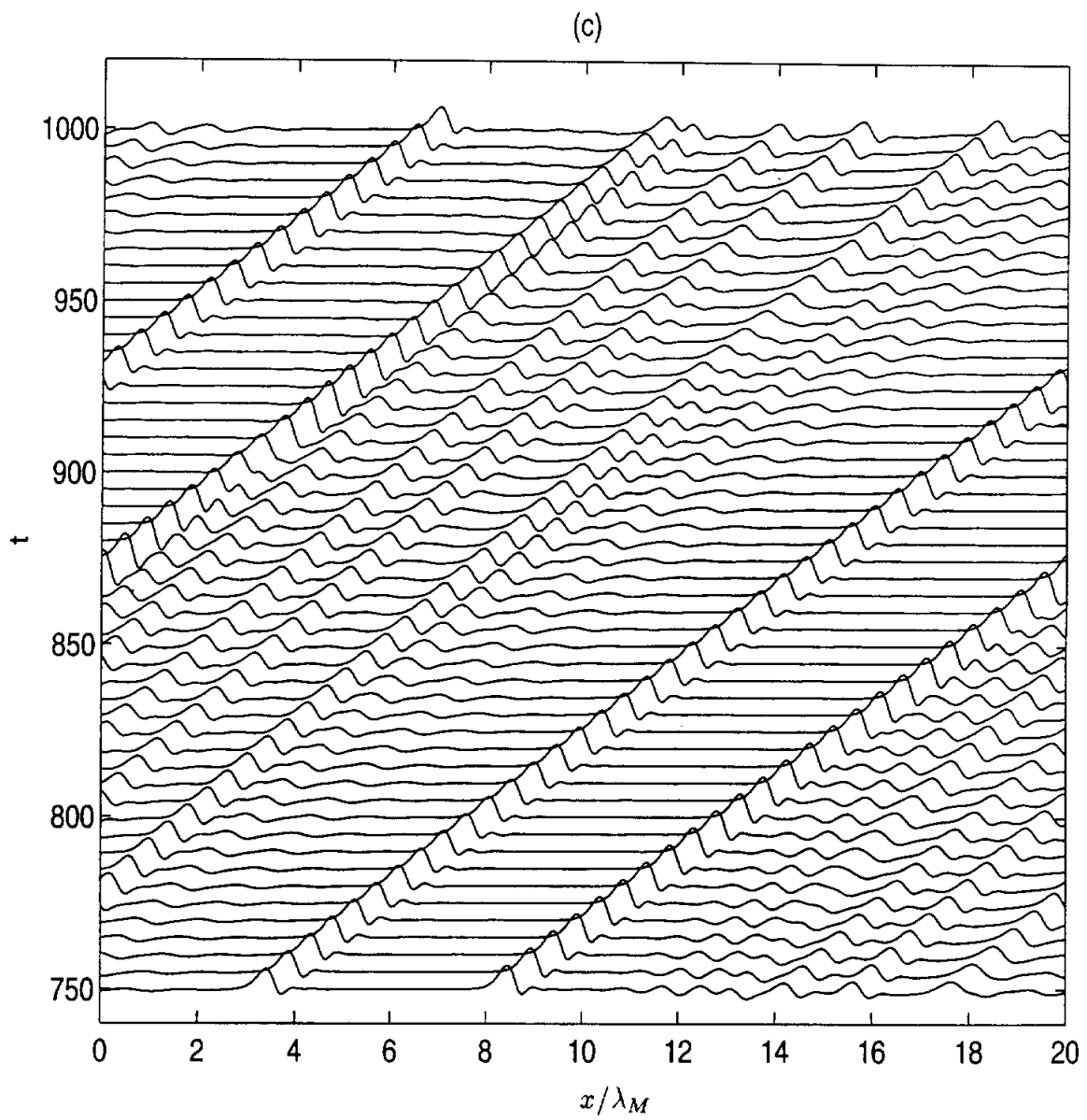
(d)
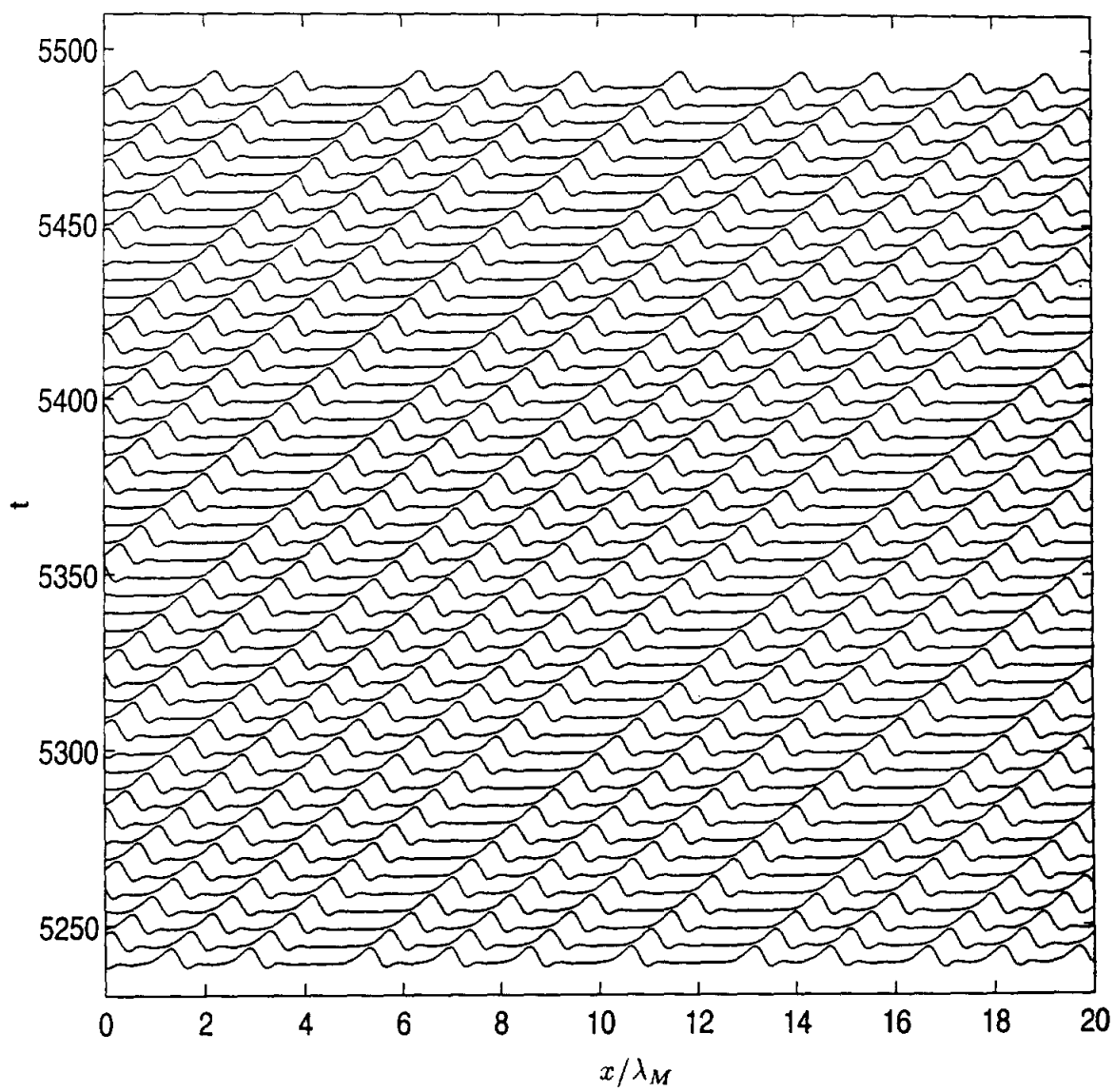
number of pulses is found to remain the same, namely, 11 in a domain of length $20\lambda_M$ (Fig.6.17d). The only changes in the domain are the relative spacing between the different solitary pulses. The solitary pulses are continuously interacting with each other to arrive at an appropriate relative distance. However, the temporal saturation of the solitary wave train is not complete in the numerical integration time $0 \le t \le 5490$. A much longer time of integration may have to be done, before complete temporal saturation can be obtained.

For the same simulation parameters as above, namely, $G = 5$, $T = 100$, $\beta = \pi/2$ and a streamwise periodic domain with length $L = 20\lambda_M$, an exponential pulse of the form $h(0,t) = 1 + 0.05e^{(-0.01(x-\frac{L}{2})^2)}$ is initially imposed, and its spatio-temporal evolution is studied. The initial dispersion of this disturbance and the evolution into solitary waveform is shown in Fig.6.18(a). The spatio-temporal evolution is qualitatively same as that seen previously, with complicated wave-splitting and wave-mergers taking place continuously, until a solitary wave-train is formed (Fig.6.18b). The notable difference from the previous simulation, is the presence of 13 solitary pulses in the wave-train in a domain of size $20\lambda_M$. Just as in the previous case, after the formation of a solitary wave train with 13 solitary pulses (around $t = 2000$), further integration in time (up to $t = 4355$) is only found to change the relative spacing between the pulses, without changing the number of solitary pulses in the domain. Thus the relative spacing between the solitary pulses, or the natural non-linear wavelength, is found to be weakly dependent on the initial conditions.

The findings of this subsection can be briefly summarized as follows:

1. Far downstream from the source, the solitary waveform is the stable waveform.

2. The wave speed is proportional to the amplitude. This has also been observed experimentally by Liu & Gollub (1994).

(a)

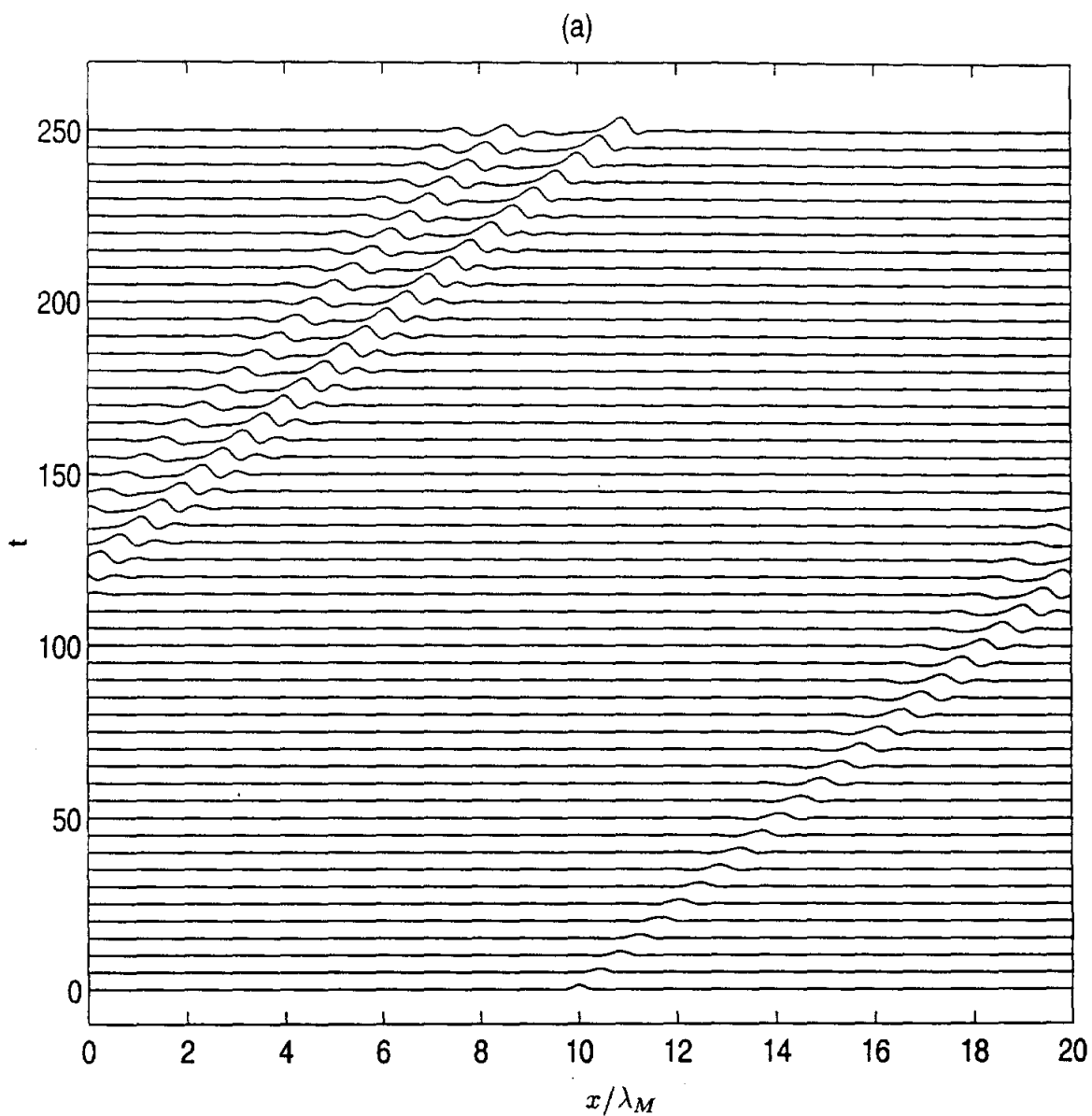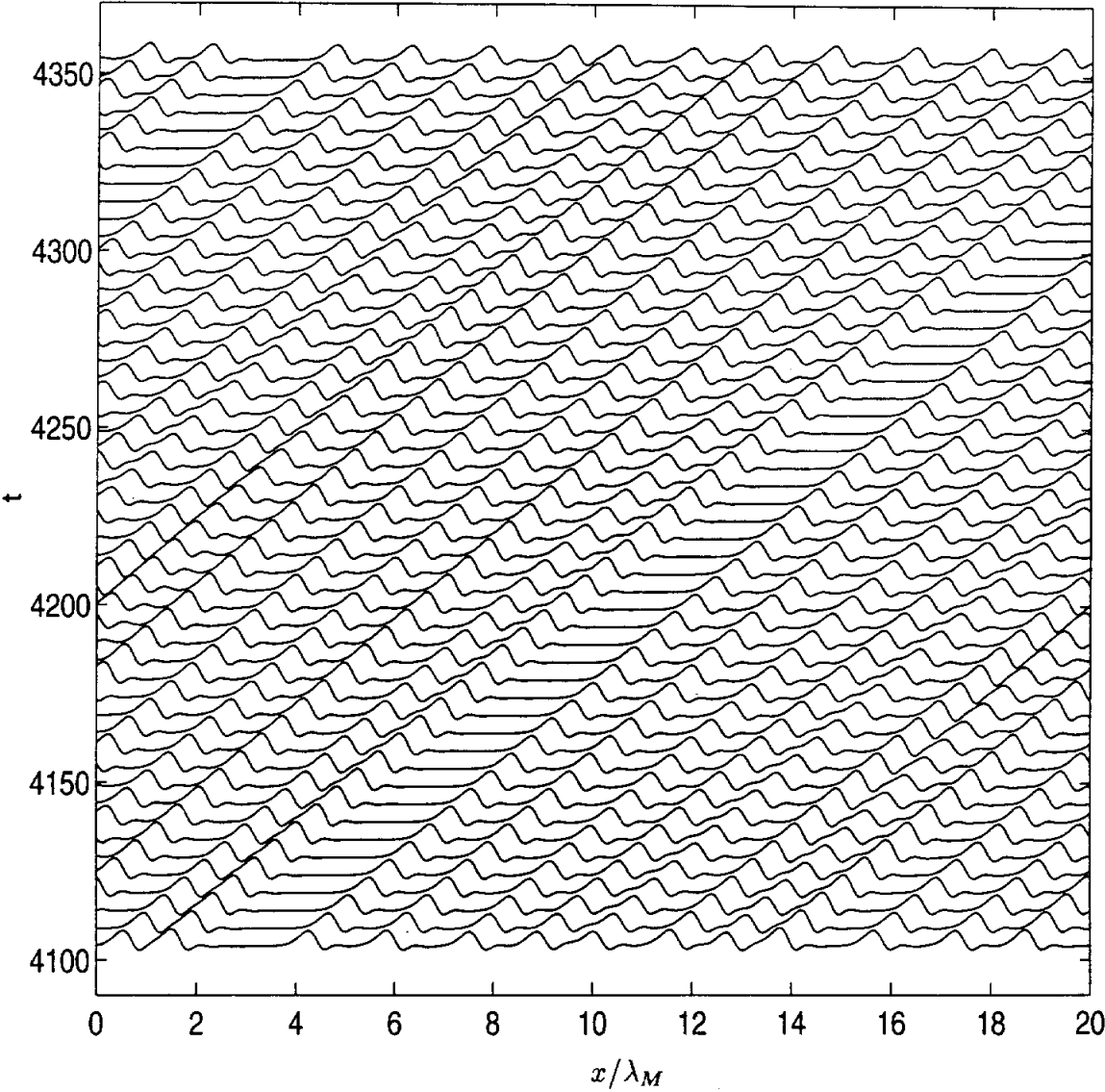Figure 6.18: Spatio-temporal evolution in a long periodic domain for $G = 5$, $T = 100$ and $\beta = \frac{\pi}{2}$. The length of the domain $L = 20\lambda_M$. The initial disturbance on the free surface is an exponential disturbance of the form $h(x, 0 = 1 + 0.05 * e^{(-0.01(x-\frac{L}{2})^2)}$. The free surface profiles are shown in intervals of $\Delta t = 5$ from: (a) $t = 0$ to $t = 250$; and (b) $t = 4105$ to $t = 4355$.

(b)

3. When the large amplitude wave approaches the slow moving small amplitude wave, there doesn't appear to be any repulsion between the two. At the end of the merger, the large amplitude wave travels downstream leaving behind an interface devoid of waves. This has also been observed experimentally by Liu & Gollub (1994).

4. There appears to be a natural nonlinear wavelength the system chooses to have at the end of the nonlinear wave evolution. However, the relative spacing between the solitary pulses is also dependent on the initial conditions.

6.7.2 Wave breaking in thin film flows

The question of wave breaking in laminar thin film flows is still an open one, and no conclusive theoretical, experimental or numerical evidence to this effect exists to date. The tendency for wave breaking arises from the thickness dependence of the local phase speed, with the crests travelling faster than the troughs resulting in steepening of the wave. The wave interaction processes described in this section could, however, inhibit the wave breaking tendency.

Theoretical interest has focused on determining if the approximate evolution equations such as the Kuramoto–Sivashinsky equation and the longwave evolution equation of the Benney type admit wave breaking solutions. The Kuramoto–Sivashinsky (KS) equation can accurately model evolution of the surface wave instability in thin film flows in the limit of small G and very large surface tension. The solutions of the KS equation are, however, smooth at all times and do not exhibit wave breaking tendency. Rosenau & Oron (1989) hypothesized that this is due to the over prediction of the effect of surface tension in the KS equation and proposed some a modification to the curvature term in the KS equation. They retained the

higher order terms in the denominator of the curvature and called their modified KS equation as the Regularized Kuramoto–Sivashinsky equation (RKS). Through numerical experiments, they show that in certain range of parameters the RKS equation exhibits wave breaking tendency. Joo, Davis & Bankoff (1991a) demonstrate that the longwave evolution equation of the Benney type (6.37) also exhibits the numerical blowup behaviour. However, both KS and longwave evolution equations are based on the assumption of finite wave amplitude and spatial gradients and lose their validity much before the onset of wave breaking. Thus, it would be interesting to determine if the numerical blowup of these evolution equations really implies wave breaking. The numerical parameters chosen by Rosenau & Oron (1989) are simulated using our full scale model and the results are shown in Fig.6.19. We find that the harmonic modes eventually saturate implying that finite amplitude permanent waveforms are the stable solution for these simulation parameters. This is contrary to what has been observed by Rosenau & Oron (1989) in their solution of the RKS equation. The RKS thus appears to have no physical relevance.

6.7.3 Long domain with non-periodic boundary conditions

Up to now, all the domains considered are periodic in streamwise direction, and what is studied is strictly the temporal stability of the thin film flows. In the experimental studies of thin film instability, however, a periodic disturbance either in the form of pressure fluctuations or film thickness perturbations are imposed at the inlet and the evolution of this disturbance in the stream-wise direction is measured (spatial stability analysis). For infinitesimal disturbances (linear stability), temporal and spatial stability give equivalent critical conditions. When the disturbances are of finite amplitude (nonlinear stability) this is not always the case, and additional
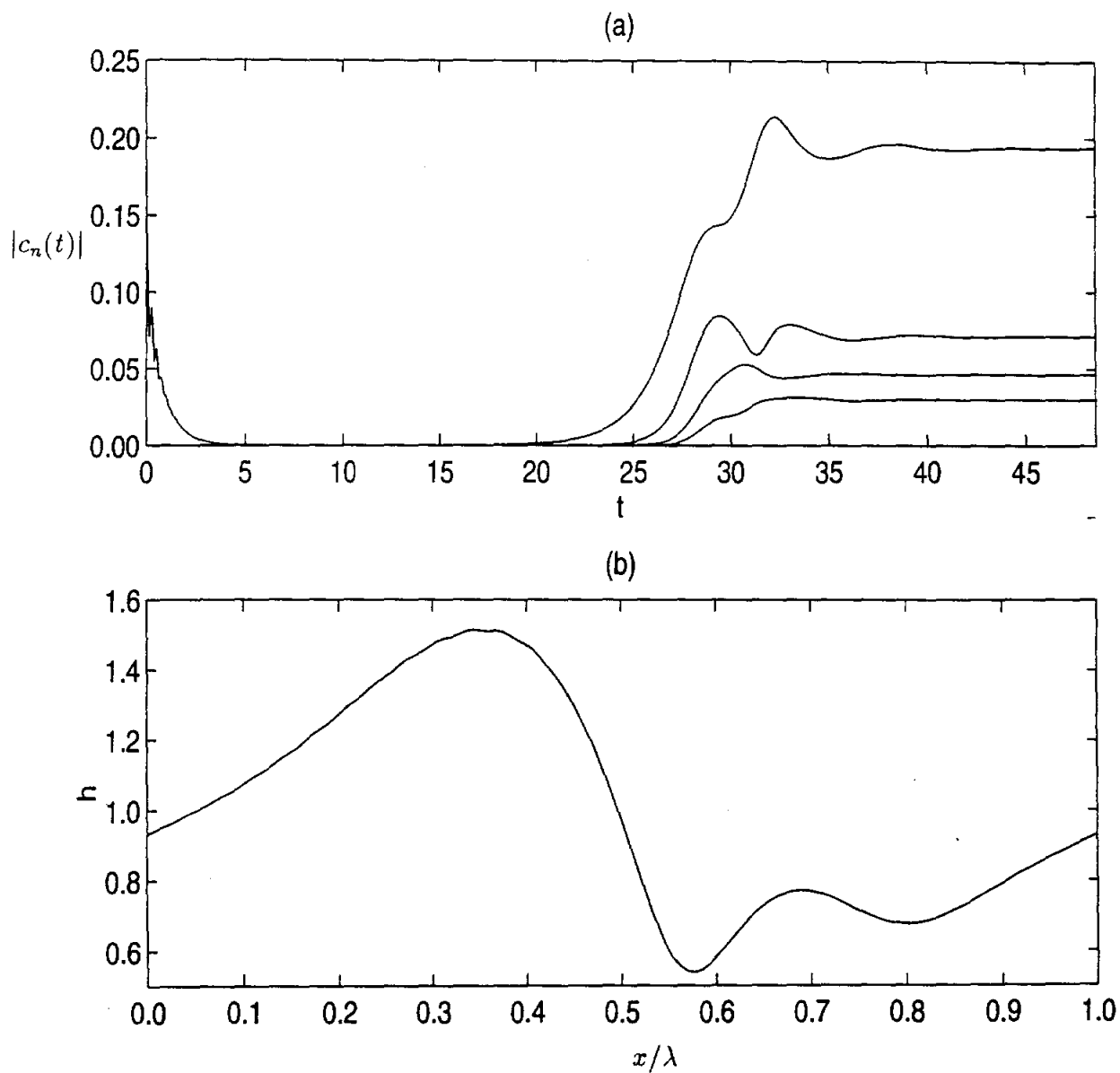
Figure 6.19: Rosenau & Oron (1989)'s wave breaking simulation with simulation parameters $G = 16.0$, $S = 51.63$, $\beta = \pi/2$ and $k = 0.2783$. The initial condition is $h(x,0) = 1 + 0.5\cos(4kx)$. (a) Evolution of the spectral coefficients $|c_n(t)|$; and (b) Final wave shape.

information can be obtained by considering both approaches. In this section, the spatial stability of the thin film flows, in a manner akin to the physical experiments, is done numerically. For this purpose, the experimental conditions of Liu & Gollub (1994) are simulated. Liu & Gollub (1994) studied the solitary wave dynamics of thin film flows. They use a 54% by weight aqueous solution of glycerin and impose periodic pressure fluctuations at the inlet. The angle of inclination $\beta = 6.4°$; and the mean film thickness is $h_0 = 0.12789cm$. These experimental conditions correspond to $G = 520.32$, $S = 676.65$, and $T = 84.10$. The thin film is initially flat and periodic disturbances are imposed at the inlet in the following manner:

$$h(0,t) = 1 + \delta \sin(\omega t), \tag{6.53}$$

where ω and δ are respectively, the non-dimensional angular frequency and amplitude of the external periodic forcing. The velocity boundary conditions at the inlet are of the Dirichlet type and are imposed based on the lubrication approximation and in such a way that the continuity equation is satisfied.

$$
\begin{aligned}
u(0,y,t) &= G\sin\beta\left(h(0,t)y - \frac{y^2}{2}\right) \\
v(0,y,t) &= \frac{1}{2}\frac{\partial h}{\partial t}\frac{y^2}{2}.
\end{aligned}
\tag{6.54}
$$

At the exit $x = L$, Sommerfeld Radiation Boundary Conditions in a manner similar to that proposed by Orlanski (1976) are imposed to let the waves leave the computational domain with minimum reflection.

First we present our results corresponding to a 1.5 Hz forcing frequency (Fig. 3 in Liu & Gollub(1994)). The amplitude of the disturbance is set to $\delta = 0.05$. The film thickness $h(x,t)$ at various instants of time starting from $t = 0.0s$ to $t = 2.6s$ in steps of 0.104 is shown in Fig.6.20(a). The primary instability being convective, the
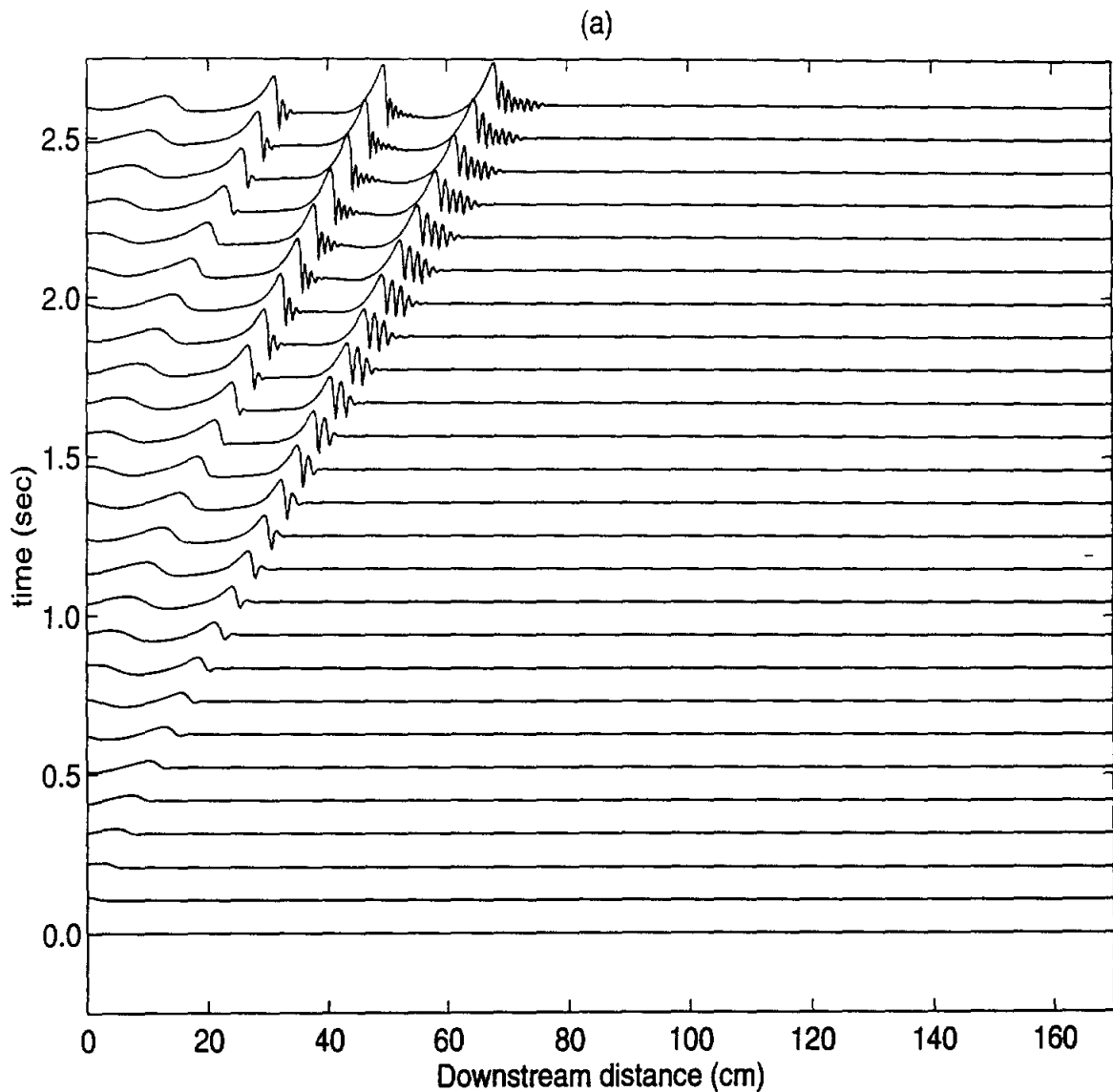
Figure 6.20: Spatio-temporal evolution with $f = 1.5Hz$ periodic forcing at the inlet. $G = 520.32$, $S = 676.65$, $\beta = 6.4deg$ and corresponds to the experimental conditions of Liu & Gollub(1994) (Fig.3). A sinusoidal perturbation of the form $h(0,t) = 1 + 0.05 * \sin(2.4546t)$ is imposed at the inlet. The free surface profiles shown are shown in intervals of $0.104s$ from: (a) $t = 0.0s$ to $t = 2.6s$; (b) $t = 2.6$ to $t = 5.2s$; and (c) $t = 5.2s$ to $t = 7.8s$.

disturbance is transported downstream by the mean flow. According to the linear stability theory the cut-off frequency for the onset of instability is $\omega_c = 37.05$. Since the imposed frequency is much smaller than the cut-off frequency, the most likely waveform is a solitary waveform, and that is what is observed. The amplitude of the disturbance quickly grows downstream and the wave becomes a symmetrical, with a sharp upstream slope and a gently trailing tail. Several small amplitude capillary ripples are formed downstream of the primary hump. In Figs.6.20(b) & 6.20(c) the subsequent free surface profiles in steps of $0.1.04s$ are shown. The wave traveling in the front grows in amplitude, travels faster and ultimately leaves the computational domain. After the initial growth, the wave profile doesn't appear to change much in its journey downstream. Thus the gas-liquid interface is filled with solitary humps having tear drop profile and there appears to be spatial saturation in the wave form. Further downstream however, spatio-temporal chaos and transverse 3-D instabilities will set in. The free surface profile given by Liu & Gollub(1994) is compared against numerically computed free surface profile in Fig.6.21. The agreement between the experimental and numerical profiles is not very good in the first half of the domain. This is most probably due to a difference in the amplitude of the inlet excitation. Liu & Gollub (1994) do not mention the amplitude of the disturbance imposed at the inlet and we set it arbitrarily to be $\delta = 0.05$. The saturated wave profiles as given in the later part of the domain (Fig.6.21c), however, show very good agreement. The significant difference is that the amplitude of the wave as predicted by the numerical calculations is slightly more than the experimental value. The capillary ripples downstream of the primary hump are captured quite well by the numerical solution.
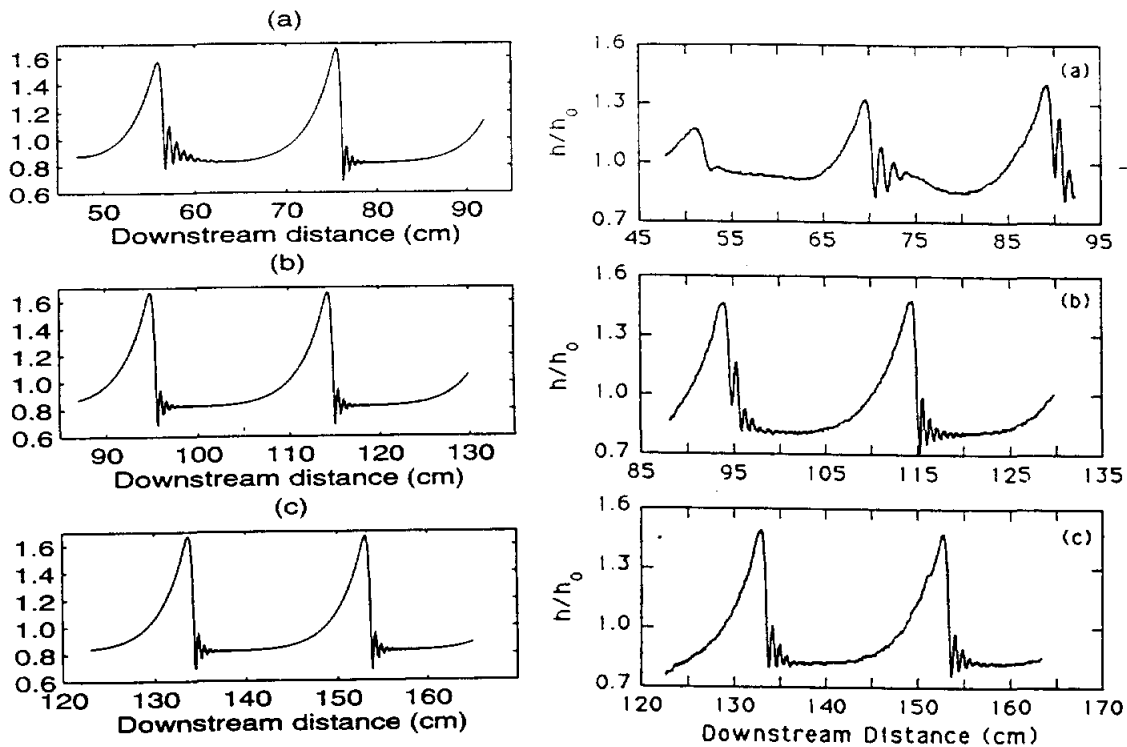
(b)
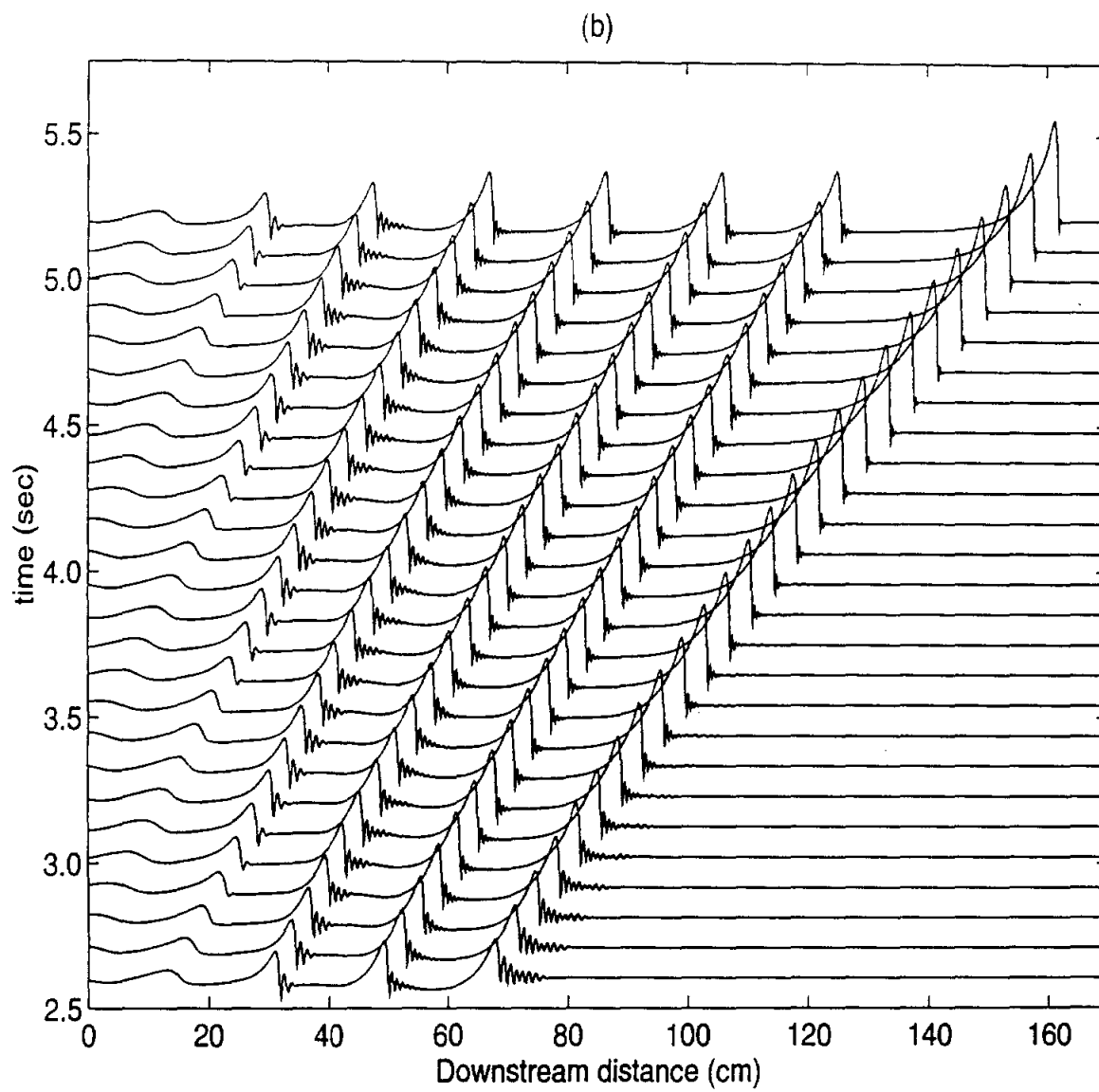
(c)
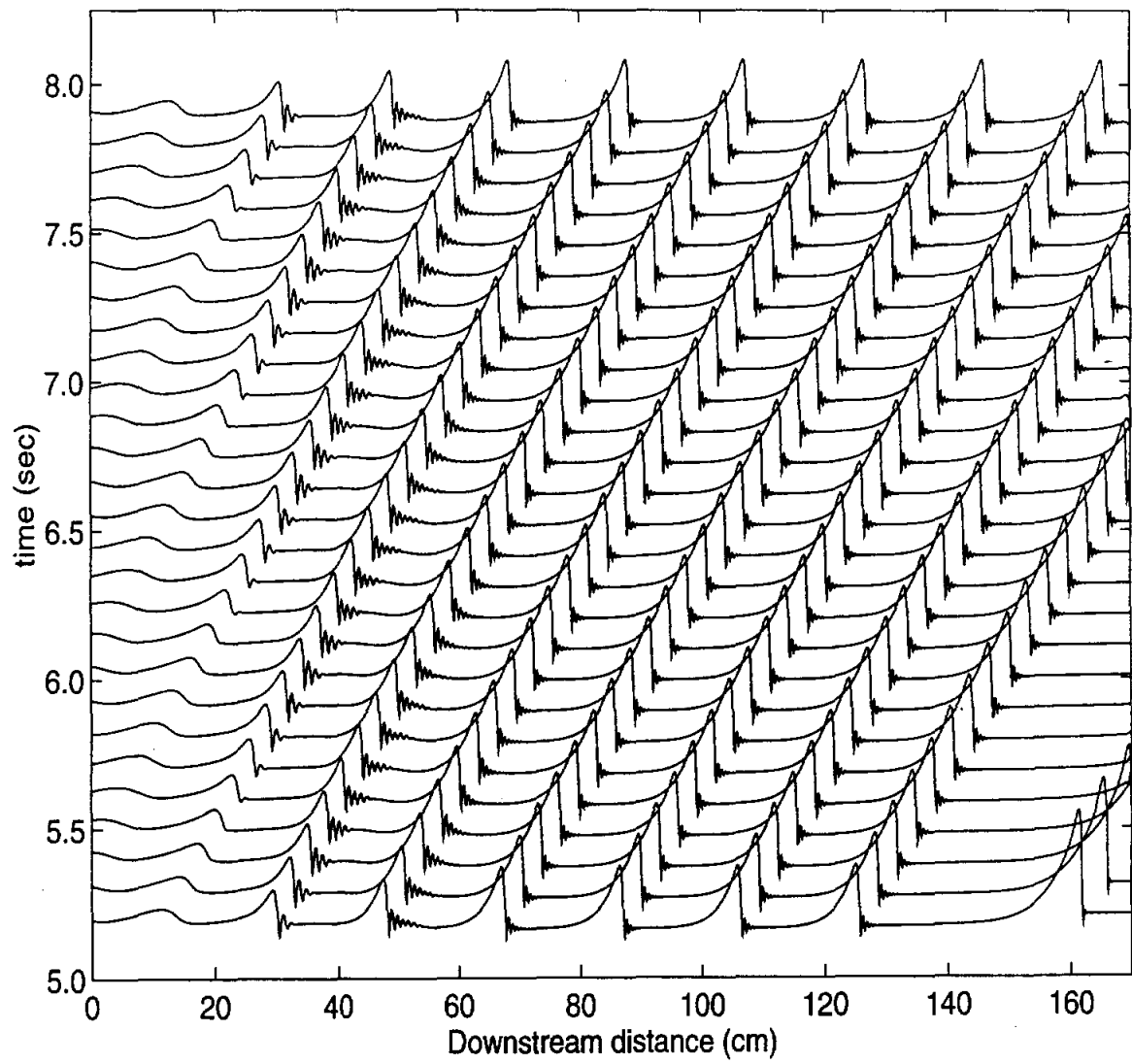
Figure 6.21: $G = 520.32$, $S = 676.65$, $\beta = 6.4deg$ and corresponds to the experimental conditions of Liu & Gollub(1994)(Fig.3). A sinusoidal perturbation of the form $h(0,t) = 1 + 0.05 * \sin(2.4546t)$ is imposed at the inlet. The wave profiles shown on the left are obtained computationally and the ones shown at the right are those measured by Liu & Gollub(1994) (Fig.3).

The experimental conditions simulated next are same as the above except that the inlet forcing frequency is increased to 4.5 Hz and the amplitude of the excitation is taken to be $\delta = 0.01$. The free surface profiles in intervals of $0.104s$ are shown in Figs.6.22(a,b,c). The inlet forcing frequency controls the spacing between the solitary humps. In this case the frequency is quite high and the solitary humps are too close to each other and never settle down to achieve steady traveling waveforms. This is analogous to the quasi-periodic behavior we observed for some wave numbers in the study of temporal instability. The experimental and numerical wave profiles are compared in Fig.6.23. Just as in the previous case, the agreement is not very good in the first part of the domain (Fig.6.23a). This either due to a difference in the forcing amplitude at the inlet or due to a difference in the way the flow-is excited at the inlet. Liu & Gollub(1994) impose fluctuations in the pressure, where as in the numerical simulations the film thickness is excited. In the later part of the domain the agreement is very good (Fig.6.23b,c). Since the solitary waves are too closely packed we do not observe spatial saturation.

Lastly, keeping the same experimental conditions as above, but increasing the inlet forcing frequency to 7 Hz, we obtain nearly sinusoidal film profiles as shown in Fig.6.24. The waves are closely packed, nearly sinusoidal and symmetrical. The forcing frequency in this case is close to the cut-off frequency, hence the almost sinusoidal wave profile. The comparison with experiments is very good in this case also (Fig.6.24(b,c)).

In §6.5, the experimental conditions of Kapitza & Kapitza (1949) were simulated numerically in a periodic domain. For one of the experimental conditions (Figs.6.8,6.9), our full-scale numerical simulations predict a quasi-periodic waveforms in contrast to the periodic waveforms reported by Kapitza & Kapitza (1949).

(a)
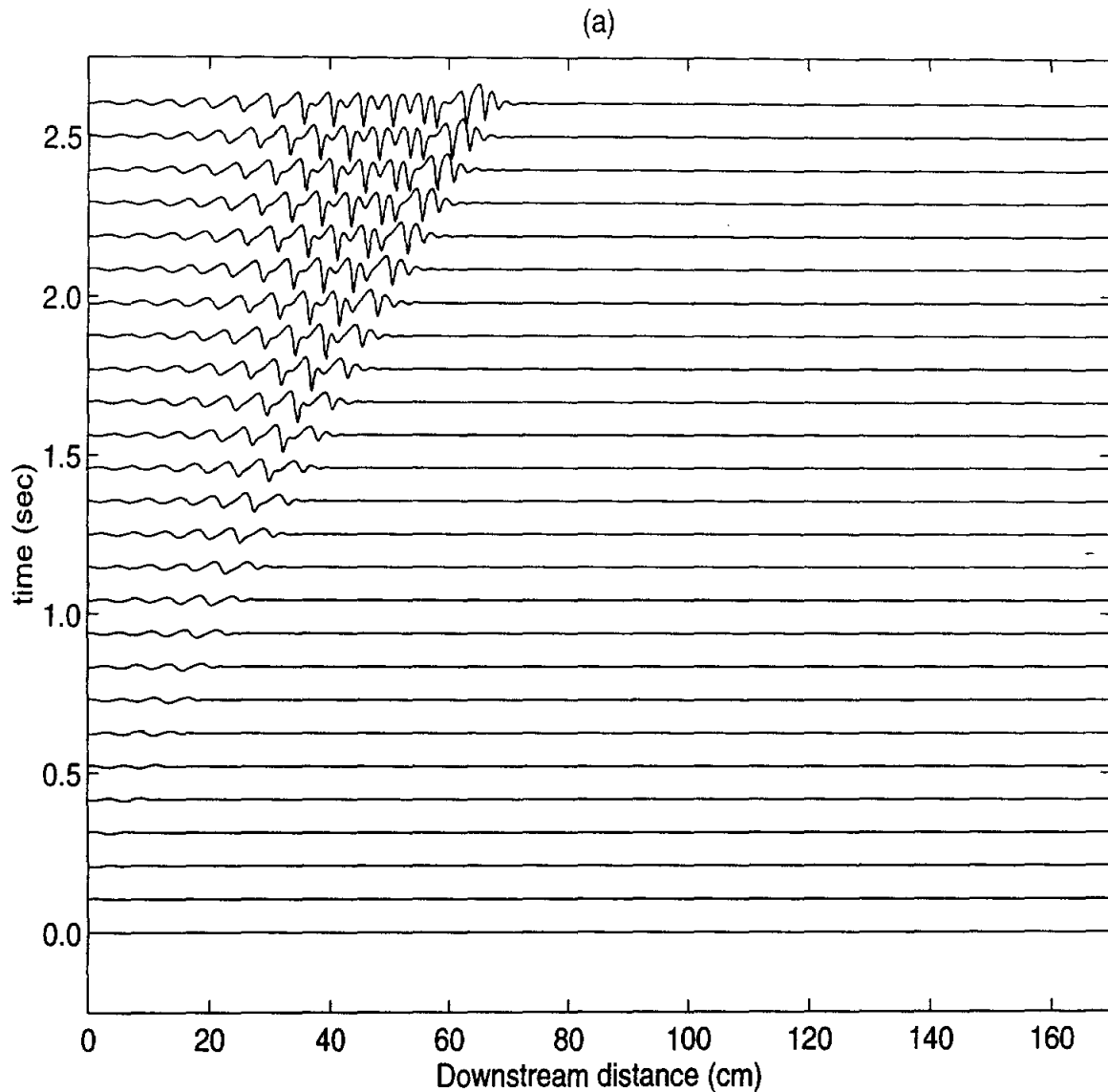
Figure 6.22: Spatio-temporal evolution with $f = 4.5Hz$ periodic forcing at the inlet. $G = 520.32$, $S = 676.65$, $\beta = 6.4deg$ and corresponds to the experimental conditions of Liu & Gollub(1994) (Fig.7). A sinusoidal perturbation of the form $h(0,t) = 1 + 0.01 * \sin(7.3638t)$ is imposed at the inlet. The free surface profiles are shown in intervals of $0.104s$ from: (a) $t = 0.0s$ to $t = 2.6s$; (b) $t = 2.6s$ to $t = 5.2s$; and (c) $t = 6.656s$ to $t = 9.4s$.

(c)
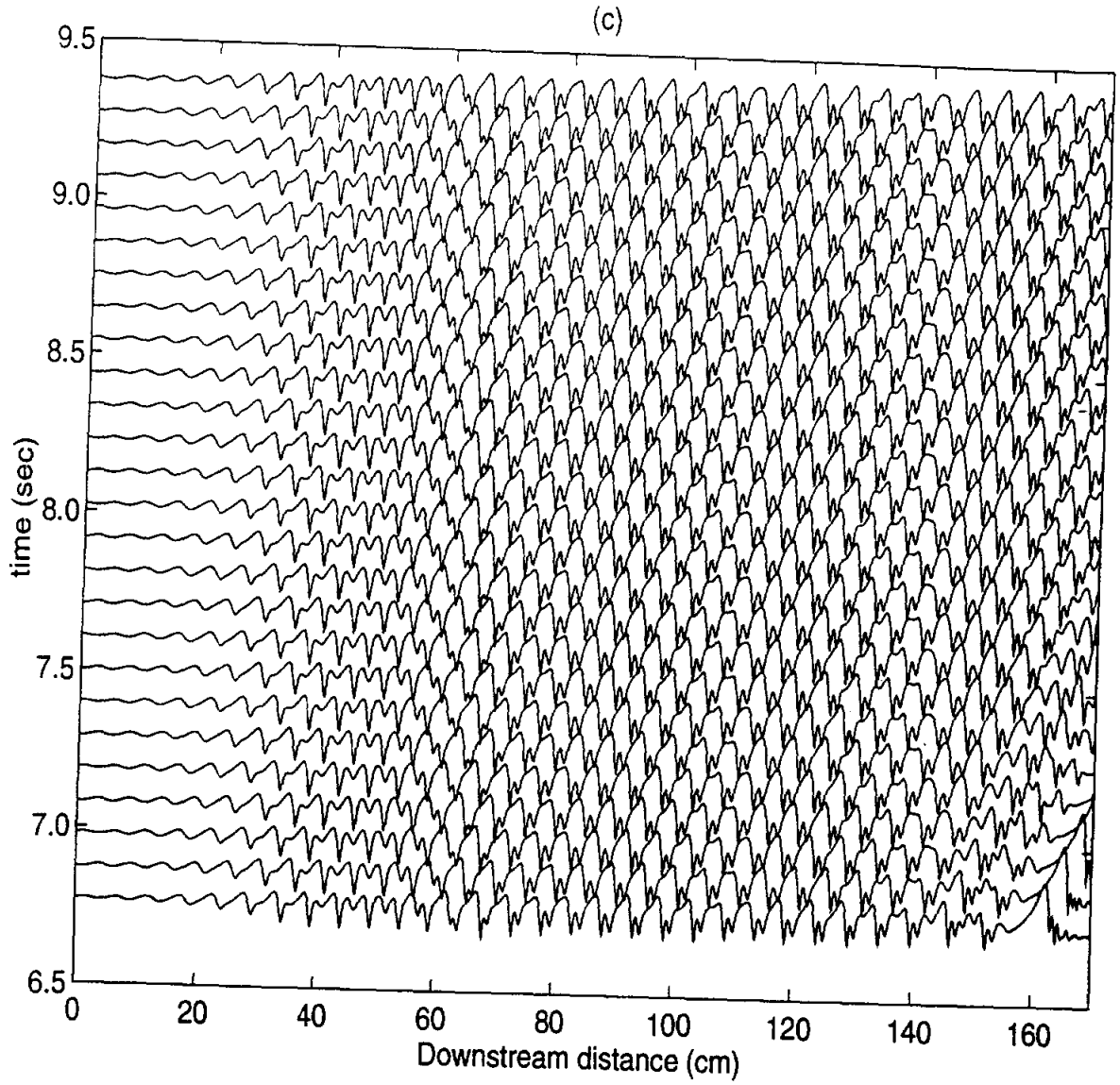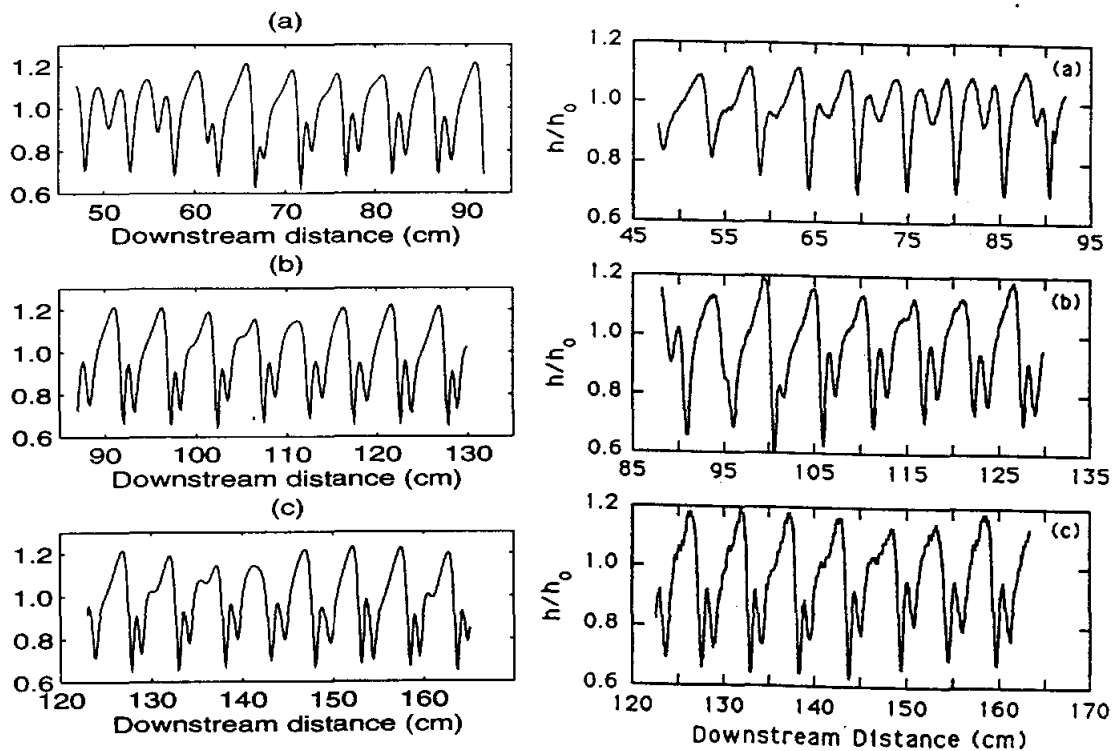
Figure **6.23**: $G = 520.32$, $S = 676.65$, $\beta = 6.4deg$ and corresponds to the experimental conditions of Liu & Gollub (1994)(Fig.7). A sinusoidal perturbation of the form $h(0,t) = 1 + 0.05 * \sin(7.3638t)$ is imposed at the inlet. The wave profiles shown on the left are obtained computationally and the ones shown at the right are those measured by Liu & Gollub (1994) (Fig.7).
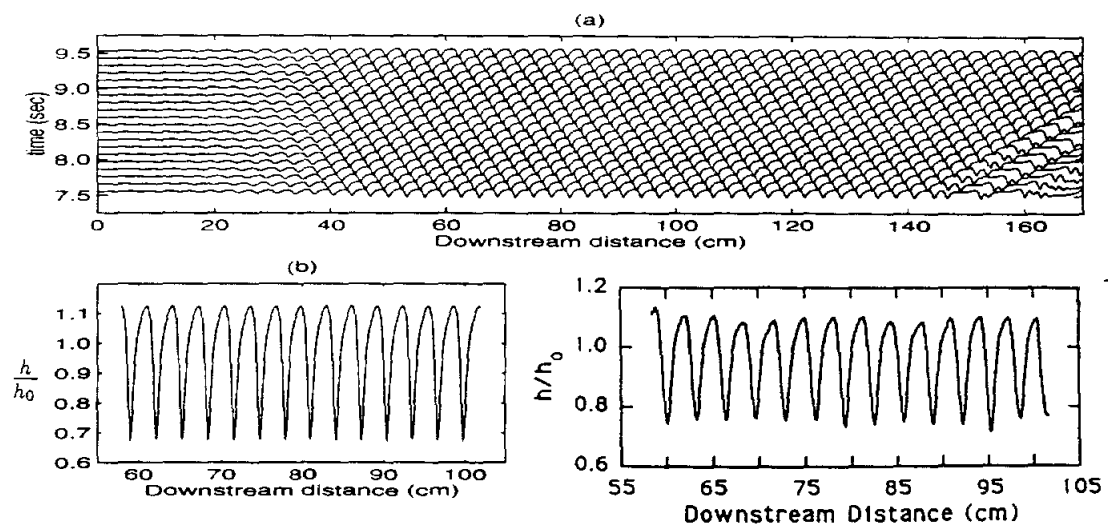
Figure 6.24: $G = 520.32$, $S = 676.65$, $\beta = 6.4deg$ and corresponds to the experimental conditions of Liu & Gollub (1994) (Fig.8). A sinusoidal perturbation of the form $h(0,t) = 1 + 0.05 * \sin(11.4548t)$ is imposed at the inlet. (a) film thicknesses in intervals of $0.104s$ from $t = 7.6s$ to $t = 9.6s$; (b) numerically computed free surface profile; and (c) experimentally reported film thickness profile (Fig.8 in Liu and Gollub (1994)).

The same experimental conditions are now numerically simulated in a long non-periodic domain and the spatial evolution of the disturbance in a manner similar to the physical experiments is simulated and the results are shown in Fig.6.25. No spatial saturation is observed in the stream-wise direction and the wave profile is quasi-periodic consistent with the temporal stability predictions.

6.8   Concluding Remarks

A numerical procedure based on the Finite Element Method has been developed to study the interfacial instabilities in isothermal thin film flows flowing down vertical or inclined planes. The numerical code is not very expensive in terms of computational time. A mesh of 2001×11 was used in the simulation of Liu and Gollub (1994)'s experimental results. A simulation time of 30 non-dimensional time units which correspond to 10 real seconds were sufficient to observe spatial saturation. This took about 30000 time steps and approximately 30 CPU hours on a SPARC-10. All the simulations presented in this chapter have been performed on a SPARC-10 computing machine.

The work presented in this chapter is the first comprehensive study of thin film instability based on the solution of the transient Navier–Stokes equations (Chippada, Ramaswamy & Joo 1995). Salamon etal (1994) did a detailed study of thin film instability, but *a priori* assume steady traveling waveforms and solve the steady state Navier–Stokes equations in a moving frame of reference. However, the stability of the waveform can only be ascertained through the solution of the initial value problem.

Extensive numerical simulations based on the direct solution of the Navier–Stokes equations reveal some interesting features of the thin film instability. In concurrence with what is known about thin film instability based on linear and ap-
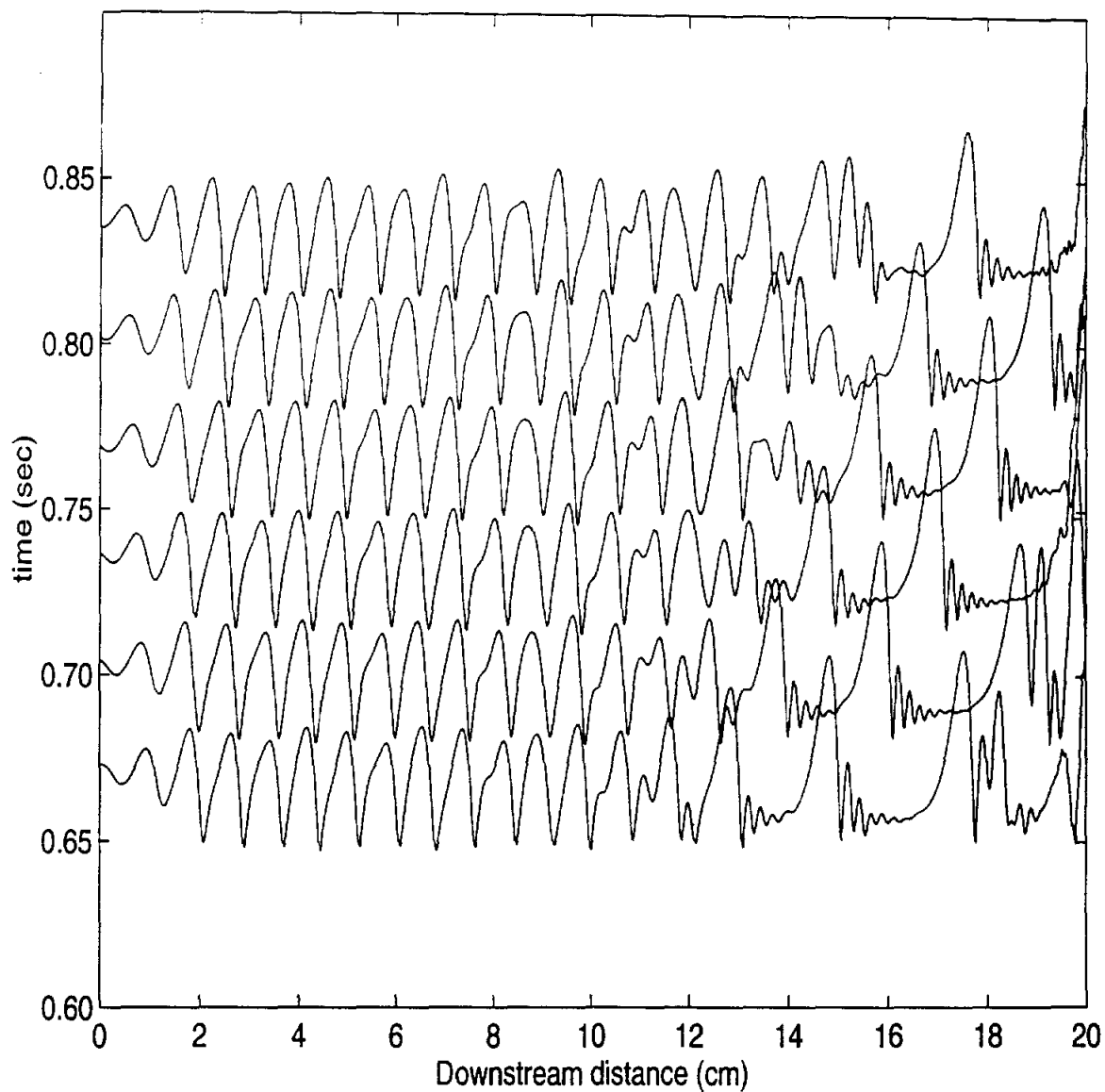
Figure 6.25: The experimental condition of Kapitza & Kapitza (1949) simulated in a long non-periodic domain. $G = 60.0$, $S = 4410$, $\beta = \pi/2$ and $\omega = 5.707$. At the inlet the free surface is perturbed as follows: $h(0,t) = 1 + \delta \sin(\omega t)$. The free surface profiles in steps of $0.033sec$ are shown.

proximate nonlinear theories, finite amplitude waveforms are the stable solution for wavenumbers smaller than the linear cut-off wavenumber k_c. For wavenumbers close to k_c, the waveforms are nearly sinusoidal. For wavenumbers much smaller than k_c, the waveforms are solitary-wave-like. This transition from nearly sinusoidal waveforms to solitary waveforms seem to pass through a quasi-steady regime, in which the spatial harmonic coefficients are in a state of constant fluctuations. The phase boundary de-lineating this regime has been obtained through extensive numerical simulations.

The spatial stability analysis of the thin film instability has also been studied by considering a very long domain with periodic forcing at the inlet and absorbing boundary conditions at the exit. Excellent agreement with the experiments of Liu & Gollub (1993) has been obtained. Depending on the frequency of excitation, the waves formed downstream are either nearly sinusoidal or solitary–like or quasi-periodic (in streamwise direction).

Due to the amplitude dependence of the wave speed complex wave interactions are likely to occur on the gas–liquid interface. Waves with larger amplitude travel faster and coalesce with smaller waves on the wave. This wave interaction is found to be completely inelastic and the resultant wave grows further in amplitude and travels downstream leaving behind a nearly flat interface. However, there appears to be a natural wavelength the system tries to have in the solitary wave regime. The resultant wavelength downstream is also weakly dependent on the initial condition.

A powerful numerical technique has been developed and used successfully to under stand many aspects of the surface wave instability in the thin film flows. A natural extension of the numerical procedure would be to do three-dimensional simulations. Very far away from the source the nonlinear waves are three-dimensional.

A numerical procedure based on the direct solution of the three-dimensional Navier–Stokes equations would help us understand this nonlinear wave regime.

Chapter 7

Turbulent Fluid Flow Over Streamwise Periodic Artificial Bedforms

7.1 Introduction

An erodible bed composed of non-cohesive sediment particles with turbulent fluid flow on top of it is rarely flat, e.g. river beds and desserts. More common is the presence of bedform features such as ripples, dunes and antidunes collectively referred to as bedforms. Ripples and dunes are found to exist in flows with Froude number less than 0.7. Ripples occur at length scales independent of the fluid depth, and depend only on the local bed properties such as grain size. Dunes occur at larger length scales that are dependent on the fluid depth. Antidunes are found to exist in flows with Froude number greater than 1.0. Unlike ripples and dunes, in the case of antidunes, strong coupling exists between the free surface (air-water) waves and the bed waves. A more detailed description and classification of bedforms can be found in ASCE (1966) and Kennedy (1969).

The formation of the bedforms is due to a complex interplay between the fluid and the bed. In particular three important features can be isolated, namely, the turbulent fluid flow, the sediment transport and the bed morphology. These three phenomena are coupled and collectively influence the formation and migration of bedforms. For example, the local sediment concentration is dependent on the fluid velocities, stresses and turbulence intensities. The sediment concentration field in turn determines the erosion and deposition of sediment particles at the bed thus

controlling the formation of bedforms. The shape of the bed (bed morphology) in turn influences the flow and turbulence field.

Several theories have been proposed which try to explain the formation of bedforms as a problem in stability. The most important and the most difficult aspect in these models is the determination of the turbulent fluid flow over the bedforms. The earliest models assumed potential flow (Kennedy 1963). A more realistic model for the fluid flow, namely, real viscous fluid flow with vorticity, was introduced by Engelund (1970) and Fredsoe (1974). However, Engelund (1970) and Fredsoe (1974) assume a constant turbulent eddy viscosity which is determined from the undisturbed fluid flow. Richards (1980) extended the theory of Engelund (1970) to incorporate a spatially varying eddy viscosity. They determine the turbulence eddy viscosity by solving the turbulence kinetic energy equation, but assume linearly varying length scale away from the bed. All these theories lose their validity when the amplitude of the bedform becomes finite. The fluid flow is known to undergo separation resulting in the formation of recirculation zones downstream of the dune peak (see Fig.7.1). Widely varying length scales exist in different parts of the fluid domain, and no complete analytical theory exists that can successfully model this type of complex turbulent flow. McLean & Smith (1986) developed a semi-analytical theory which uses different solution techniques in different parts of the fluid domain. The internal boundary layer is solved using boundary layer assumptions and asymptotic expansions and match it with the external wake solution calculated based on the wake solution behind a circular cylinder. Nelson & Smith (1989) extend the theory to include the effects of short wavelengths and recirculation zone. These semi-analytical theories are not universal and involve some parameters which need to be fine-tuned to fit the field conditions.
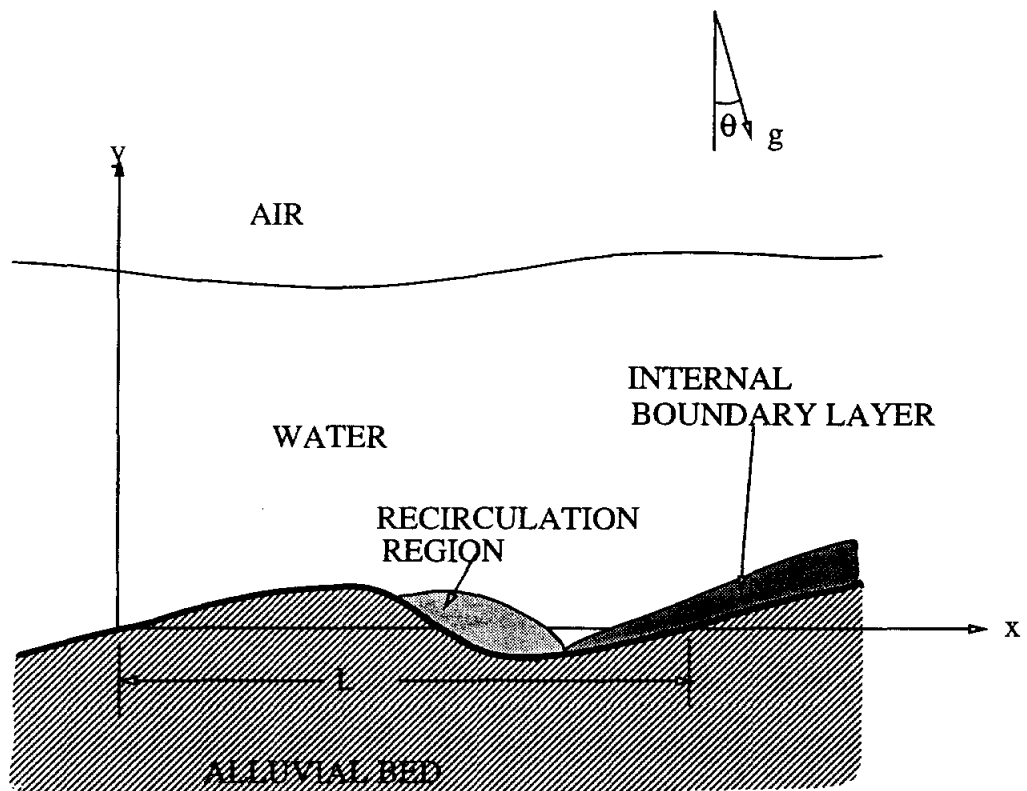
Figure 7.1: Schematic description of fluid flow over periodic bedforms

There remains a need for obtaining accurate mean flow and turbulence characteristics of the fluid flow over bedforms. It is believed that a good understanding of the fluid flow mechanisms are essential to improve the existing bedform stability models. Therefore, the goal of this work is to develop a numerical procedure capable of predicting the turbulent fluid flow over artificial fixed bedforms. In addition, an accurate computation of fluid flow over bedforms can be used for improved prediction of effective roughness of channels which would be of use to hydrologists.

Due to the limitations in the existing turbulence theories, the only means of obtaining detailed mean flow and turbulence characteristics are experimental and numerical. Raudkivi (1966), Lyn (1993) and Nelson, McLean & Wolfe (1993) are some of the experimental studies that have measured the mean flow and turbulence characteristics in fluid flow over bedforms. The presence of sediments in suspension complicate the measurements. In addition if the bedforms are erodible, the bedforms migrate slowly downstream due to the continuous erosion and deposition of sediments particles at the bed and the fluid flow is not stationary in the strict sense. To overcome these difficulties, the laboratory plume studies measure the mean flow turbulence characteristics for fluid flow over artificial, fixed and non-erodible bedforms, whose size and shape corresponds to naturally occurring bedforms. Numerical studies invariably solve the Reynolds Averaged Navier–Stokes (RANS) equations instead of the original Navier–Stokes equations due to the limitations imposed by the existing computational architecture. Due to the presence of variety of flow regimes such as internal boundary layer and recirculation zone, the mixing length closure models are inaccurate and higher order turbulence models need to be used. Richards & Taylor (1981) used a one-equation turbulence kinetic energy closure model and specified the length scale as linearly varying away from the wall. Mendoza & Shen

(1990) use a two-equation $k - \epsilon$ model along with an Algebraic Stress Model to compute the turbulence field. The presence of recirculation zone requires that at the minimum a two-equation closure model be used to compute the turbulence field with reasonable accuracy.

To our knowledge, all the previous numerical studies make the rigid-lid approximation, i.e., they replace the unknown air-water interface with a known rigid, free-slip wall. This eliminates the free boundary simplifying the problem considerably. The rigid lid approximation gives reasonably accurate results for flows with small Froude numbers ($F \ll 1$). For higher Froude number flows it is no longer a reasonable assumption since the free surface deflection is not insignificant anymore. In this work, we develop a numerical procedure capable of handling the air-water free surface in a simple manner. Thus the numerical algorithm developed in this work is capable of simulating high Froude number flows as well. The turbulence is modeled through a $k - \epsilon$ closure model coupled with the Boussinesq Eddy Viscosity hypothesis and the RANS equations are solved using the Galerkin Finite Element Method. The emphasis of this work is on the accurate determination of the mean flow and turbulence field. But, we also compute the sediment load using the existing empirical models to understand the influence of the flow field on the sediment load characteristics.

7.2   Problem Definition and Fluid Flow Modeling

The fluid flow geometry is shown schematically in Fig.7.1. The bottom boundary consists of bedforms which are periodic in the stream-wise direction with wavelength L. Even though, the bedforms are known to migrate downstream, the phase velocity of the bedform migration is very small compared to the stream-wise fluid velocities.

Hence, we assume that the bedform geometry does not change with time, i.e. the bed is assumed to be non-erodible and determine the final steady-state equilibrium velocity and turbulence field. The channel bed is inclined at a small angle θ with the horizontal. Thus, the flow is driven by gravity. x and y axes are as shown in the figure and $b(x)$ represents the bed-liquid interface. $h(x,t)$ is the height of the liquid-air interface from the x-axis.

The Reynolds number based on the mean fluid depth is usually much greater than the cut-off Reynolds number for transition to turbulence in open channel flows. Hence, the fluid flow occurring in nature over bedforms is turbulent in nature. This turbulent fluid flow is modeled through the Reynolds Averaged Navier–Stokes equations (RANS), written as:

$$\frac{\partial u}{\partial t} + u\frac{\partial u}{\partial x} + v\frac{\partial u}{\partial y} = g\sin\theta - \frac{1}{\rho}\frac{\partial p}{\partial x} + (\nu + \nu_T)\,\nabla^2 u \tag{7.1}$$

$$\frac{\partial v}{\partial t} + u\frac{\partial v}{\partial x} + v\frac{\partial v}{\partial y} = -g\cos\theta - \frac{1}{\rho}\frac{\partial p}{\partial y} + (\nu + \nu_T)\,\nabla^2 v \tag{7.2}$$

$$\frac{\partial u}{\partial x} + \frac{\partial v}{\partial y} = 0 \tag{7.3}$$

The turbulent eddy viscosity ν_T is determined through the two-equation $k-\epsilon$ closure model, which has been explained in chapter 4.

The boundary conditions at the bed are the no-slip conditions given by:

$$\left.\begin{array}{rcl} u &=& 0 \\ v &=& 0 \end{array}\right\} \quad \text{at } y = b(x). \tag{7.4}$$

The boundary conditions at the free surface are given by:

$$
\left.\begin{array}{rcl}
-p + 2\mu\dfrac{\partial u_n}{\partial n} & = & -p_a + \dfrac{\sigma}{R} \\[2ex]
\mu\left(\dfrac{\partial u_\tau}{\partial n} + \dfrac{\partial u_n}{\partial \tau}\right) & = & 0 \\[2ex]
\dfrac{\partial h}{\partial t} + u\dfrac{\partial h}{\partial x} & = & 0
\end{array}\right\} \quad \text{at} \quad y = h(x,t). \tag{7.5}
$$

The first two stress conditions are imposed in the solution of the Navier–Stokes equations and the third condition, namely, the kinematic free surface condition is used to update the free surface location every time step. The moving boundary problem is handled through the Arbitrary Lagrangian–Eulerian (ALE) procedure which has been explained in chapter 3. The boundary conditions in the streamwise direction are the periodic conditions given by:

$$
\phi(x = 0) = \phi(x = L) \tag{7.6}
$$

where, ϕ stands for u, v, p, k, ϵ and h. Even though we are interested only in the steady state flow and turbulence field, since the procedure used is a transient one, we also need to impose appropriate initial conditions. The initial velocity field is specified based on the universal log-law and in such a way that it satisfies the divergence free condition (Eq.7.3). The initial conditions for k and ϵ are imposed so that they vary linearly in the following manner (Alfrink & van Rijn 1983):

$$
k(x,y,t=0) = \left(1 - \frac{y - b(x)}{h(x,t=0) - b(x)}\right)\frac{u_*^2(x)}{\sqrt{C_\mu}} \tag{7.7}
$$

$$
\epsilon(x,y,t=0) = \left(1 - \frac{y - b(x)}{h(x,t=0) - b(x)}\right)\frac{u_*^3(x)}{\kappa y} \tag{7.8}
$$

As explained in chapter 5, the Galerkin Finite Element Method along with a Chorin-type projection scheme is used to solve the RANS.

All the results presented in this chapter have been obtained using a 61 × 11 mesh on SPARC-10 computing devices. A typical Finite Element Mesh is shown in Fig.7.2.

7.3   Sediment Transport Modeling

Though, the primary focus of this work is the computation of the flow and turbulence field, a numerical model capable of simulating the sediment transport is also implemented in the code. and the details of this sediment transport model are briefly explained in this section.

The transport of sediment particles, which could be sand, silt, gravel or even boulders, downstream by the fluid flow is termed sediment transport (Henderson 1966). The sediment materials can be broadly divided into two classes, namely, cohesive and noncohesive materials. In cohesive sediment materials there exist adhesive forces between the sediment particles, e.g., clay. In noncohesive sediment materials, no attractive forces exist between the sediment particles, and only this type of sediment transport is modeled in this work.

For the sake of argument, consider a sediment bed with stagnant fluid on top of it. No type of sediment transport is expected in this state. Let the fluid be set in motion through some means such as a pump, or by tilting the plume. It will be found that for low fluid velocities, still there would be no movement of the sediment particles from the bed. As the fluid motion is continuously increased, at some point we would find a perceptible motion of the sediment particles. Thus, a certain threshold fluid velocity or shear stress is required to set the sediment particles in motion. The most commonly used expression for this threshold condition is that given by Shields (1936). When the sediment particles start to move, initially, they
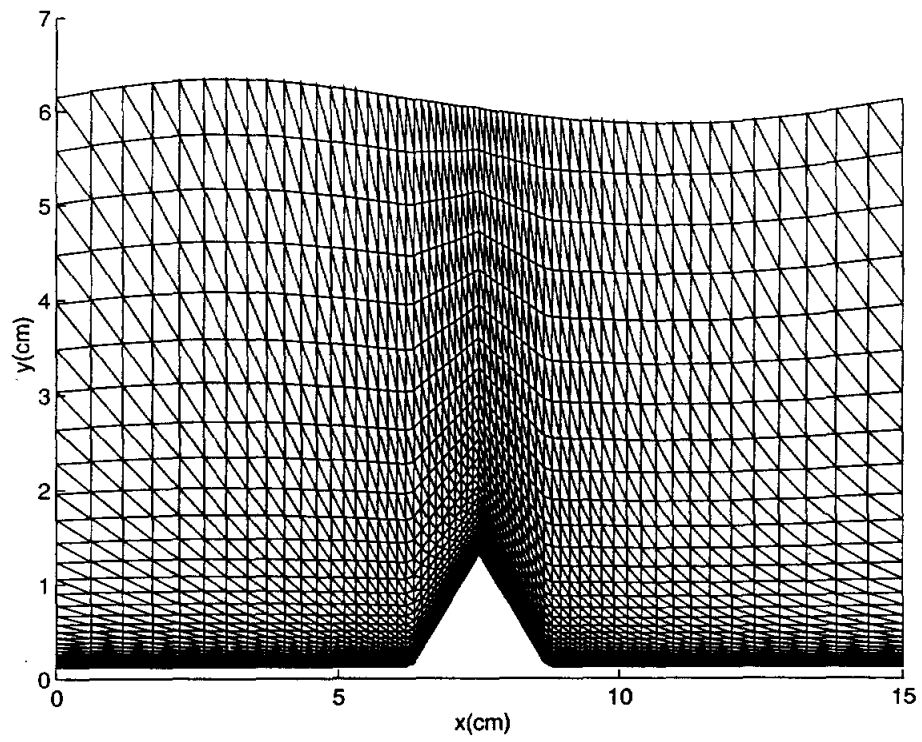
Figure 7.2: Typical Finite Element mesh

roll and slide along the bed and are in continuous contact with the bed. With further increase in the fluid velocity, the particles undergo occasional jumps called saltations. This type of transport of the sediment particles where they are either rolling, sliding or saltating is called the *bed load* transport. A further increase in the fluid velocities causes the sediment particles to go into suspension. The weight of the sediment particles is supported by turbulence forces and the transport of the sediment particles in suspension is termed the *suspended load* transport. The bed load transport is influenced to a large extent only by the fluid friction at the bed, whereas, the suspended load transport is influenced by both, the bed friction and the fluid velocities in bulk flow.

Many of the mechanisms of the sediment transport are not very well understood and the theories proposed to compute the sediment transport in general tend to be empirical in nature. In general the naturally occurring sediment beds are composed of sediment particles that vary widely in sizes and shapes. The process of entrainment of the sediment particles are stochastic in nature, and no clear understanding exists about the influence of the suspended sediment particle on the fluid flow and turbulence characteristics. Thus, most of the models proposed to compute the bed load transport are only heuristic in nature. We chose a sediment transport model proposed by van Rijn (1984a,b,c) to compute the sediment transport. The hydrodynamics code developed in chapters 3, 4 & 5 is coupled with the sediment transport model and the influence of the bed morphology on the sediment load distribution is studied. With the availability of better sediment transport models, they can be linked to the hydrodynamics code in a straight forward manner.

The sediment transport model developed by van Rijn (1984a,b,c) is briefly explained next. In this sediment transport model, the bed load transport is computed

using an empirical equation which is a function of the local bed shear stress and the suspended sediment concentration is modeled through a continuum advection–diffusion transport equation. First, the following three nondimensional parameters are computed:

$$D_* = D_{50} \left[\frac{(s-1)\,g}{\nu^2} \right]^{1/3} \tag{7.9}$$

$$T = \frac{u_*^2 - u_{*,cr}^2}{u_{*,cr}^2} \tag{7.10}$$

$$Z = \frac{w_s}{\beta \kappa u_*} \tag{7.11}$$

D_* is called the particle parameter, T is called the transport parameter and Z is called the suspension parameter. D_{50} is 50th percentile sediment particle diameter, $s = \rho_s/\rho$ is the specific density of the sediment material, g is the gravitational acceleration, ν is the kinematic viscosity of the fluid, $u_* = \sqrt{\tau_w/\rho}$ is the friction velocity at the bed, τ_w is the shear stress at the bed, $u_{*,cr}$ is the critical bed shear velocity needed for the initiation of the sediment movement as proposed by Shields (1936), and κ is the von Karman constant usually set to 0.40. The Shields critical bed shear velocity $u_{*,cr}$ is computed as follows:

$$
\begin{aligned}
D_* \leq 4, & \qquad \Theta_{cr} = 0.024\,(D_*)^{-1} \\[4pt]
4 < D_* \leq 10, & \qquad \Theta_{cr} = 0.014\,(D_*)^{-0.64} \\[4pt]
10 < D_* \leq 20, & \qquad \Theta_{cr} = 0.04\,(D_*)^{-0.10} \\[4pt]
20 < D_* \leq 150, & \qquad \Theta_{cr} = 0.013\,(D_*)^{0.29} \\[4pt]
150 < D_*, & \qquad \Theta_{cr} = 0.055
\end{aligned}
\tag{7.12}
$$

where, $\Theta_{cr} = u_{*,cr}^2 / \left((s-1)\,g D_{50} \right)$.

The bed load transport S_b is computed from the following empirical equation (van Rijn 1984a):

$$S_b = 0.053 \left[(s - 1) \, g \right]^{0.5} D_{50}^{1.5} \frac{T^{2.1}}{D_*^{0.3}} \tag{7.13}$$

The bed load transport is influenced by the local slope of the bed also. For instance, on the downstream slope of the dune, the sediment particles have a tendency to roll down. This must be taken into account in the computation of the bed load transport. Let τ_g represent the effective shear stress at the bed due to local slope of the bed and it is calculated as:

$$\tau_g = u_{*,cr}^2 \frac{\sin(\alpha)}{\sin \alpha_0}, \tag{7.14}$$

where α is the local slope of the bed, and α_0 is the angle of repose usually set to 30^0. This effective shear stress due to the local slope of the bed is added to the shear stress at the bed τ_w, and this total shear stress at the bed is used in the determination of the transport parameter T to be used in the computation of the total bed load transport. Note that, the local bed slope only influences the bed load transport and the suspended sediment transport is independent of it.

Let c represent the suspended sediment concentration defined as volume of sediment material per unit volume of the sediment-laden water. For dilute suspensions ($c \ll 1$) the suspended sediment concentration can be assumed to obey the advection- diffusion equation of the form:

$$\frac{\partial c}{\partial t} + u \frac{\partial c}{\partial x} + v \frac{\partial c}{\partial y} = (\nu + \nu_T) \nabla^2 c - \frac{\partial}{\partial y} (w_s c) \tag{7.15}$$

The above equation is solved through the ALE formulation and the numerical procedure outlined in chapters 3 and 5. Note that in the above equation, it is assumed

that the turbulent mixing coefficient ν_{Tc} of the sediment concentration is same as the turbulent eddy viscosity ν_T. Various researchers have previously used mixing coefficients of the form $\nu_{Tc} = \beta\nu_T$, where β is a constant with values ranging from $0.8 - 1.3$. We arbitrarily set the value of β to be 1.0, for lack of better information. w_s is the settling velocity of the sediment particles due to its weight and is computed as follows:

$$D_s < 100\mu m, \qquad w_s = \frac{1}{18}\frac{(s-1)\,gD_*^2}{\nu}$$

$$100\mu m \leq D_s < 1000\mu m, \quad w_s = 10\frac{\nu}{D_s}\left[1 + \frac{0.01\,(s-1)\,gD_*^3}{\nu^2}\right]^{0.5} - 1 \qquad (7.16)$$

$$D_s > 1000\mu m, \qquad w_s = 1.1\left[(s-1)gD_s\right]^{0.5}$$

D_s is the effective particle size of the suspended sediment computed as follows:

$$\frac{D_s}{D_{50}} = 1 + 0.011\,(\sigma_s - 1)\,(T - 25), \qquad (7.17)$$

where σ_s is the standard deviation of the the particle size distribution. The fall velocity calculated from the above expression is corrected for the local sediment concentration effect as follows:

$$w_{s,m} = (1 - c)^4\,w_s. \qquad (7.18)$$

The boundary condition at the free surface is the no flux condition given by:

$$\nu_T\frac{\partial c}{\partial y} = w_s c \quad \text{at} \quad y = h(x,t) \qquad (7.19)$$

At the sediment bed we impose a reference concentration c_a based on the local shear stress at a small reference level above the bed a.

$$c = c_a \quad \text{at} \quad y = a + b(x) \qquad (7.20)$$

The reference level a and the reference concentration c_a are computed as follows:

$$a = max\left(k_s, 0.01h\right), \tag{7.21}$$

and

$$c_a = 0.015 \frac{D_{50}}{a} \frac{T^{1.5}}{D_*^{0.3}}. \tag{7.22}$$

Thus, the reference level is set to either the equivalent sand roughness height k_s or 1 % of the flow depth, which ever is more. Note that, in the $k - \epsilon$ turbulence model, the wall functions approach is used for the specification of the boundary conditions at the bottom bed. The first numerical grid point is placed at a small distance away from the bed such that it lies in the fully turbulent log layer. With the inclusion of the suspended sediment model, there is an additional restriction on the placement of the first numerical node near the wall. The first grid point is placed at a small distance away from the wall so that the conditions set by the $k - \epsilon$ model and the suspended sediment model are both satisfied. Similar to the flow variables, periodic boundary conditions are imposed in the streamwise direction. The initial condition for the suspended sediment profile is imposed in the following manner:

$$
\begin{aligned}
y < 0.5h, \quad c &= c_a \left(\frac{a\left(h-y\right)}{y\left(h-a\right)}\right)^Z \\
y \geq 0.5h, \quad c &= c_a \left(\frac{a\left(h-y\right)}{y\left(h-a\right)}\right)^Z e^{-4Z(y/h-0.5)}
\end{aligned}
\tag{7.23}
$$

Once the suspended sediment concentration is computed, the total suspended sediment load is computed as follows:

$$S_s(x,t) = \int_{y=b(x)}^{y=h(x,t)} u(x,y,t)c(x,y,t)\,dy \tag{7.24}$$

From the model outlined in the previous few paragraphs, it is apparent that the sediment transport model is very complex with several empirical parameters in it. van Rijn (1984a,b,c) has fine tuned his constants to obtain good agreement with a wide variety of plume and field data. Several other assumptions are made in the flow and sediment transport model. With the presence of sediments in suspension, the fluid flow is a two-phase flow. However, we model the suspended sediment concentration c as a passive scalar quantity which follows the fluid motion without it in turn influencing the fluid flow. With all these assumptions it is obvious that the sediment transport model is only of an approximate nature. But, unfortunately no good rigorous model exists that can model the sediment transport accurately.

7.4   Results and Discussion

Lyn (1993) obtained experimental measurements of the mean flow and turbulence characteristics for flow over two-dimensional periodic array of artificial bedforms as shown in Fig.7.3. The Type I bedform is a periodic array of 45^0 triangular elements with height $1.2cm$ and wave length $15cm$. The Type II bedform differs from the Type I bedform in the upstream geometry. The Type II bedform comprises of triangular elements with gentle upstream slope and sharp downstream slope and resembles more closely the naturally occurring bedforms. The above described two types of bedforms are studied to understand the influence of the bedform shape on the mean flow and turbulence characteristics.

In the first part of our work, we study the mean flow and turbulence characteristics invoking the rigid-lid approximation. The unknown air-water interface is replaced with a frictionless impermeable surface and the surface pressure is not fixed and is computed as part of the solution. The computational mesh points are
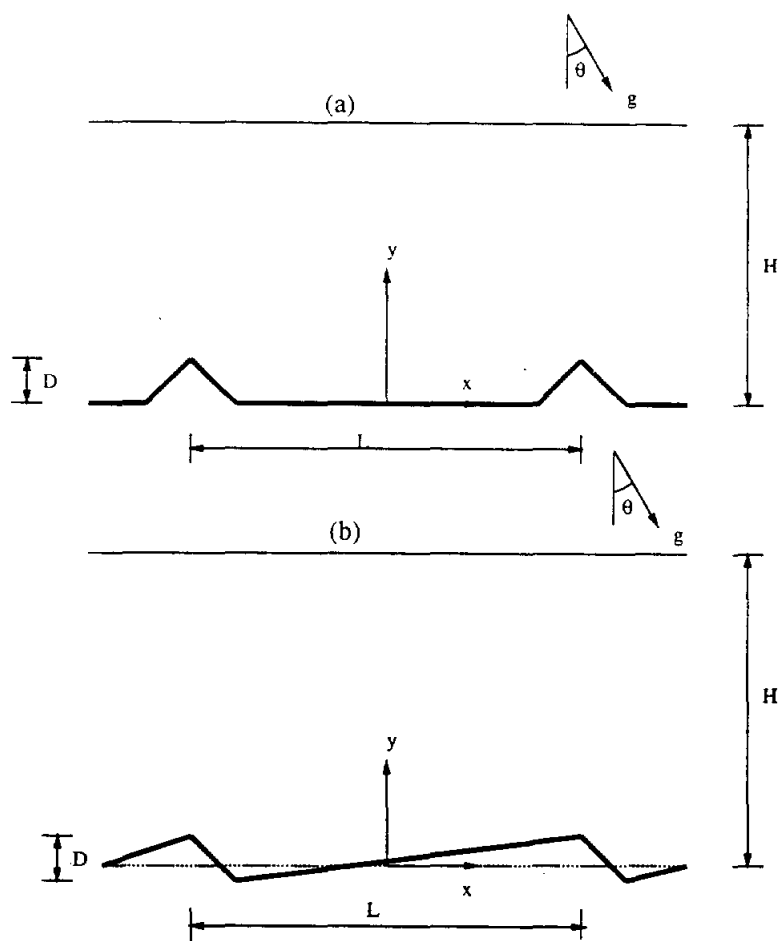
Parameter	case 1	case 2
Bedform	Type I	Type II
Flow depth, H (cm)	6.1	6.1
Wave length, L(cm)	15	15
Bedform height, D(cm)	1.2	1.2
Energy slope, θ	0.00525	0.00145

Figure 7.3: Bedform shapes: (a) Type I bedform with 45° upstream and downstream faces; (b) Type II bedform with 45° downstream slope and a gentle upstream slope.

thus fixed in space and the ALE formulation reduces to pure Eulerian formulation. The rigid-lid approximation is thought to be a good approximation for low Froude number flows. In the second part of our work, the air-water interface is allowed to deform and its equilibrium position is determined as part of the solution. The influence of the free surface on the quantities of interest such as shear stress at the bed is examined. For flow over Type II bedform the sediment load distribution along the channel length is also determined. Of special importance is the suspended load distribution in the flow separation region as it is thought that the high levels of turbulence associated with flow separation enhance the ability of the flow to transport sediment particles in suspension.

7.4.1 Mean flow and turbulence characteristics with the free surface assumed to be rigid frictionless lid

The mean flow and turbulence characteristics with the free surface assumed as a frictionless rigid lid are presented in this section.

The steady state mean flow velocities u and v at various cross-sections for flow over Type I bedform with rigid-lid approximation are shown in Fig.7.4(a,b). The Nikuradse equivalent sand roughness height k_s was taken to be equal to the sand grain diameter ($= 0.25mm$) in this simulation. At a short distance downstream of the dune crest, the shear layer separates, resulting in a region of recirculation, which can be easily identified by negative u velocities. The separated shear layer re-attaches to the bed some point downstream. The reattachment length L_r is found to be $3.914cm = 3.26D$, where D is the height of the dune. Lyn (1993) measured velocity profiles at only four cross-sections and couldn't determine the exact reattachment length. From the point of reattachment, an internal boundary
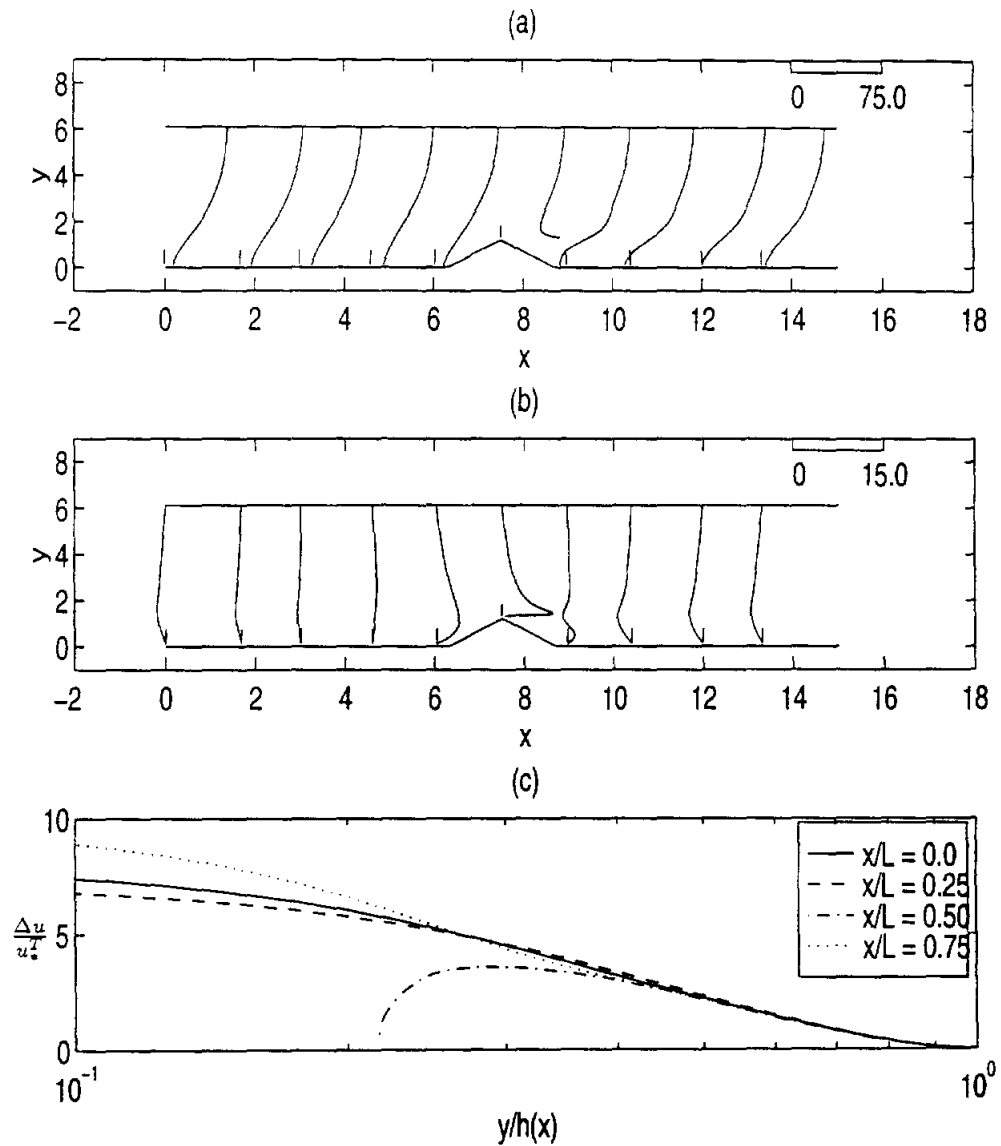
Figure 7.4: Mean flow characteristics for flow over Type I bedform with rigid-lid approximation: (a) horizontal velocity u (in cm/s); (b) vertical velocity v (in cm/s); (c) Velocity defect profiles.

layer begins to grow and the velocity profiles begin to relax towards the flat bed profiles. Following Lyn (1993), the velocity defect $\Delta u = u_{max} - u$, normalized with the total friction velocity $u_*^T = \sqrt{gHsin\theta}$ is plotted against y/H, where y is the vertical distance from the mean bed level (Fig.7.4c). $\Delta u/u_*^T$ collapse very nicely onto a single curve for $y/H > 0.4$, consistent with the experimental findings of Lyn (1993). Thus, the flow is disturbed due to the presence of triangular bedform and this disturbance persists up to $y/H < 0.4$ in the channel. The fluid above $y/H > 0.4$ is relatively undisturbed and the bedform can be thought to act as macro-roughness element.

The most important feature of the velocity profiles shown in Fig.7.4(a,b) is the large vertical and horizontal velocities at the dune crest. To obtain a better insight into the flow field, the area contour plots for u, v and dynamic pressure $\tilde{p} = p - g(h - y)cos\theta$ are shown in Fig.7.5. Flow near the dune crest is similar to flow around a sharp corner and is associated with large pressure gradients and centrifugal accelerations due to the streamline curvature. This local acceleration results in large horizontal and vertical velocities at the crest of the dune. Lyn(1993) also reported the significant positive vertical velocity at the dune crest. The horizontal and vertical velocities just upstream and downstream of the dune crest are shown in Fig.7.6(a,b). The local acceleration is not limited to the dune crest alone and is felt in a small region around the tip of the dune. Due to the local acceleration associated with the streamline bending, the shear stress at the dune crest is very high (Fig.7.6c). If the bed were erodible, the tip of the dune would be washed away immediately and the resulting bedform would be smooth without any sharp corners. Since we used the rigid-lid approximation, looking at the surface pressures on the rigid-lid can give us a crude estimate of what the surface deformation is likely
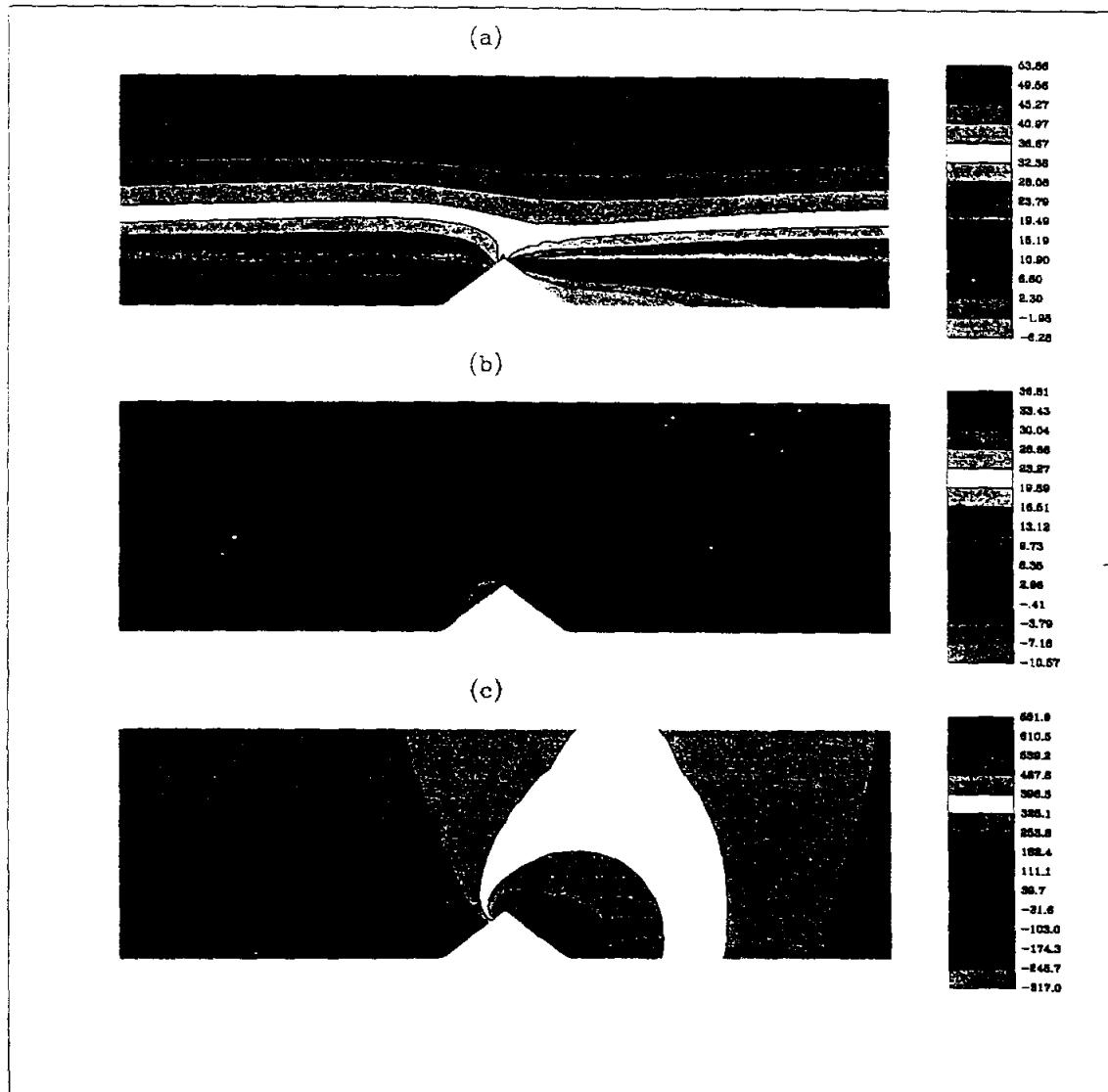
Figure 7.5: Mean flow characteristics for flow over Type I bedform with rigid-lid approximation: (a) horizontal velocity u (in cm/s); (b) vertical velocity v (in cm/s); (c) dynamic pressure $\tilde{p}/\rho = p/\rho - g(h - y)cos\theta$ (in cm^2/s^2).
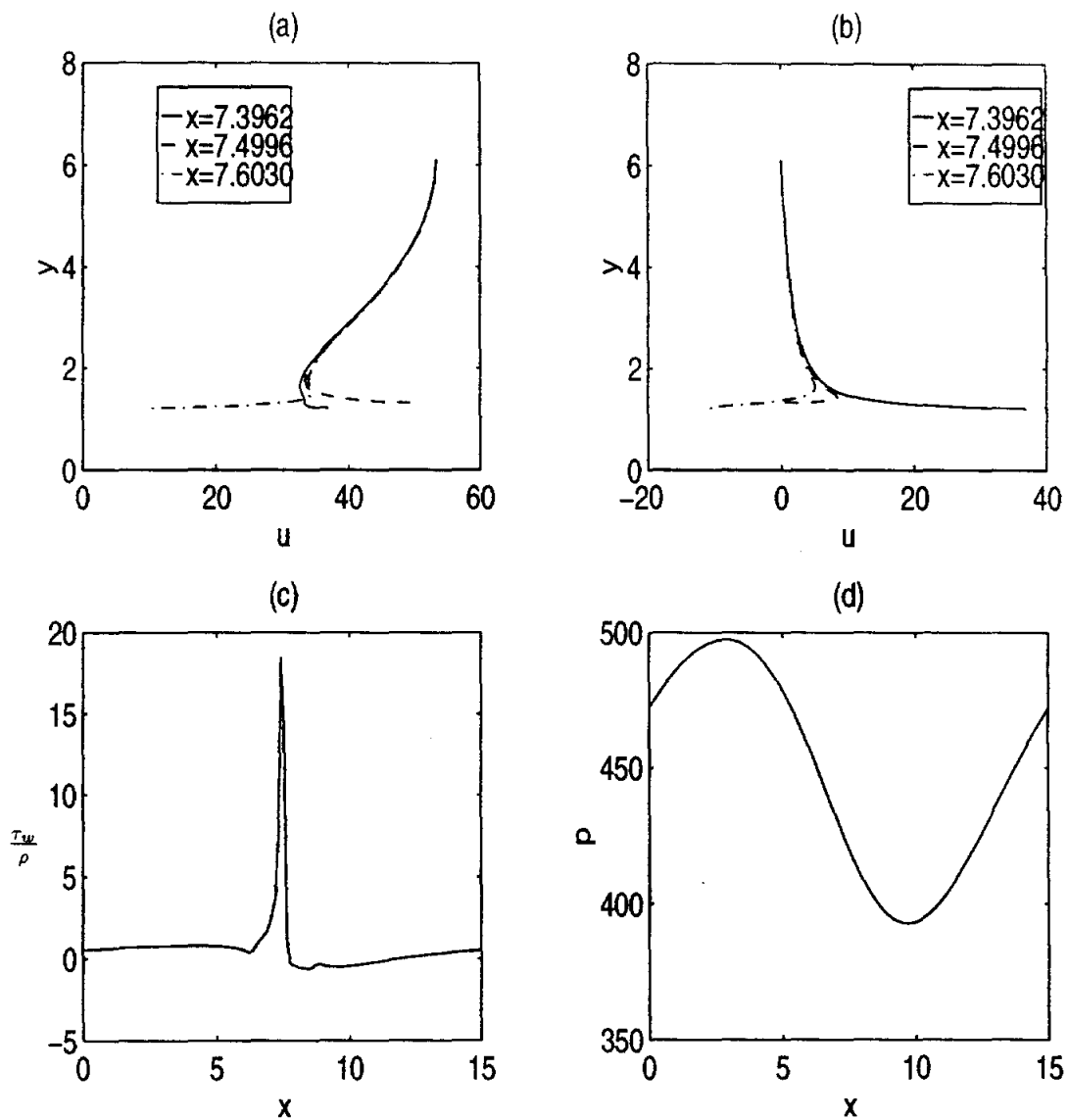
Figure 7.6: Turbulent flow over Type I bedform with rigid-lid approximation: (a) horizontal velocities in the vicinity of dune crest (in cm/s); (b) vertical velocities in the vicinity of dune crest (in cm/s); (c) shear stress (τ_w/ρ) at the bed in (cm^2/s^2); (d) surface pressure on the air-liquid interface (in cm^2/s^2).

to be. The maximum deviation of the surface pressure form the mean pressure is about $50cm^2/s^2$ as shown in Fig.7.6(d). If the free surface were allowed to deform the hydrostatic pressure would compensate for this. Thus the maximum surface deflection would be approximately $50/gcos\theta \approx 0.05cm$. The surface deflection is not very significant and the rigid-lid approximation is probably quite good in this case. A better estimate of the surface deflection can be obtained if we let the free surface to deform and these results are discussed in the latter part of this section.

The original motivation for choosing to simulate the experimental cases of Lyn (1993) is to make quantitative comparisons. Lyn (1993) reports the flow rate for the above described case as $154.90cm^2/s$. However, at steady state, the flow rate predicted by the numerical simulation is $215cm^2/s$. We believe the discrepancy-is due to the fact that, we can not obtain perfect periodic conditions in experiments as we do in numerical simulations. The equilibrium is achieved when the gravity force is exactly balanced by the fluid friction at the bed. The friction at the bed retards the flow, and this effect diffuses slowly upward based on the molecular and turbulent viscosity. Sufficiently large number of bedforms are required, so that the momentum diffusion over the entire fluid layer can take place, and the fluid flow reach equilibrium (steady state). This is in many respects, similar to the spatial and temporal stability analyses explained in the previous chapter on thin-film flows. What we are investigating numerically is the temporal stability, wherein the domain is periodic in space and evolving in time. Whereas, what is being determined experimentally by Lyn (1993) and other experimenters is the spatial stability, wherein the disturbance is evolving in the downstream direction. In their earlier studies (Nelson & Smith 1989; Nelson, McLean & Wolfe 1993) they use only five periodic bedforms, and find that the flow starts reaching only around fifth

bedform. In their subsequent study, they increase the number of periodic bedforms to 20 (McLean, Nelson & Wolfe 1994). Due to this discrepancy in flow rates, our velocities are higher than Lyn (1993) and it is not possible to make quantitative comparison. Qualitatively however, the numerical predictions compare very well with the experimental predictions of Lyn (1993).

With the flow rate of $215cm^2/s$ and a mean flow depth of $6.1cm$, the Froude number of this flow $Fr = Q/\sqrt{gH^3}$ turns out to be 0.45. Note that, this is no longer a small Froude number flow, and we should expect to observe significant free surface deformation.

The turbulence characteristics, namely, the turbulence kinetic energy k, the turbulence eddy viscosity ν_T and the Reynolds shear stress $-\overline{u'v'}$, at various cross-sections are shown in Fig.7.7(a,b,c). Large values of k, ν_T and $-\overline{u'v'}$ are found near the dune crest which are a direct result of the local acceleration associated with sharp corner. Separation turbulence dominates the wall generated turbulence which has also been observed experimentally by Nelson etal (1993). The maximum k occurs at about the center of the wake. Downstream of the reattachment point the profiles relax towards the flat bed profiles. However, due to the relatively short wavelength, the fluid quickly runs into another dune and the flow separation results without fluid ever attaining flat bed turbulence characteristics. The turbulence eddy viscosity ν_T has two maxima for some distance downstream of the dune crest. The top one is due to the local acceleration at the dune tip and the bottom one is due to the free stream turbulence associated with flow separation. The Reynolds shear stress $-\overline{u'v'}$ has a similar qualitative behavior as k and ν_T. To obtain a better view of the turbulence field, the area contour plots of turbulence parameters k, ϵ and ν_T

Figure 7.7: Turbulence characteristics for flow over Type I bedform with rigid-lid approximation: (a) turbulence kinetic energy k (in cm^2/s^2); (b) eddy viscosity ν_T (cm^2/s); (c) Reynolds shear stress $-\overline{u'v'}$ (in cm^2/s^2).

are shown in Fig.7.8. To particularly note are the large eddy viscosities upstream of the dune crest which is due to the local acceleration at the dune crest.

Flow over Type II bedform with energy slope 0.00145 is simulated next. The equilibrium horizontal and vertical velocities at different cross-sections are shown in Fig.7.9(a,b). The separation region can be identified by the negative u and v velocities. The reattachment length L_r was found to be 2.36cm in this case. The considerably smaller separation zone in this case compared to the Type I bedform is due to the different upstream geometry. An internal boundary layer grows from the point of reattachment and the flow profiles relax towards the flat bed profiles. Due to the shorter reattachment length, the flow field has a longer redevelopment length and shows greater relaxation towards the flat bed profiles than in the case of Type I bedform. Just as in the previous case, the flow undergoes local acceleration resulting in very high vertical and horizontal velocities at the dune crest. The velocity defect $\Delta u = u_{max} - u$, the normalized with the total shear velocity $u_*^T = \sqrt{gHsin\theta}$ at four different cross-sections is shown in Fig.7.9(c). Except for the velocity defect profile at the dune crest $x/L = 0.50$, at all other three cross-sections, the Δu profiles collapse very nicely onto the same curve. The velocity defect profile at the dune crest differs from the rest due to the local acceleration associated with stream line bending.

Similar to the previous case, the equilibrium flow rate computed numerically is $280cm^2/s$ as opposed to the experimental flow rate of $164.90cm^2/s$ reported by Lyn (1993). Based on a flow rate of $280cm^2/s$ and mean flow depth of $6.1cm$, the Froude number for this flow is $Fr = 0.59$. Thus in this case, the Froude number is more than in the previous case, and we should observe even greater free surface
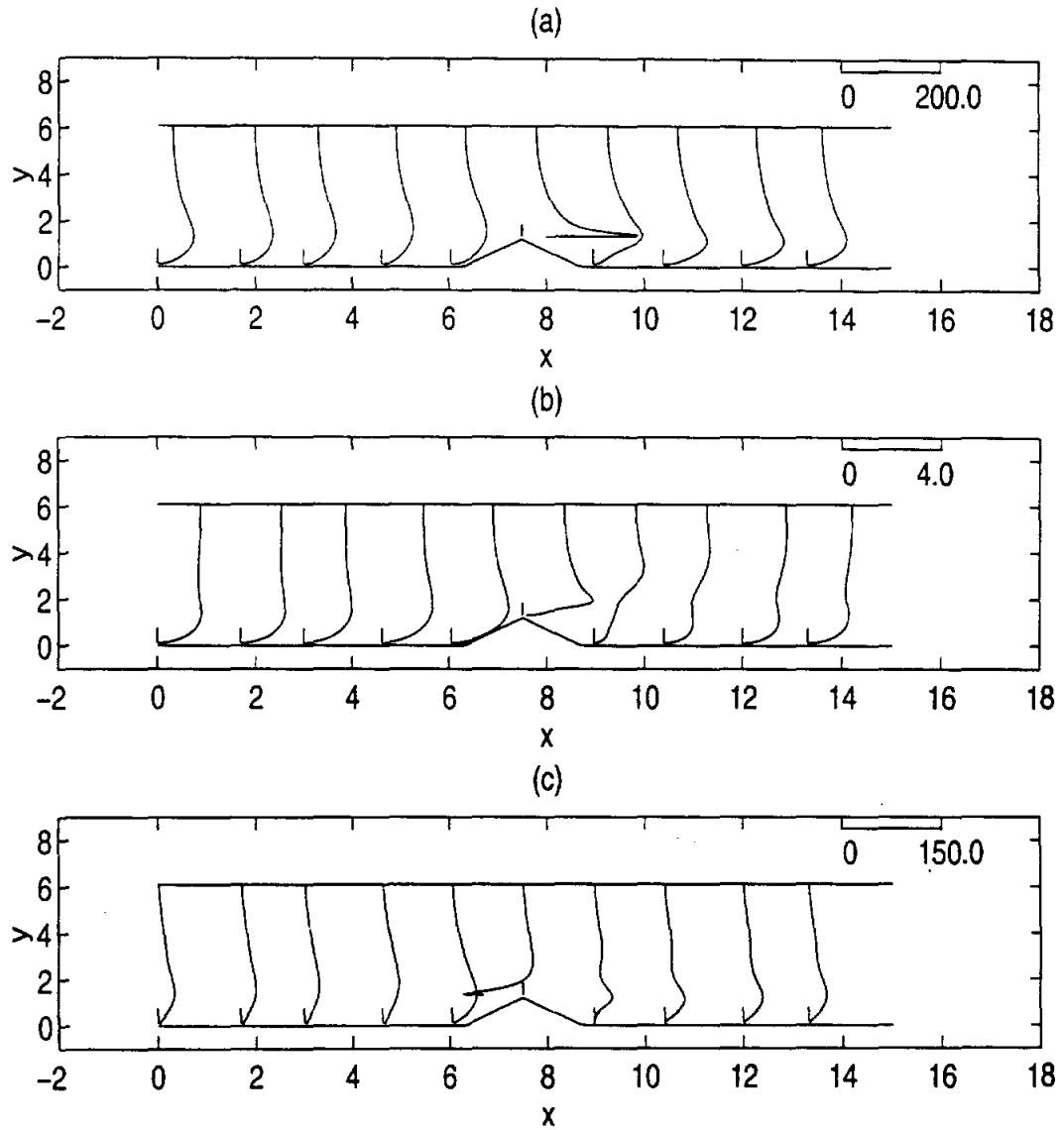
Figure 7.8: Turbulence flow characteristics for flow over Type I bedform with rigid-lid approximation: (a) turbulence kinetic energy k (in cm^2/s^2); (b) rate of dissipation of turbulence kinetic energy ϵ (in cm^2/s^3); (c) eddy viscosity ν_T (in cm^2/s).

Figure 7.9: Mean flow characteristics for flow over Type II bedform with rigid-lid approximation. (a) horizontal velocity u (in cm/s); (b) vertical velocity v (in cm/s); (c) velocity defect profiles.

deformation. We will simulate this case without making the rigid-lid approximation in the next subsection to determine the free surface deformation.

The turbulence kinetic energy k, eddy viscosity ν_T and the Reynolds shear stress $-\overline{u'v'}$ at various cross-sections are shown in Fig.7.10(a,b,c). Very large values are found at the dune crest due to local acceleration. Wake turbulence associated with flow separation dominates the wall generated turbulence. Rest of the qualitative details are similar to that observed in the previous case.

The shear stress at the bed $\tau_w(x)$ is shown in Fig.7.11(a). Very large values are observed at dune crest due to local acceleration. It would be interesting to compute the sediment load distribution in the channel for this flow field. The turbulent flow field picks up the sediment particles and transports it downstream in the form of bed load and suspended sediment load. As explained in the previous section on the mathematical formulation, the bed load is computed using an empirical formula proposed by van Rijn(1984a) which is a function of sediment particle parameters such as density, diameter and the shear stress at the bed. As would be expected, the bed load transport($S_b(x)$) is very high in regions with large shear stress (Fig.7.11b) such as the dune crest. The suspended sediment concentration is computed using an advection-diffusion transport equation for the suspended sediment concentration (Eq.7.15). Integrating in the y direction the suspended load $(S_s(x))$ as a function x is computed as follows:

$$S_s(x) = \int_{b(x)}^{h(x)} uc\,dy \tag{7.25}$$

The suspended load $(S_s(x))$ distribution along the channel is shown in Fig.7.11(b). The suspended sediment distribution is dependent on both the flow field and the shear stress at the bed and is thus only weakly dependent on the shear stress.
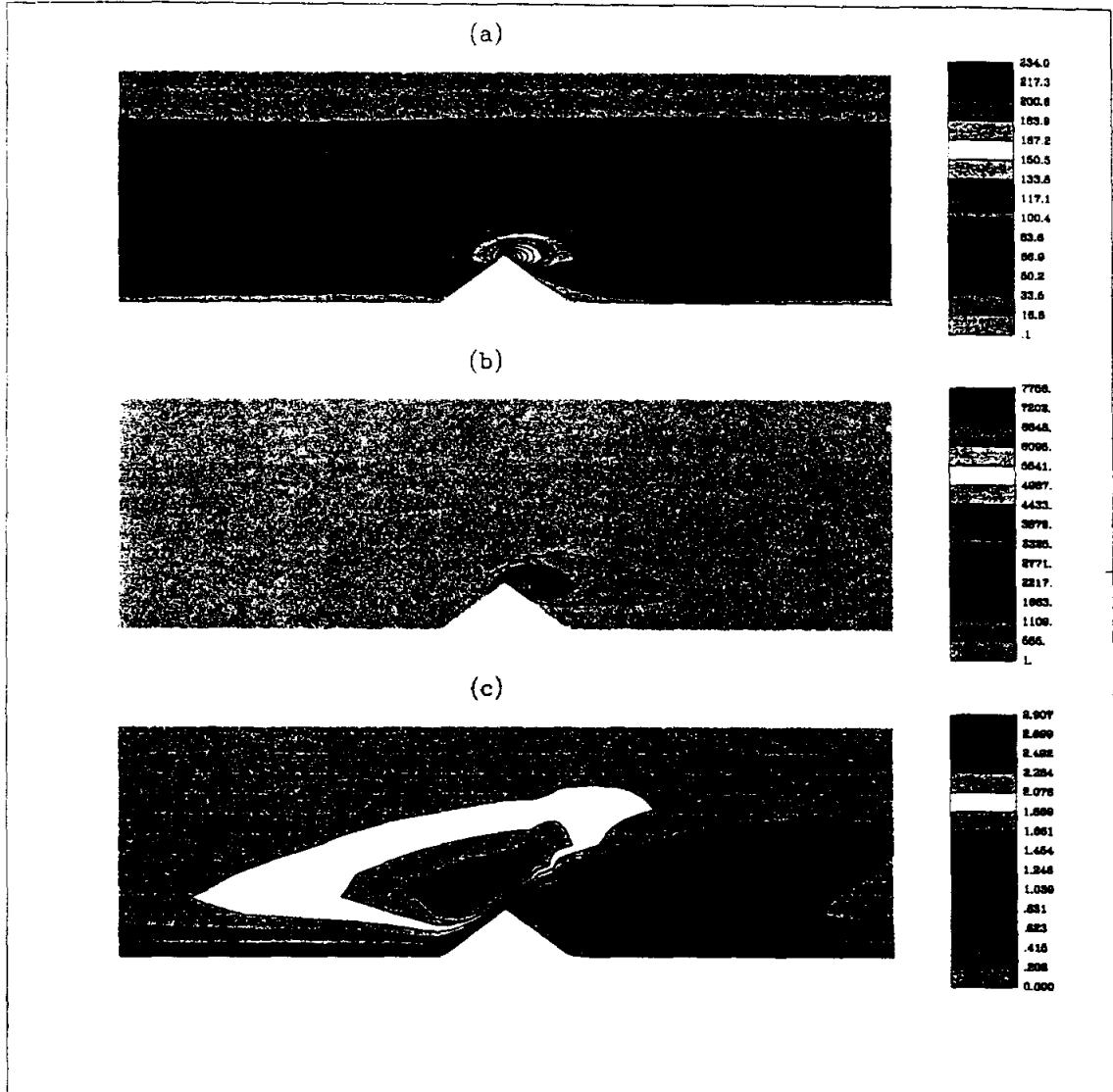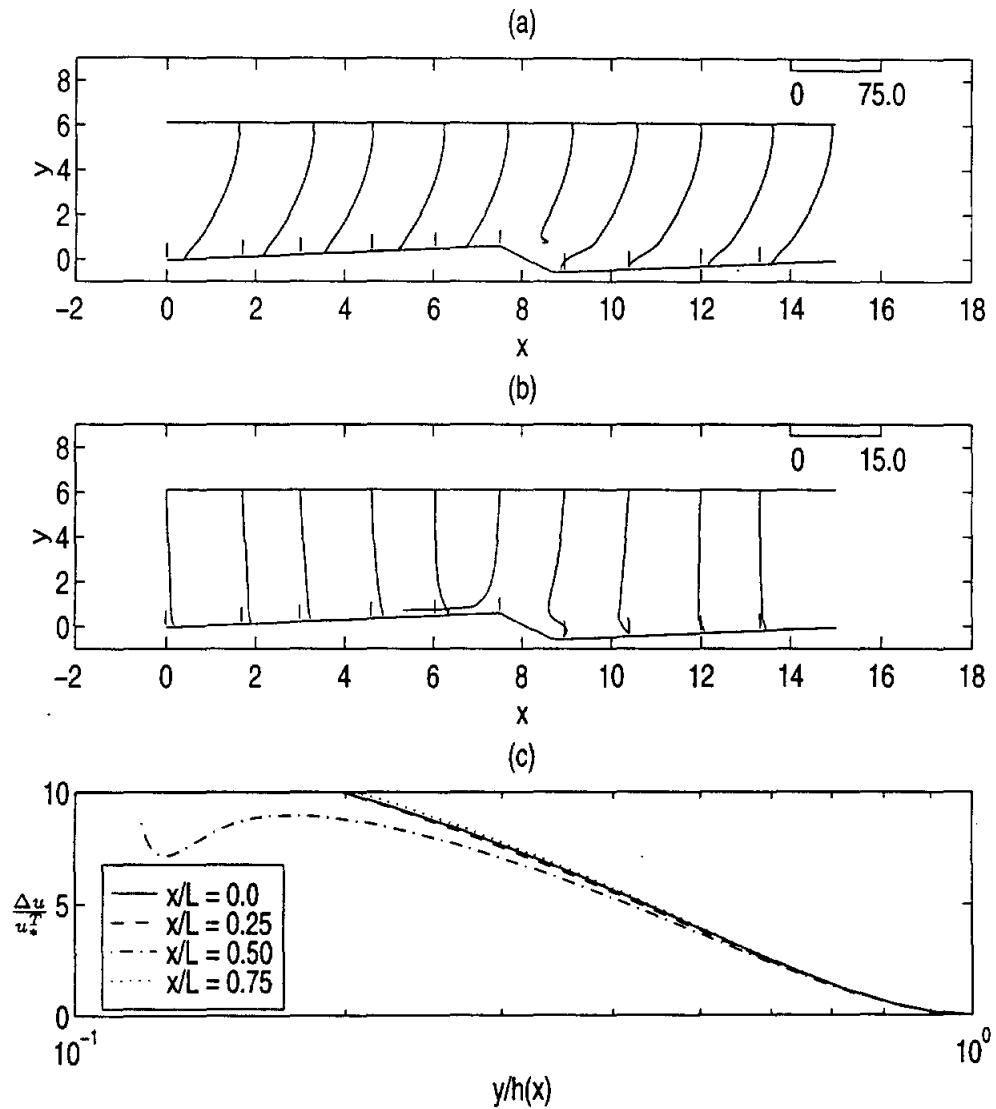
(a)

(b)

(c)
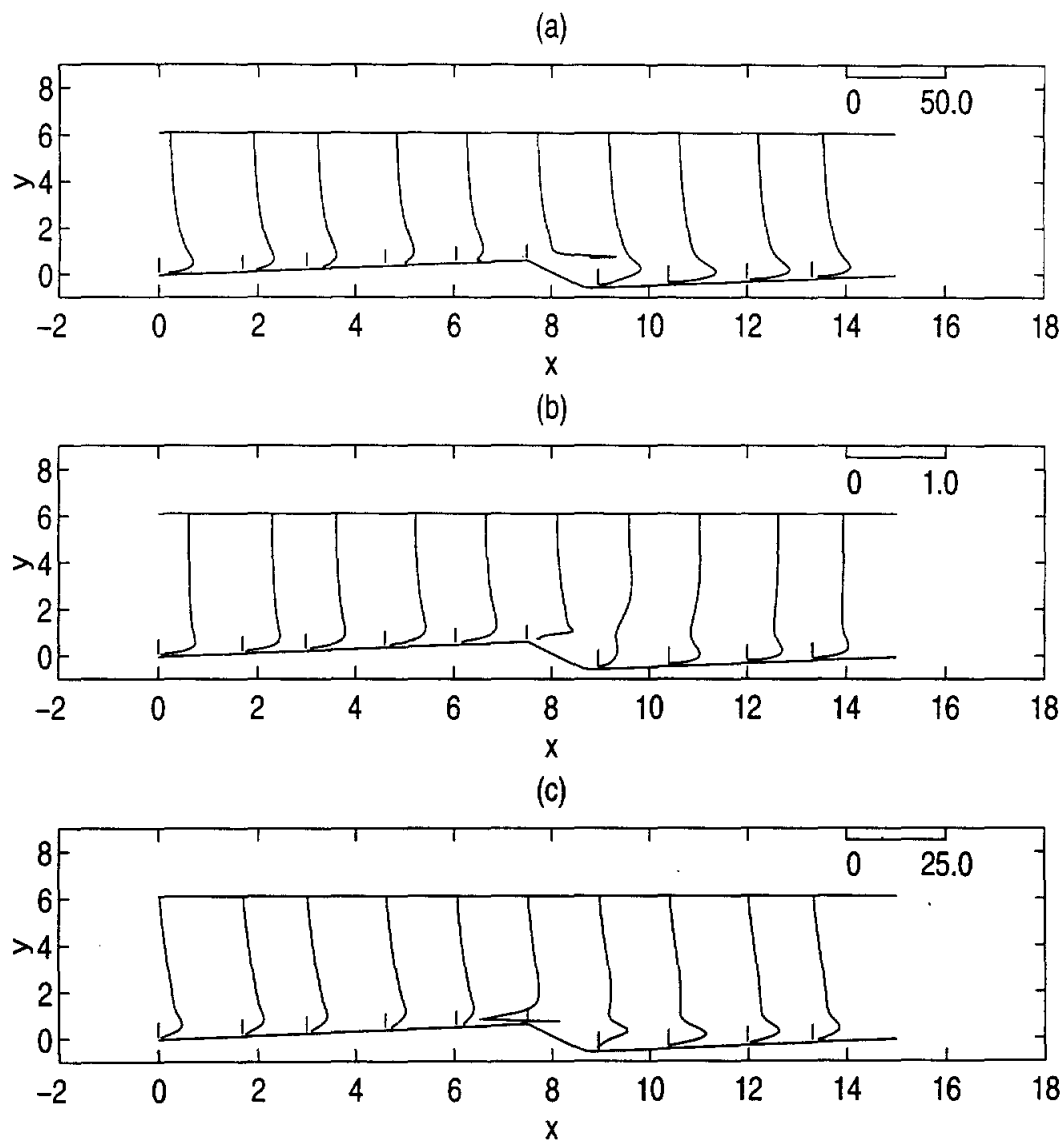
Figure 7.10: Turbulence characteristics for flow over Type II bedform with rigid-lid approximation: (a) turbulence kinetic energy k (in cm^2/s^2); (b) eddy viscosity ν_T (in cm^2/s); (c) Reynolds shear stress $-\overline{u'v'}$ (in cm^2/s^2).
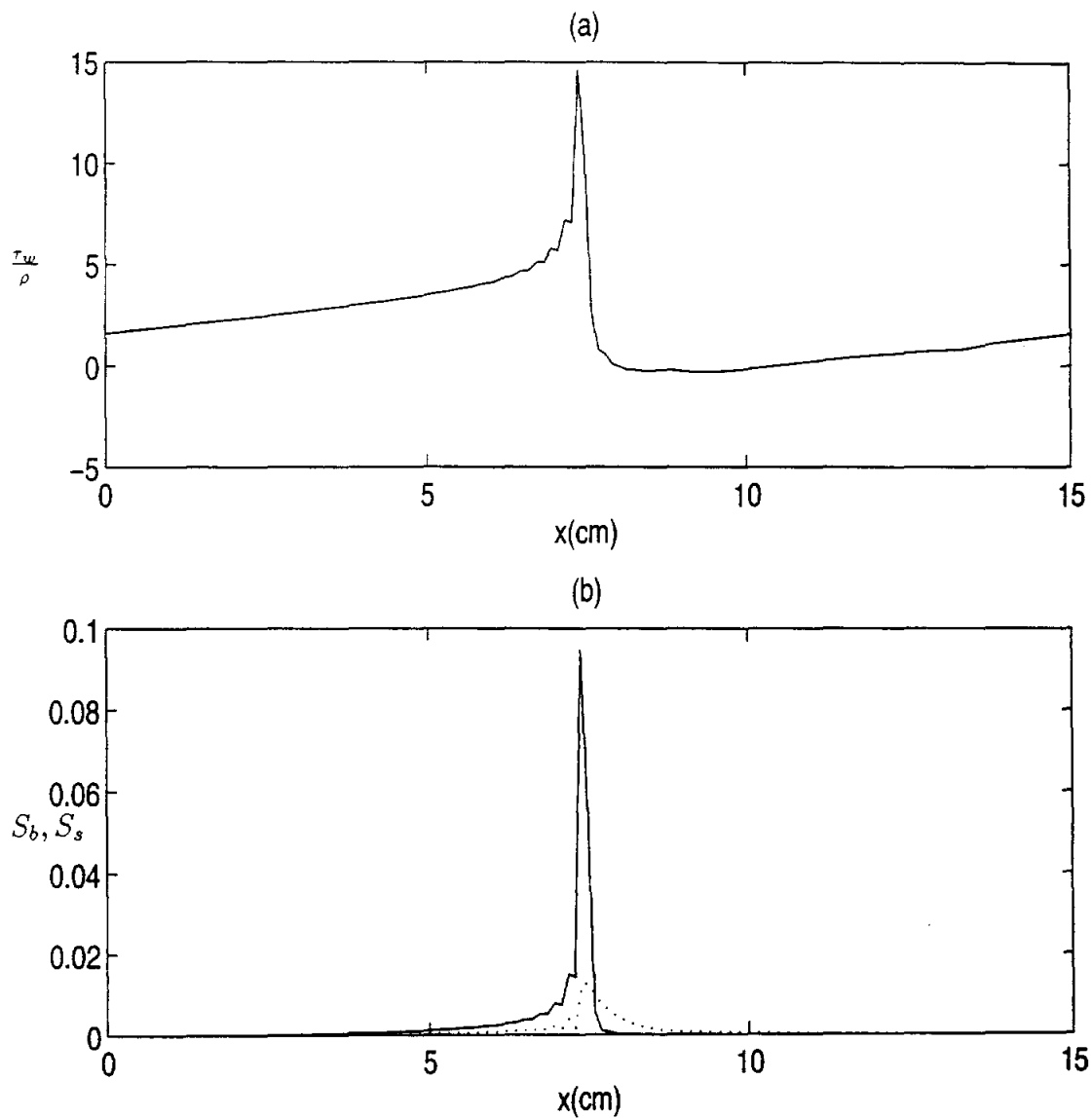
Figure 7.11: Flow over Type II bedform with rigid-lid approximation: (a) shear stress at the bed (in cm^2/s^2); and (b) sediment load in the form of bed load (continuous line, in cm^2/s) and suspended load (dotted line, in cm^2/s).

Downstream of the dune crest in the flow separation region, the bed load transport is negligible, where as there is significant amount of suspended load. Thus models which neglect the suspended load and take into account only the bed load would be inaccurate in the separation region. The significant suspended sediment concentration is due to the wake turbulence which maintains the sediment particles in suspension. In our suspended sediment modeling, the sediment concentration is modeled as passive scalar and hence doesn't influence the flow field. Near the bed, a small layer of sediment particles of the order of few particle diameters thickness moves as bed load and is known to enhance the effective roughness of the bed. Following van Rijn(1984c), the effective sand roughness height k_s is taken to be equal to $3D_{50}$ where D_{50} is the median diameter of the sediment particle. The flow field has been computed with $k_s = 0.25mm$ and the sediment transport calculations correspond to sediment bed with $0.08mm$ sediment particle size. The sediment particle size is very small and consequently, we find significant levels of suspended sediment transport. However, the suspended sediment load is known to decrease with an increase in the particle size. Thus, whether suspended sediment load also needs to be considered along with the bed load is dependent on the sediment material.

7.4.2 Mean flow and turbulence characteristics without the rigid-lid assumption

In this section we present the results for the simulations in which the air-liquid interface is allowed to deform. The location of the free surface is computed along with the fluid flow and turbulence field using the ALE formulation.

The horizontal velocity u at various cross-sections for the flow over Type I bedform are shown in Fig.7.12. The horizontal velocity profiles look very similar to
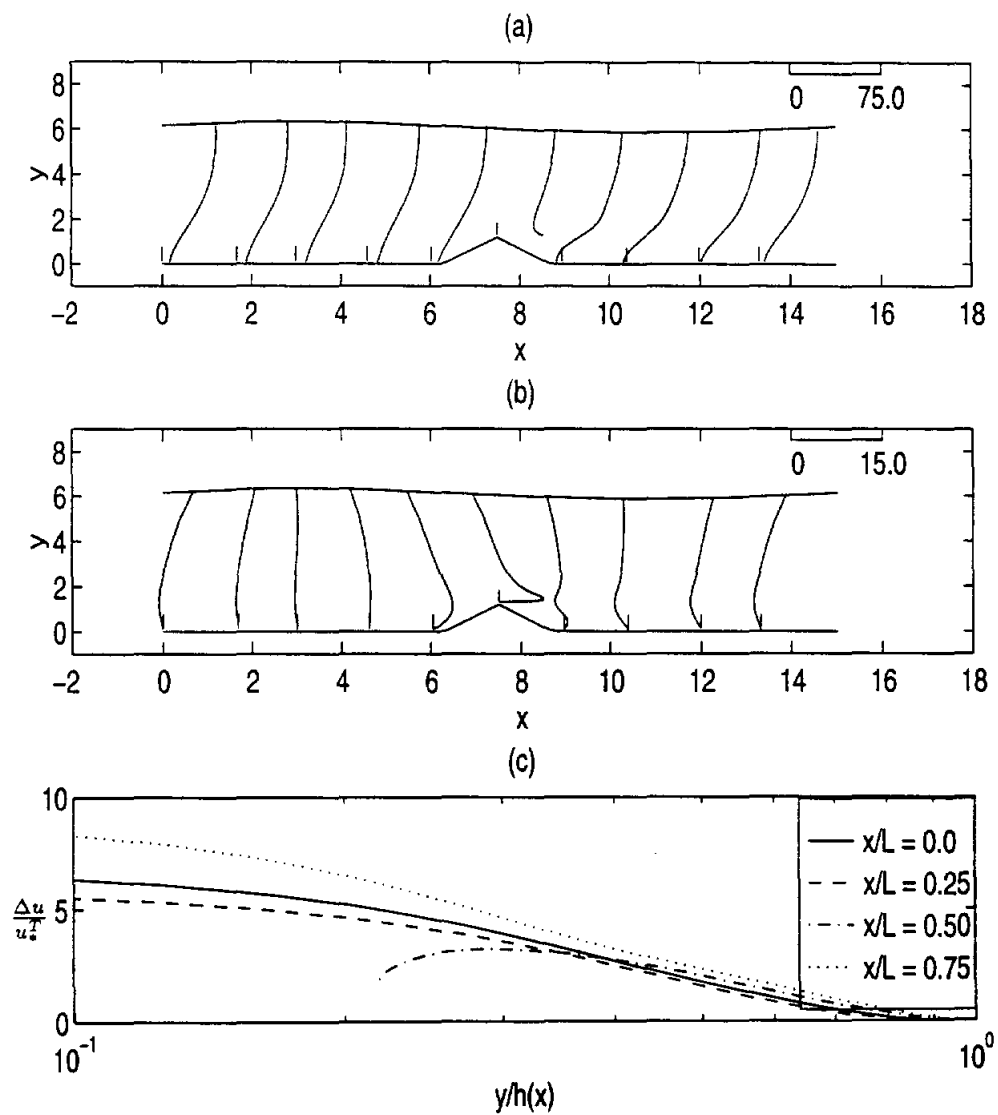
Figure 7.12: Flow over Type I bedform with the free surface allowed to deform: (a) horizontal velocity u (in cm/s), (b) vertical velocity v (in cm/s), and (c) the velocity defect profiles.

when the free surface was assumed to be rigid (Fig.7.4). The most important features are the local acceleration at the tip of the dune, separation of the boundary layer downstream of the crest, and the reattachment and subsequent growth of the internal boundary. The recirculation length is found to be $3.25cm$ as opposed to a $3.9cm$ recirculation length observed when the free surface was assumed to be a rigid lid. The vertical velocity profiles are shown in Fig.7.12(b). The vertical velocity profiles especially near the free surface are markedly different from that obtained previously with the rigid-lid assumption (Fig.7.4b). The velocity defect profiles are plotted in Fig.7.12(c), and fall on a single curve for $y/h(x) > 0.4$ just as in the previous simulations with rigid-lid assumption (Fig.7.4c).

The turbulence kinetic energy k, the eddy viscosity ν_T and the Reynolds shear stress $-\overline{u'v'}$ are shown in Fig.7.13. The qualitative behavior is seen to be very similar to that observed previously with the rigid-lid assumption. The turbulence associated with separation wake completely dominates the wall generated turbulence.

The equilibrium free surface profile is shown in Fig.7.14(a) and compared with the rigid-lid assumption. The maximum free surface deflection is approximately $0.3cm$. The minimum free surface height occurs near the point of reattachment and the maximum free surface height occurs well upstream of the dune crest. The most important quantity of interest is the shear stress at the bed, and a comparison is made between that obtained with and without the rigid-lid approximation. The shear stress is found to be lower in the case where the free surface was allowed to deform, compared to that obtained with the rigid-lid assumption. A very big difference in the shear stress is found near the tip of the dune, and this can have profound influence on the sediment transport and bedform formation modeling.
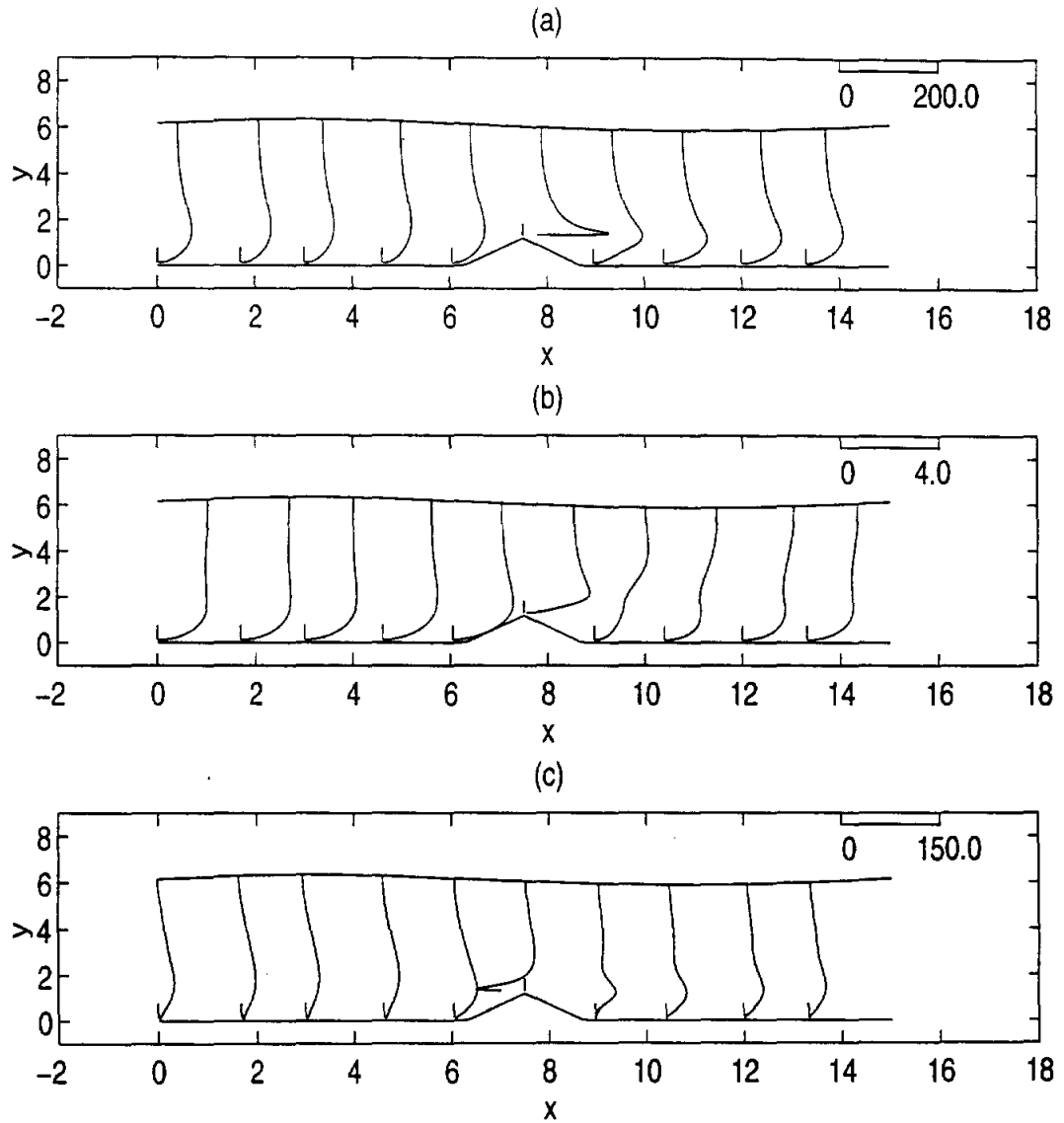
Figure 7.13: Flow over Type I bedform with the free surface allowed to deform: (a) turbulence kinetic energy k (in cm^2/s^2), (b) eddy viscosity ν_T (in cm^2/s), and (c) Reynolds stress $-\overline{u'v'}$ (in cm^2/s^2).
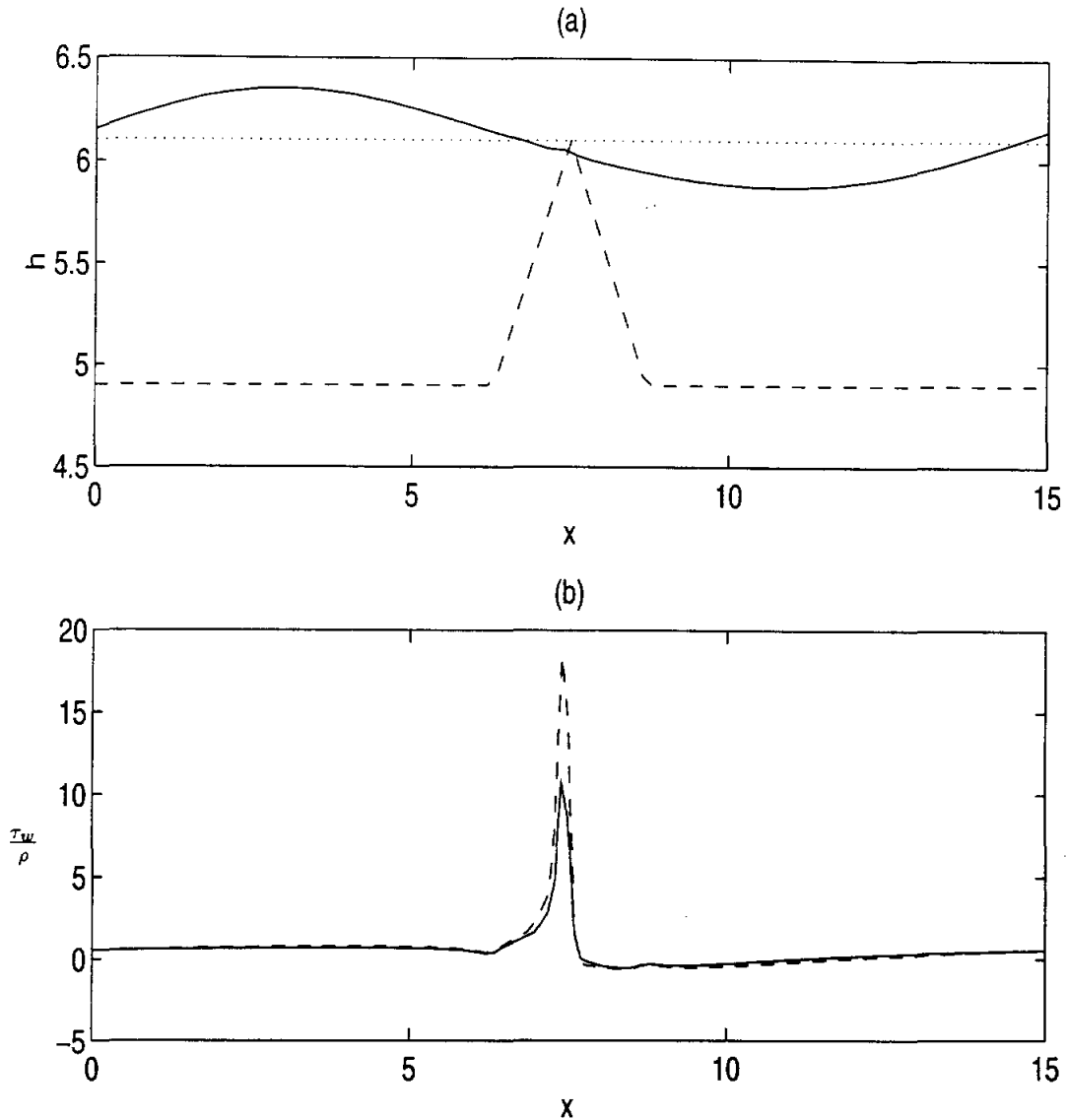
Figure 7.14: Comparison between the solutions obtained with and without the rigid-lid assumption: (a) The continuous line corresponds to the equilibrium free surface profile (in cm), the broken line corresponds to the bed profile (shifted upwards), and the dotted line is the rigid-lid; (b) the shear stress (in cm^2/s^2) shown in continuous line is obtained by allowing the free surface to deform and the broken line is obtained by making the rigid-lid approximation.

Flow over Type II bedform (Case 2) with energy slope 0.00145 is simulated next. The rigid-lid approximation is not made, and the free surface location is determined through the ALE formulation. Unlike the previous case, the fluid flow does not go towards steady state. Instead waves are found to occur in this case on the air-liquid interface, leading to a time-periodic free surface height as shown in Fig.7.15. Note that, oscillatory behaviour at $x = 0$ is different form that at $x = L/2$. At $x = 0$, the free surface height oscillates between a minimum of $5.9 cm$ and a maximum of $7.1 cm$. Where as, at $x = L/2$, the free surface height oscillates between $5.3 cm$ and $6.0 cm$. This tells us that this is not a traveling wave. It is probably a standing wave. This can be better understood through the spatio-temporal evolution of the free surface profile shown in Fig.7.16. The wave is found to propagate both upstream and downstream, alternately. This is unlike that seen in thin-film flows (chapter 6), where the surface waves were found to travel downstream. This is due to the fact that the fluid flow is in a subcritical state $(Fr < 1)$, and the disturbance can travel both upstream and downstream. The time history of the shear stress at the bed is shown in Fig.7.17. The shear stress at the bed is also seen to be time-periodic. This type of periodic behaviour can have profound influence on the sediment load and consequently, the bedform formation. Also, the deformation of the free surface is quite large, and the simulations made with the rigid-lid approximation would be expected to perform poorly.

As mentioned briefly in chapter 2, gravity surface waves are found to exist on open-channel flows with Froude numbers greater than a cut-off value usually in the range $1 - 2$. However, these estimates are for flow over a smooth wall. In our case, the bed is filled with bedforms, which probably, reduce the cut-off value for initiation
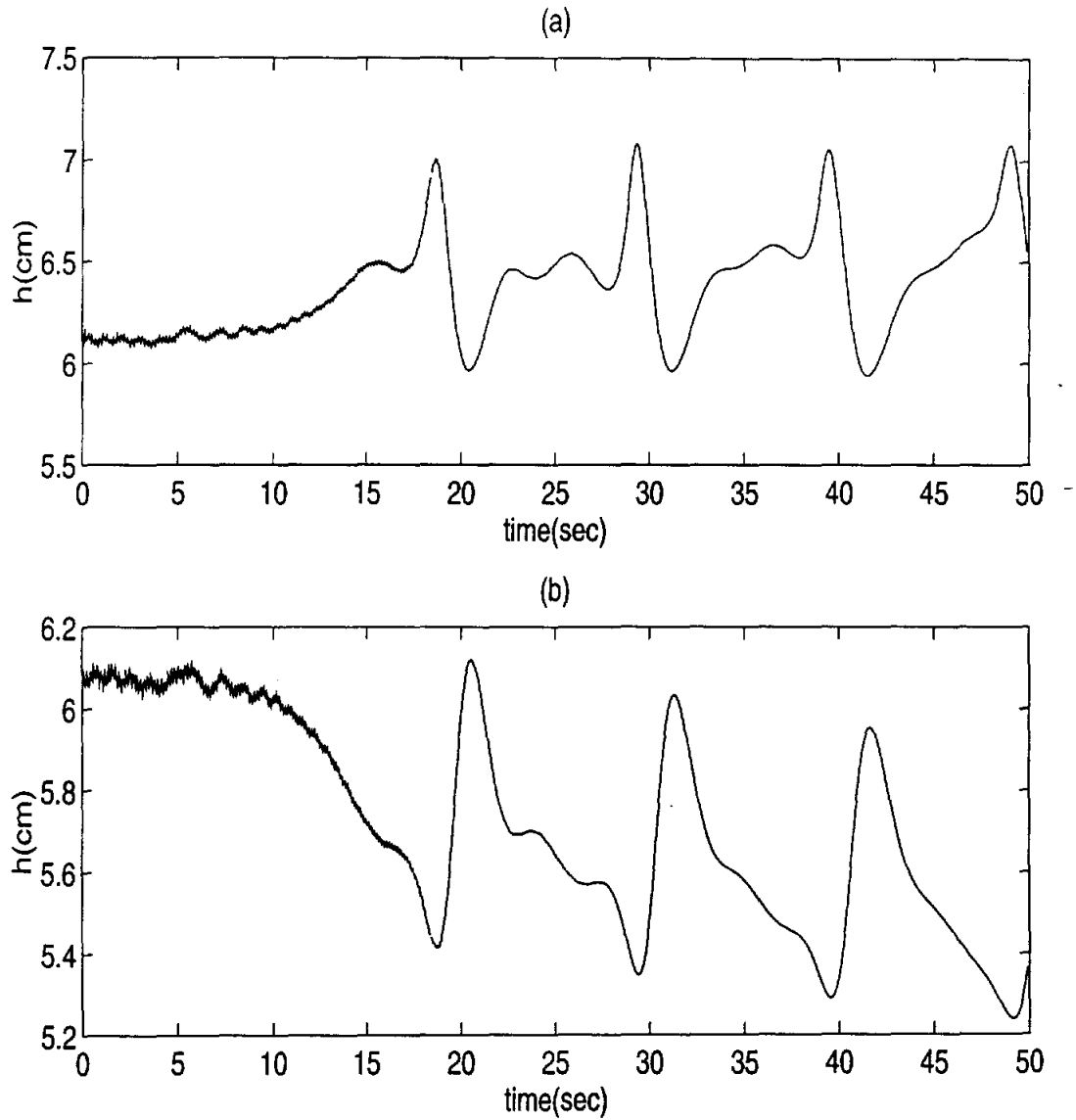
Figure 7.15: Flow over Type II bedforms. Time history of the free surface height at (a) $x = 0$ and (b) $x = 7.5cm$ (the crest of the bedform).

Figure 7.16: Spatio-temporal evolution of the free surface profiles in the case of flow over Type II bedform without making the rigid-lid approximation.

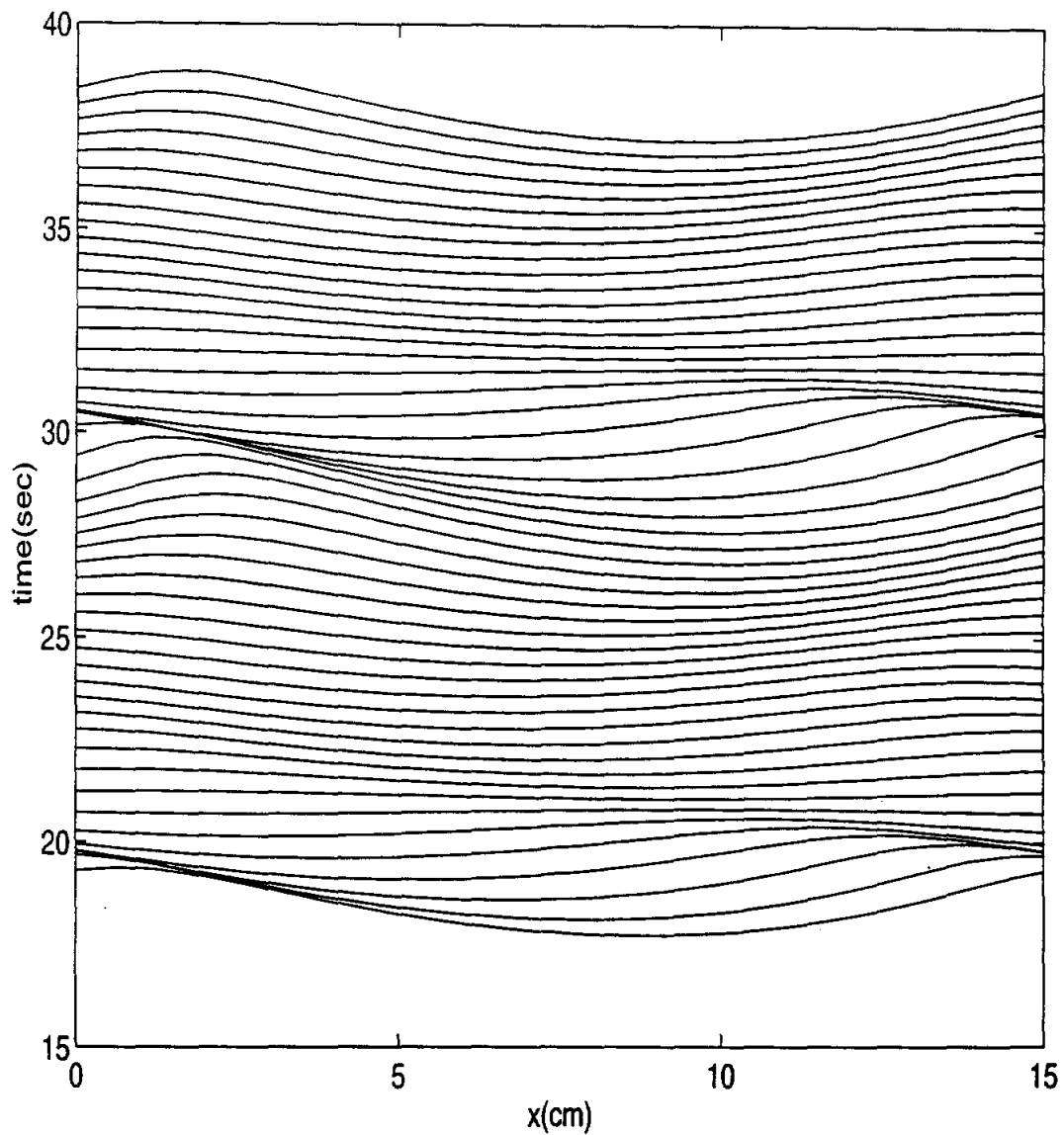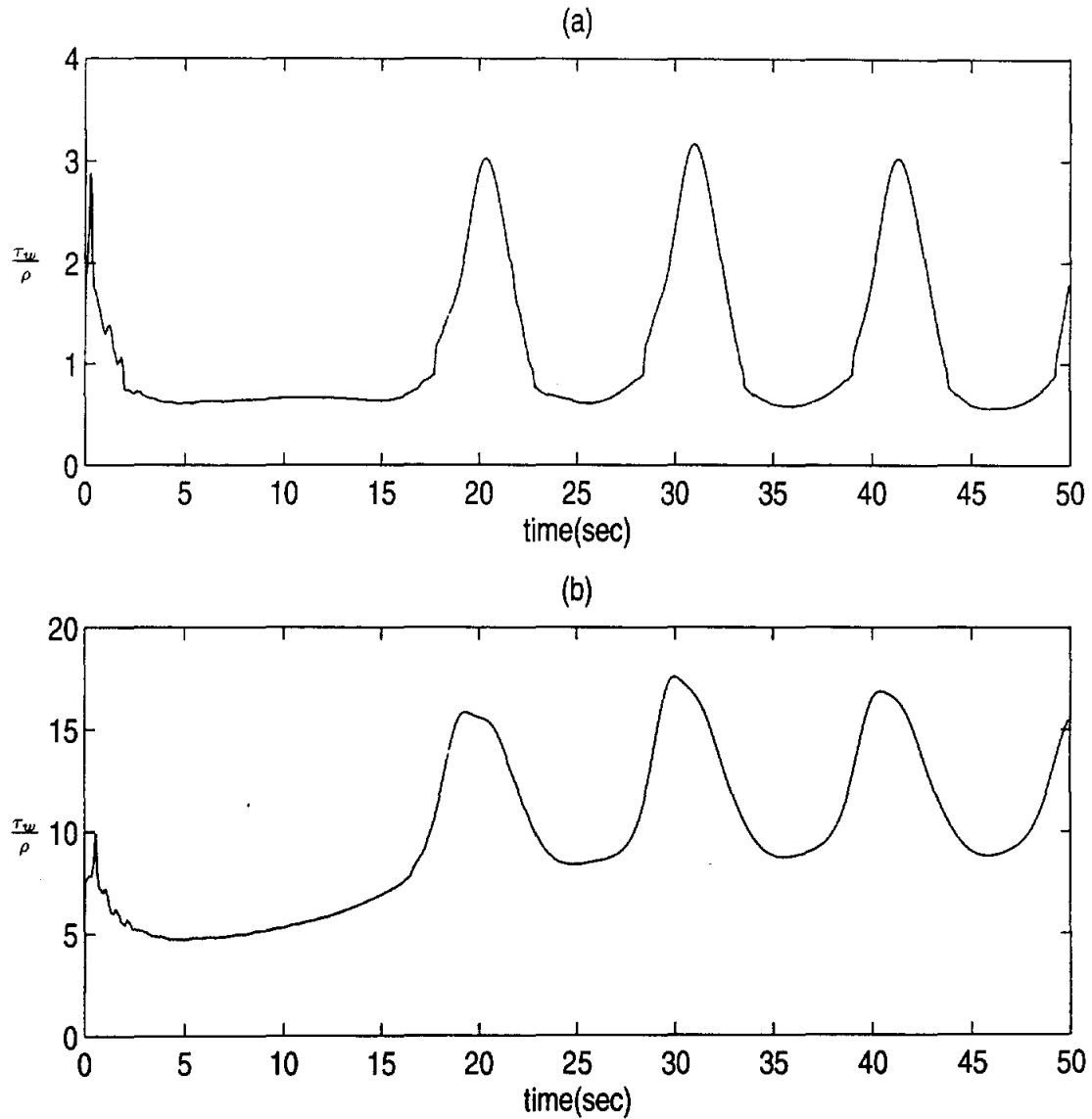Figure 7.17: Flow over Type II bedform without making the rigid-lid approximation. Time history of the shear stress (τ_w/ρ) at the bed at (a) $x = 0$; and (b) $x = 7.5cm$ (the crest of the bedform).

of gravity waves on the free surface. Thus, even with a Froude number flow of only $Fr = 0.59$, we are observing surface waves on the free surface.

With the same bedform geometry as the previous case, that is Type II bedform, but with energy slope 0.00400 is simulated next. Due to the greater energy slope, the flow rate increases resulting in higher Froude number flow, which in this case is close to $Fr = 1.0$. Steady traveling waves on the free surface are found to exist in this case (Fig.7.18). The waves are traveling downstream and the flow is in a supercritical state.

7.5 Concluding remarks

A numerical method has been developed to study the turbulent fluid flow over stream-wise periodic bedforms. The procedure can handle the free boundary in a straight forward manner through the ALE procedure, and gives us the capability to simulate high Froude number flows. Numerical procedures with the rigid-lid approximation developed previously (Mendoza & Shen 1990) are strictly valid only for very small Froude number flows.

Study of the turbulent flow over artificial bedforms has revealed certain interesting features not previously reported. Due to the local acceleration associated with streamline bending, very large velocities and shear stresses exist at the tip of the dune. If the bed were erodible, the tip of the bed would be the first area that would be washed out, and the resulting bedform would be smooth. The influence of the bedform is restricted to the bottom half of the fluid layer, and velocity defect profiles for the top half of the fluid layer are found to be self similar with respect to the total friction velocity $u_*^T = \sqrt{gH\cos\theta}$. The separation wake turbulence is found to dominate the wall generated turbulence completely, and the maximum eddy vis-
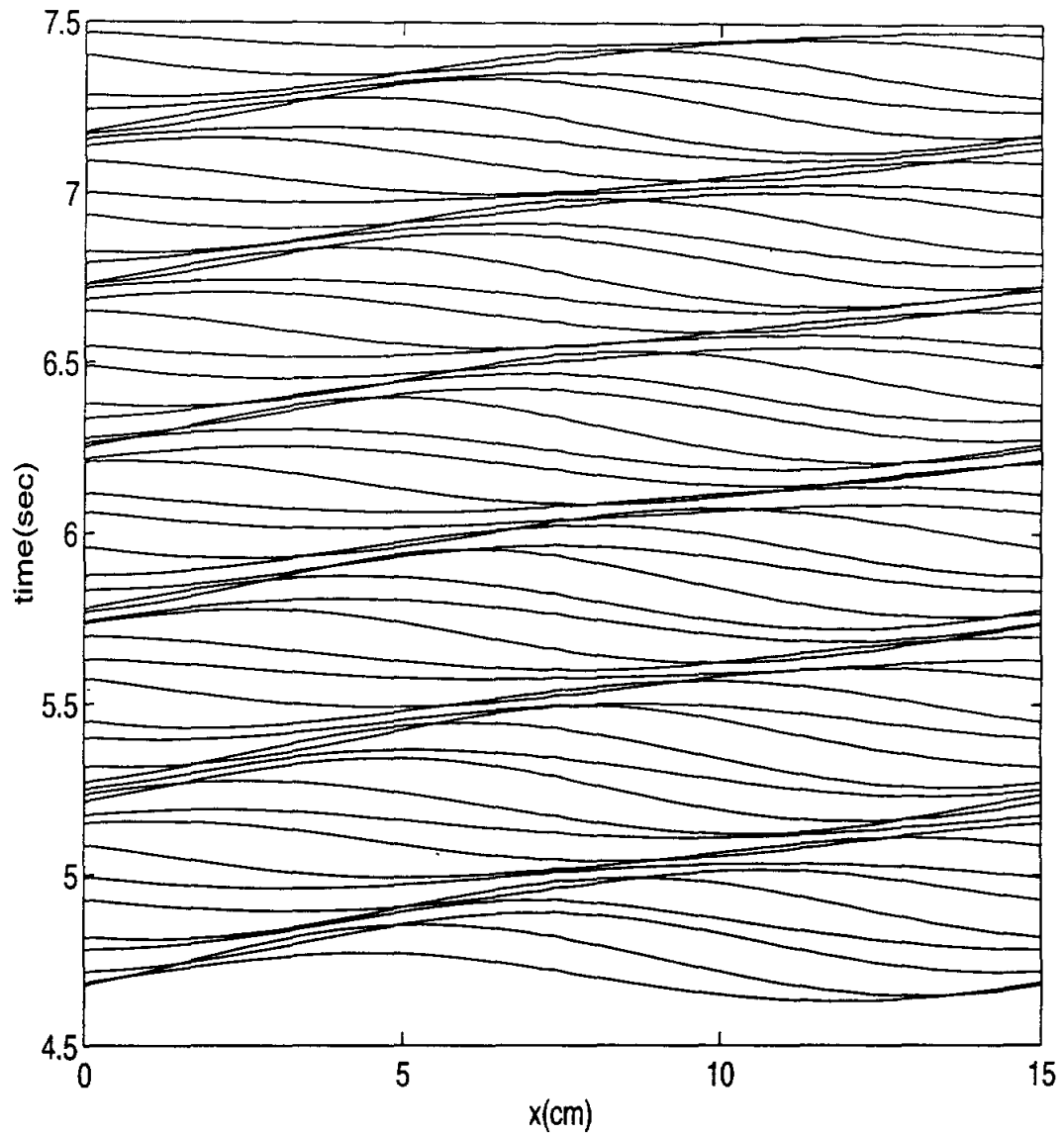
Figure 7.18: Spatio-temporal evolution of the free surface profiles in the case of flow over Type II bedform with energy slope 0.004, and without making the rigid-lid approximation.

cosities and Reynolds stresses occur at a distance, approximately equal to the dune height, away from the bed.

In the case of flow over Type I bedform with energy slope 0.00525, a maximum free surface deflection of 0.3*cm* was found. However, the biggest difference between the two simulations, namely, with and without making the rigid-lid assumption, is in the shear stress values. The simulations without making the rigid-lid approximation predict a much smaller value of shear stress at the peak.

In the case of Type II bedform with energy slope 0.00145, no steady state solution was found. Instead standing waves were found to occur on the free surface and the waves propagate both upstream and downstream since the fluid flow is in a subcritical state. This periodic free surface waves, result in periodic shear stresses at the bed and this can have profound influence on the sediment load characteristics and bedform formation.

Chapter 8

Hydraulic Jump

8.1 Introduction

Hydraulic jump is one of the most interesting phenomena occurring in open channel flows and is analogous to shock wave in compressible flows. The free surface rises sharply across the hydraulic jump and the flow character changes across the jump, going from a supercritical state to a subcritical state. There is intense turbulent mixing in the hydraulic jump region and a large amount of energy dissipation occurs in the jump region. Because of its energy-dissipating capacity the hydraulic jump is widely used as an energy dissipator below dams, spillways and other outlet works (Chow 1959; Rajaratnam 1967). The hydraulic jump has many other practical applications as described by Chow(1959). The hydraulic jump may occur when there is supercritical flow in a channel having an obstruction or a rapid change in cross- sectional area (Shames 1992). Usually a stationary jump is referred to as a hydraulic jump and a jump propagating into quiescent fluid is referred to as hydraulic bore. A hydraulic bore is very similar to a hydraulic jump and can be visualized as a hydraulic jump in a moving frame of reference. The important difference between a bore and a jump is that the bottom boundary layer is weaker in the bore compared to hydraulic jump (Madsen and Svendsen 1983).

Rajaratnam (1967) defines the classical jump as a jump formed in a smooth, wide, and horizontal rectangular channel. A typical hydraulic jump is shown schematically in Fig.8.1. h_1 and U_1 are respectively, the depth and mean horizontal velocity
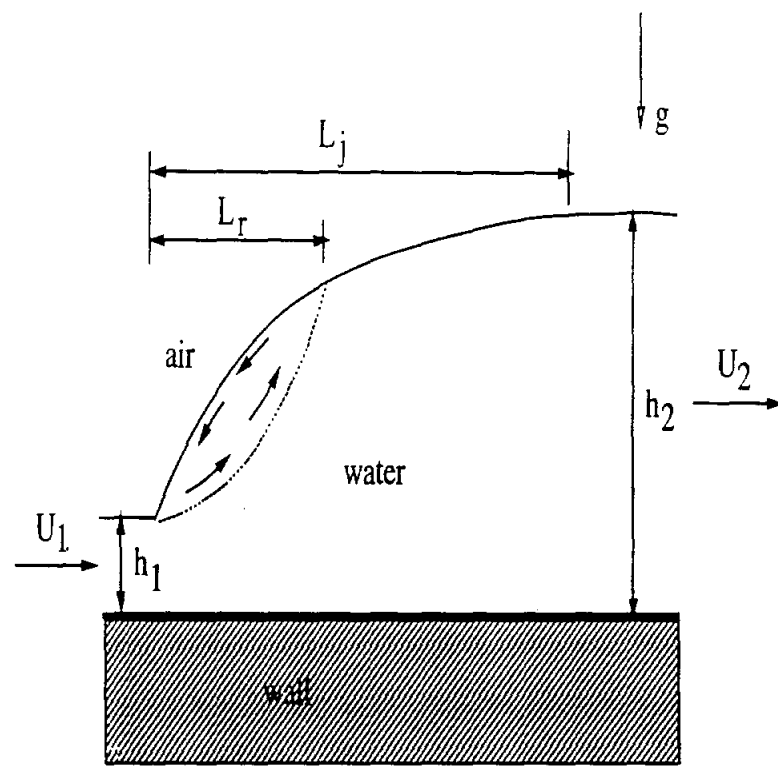
Figure 8.1: Schematic sketch of a hydraulic jump

of the supercritical flow just upstream of the jump. h_2 and U_2 are respectively, the flow depth and mean horizontal velocity of the subcritical flow just downstream of the jump. A hydraulic jump is characterized by the formation of the surface roller and air-entrainment into the roller. L_r is the length of the surface roller and L_j is the length of the jump. The most important non-dimensional number in the open channel flows is the Froude number defined as:

$$Fr = \frac{U}{\sqrt{gh}} \tag{8.1}$$

where U is the mean velocity and h is the flow depth. There are three distinct regimes in an open channel flow:

- $Fr > 1$, supercritical flow;

- $Fr = 1$, critical flow; and

- $Fr < 1$, subcritical flow

Froude number is the ratio of the mean velocity to the gravity wave celerity. Thus in a supercritical flow, the wave celerity is less than the mean velocity and the disturbance can only travel downstream. In a subcritical flow, however, the disturbance can travel both upstream and downstream. The Froude number is thus analogous to Mach number in compressible flows.

The quantities of primary interest in hydraulic jump are the downstream quantities such as h_2 and U_2, the profile of the jump and the energy loss across the jump. Knowing upstream quantities U_1 and h_1, the downstream quantities h_2 and U_2 can be determined analytically if the following assumptions are made:

- uniform velocity profile;

- pressure is hydrostatic;

- bottom friction is negligible and can be neglected; and

- surface tension can be neglected

Using the integral conservation of mass and conservation of momentum, a relation relating h_1 and h_2, can be derived and is also called as the *Belanger momentum equation* (Rajaratnam 1967).

$$\frac{h_2}{h_1} = \frac{1}{2}\left(\sqrt{1 + 8F_1^2} - 1\right) \tag{8.2}$$

Even though there is conservation of momentum, there is a loss of energy across the hydraulic jump. Define the specific energy as $E = U^2/2 + gh$. The loss of specific energy across the jump, $E_L = E_2 - E_1$, can be expressed as (Rajaratnam 1967):

$$\frac{E_L}{E_1} = \frac{1}{8}\frac{\left(\sqrt{1 + 8F_1^2} - 3\right)^3}{(2 + F_1^2)\left(\sqrt{1 + 8F_1^2} - 1\right)} \tag{8.3}$$

The specific energy loss across the jump depends on F_1, with a larger F_1 resulting in a greater energy loss across the jump.

The nature of the hydraulic jump is strongly dependent on the supercritical Froude number F_1. Chow (1959) classified the hydraulic jump into the following categories based on F_1:

- $F_1 = 1 - 1.7$, undular jump;

- $F_1 = 1.7 - 2.5$, weak jump;

- $F_1 = 2.5 - 4.0$, oscillating jump;

- $F_1 = 4.5 - 9.0$, steady jump

- $F_1 \geq 9.0$, strong jump

The above listed various types of jumps are shown schematically in Fig.8.2. The various jumps as listed above are not completely distinct and overlap to certain extent depending on the local conditions.

8.2   Literature Review

Hydraulic jump was first described by Leonardo da Vinci (Rouse & Ince 1957). The first systematic analysis of the hydraulic jump was undertaken by Bidone (1820) and Bélanger (1828). The hydraulic jump has been extensively studied since then and are listed by Chow (1959). A good review of all the work done on hydraulic jump prior to 1967 can be found in Rajaratnam(1967). Most of the earliest investigations have been experimental with the aim of finding the external characteristics of the jump such as length of the jump and the roller, surface profile of the jump and the sequent depth ratio h_2/h_1 of the jump.

The earliest numerical studies neglected the variations in the physical quantities along the vertical (and cross-sectional) direction and assumed the pressure to be hydrostatic. This results in one dimensional St. Venant equations and the shear stress at the bed was modeled using uniform flow relations such as Manning's or Chezy's equation (Lai 1986). Basco (1983) has developed one dimensional open channel flow equations which take into account the non-hydrostatic effects of pressure and these are called the Boussinesq equations. Most of the numerical study of open channel flows has been to solve these one dimensional St. Venant equations or Boussinesq equations (Lai 1986; Basco 1983). The method of characteristics, the Finite Difference Method and the Finite Element Method have been used in the solution of these one-dimensional equations. The hydraulic jump is modeled as a
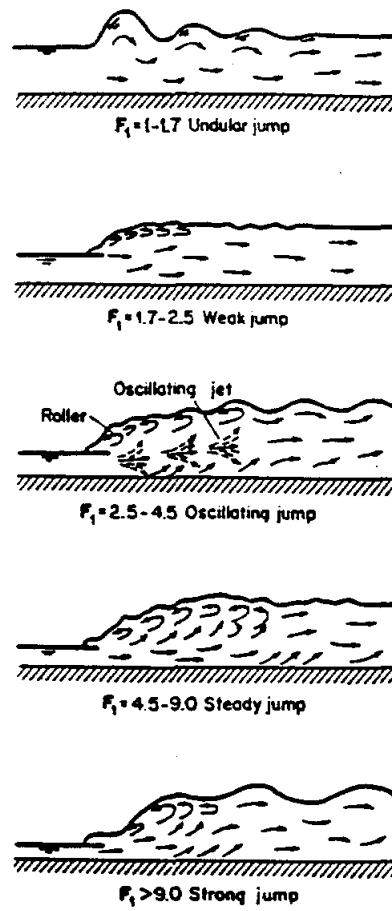
Figure 8.2: Various types of hydraulic jump (adapted from Chow (1959))

discontinuity and the surrounding fluid flow is computed using the one-dimensional equations. These one-dimensional equations however, do not describe the internal characteristics of the hydraulic jump and depend for their accuracy on the empirical relations employed to model the bed friction. A some what more accurate one-dimensional model based on the depth-averaged flow and $k - \epsilon$ turbulence equations and hydrostatic pressure has been developed by Madsen and Svendsen (1983) for the study of hydraulic jump.

For a description of the internal flow field and the turbulence characteristics of the hydraulic jump, the two-dimensional or three-dimensional Navier- Stokes equations without any depth averaging will need to be solved. Two- dimensional modeling of hydraulic jump is however computationally very intensive and only recently with the increased computing power it is becoming feasible. Rahman (1991) solved the steady two- dimensional flow equations to simulate a hydraulic jump. Finite- differences in curvilinear boundary-fitted coordinate system was used and the free surface was determined iteratively by minimizing the error in pressure at the free surface. Lemos (1992a,b) solved the unsteady flow equations and updated the free surface in time using the Volume-Of-Fluid (VOF) method. Both of them modeled turbulence using the $k - \epsilon$ closure equations.

8.3 Problem Definition

A typical 2-D hydraulic jump flow configuration is shown in Fig.8.3. The flow is bounded below by a non-erodible plane wall and at the top by a moving free surface whose height from the bed is taken to be $h(x,t)$. $x = 0$ is the inlet cross-section and is designated as station 1. $x = L$ is the exit cross-section and is designated as station 2. section $1'$ corresponds to the cross-section just upstream of the jump when the
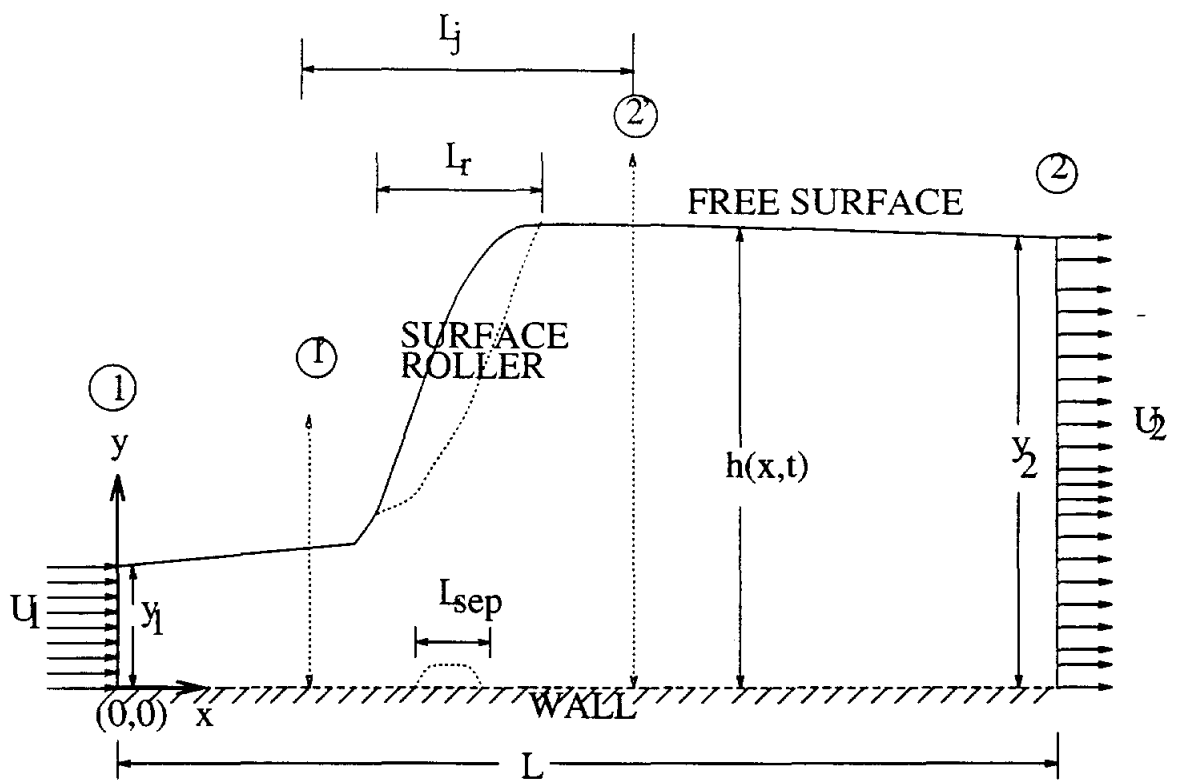
Figure 8.3: Typical Geometry for a hydraulic jump

free surface begins to rise abruptly and section 2' corresponds to the cross-section just downstream of the hydraulic jump. The subscripts 1,1',2 and 2' refer to the cross-section at which the quantity in question is evaluated.

The governing equations for the fluid flow are the Reynolds Averaged Navier–Stokes (RANS) equations and the continuity equation.

$$u_{,x} + v_{,y} = 0 \tag{8.4}$$

$$u_{,t} + uu_{,x} + vu_{,y} = -gh_{,x} - \frac{1}{\rho}\tilde{p}_{,x} + (\nu + \nu_T)\nabla^2 u \tag{8.5}$$

$$v_{,t} + uv_{,x} + vv_{,y} = -\frac{1}{\rho}\tilde{p}_{,y} + (\nu + \nu_T)\nabla^2\nabla v \tag{8.6}$$

u and v are the velocities in x and y directions respectively. t is the time and $\bar{\nu}$ is the laminar viscosity. ν_T is the kinematic eddy viscosity and is determined using the $k - \epsilon$ model described in chapter 4. $\tilde{p}$ is the non-hydrostatic pressure and is related to the pressure p as follows:

$$p = \rho g[h(x) - y] + \tilde{p} \tag{8.7}$$

The boundary conditions at the wall are the usual no-slip, impermeability conditions:

$$\left.\begin{array}{rcl} u &=& 0 \\ v &=& 0 \end{array}\right\} \quad \text{at} \quad y = 0. \tag{8.8}$$

Since, the turbulence model used is only valid in the fully turbulent outer layer, the wall function approach is used to impose the boundary conditions at the wall and these are described in chapter 4.

At the free surface we have the stress-continuity conditions and the kinematic free surface condition. Assuming the datum atmospheric pressure to be zero, and

neglecting the viscous stresses at the free surface. since in general they are small compared to the inertial forces. we have the following simplified boundary conditions at the free surface:

$$\left. \begin{array}{rcl} \tilde{p} & = & 0 \\ \dfrac{\partial u}{\partial n} & = & 0 \\ \dfrac{\partial v}{\partial n} & = & 0 \\ \dfrac{\partial h}{\partial t} + u\dfrac{\partial h}{\partial x} & = & v \end{array} \right\} \quad \text{at} \quad y = h(x,t). \tag{8.9}$$

The first condition is imposed in the pressure Poisson equation, and the next two are imposed in the solution of the momentum equations. The last condition is used to update the free surface location.

The boundary condition for u at the inlet depends on the state of the flow entering the fluid domain. If the flow at the inlet is assumed to be undeveloped then the boundary conditions for velocity at the inlet is given by:

$$\left. \begin{array}{rcl} u & = & U_1 \\ v & = & 0 \end{array} \right\} \quad \text{at} \quad x = 0. \tag{8.10}$$

On the other hand if the flow at the inlet is assumed to be fully developed then velocity field satisfying the logarithmic law is to be specified at the inlet.

$$\left. \begin{array}{rcl} u & = & \dfrac{u_*}{\kappa} ln\, E\dfrac{yu_*}{\nu} \\ v & = & 0 \end{array} \right\} \quad \text{at} \quad x = 0. \tag{8.11}$$

$u_* = \sqrt{\tau_w/\rho}$ is the shear velocity, τ_w is the shear stress at the wall, E is a constant dependent on the roughness of the wall and κ is the von Karman constant taken to be equal to 0.4. In a very long fluid column, if the hydraulic jump occurs very close the inlet, then the fluid flow is most probably in an undeveloped state. Thus, the

fluid flow entering the fluid domain is assumed to be potential flow, and without turbulence. If the hydraulic jump occurs far downstream from the inlet, there is sufficient time for the flow to come to equilibrium, and the fluid flow just upstream of the hydraulic jump is a fully developed turbulent flow.

At the exit a fully developed velocity profile boundary condition is imposed.

$$\left.\begin{array}{l} \dfrac{\partial u}{\partial x} = 0 \\ \dfrac{\partial v}{\partial x} = 0 \end{array}\right\} \quad \text{at} \quad x = L. \tag{8.12}$$

The finite element mesh used was 401×41 is the case of inlet supercritical Froude number $F_1 = 2.0$, whereas a numerical mesh of 801×11 was used for $F_1 = 4.0$. In the case of $F_1 = 2.0$, uniform mesh spacing was used. However, in the case of $F_1 = 4.0$ the following mesh spacing was used in the x direction:

$$\Delta x = \left\{\begin{array}{lll} \dfrac{L}{3}\dfrac{1}{200} & \text{for} & 0 \le x \le \dfrac{L}{3} \\[2mm] \dfrac{L}{3}\dfrac{1}{400} & \text{for} & \dfrac{L}{3} \le x \le \dfrac{2L}{3} \\[2mm] \dfrac{L}{3}\dfrac{1}{200} & \text{for} & \dfrac{2L}{3} \le x \le L \end{array}\right. \tag{8.13}$$

This type of a mesh spacing is used for $F_1 = 4.0$ to obtain fine mesh spacing in the jump region. A typical finite element mesh is shown in Fig.8.4. Note that, the mesh shown is only for part of the physical domain.

8.4 Results and Discussion

Let y_1 and y_2 be the flow depths upstream and downstream of the hydraulic jump respectively and U_1 the mean horizontal velocity of flow at the inlet. A hydraulic jump on a straight 2-D horizontal channel is influenced by the following parameters:

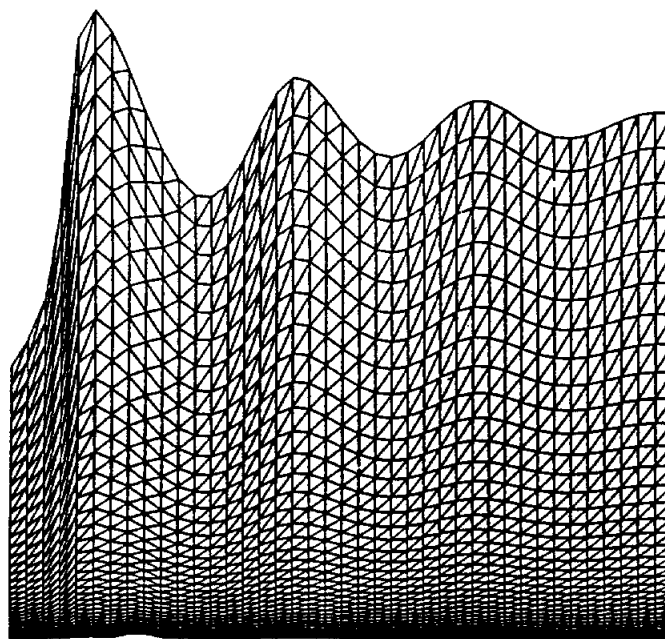1. Inlet Reynolds number $Re_1 = U_1 y_1 / \nu$.

Figure 8.4: Finite Element Mesh for part of the domain

2. Inlet Froude number $F_1 = U_1/\sqrt{gy_1}$.

3. Wall roughness height k_s.

4. Type of flow at the inlet; whether fully developed (FD) or undeveloped (UD).

The governing equations have been solved in a non-dimensional form with the inlet flow height y_1 and inlet mean velocity U_1 used as reference length and reference velocity respectively. We simulated the hydraulic jump with four different inlet conditions which are listed in Table 8.1.

For all our simulations inlet Reynolds number $Re_1 = 1.0 \times 10^6$ and and the wall is hydraulically smooth ($k_s = 0.0$).

Mathematically, the jump will occur when y_1, y_2 and F_1 satisfy the *Belanger momentum equation* (Chow 1959):

$$\frac{y_2}{y_1} = \frac{\sqrt{8F_1^2 + 1} - 1}{2} \qquad (8.14)$$

In the numerical model the downstream subcritical flow height y_2 is determined from the above equation and is specified as an essential boundary condition in the solution of free surface kinematic equation. In nature however, hydraulic jump occurs when supercritical flow encounters an obstacle or sudden change of cross-section. It is being assumed that the properties of the hydraulic jump numerically simulated by

case	F_1	Re_1	k_s	inflow state	y_1	y_2	L
2(UD)	2	1.0×10^6	0.0	Undeveloped	1.0	2.37	237.0
2(FD)	2	1.0×10^6	0.0	Fully developed	1.0	2.37	237.0
4(UD)	4	1.0×10^6	0.0	Undeveloped	1.0	5.17	517.0
4(FD)	4	1.0×10^6	0.0	Fully developed	1.0	5.17	517.0

Table 8.1: List of simulation parameters

specifying the downstream subcritical flow height y_2 are nearly the same as the naturally occurring ones. The nature of the hydraulic jump is mostly dependent on the upstream supercritical flow conditions and the effect of the downstream boundary condition is mostly on the location of the hydraulic jump.

The flow after it enters the domain slows down due to friction at the wall and the free surface height rises. As shown in Fig.8.3, $1'$ is the cross-section just upstream of the jump and $2'$ is the cross-section just downstream of the jump. The flow heights and Froude numbers for sections $1'$ and $2'$ are listed in Table 8.4. For comparison with theoretical and experimental results we will need to use supercritical Froude number $F_{1'}$ and not inlet Froude number F_1.

The velocity vectors in the hydraulic jump region for the four different cases that have been simulated is shown in Fig.8.5. The plot is drawn to scale to draw attention to the vastly differing length scales in horizontal and vertical directions. The subsequent figures are not drawn to scale and we caution the reader not to be misled by what appears to be rapid changes in free surface height. The x and y coordinates of the four corner points are shown on all the plots so that it will be clear what part of the fluid domain we are looking at. Due to reasons already explained in the section on turbulence the first numerical grid point is not placed on the wall but is placed at a small distance away from the wall in such a way that it lies in the completely turbulent wall layer. Thus the bottom surface of all the plots do not correspond to the wall and a small layer of fluid close to the wall is not represented in our plots.

In Fig.8.6 the variation u/U_1, v/U_1 and and $\tilde{p}/\rho U_1^2$ for the complete flow domain, i.e. $0.0 \leq x \leq L$, is shown for the case $F_1 = 2(\mathbf{UD})$. According to Chow (1959) an undular jump is formed for $1.0 < F_1 < 1.7$ and a weak jump is formed for $1.7 <$

case	$x_{1'}$	$F_{1'}$	$F_{2'}$	$y_{1'}$	$y_{2'}$	$E_{1'}$	$E_{2'}$	$\frac{E_L}{E_{1'}}$	L_r/y_2	L_j/y_2	L_{sep}/y_2
2(UD)	100.2	1.78	0.53	1.07	2.36	2.79	2.71	0.028(0.056)	0.00	15	0.25
2(FD)	103.2	1.82	0.54	1.06	2.38	2.83	2.74	0.031(0.062)	0.25	15	0.25
4(UD)	245.5	3.27	0.37	1.13	5.52	7.27	5.52	0.240(0.296)	1.83	15	0.00
4(FD)	204.5	3.42	0.35	1.10	5.63	7.63	5.63	0.262(0.318)	2.33	15	0.00

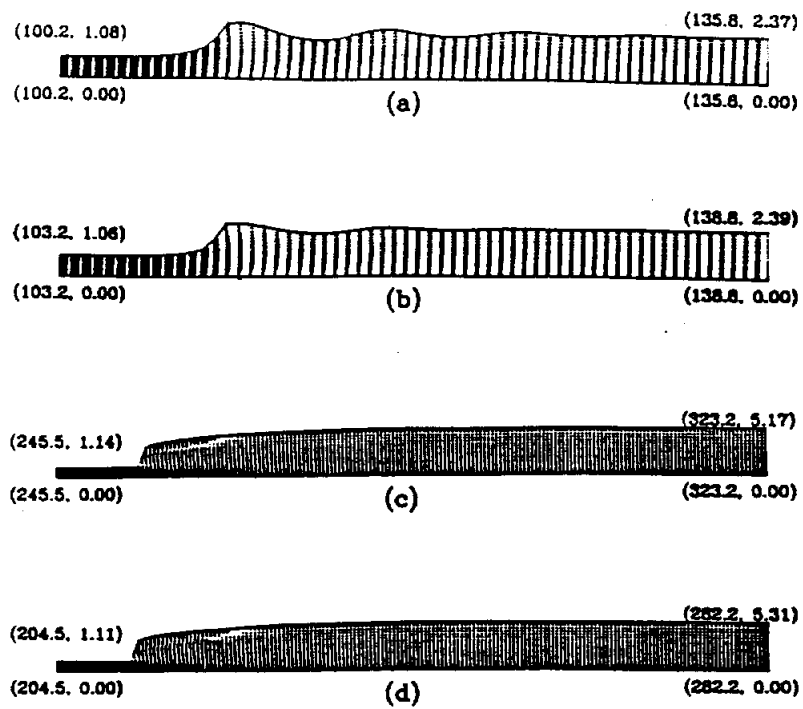Table 8.2: External characteristics of hydraulic jump

Figure 8.5: Velocity vectors in the hydraulic jump region: (a) $F_1 = 2(UD)$, (b) $F_1 = 2(FD)$, (c) $F_1 = 4(UD)$, (d) $F_1 = 4(FD)$.
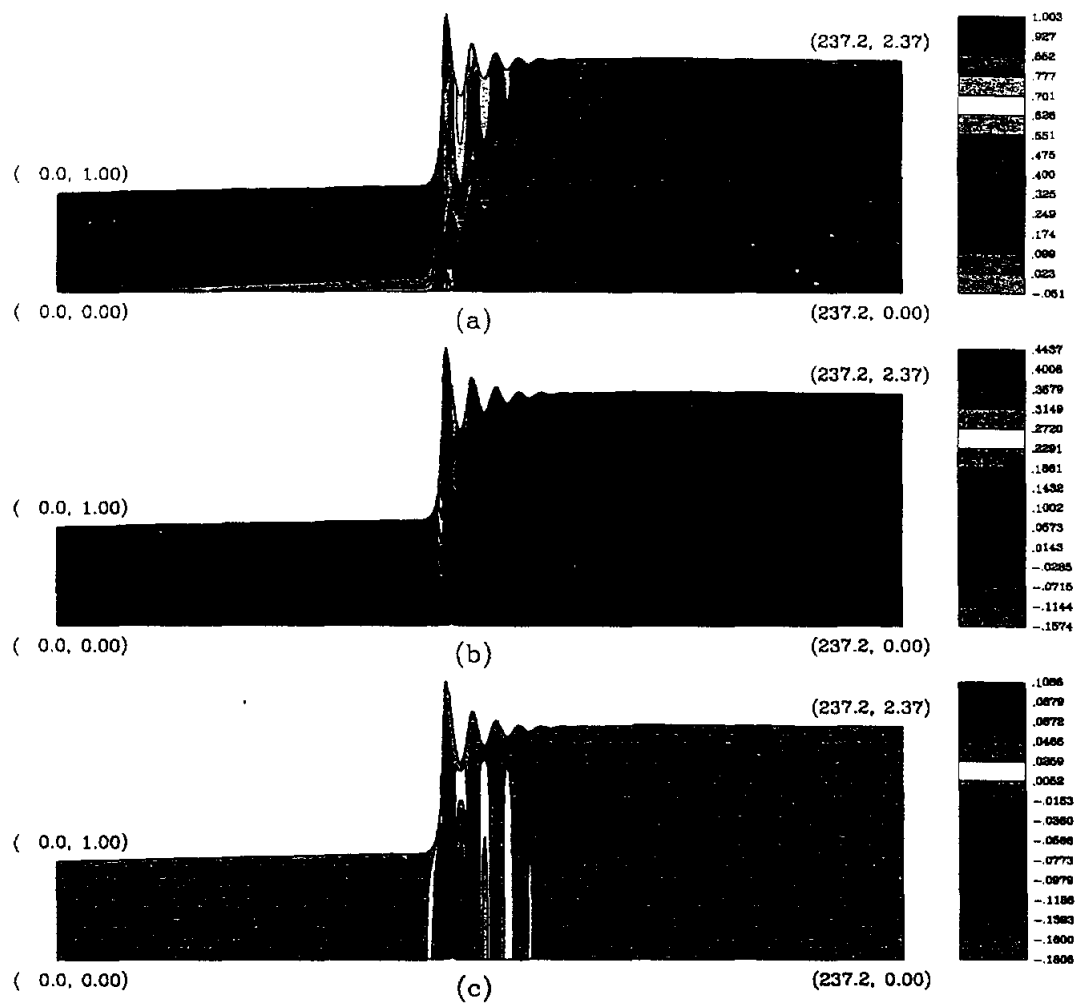
Figure 8.6: Mean flow field for $F_1 = 2(\mathbf{UD})$ (a)u/U_1; (b)v/U_1; and (c)$\tilde{p}/\rho U_1^2$.

$F_1 < 2.5$. In our case $F_{1'} = 1.78$ and the jump appears to exhibit characteristics of both undular jump and weak jump. The free surface in the jump region is wavy and the flow downstream of the jump is smooth and steady. The vertical velocity v and non-hydrostatic pressure correction $\tilde{p}$ are significant only in the jump region.

To get a better understanding of the nature of flow in the jump, u/U_1, v/U_1 and $\tilde{p}/\rho U_1^2$ are plotted for the jump region only, i.e. $x_{1'} \leq x \leq x_{2'}$, in Fig.8.7 for $F_1 = 2(\mathbf{UD})$. A small recirculation region exists under the jump. Boundary layer separation in hydraulic jumps has been suspected for long and Leutheusser & Alemu (1979) presented experimental evidence confirming the presence of flow separation under hydraulic jump. Even though the flow appears to be be slowing down and stagnating near the free surface, there is no surface roller i.e, there is no backward flow on the free surface. Departure of pressure from the hydrostatic value is quite large with $\tilde{p}/\rho U_1^2$ being as high as 0.18.

The variation $\frac{k}{\rho U_1^2}$, $\frac{\epsilon}{\rho U_1^3/y_1}$ and $\frac{\nu_T}{U_1 y_1}$ is shown in Fig.8.8 for $F_1 = 2(\mathbf{UD})$. The maximum value of turbulent kinetic energy k is only 1.2% of the inlet kinetic energy and occurs near the separation zone. The dissipation rate of turbulence kinetic energy ϵ takes very large values near the wall. In fact the boundary condition for ϵ at the wall was $\epsilon_P = \frac{u_\tau^3}{\kappa y_P (1.0 - e^{-y_P^+/26})}$. In the rest of the flow domain ϵ is not as high as it is at the wall and hence the linear plot shows an essentially constant field for ϵ. The region of maximum turbulence kinetic energy and maximum turbulent viscosity are not the same. Maximum turbulence kinetic energy occurs further downstream of the maximum turbulence kinetic energy cross-section. This is due to the important role played by convection which transports k downstream.

The production(G), dissipation(ϵ) and convection of turbulent kinetic energy for $F_1 = 2(\mathbf{UD})$ are plotted in Fig.8.9 for the flow domain obtained after eliminating
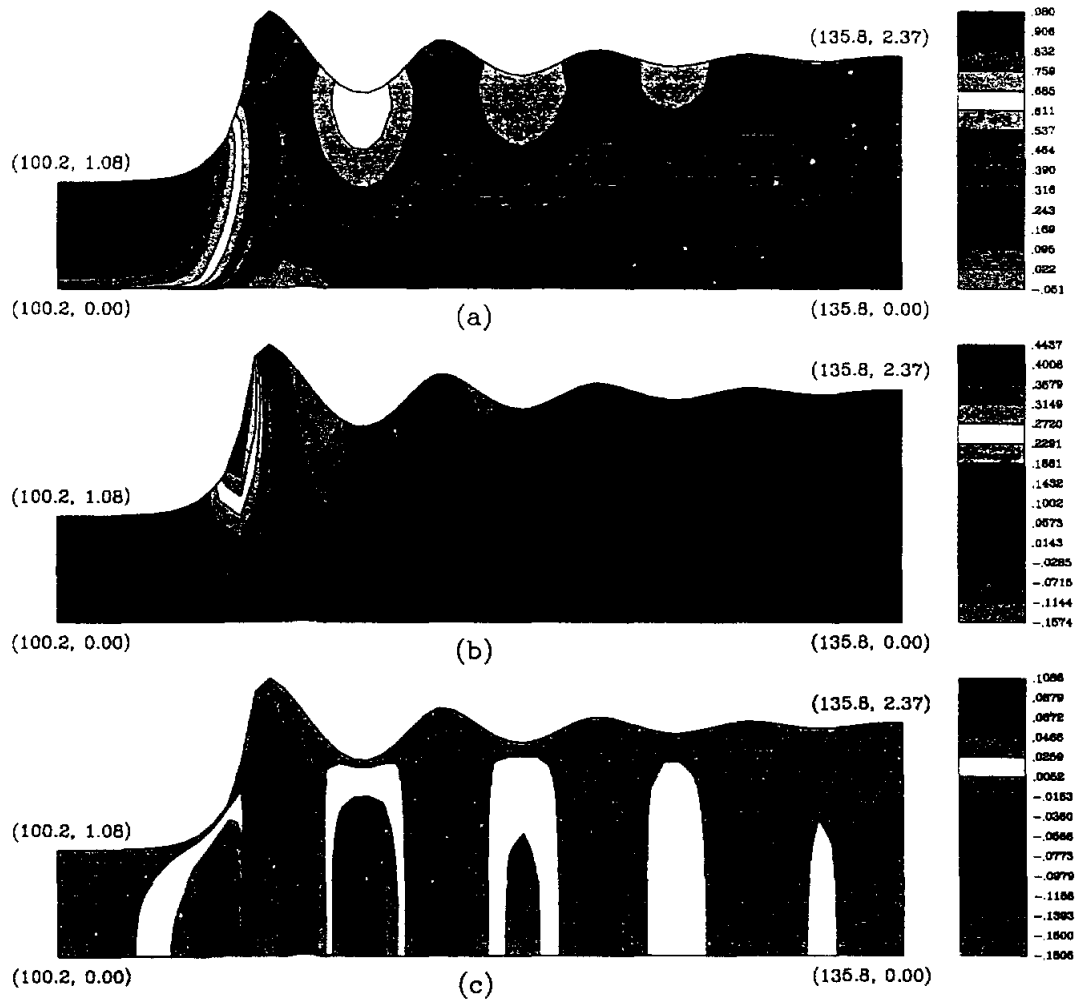
Figure 8.7: Mean flow field for $F_1 = 2(\mathbf{UD})$ (a)u/U_1; (b)v/U_1; and (c)$\tilde{p}/\rho U_1^2$.
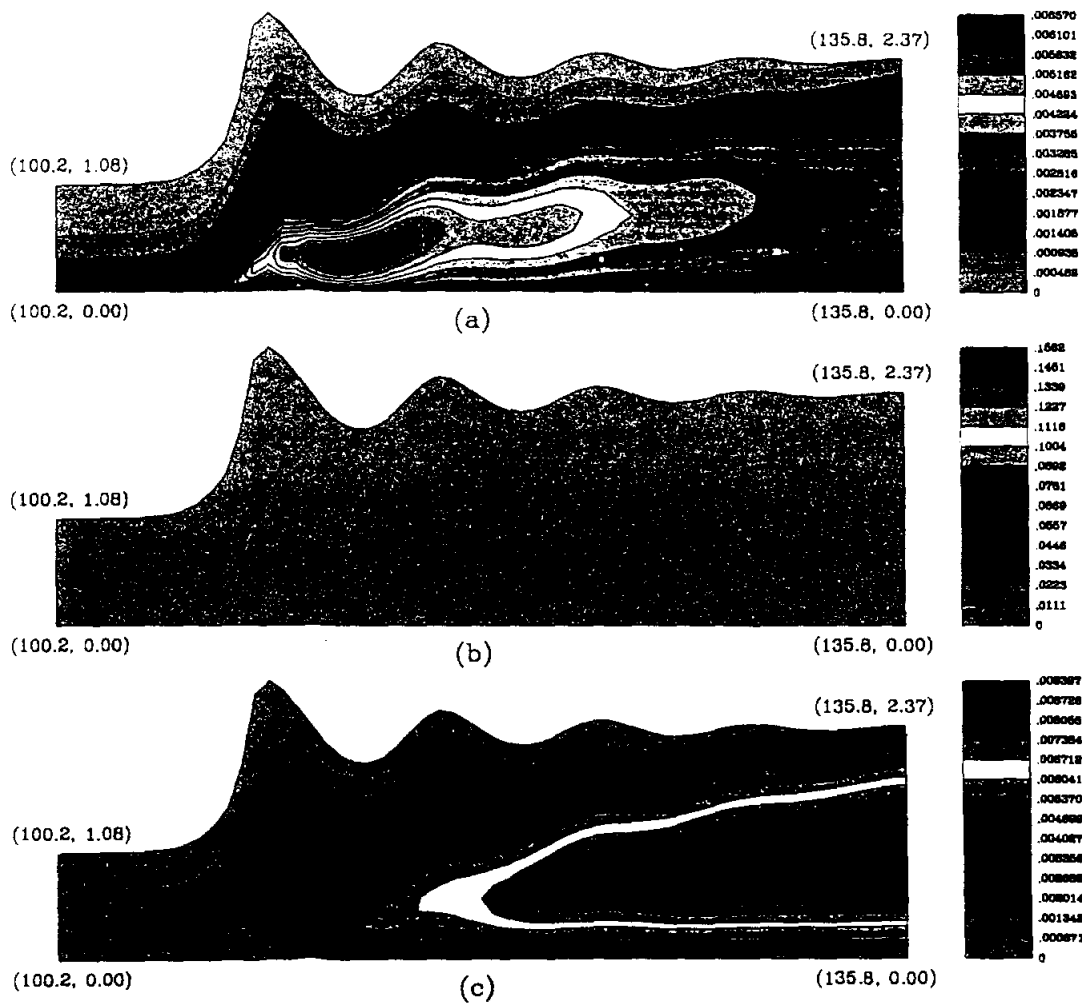
Figure 8.8: Turbulence characteristics for $F_1 = 2(\text{UD})$ (a) k; (b) ϵ; and (c)ν_T.

a small layer of fluid near the wall (4 finite element cells) where production and dissipation of turbulence kinetic energy is very high. This makes it possible to study the variation of G and ϵ in the rest of the flow domain. Production and dissipation are both large in the separated flow region. The difference between production and dissipation equals convection. Convection of turbulent kinetic energy is quite significant in some regions of the flow. It is as large as ϵ itself in some areas. The zero equation turbulence models like Prandtl's mixing length models assume that that production and dissipation are in balance every where and neglect transport of turbulent kinetic energy. But in separation flows convection of kinetic energy is quite significant and justifies our use of higher order turbulence model.

The variation of u/U_1, v/U_1 and $\tilde{p}/\rho U_1^2$ when the flow at the inlet is fully developed and the $F_1 = 2$ (designated as **2(FD)**)is shown in Fig.8.10. The jump is less undular compared to the case when the inflow was undeveloped. This could be due to higher supercritical Froude number $F_{1'} = 1.82$ compared to the previous case. The biggest difference from the previous case $(F_1 = \mathbf{2(UD)})$ is the presence of a surface roller.

In Fig.8.11 the variation of turbulence parameters $\frac{k}{\rho U_1^2}$, $\frac{\epsilon}{\rho U_1^3/y_1}$ and $\frac{\nu_T}{U_1 y_1}$ is shown for $F_1 = \mathbf{2(FD)}$. The maximum turbulence kinetic energy k is about 5.0% of the inlet kinetic energy and occurs in the surface roller region. The higher values of k and ν_T compared to the previous case when inflow was undeveloped is solely due to the presence of surface roller. Surface roller from our simulations appears to be the most important turbulence generating mechanism and is consistent with the findings of Rouse, Siao & Nagaratnam (1958).

The production, dissipation and convection of turbulent kinetic energy are shown in Fig.8.12 for $F_1 = \mathbf{2(FD)}$. As in the previous turbulence budget plot a very small
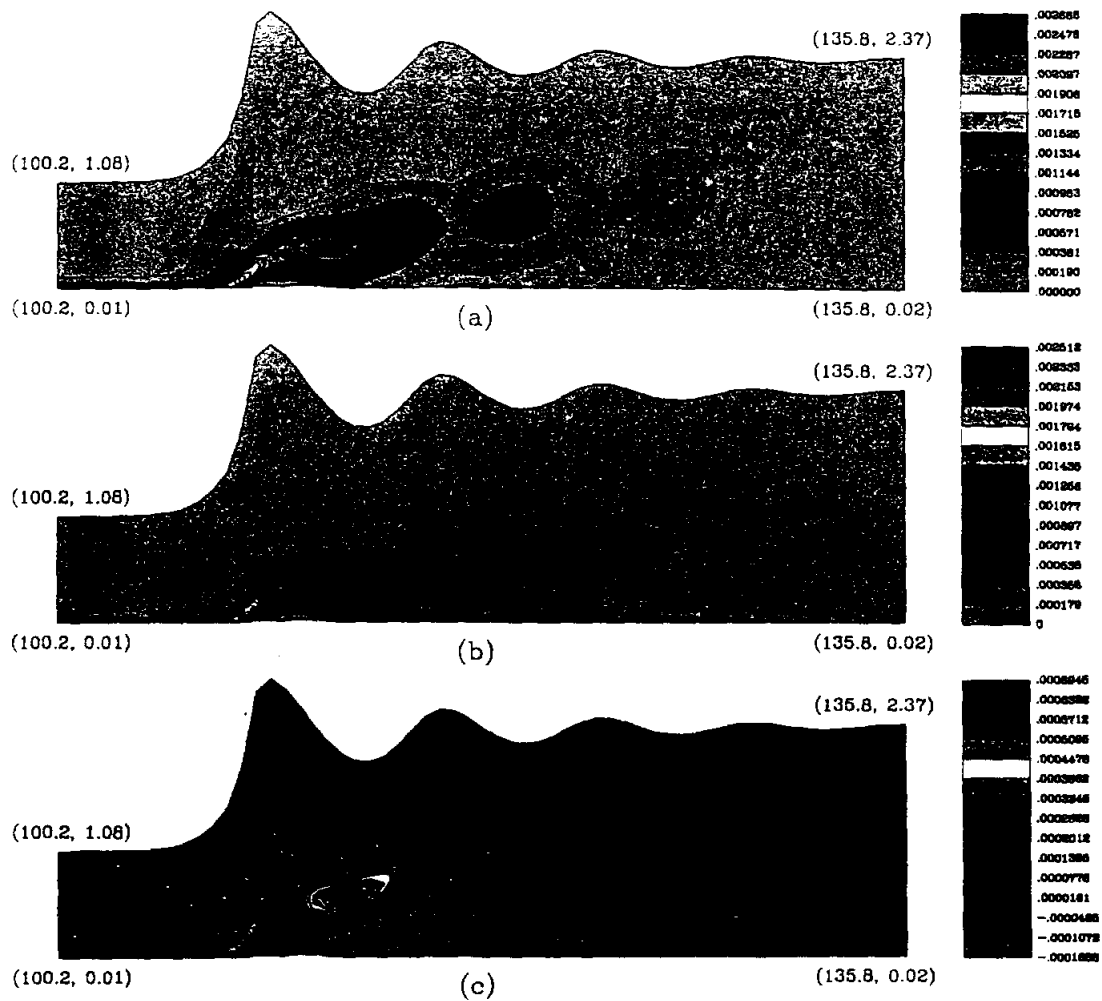
Figure 8.9: Turbulence kinetic energy budget for $F_1 = 2(\text{UD})$ (a) production ; (b) dissipation; and (c)convection.

Figure 8.10: Mean flow for $F_1 = 2$(FD) (a)u/U_1; (b)v/U_1 vertical velocity; and (c)$\tilde{p}/\rho U_1^2$.

Figure 8.11: Turbulence characteristics for $F_1 = 2(\mathbf{FD})$ (a) k; (b) ϵ; and (c)ν_T.
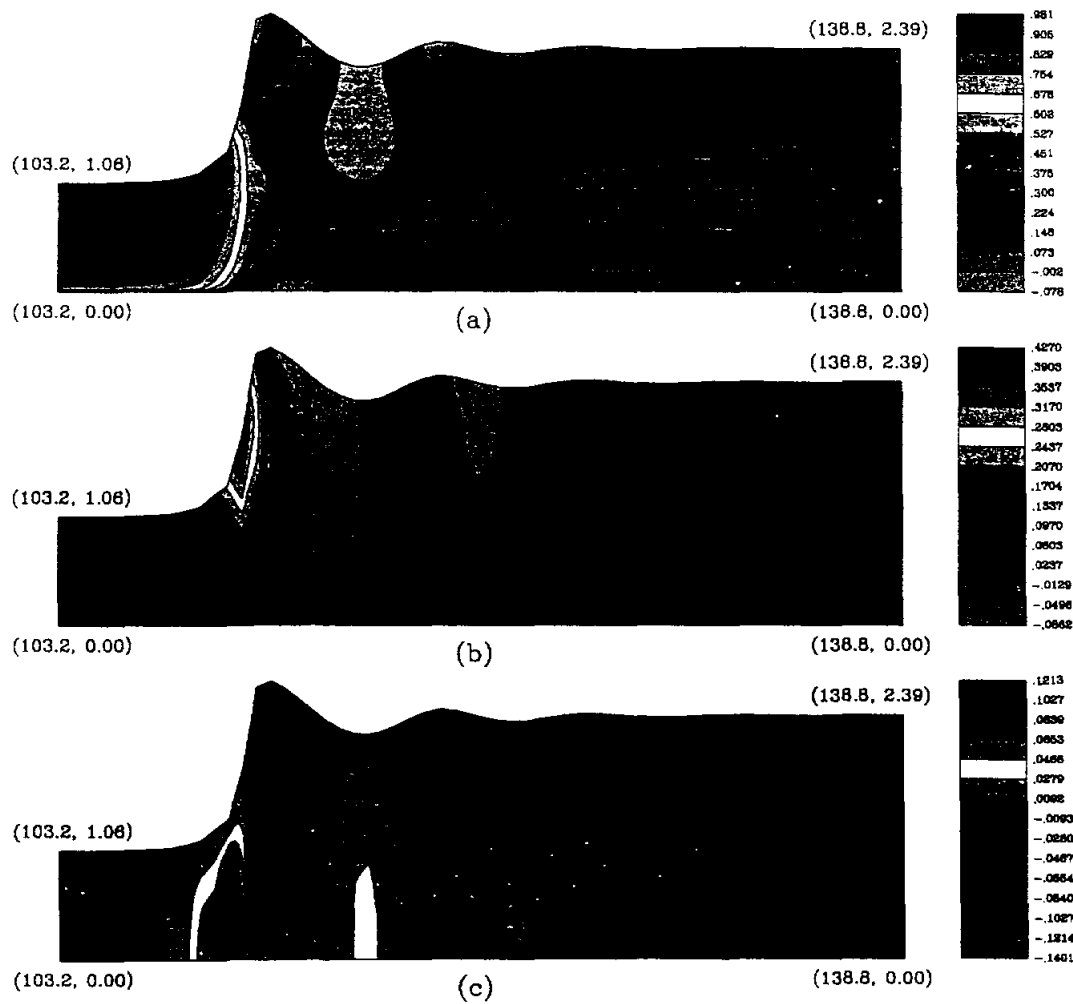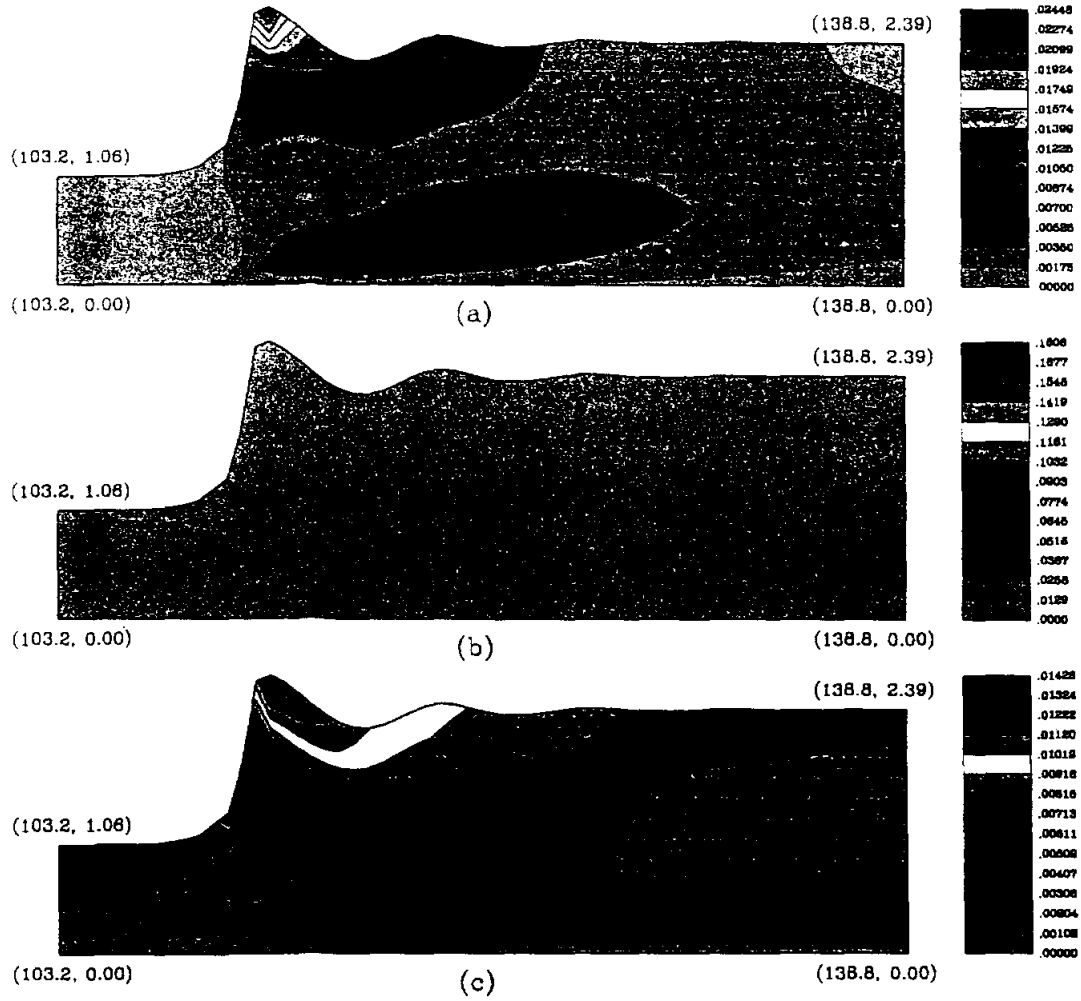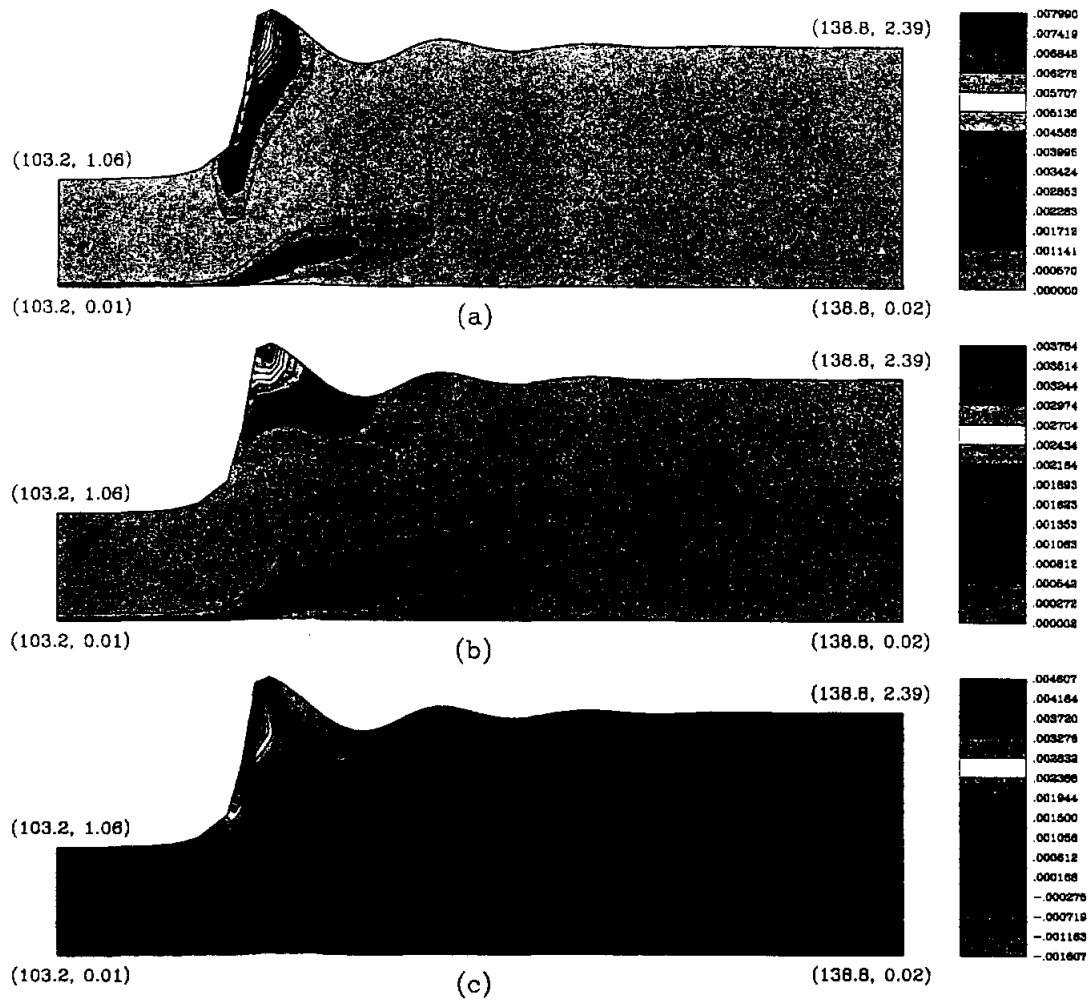
Figure 8.12: Turbulence kinetic energy budget for $F_1 = 2(\text{FD})$ (a) production ; (b) dissipation; and (c)convection.

layer (4 finite element cells) near the wall is not represented in this plot. The production(G) and dissipation(ϵ) of turbulent kinetic energy are very large in the surface roller region. Dissipation is only half of production in the surface roller region and the rest of the produced kinetic energy is convected away by the mean flow and once again justifies the use of $k - \epsilon$ closure model.

For the cases $F_1 = 2(\mathbf{UD})$ and $F_1 = 2(\mathbf{FD})$ it was possible to obtain steady state solutions. The code took around 4000 time steps to reach steady state. For $F_1 = 4$ however it was not possible to obtain steady state solution. The code did not converge to steady state even after $10,000$ time steps. Chow (1959) classifies hydraulic jumps with $2.5 < F_1 < 4.5$ as oscillating jump. We are not certain if our inability to achieve steady state solutions for $F_1 = 4.0$ is due to the physical nature of the oscillating jump. Thus the results presented by us for $F_1 = 4(\mathbf{UD})$ and $F_1 = 4(\mathbf{FD})$ are not steady state solutions but solutions obtained after simulating the jump for long times (after about 10,000 time steps and $2200 y_1/U_1$ time units).

For $F_1 = 4(\mathbf{UD})$ and $F_1 = 4(\mathbf{FD})$ no separation of boundary layer was observed. The jump did not exhibit undular behavior and a strong surface roller was found to occur. In Fig.8.13 u/U_1, $\frac{k}{\rho U_1^2}$ and $\nu_T/U_1 y_1$ are shown for $F_1 = 4(\mathbf{UD})$. Just as in the previous cases the k has large values in the roller region whereas ν_T achieves maximum values downstream of the roller. Based on Leutheusser & Alemu (1979)'s experiments we would expect a larger separation zone for $F_1 = 4$. Leutheusser & Alemu (1979) found the length of recirculation to increase with increasing F_1 and decrease with increasing inlet Reynolds number Re_1. The reasons for the absence of recirculation zone for $F_1 = 4$ are not clear. For $F_1 = 4(\mathbf{FD})$ the maximum values of k and ν_T were found to be higher than for $F_1 = 4(\mathbf{UD})$. The rest of the qualitative behavior is the same.
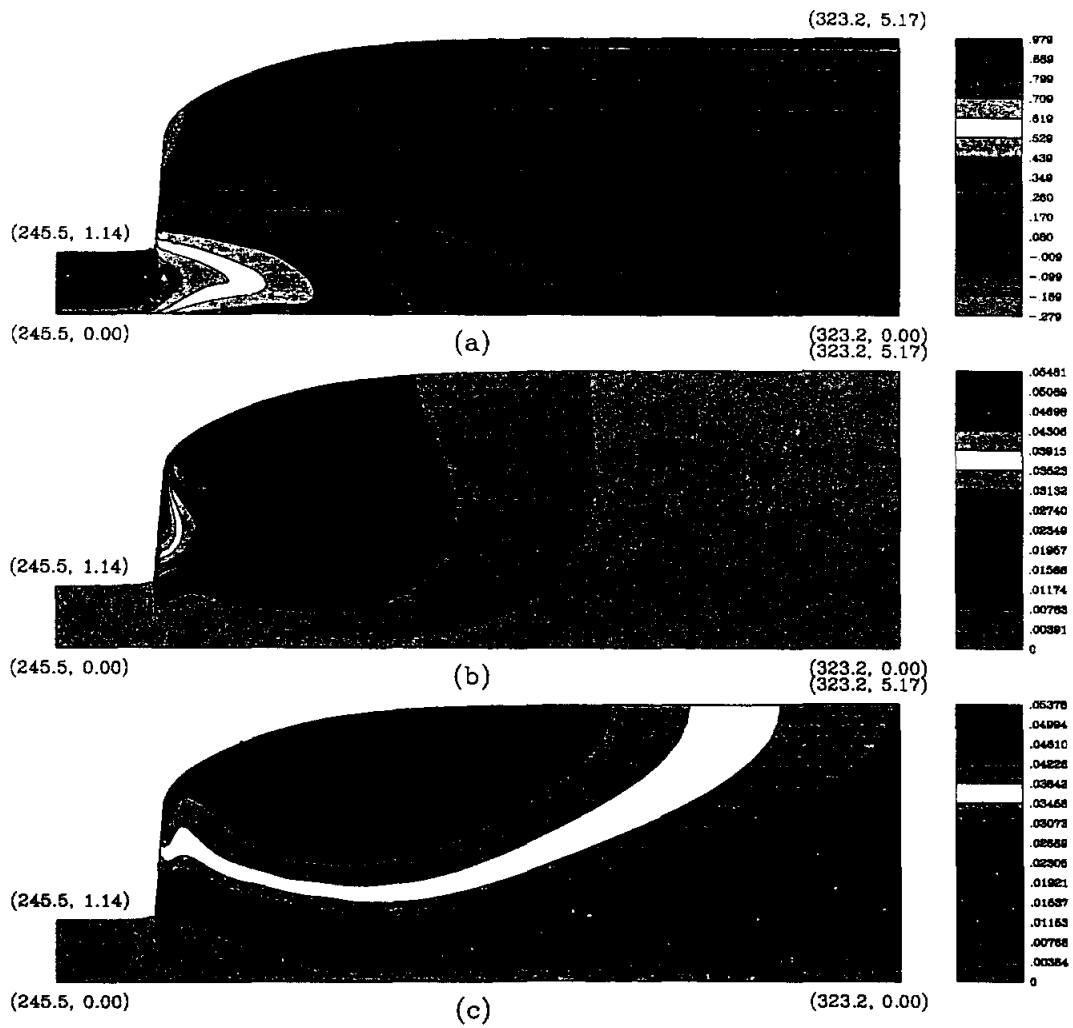
Figure 8.13: Mean flow and turbulence characteristics for $F_1 = 4(\mathbf{UD})$ (a) u/U_1; (b) $k/\rho U_1^2$; and (c)$\nu_T/U_1 y_1$.

The various parameters such as length of the roller L_r, length of the recirculation zone L_{sep} and specific energy loss across the jump $E_L/E_{1'}$ for all the four cases we simulated are listed in Table 8.4. The length of the hydraulic jump L_j is defined to be the horizontal distance from the toe of the jump to a point downstream where the influence of the jump has become negligible and flow conditions are determined by the characteristics of the channel alone. This definition for L_j has been proposed by Leutheusser & Alemu (1979) and found the length of the jump to be approximately 12 to 15 times the downstream subcritical flow height y_2. Determination of the cross-section downstream where the influence of the jump is negligible is not very easy and consequently we arbitrarily fixed the jump length to be $15y_2$. The actual jump length is lesser than $15y_2$.

The specific energy E at a cross-section is defined as follows

$$E = y + \frac{1}{2g} \int_0^y u^2 \, dy' \tag{8.15}$$

The loss of specific energy $E_L = E_{1'} - E_{2'}$ assuming uniform flow, hydrostatic pressure and negligible wall friction can be shown to be to be dependent on the supercritical Froude number as (Rajaratnam 1967)

$$\frac{E_L}{E_1'} = \frac{1}{8} \frac{(\sqrt{1 + 8F_{1'}^2} - 3)^3}{(2 + F_{1'}^2)(\sqrt{1 + 8F_{1'}^2} - 1)} \tag{8.16}$$

The values shown in the brackets for $E_L/E_{1'}$ in Table 8.4 are those obtained from Eq.8.16. The specific energy loss across a hydraulic jump is more if the flow at the inlet is fully developed and is consistent with Leutheusser & Alemu (1979)'s finding. Experimental measurements indicate that actual E_L is smaller than that predicted by Eq.8.16 for $F_1 < 2$ (Chow 1959). This explains the difference in $E_L/E_{1'}$ obtained by us and that given by Eq.8.16 for $F_1 = 2$.

The variation of skin friction coefficient $C_f = \tau_w / \frac{1}{2}\rho U_1^2$ is shown in Fig.8.14. The value of C_f upstream of the jump is approximately 0.0026 and decreases to about 0.0005 downstream of the jump. From experimental data, Rajaratnam (1967) found the C_f to decrease from about 0.0037 at the beginning of the jump to about 0.0001 near the end of the jump for the whole range of Froude numbers from 3.20 to 9.78. The values for C_f obtained by us are lower than those presented by Rajaratnam. This could be due to the assumption of hydraulically smooth wall by us.

8.5 Concluding remarks

A numerical model capable of simulating two-dimensional open-channel flows without any depth averaging has been developed. The *a priori* unknown air-water interface is handled through a mixed Lagrangian–Eulerian procedure called the ALE formulation which handles fairly large free surface deformation without appreciable mesh distortion. The turbulence is modeled using a two equation $k - \epsilon$ model which gives us the ability to simulate complex flows involving boundary layer separation.

A very interesting but difficult problem in open-channel flows, namely, the hydraulic jump has been simulated using the numerical model developed in this work. The free surface rises abruptly across the jump region and intense turbulent mixing is known to occur in this region. Successful simulation of this very difficult problem shows that the numerical procedure developed in this work is robust, and can handle high gradient regions.

In the case of hydraulic jump with inlet supercritical Froude number $F_1 = 2.0$, small recirculation zone was found to exist at the bed in the jump region. Due to the abrupt rise in the free surface, the flow tends to slow down near the free surface, with the formation of a surface roller. The recirculation zone near the bed and
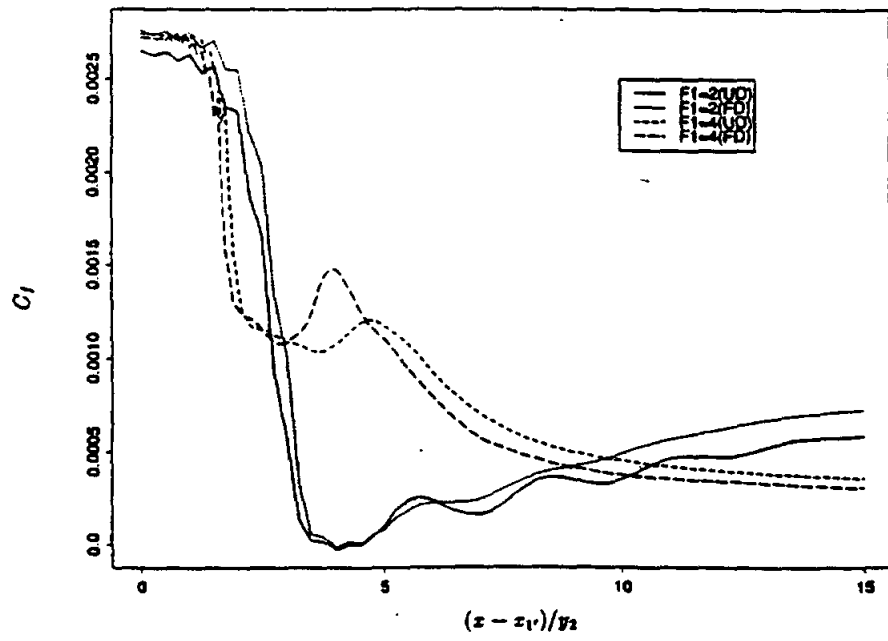
Figure 8.14: Variation of skin friction coefficient C_f along the jump

the surface roller at the free surface influence the turbulence field significantly and dominate the wall generated turbulence. Significant departure of the pressure field from the hydrostatic pressure is observed in the jump region, showing the necessity for a full-scale numerical model without depth averaging in the simulation of rapidly varying flows such as hydraulic jumps and bores.

For hydraulic jumps with higher supercritical inlet Froude numbers, breaking of the free surface is known to occur with the entrainment of air into the water phase. Thus, the fluid flow is no longer a single-phase flow, rather it is a two-phase flow containing both air and water. Thus for successful simulation of high Froude number flows, two-phase flow models may have to used.

Chapter 9

General Conclusions

9.1 Conclusion

The following conclusions may be arrived at based on the work presented so far:

1. An accurate and efficient numerical procedure has been developed which can simulate many types of gravity-driven flows. The computational efficiency derives in part from the ALE procedure, which allows us to handle the large free surface deformations in a straight forward manner without any mesh entanglement. The computational efficiency is also in part due to the Chorin-type projection scheme which decouples the pressure field from the velocity field, thus allowing us to compute them sequentially. All the results presented in the thin-film flows and turbulent flows over bedforms, have been obtained using a SPARC-10 machine. Only the hydraulic jump results have been obtained on a CRAY-YMP. Quantitative comparisons with experiments in thin-film flows, establishes the accuracy of the numerical procedure. The comparisons in the case of turbulent flow simulations have been only qualitative, and some more rigorous validation may be required to establish the accuracy in the case of complex turbulent flows.

2. An extensive numerical study of the surface wave instability in isothermal thin-film flows has been done. Both spatially periodic and non-periodic domains have been considered. Extensive parametric revealed a phenomena in

the finite amplitude wave regimes, namely, the quasi-periodic wave evolutions. Even though, this type of a behaviour was alluded to previously, in the context of other simplified systems, no systematic study, such as done in this dissertation has been reported previously. Complex wave interactions such as wave-splitting and wave-mergers have been simulated. The wave interactions observed in our numerical simulations are in excellent qualitative agreement with the experimental observations of Liu & Gollub (1994). Evolution of a time-periodic disturbance in a a long non-periodic spatial domain has been simulated and are in excellent qualitative and quantitative agreement with the experiments of Liu & Gollub (1994). This is especially gratifying, since it establishes that the numerical code developed in this dissertation can be used to perform "computational experiments."

3. A numerical procedure capable of simulating turbulent fluid flows over artificial stream-wise periodic bedforms has been developed. In the context of turbulent flows over bedforms, the work presented in this dissertation is the first study which does not invoke the rigid-lid approximation, but computes the equilibrium free surface shape along with the mean and turbulence field. Thus, the numerical procedure can be used for studying high Froude number flows also. Our numerical simulations reveal the existence of very large shear stresses at the tip of the dune due to local accelerations associated with stream-line bending. This local acceleration is seen to be more when we make the rigid-lid approximation. The turbulence associated with separation wake is found to dominate the wall generated turbulence. Consequently, the maximum turbulence intensities occur at a distance approximately of the order of dune height away from the bed. The suspended sediment load downstream of

the dune peak is found to be significant, and needs to be taken into account in the bedform formation theories, at least in some cases.

4. The celebrated hydraulic jump problem in open-channel flows has been numerically simulated. The numerical simulation of hydraulic jump is very challenging due to the presence of very high spatial gradients in the jump region, and is in many respects similar to shock wave in compressible flows. In some cases a small recirculation zone is found to be present at the foot of the jump. The mixing layer turbulence associated with the recirculation zone and surface roller are found to dominate the wall generated turbulence.

9.2 Future Work

Some of the possible future research directions are listed below:

1. In reality, the fluid flows existing in nature are three-dimensional. The numerical code developed in this dissertation can be extended to three-dimensions in a straight forward manner. However, the limitations arise not from implementation, but from the excessive computational time and memory required for full-scale 3-D simulations.

2. In the thin-film flow study, it has been mentioned that the presence of surface waves on the interface is known in increase heat and mass transfer in both the liquid and gaseous phases. Thus extending the isothermal numerical procedure to include heat transfer would help us study this aspect quantitatively.

3. Another area which can be improved upon is the turbulence modeling. The $k - \epsilon$ model used in this work, appears to give reasonably good results without excessive computational cost. Other closure models that are supposedly more

accurate, are very expensive computational requirements wise. Thus, there exists a need to develop closure models that model the physics accurately without being very expensive computationally. The Large Eddy Simulation (LES) appears to be promising but lot more work needs to be done, before they could be used for solving real-life fluid flow problems.

Bibliography

[1] Alekseenko, S. V., Nakoryakov, V. Ye. and Pokusaev, B.G., "Wave formation on a vertical falling liquid film," *AIChE J.*, **31**, pp.1446-1460 (1985).

[2] Alfrink, B. J. and van Rijn, L. C., "Two- equation turbulence model for flow in trenches," J. Hydraulic Engg., **109**, pp.941-958 (1983).

[3] Amsden, A. A. and Hirt, C. W., "YAQUI: an arbitrary Lagrangian–Eulerian computer program for fluid at all speeds." *Los Alamos Scientific Laboratory Report*, **LA-5100** (1973).

[4] Anderson, D. A., Tannehill, J. C. and Pletcher, R. H., *Computational Fluid Mechanics and Heat Transfer*, p.247, McGraw-Hill Book Co., (1984).

[5] Anshus, B. E. and Goren, S. L., "A method of getting approximate solutions to the Orr–Sommerfeld equation for flow on a vertical wall," *AIChE J.*, **12**, pp.1004-1008 (1964).

[6] A.S.C.E. Task Force on Bed Forms in Alluvial Channels, 1966: "Nomenclature for bedforms in alluvial channels," *Proc. A.S.C.E. J. Hyd. Div.*, **92**, pp.51-64 (1966).

[7] ASCE Task Committee on Turbulence Models in Hydraulic Computations, "Turbulence Modeling of Surface Water Flow and Transport," *J. of Hyd. Engg.*, **114**, pp.970-1073, part:1-5, (1988).

[8] Atherton, R. W. and Homsy, G. M., "On the derivation of evolution equations for interfacial waves," *Chem. Engng Commun.*, bf 2, pp.57-77, (1976).

[9] Bach, P. and Villadsen, J., "Simulation of the vertical flow of a thin, wavy film using a finite element method," *Int. J. Heat Mass Transfer*, **27**, pp.815-827, (1984).

[10] Basco, D. R., "Introduction to the rapidly- varied unsteady free- surface flow computation," USGS, Water Resour. Invest. Report N. 83-4284, U.S. Geological Survey, Reston, Va. (1983).

[11] Behr, M. A., Franca, L. P. and Tezduyar, T. E., "Stabilized finite element methods for the velocity-pressure-stress formulation of incompressible flows," *University of Minnesota Supercomputer Institute Research Report*, UMSI 92/8, January (1992).

[12] Bèlanger, J. B., "Essai sur la solution numèrique de quelques problèmes relatifs au mouvement permanent des eaux courantes (Essay on the Numerical Solution of Some Problems Realtive to the Steady Flow of Water)," Carilian-Goeury, Paris, (1828).

[13] Bell, J. B., Colella, P. and Glaz, H. M., "A second-order projection method for the incompressible Navier–Stokes equations," *J. Comp. Phys.*, **85**, 257–283 (1989).

[14] Belytschko, T. B. & Flanagan, D. P., "Finite element methods with user-controlled meshes for fluid–structure interaction," *Comput. Meth. Appl. Mech. Eng.*, **33**, 669-688 (1982).

[15] Benim, A. C. and Zinser, W., "Investigation into the finite element analysis of confined turbulent flows using a $k - \epsilon$ model of turbulence," *Comput. Meth. Appl. Mech. Engg.*, **51** 507-523, (1985).

[16] Benjamin, T. B., "Wave formation in laminar flow down an inclined plane," *J. Fluid Mech.*, **2**, pp.554-574, (1957).

[17] Benney, D. J., "Long waves on liquid films," *J. Math. & Phys.*, **45**, pp.150-155, (1966).

[18] G. Bidone, "Expèriences sur le remous et la propagation des ondes (Experiments on backwater and the propagation of waves)," *Memorie della Reale Academia delle Scienze di Torino*, Turin, **25**, pp.21-112 (1820).

[19] Chan, R. K. -C., "A generalized arbitrary Lagrangian Eulerian method for incompressible flows with sharp interfaces," *J. Comp. Phys.*, **17**, pp.311-331 (1975).

[20] Chang, H. -C., Demekhin, E. A. and Kopelevich, D. I., "Nonlinear evolution of waves on a vertically falling film," *J. Fluid Mech.*, **250**, pp.433-480 (1993).

[21] Chang, H. -C., "Wave evolution on a falling film," *Ann. Rev. Fluid Mech.*, **26**, pp.103-136 (1994).

[22] Cheng, M. and Chang, H. -C., "Competition between subharmonic and sideband secondary instabilities," *Phys. Fluids*, **7**, pp.34-54 (1995).

[23] Chin, R. W., Abernathy, F. F. and Bertschy, J. R., "Gravity and shear wave stability of free surface flows. Part 1. Numerical calculations," *J. Fluid Mech.*, **168**, pp.501-513 (1986).

[24] Chorin, A. J., "A Numerical Method for Solving Viscous Incompressible Flow Problems," *J. Comput. Phys.*, **2**, pp.12-26, (1967).

[25] Chippada, S., Ramaswamy, B. and Wheeler, M. F., "Numerical simulation of hydraulic jump," *Int. J. Num. Meth. Engg.*, **37**, pp.1381-1397 (1994).

[26] Chippada, S., Ramaswamy, B. and Joo, S. W., "A full-scale numerical study of interfacial instabilities in thin film flows," *to be submitted to J. Fluid Mech.* (1995).

[27] Chow, V. T., *Open-Channel Hydraulics*, McGraw Hill Book Co., (1959).

[28] Churchill, S. W., "Viscous Flows: The Practical Use of Theory," *Buuterworth Series in Chemical Engineering*, (1988).

[29] Donea, J., Giuliani, S. and Halleux, J. P., " An arbitrary Lagrangian Eulerian finite element method for transient dynamic fluid–structure interactions," *Comp. Meth. Appl. Mech. Eng.*, **33**, 689-723 (1982).

[30] Donea, J., Giuliani, S. and Laval, H., "Finite element solution of the unsteady Navier–Stokes equations by fractional step method," *Comp. Meth. Appl. Mech. Eng.*, **30**, 53–73 (1982).

[31] Donea, J., "Arbitrary Lagrangian Eulerian finite element methods," in *Computational Methods for Transient Analysis* (ed. Belytschko, T. B. & Hughes, T. J. R.), 474-516 (1983).

[32] Dressler, R. F., "Mathematical solution of the problem of roll-waves in inclined open channels," *Commun. Pure Appl. Math.*, **2**, pp.149-194 (1949).

[33] Dukler, A. E., "Characterization, effects and modeling of the wavy gas-liquid interface," In *Progress in Heat and Mass Transfer* (ed. G.Hetstroni, S.sideman & J.P. Hartnet), 6, pp.207-234, Pergamon, (1972).

[34] Dukowicz, J. K. and Ramshaw, J. D., "Tensor viscosity method for convection in numerical fluid dynamics," *J. Comput. Physics*, **32**, pp.71-79, (1979).

[35] Engelund, F,. "Instability of erodible beds," *J. Fluid Mech.*, **42**, pp.225-244 (1970).

[36] Finlayson, B. A., *Numerical methods for problems with moving fronts*, Ravenna Park Publishing Inc., Seattle, Washington, USA, 434–456 (1992).

[37] Floryan, J. M. and Rasmussen, H., "Numerical methods for viscous flows with moving boundaries," *Appl Mech Rev*, **42**, pp.323-341, (1989).

[38] Fredsoe, J., "On the development of dunes in erodible channels," *J. Fluid Mech.*, **64**, pp.1-16 (1974).

[39] Fulford, G. D., "The Flow of Liquids in Thin Films," *Adv. in Chemical Engg.*, **5**, Academic Press, N.Y., (1964).

[40] Gjevik, B., "Occurrence of finite-amplitude surface waves on flalling liquid films," *Phys. Fluids*, **13**, pp.1918-1925 (1970).

[41] Glowinski, R., "Splitting methods for the numerical solution of the incompressible Navier–Stokes equations," in *Vistas in Applied Mathematics, Optimization and Software* (ed. Balakrishna, A. V., etal), 57–95 (1986).

[42] Gresho, P. M., "On the theory of semi-implicit projection methods for viscous incompressible flow and its implementation via a finite element method that

also introduces a nearly consistent mass matrix. Part 1: Theory," *Int. J. Num. Meth. Fluids*, **11**, pp.587-620, (1990).

[43] Gresho, P. M. and Chan, S. T., "On the theory of semi-implicit projection methods for viscous incompressible flow and its implementation via a finite element method that also introduces a nearly–consistent mass matrix Part 2: Implementation," *Int. J. Num. Meth. Fluids*, **11**, 621–660 (1990).

[44] Gresho, P. M., Chan, S. T., Christon, M. A. and Hindmarsh, A. C., "A little more on stabilized Q_1Q_1 for transient viscous incompressible flow." in *Proceedings of the International Conference on Monsoon Validity and Prediction*, Trieste, Italy (1994).

[45] Harlow, F. H. and Welch, J. E., "Numerical study of large-amplitude free-surface motions," *Phys. Fluids*, **9**, pp.842-851 (1966).

[46] Henderson, F. M., *Open Channel Flow*, Macmillan, (1966).

[47] Hinze, J. O., *Turbulence*, McGraw Hill Book Co., (1975).

[48] Hirt, C. W., Cook, J. L. and Butler, T. D., "A Lagrangian Method for Calculating the Dynamics of an Incompressible Fluid with Free Surface," J. Comput. Phys., **5**, pp.103-124, (1970).

[49] Hirt, C. W., Amsden, A. A. and Cook, J. L., "An arbitrary Lagrangian-Eulerian Computing Method for all flow speeds." *J. Comp. Phys*, **14**, pp.227-253, (1974).

[50] Hirt, C. W. and Nichols, B. D., "Volume of fluid (VOF) method for the dynamics of free boundaries," J. Comput. Phys., **39**, pp.201-255, (1981).

[51] Ho, L. -W. and Patera. A. T., "A Legendre Spectral Element Method for simulation of unsteady incompressible viscous free-surface flows," *Comp. Meth. Appl. Mech. Eng.*, **80**, pp.355-366 (1990).

[52] Hooper, A. P. and Grimshaw. R., "Nonlinear instability at the interface between two viscous fluids," *Phys. Fluids*, **28**, pp.37-45 (1985).

[53] Hopf, L., "Turbulenz bei einem Flusse," *Ann. Phys.*, Ser. 4, **32**, pp.777 (1910).

[54] Huerta, A. and Liu, W. K., "Viscous flow with large free surface motion," *Comput. Meth. Appl. Mech. Eng.*, **69**, pp.277-324 (1988).

[55] Hughes. T. J. R., Liu, W. K. and Zimmerman, T., "The Lagrangian–Eulerian finite element formulation for incompressible viscous flow," *Comput. Meth. Appl. Mech. Eng.*, **29**, pp.329–349 (1981).

[56] Hughes, T. J. R., Franca, L. P. and Balestra, M., "A new finite element formulation for computational fluid mechanics: V. Circumventing the Babuska-Brezzi condition: A stable Petrov-Galerkin formulation of the Stokes problem accommodating equal order interpolation," *Comp. Meth. Appl. Mech. Eng.*, **59**, pp.85-99 (1986).

[57] Joo, S. W., Davis, S. H. and Bankoff, S. G., "On falling film instabilities and wave breaking," *Phys. Fluids A*, **3**(1), pp.231-232 (1991a).

[58] Joo, S. W., Davis, S. H. and Bankoff, S. G., "Long-wave instabilities of heated falling films: two-dimensional theory of uniform layers," *J. Fluid Mech.*, **230**, pp.117-146, (1991b).

[59] Joo, S. W. & Davis, S. H., "Irregular waves on viscous falling films," *Chem. Eng. Commun.*, **118**, pp.111-123 (1992).

[60] Kawahara, M., Hirano, H. and Tsubota, K., "Selective lumping finite element method for shallow water flow," *Int. J. Num. Meth. Fluids*, **2**, pp.89-112, (1982).

[61] Kapitza, P. L. and Kapitza, S. P., "Wave flow of thin layers of a viscous fluid:III. Experimental study of undulatory flow conditions. *Zh. Exp. Teor. Fiz.* **19**, p.105, (1949). Also in *Collected papers of P. L. Kapitza* (ed. D. Ter Haar), vol.**2**, pp.690-709, Pergamon, (1965)

[62] Kennedy, J. F., "The mechanics of dunes and antidunes in erodible channels," *J. Fluid Mech.*, **16**, pp.521-544 (1963).

[63] Kennedy, J. F., "The formation of sediment ripples, dunes, and antidunes," *Ann. Rev. Fluid Mech.*, **1**, pp.147-168 (1969).

[64] Kheshgi, H. S. and Scriven, L. E., "Disturbed film flow on a vertical plate," *Phys. Fluids*, **30**(4), pp.990-997 (1987).

[65] Kim, J. and Moin, P., "Application of a fractional–step method to incompressible Navier–Stokes equations," *J. Comp. Phys.*, **59**, 308–323 (1985).

[66] Krantz, W. B. and Goren, S. L., "Stability of thin liquid films flowing down a plane," *Ind. Eng. Chem. Fund.*, **10**, pp.91-101 (1971).

[67] Lacroix, M. and Garon, A., "Numerical solution of phase change problems: an Eulerian–Lagrangian approach," *Num. Heat Transfer*, **19**, pp.57-78 (1992).

[68] Lacy, C. E., Sheintuck, M. and Dukler, A. E., "Methods of deterministic chaos applied to the flow of thin wavy films," *AIChE J.*, **37**, pp.481-489 (1991).

[69] Lai, C., "Numerical modeling of unsteady open-channel flow," *Adv. in Hydroscience*, **14**, 161-333 (1986).

[70] Launder, B. E. and Spalding. D. B., "The Numerical Compuation of Turbulent Flows," *Comput. Meth. Appl. Mech. Engg.*, **3**, 269-289, (1974).

[71] Le, H. and Moin, P., " An improvement of fractional step method for the incompressible Navier–Stokes equations," *J. Comp. Phys.*, **92**, 369–379 (1991).

[72] Lee, J.-J. and Mei, C. C., "Stationary waves on an inclined sheet of viscous fluid at high Reynolds and moderate Weber numbers," *Private Communication* (1995).

[73] Lemos, C. M., "A simple numerical technique for turbulent flows with free surfaces," *Int. J. Num. Meth. Fluids*, **15**, pp.127-146, (1992a).

[74] Lemos, C. M., *Wave breaking : A numerical study*, Lecture Notes in Engineering, ed. C.A. Brebbia and S.A. Orszag, Springer-Verlag, (1992b).

[75] Leutheusser, H. J. and Alemu, S., "Flow separation under hydraulic jump," *J. Hyd. Research*, **17**, pp.193-206 (1979).

[76] Lin, S. P., "Finite-amplitude stability of a parallel flow with a free surface," *J. Fluid Mech.*, **36**, pp.113-126 (1969).

[77] Lin, S. P. and Wang, C. Y., "Modeling wavy film flows," in *Encyclopedia of Fluid Mechanics* (ed. N. P. Chermemisinoff) 1, pp.931-951, Gulf, (1985).

[78] Liu, W. K., Chang, H., Chen, J. & Belytschko, T., "Arbitrary Lagrangian Eulerain Petrov–Galerkin finite elements for for nonlinear continua," *Comp. Meth. Appl. Mech. Eng.*, **68**, 259–310 (1988).

[79] Liu, J., Paul, J. D. and Gollub, J. P., "Measurements of the primary instabilities of flim flows," *J. Fluid Mech.*, **250**, pp.69-101, (1993).

[80] Liu, J. and Gollub, J. P., "Onset of spatially chaotic waves on flowing films," *Physical Review Letters*, **70**, pp.2289-2292, (1993).

[81] Liu, J. and Gollub, J. P., "Solitary wave dynamics of film flows," *Phys. Fluids*, **6**(5), pp.1702-1712 (1994).

[82] Lyn, D. A., "Turbulence measurements in open-channel flows over artificial bedforms," *J. Hyd. Engg.*, **119**, pp.306-326 (1993).

[83] Madsen, P. A., and Svendsen, I. A., "Turbulent bores and hydraulic jumps," *J. Fluid Mech.*, **129**, pp.1-25 (1983).

[84] Malamataris, N. T. and Papanastasiou, T. C., "Unsteady free surface flows on truncated domains," *Ind. Eng. Chem. Res.*, **30**, pp.2211-2219 (1991).

[85] McLean, S. R. and Smith, J. D., "A model for flow two-dimensional bedforms," **112**, pp.300-317 (1986).

[86] McLean, S. R., Nelson, J. M. and Wolfe, S. R., "Turbulence structure over two-dimensional bedforms: Implications for sediment transprt," *J. Geophysical Research*, **99**, No. C6, pp.12,729-12,747 (1994).

[87] Mendoza, C. and Shen, H. W., "Investigation of flow over dunes," *J. Hyd. Engg.*, **116**, pp.459-477 (1990).

[88] Mizukami, A. & Tsuchiya, M., "A finite element method for the three-dimensional non-steady Navier–Stokes equations," *Int. J. Num. Meth. Fluids*, **4**, 349–357 (1984).

[89] Nakaya, C., "Long waves on a thin fluid layer flowing down an inclined plane," *Phys. Fluids*, **18**, pp.1407-1412 (1975).

[90] Nelson, J. M. and Smith, J. D., "Mechanics of Flow Over Ripples and Dunes," *J. Geophysical Research*, **94**, No.C6, pp.8146-8162 (1989).

[91] Nelson, J. M., McLean, S. R. and Wolfe, S. R., "Mean flow and turbulence fields over two-dimensional bedforms," *Water Resources Research*, **29**, No.11, pp.3935-3953 (1993).

[92] Nusselt, W., "Die oberflächenkondensation des Wasserdampfes," *Z. Ver. Deut. Ing.*, **60**, pp.541-569 (1916).

[93] Oden, J. T., "Theory and implementation of high-order adaptive hp methods for analysis of incompressible viscous flows," in *Computational Nonlinear Mechanics in Aerospace Engineering*, (ed. Atluri, S. N.), AIAA Inc., 321–363 (1992).

[94] Orlanski, I., *J. Comp. Phys.*, **21**, pp.251 (1976).

[95] Patankar, S. V., *Numerical Heat Transfer & Fluid Flow*, Hemisphere, Washington, D.C. (1980).

[96] Pierson, F. W. and Whitaker, S., "Some theoretical and experimental observations of the wave structure of falling liquid films," *Ind. Engng Chem. Fundam.*, **16**, pp.401-408 (1977).

[97] Pironneau, O., "On the transport–diffusion algorithm and its applications to the Navier–Stokes equations," *Nuemrische Mathematic*, **38**, 309–332 (1982).

[98] Portalski, S. and Clegg, A. J., "An experimental study of wave inception on falling liquid films," *Chem. Eng. Sci.*, **27**, pp.1257-1265 (1972).

[99] Pracht, W. E., "Calculating three-dimensional fluid flows at all speeds with an Eulerian–Lagrangian computing mesh," *J. Comp. Phys.*, **17**, 132–159 (1975).

[100] Prokopiou, Th., Cheng, M. and Chang, H. -C., "Long waves on inclined films at high Reynolds number," *J. Fluid Mech.*, **222**, pp.665-691 (1991).

[101] Pumir, A., Manneville, P. and Pomeau, Y., "On solitary waves running down an inclined plane," *J. Fluid Mech.*, **135**, pp.27-50 (1983).

[102] Rahman, M. M., Faghri, A. and Hankey, W. L., "Computation of turbulent flow in a thin layer of fluid involving a hydraulic jump," *J. Fluids Engg.*, **113**, pp.411-418, (1991).

[103] Rajaratnam, N., *Adv. in Hydroscience*, **4**, 197-280, (1967).

[104] Ramaswamy, B. and Kawahara, M., "Arbitrary Lagrangian–Eulerian Finite Element Method for unsteady, convective, incompressible viscous free surface fluid flow," *Int. J. Num. Meth. Fluids*, **7**, pp.1053–1075 (1987a).

[105] Ramaswamy, B. and Kawahara, M., "Lagrangian Finite Element Analysis Applied to Viscous Free Surface Fluid Flow," *Int. J. Num. Methods Fluids*, **7**, pp.953-984, (1987b).

[106] Ramaswamy, B. and Kawahara, M., "An equal order velocity pressure finite element formulation for solving the time-dependent incompressible Navier–Stokes equations," *Bull. Facul. Sci. & Eng.*, Chuo Univ., pp.63-104 (1987c).

[107] Ramaswamy, B., Jue, T. C. and Akin, J. E., "Semi-implicit and explicit finite element schemes for coupled fluid/thermal problems," *Int. J. Numer. Meth. Eng.*, **34**, 675-696 (1992).

[108] Rannacher, R., "On Chorin's projection method for the incompressible Navier–Stokes equations," in *The Navier–Stokes Equations II - Theory and Numerical Methods*, (ed. J. G. Heywood etal), Lecture Notes in Mathematics, Vol.1530, Springer, Berlin, (1992).

[109] Raudkivi, A. J., "Bedforms in alluvial channels," *J. Fluid Mech.*, **26**, pp.507-514 (1966).

[110] Rice, J. G. and Schnipke, R. J., "An equal-order velocity-pressure formulation that does not exhibit spurious pressure modes," *Comp. Meth. Appl. Mech. Eng.*, **58**, pp.135-149 (1986).

[111] Richards, K. J., "The formation of ripples and dunes on an erodible bed," *J. Fluid Mech.*, **99**, pp.597-618 (1980).

[112] Richards, K. J. and Taylor, P. A., "A numerical model of flow over sand waves in water of finite depth," *Geophys. J. R. Astron. Soc.*, **65**, pp.103-128 (1981).

[113] Rosenau, P. and Oron, A., "Evolution and breaking of liquid film flowing on a vertical cylinder," *Phys. Fluids A*, **1**(11), pp.1763-1766 (1989).

[114] Roskes, G. J., "Three-dimensional long waves on a liquid film," *Phys. Fluids*, **13**, pp.1440-1445 (1970).

[115] Rosten, H. I. and Worrell, J. K., "Generalized wall functions for turbulent flow,' PHOENICS *J. Comp. Fluid Dynamics and Applications*, **1**, pp.81-109, (1988).

[116] Rouse, H., and Ince, S., *History of Hydraulics*, Iowa Institute of Hydraulic Research, State Univ. of Iowa, Iowa City, Iowa (1957).

[117] Rouse, H., Siao, T. T. and Nagaratnam, S., "Turbulence characteristics of the hydraulic jump," *J. Hyd. Div. ASCE*, (1958).

[118] Salamon, T. R., Armstrong, R. C. and Brown, R. A., "Traveling waves on vertical films: Numerical analysis using the Finite Element Method," *Phys. Fluids*, **6**, pp.2202-2220, (1994).

[119] Schneider, G. E., Raithby, G. D. and Yovanovich, M. M., "Finite-element solution procedures for solving the incompressible, Navier–Stokes equations using the equal order variable interpolation," *Num. Heat Transfer*, **1**, pp.443-451 (1978).

[120] Shames, I. H., *Mechanics of Fluids*, 3rd ed. McGraw-Hill, Inc., (1992).

[121] Shaw, C. T., "Using a segregated finite element scheme to solve the incompressible Navier–Stokes equations," *Int. J. Num. Meth. Fluids*, **12**, pp.81-92 (1991).

[122] Shen, J., "On Error Estimates of Projection Methods for Navier-Stokes Equations: First-Order Schemes," *SIAM J. Numer. Anal.*, **29**, pp.57-77, (1992).

[123] Shields, A., "Anwendung der Ahnlichkeits-Mechanik und der Turbulenz-Forschung auf die Geschiebe-bewegung," *Mitt. Preuss. Versuchsanst. Wasser Schiffsbau*, **26**, pp.1-26 (1936).

[124] Silliman, W. J. and Scriven, L. E., *J. Comput. Phys*, **34**, 287 (1980).

[125] Sivashinsky, G. I. and Michelson, D. M., "On the irregular wavy flow of liquid film down a vertical plane," *Prog. Theor. Phys.*, **63**, pp.2112 (1980).

[126] Soulaimani, A., Fortin, M., Dhatt, G. and Ouellet, Y., "Finite element simulation of two- and three-dimensional free surface flows," *Computer Methods in Applied Mechanics and Engineering,'* **86**, pp.265-296 (1991).

[127] Stainthorp, F. P. and Allen, J. M., "The development of ripples on the surface of liquid film flowing inside a vertical tube," *Trans. Inst. Chem. Engrs.* **43**, pp.85-91 (1965).

[128] Temam, R., *On the theory and numerical analysis of the Navier–Stokes equations*, North-Holland, Amsterdam (1971).

[129] Van Kan, J., "A second-order accurate pressure correction scheme for viscous incompressible flow," *SIAM J. on Scientific & Statistical Computing*, **7**, 870-891 (1986).

[130] van Rijn, L. C., "Sediment Transport, Part 1: Bed Load Transport," *J. of Hyd. Engg.*, **110**, pp.1431-1456, (1984a).

[131] van Rijn, L. C., "Sediment Transport, Part 2: Suspended Load Transport," *J. of Hyd. Engg.*, **110**, pp.1613-1642, (1984b).

[132] van Rijn, L. C., "Sediment Transport, Part 3: Bed Forms and Alluvial Roughness," *J. of Hyd. Engg.*, **110**, pp.1733-1753, (1984c).

[133] Whitaker, S., "Effect of surface active agents on stability of falling liquid films," *Ind. Engng Chem. Fundam.*, **3**, pp.132-142 (1964).

[134] White, F. M., *Viscous Fluid Flow*, McGraw-Hill, (1991).

[135] Yih, C. -S., "Stability of parallel laminar flow with a free surface," *Proc. 2nd US Congr. Appl. Mech.*, pp.623-628, ASME, (1955).

[136] Yih, C. -S., "Stability of liquid flow down an inclined plane," *Phys. Fluids*, **6**, pp.321-324, (1963).

[137] Zienkiewicz, O. C. and Wu, J., "Incompressibility without tears - how to avoid restrictions of mixed formulation," *Int. J. Num. Meth. Eng.*, **34**, pp.1189-1203 (1991).

[138] Zienkiewicz, O. C. and Wu, J., "A general explicit or semi-explicit algorithm for compressible and incompressible flows," *Int. J. Num. Meth. Eng.*, **35**, pp.457-479 (1992).